The University Of Sheffield.

The Design of Novel Pattern Reconfigurable Antennas for Mobile Networks

By:

Yingjie You

A thesis submitted in partial fulfilment of the requirements for the degree of

Doctor of Philosophy

The University of Sheffield

Faculty of Engineering

School of Electrical Engineering and Electronics

Submission Date: 31st January 2017

Abstract

This research evaluates a beam reconfigurable basestation transceiver for cellular applications from both a systems and antenna design perspective. The novelty in this research is the investigation of an automatic azimuth beamwidth switching antenna, which can effectively respond to homogeneous traffic distribution in a cellular mobile network. The proposed technique which this antenna uses is azimuth beam switching which incorporates PIN diodes to provide a reconfigurable reflecting ground plane for a three sector antenna. Numerical systems analysis has been carried out on a hexagonal homogeneous cellular network to evaluate how this reconfigurable antenna can balance mean and cell edge capacity through azimuth beamwidth reconfiguration. The optimum azimuth beamwidth is identified as 60°, which achieves the best cell capacity, and by reconfiguring the azimuth beamwidth from 60° to 110°, the maximized capacity at the edges of the cell can be improved. The influence of mechanical tilt, inter site distance, path loss model and vicinity of the cell edge for this antenna are described. This research shows that a mean cell edge improvement from 15Mbit/s to 18Mbit/s is achievable when beamwidth reconfiguration is used, and that this improvement is consistent for cell sizes from 500m to 1500m. Results from a test of an as-manufactured reconfigurable antenna are presented here, and show similar results compared to simulations.

To overcome network coverage deterioration at large antenna downtilt angles in a homogeneous cellular mobile network, different beam shaping techniques in the elevation plane, including antenna sidelobe suppressing and null filling, are discussed here. By filling up the first upper-side null for a 12-element antenna array, both the average cell edge and cell capacity can be improved. The application of this beam shaping pattern for a 12-element array is described here, for the purpose of optimising a specific cell within a mobile network which is shown below average coverage and/or capacity. By choosing a proper antenna downtilt angle for this specific cell, whilst keeping the optimum tilt angle for other cells in the network, the cell's coverage/capacity can be increased without impacting too much on the performance of other surrounding cells.

Lastly, the effects of number of antenna elements for a 60° azimuth beamwidth antenna array on the network coverage/capacity are discussed here. This research shows that, as a result of an increasing number of antenna elements in an elevation direction, network capacity can be increased along with the optimum tilt angle. This suggests that a high gain antenna array in a cellular mobile network can be potential for large site deployment and fewer installations.

Acknowledgements

To fully complete my PhD study, I would like to thank to my supervisor Dr. Lee Ford for his patient guidance and continuous support. I also want to express my gratitude to my other supervisors Professor Tim O'Farrell and Dr. Jonathan M Rigelsford. I greatly appreciate all of their advice with regards to my PhD, and I am confident that I will be able to use these research skills in my future projects.

I would like to thank all of my other colleagues in the communication group at the University of Sheffield as well. Our discussions together, and their valued experience, have helped me to clarify challenging technical issues and I wish them all the best for the future.

I would also like to pass my sincere gratitude to my family and friends, who have provided me with moral support through my research. I would especially like to thank my husband Nathan Edge for his care and love, without which I would not have been able to complete my research.

Last, but not least, I would pass my gratitude to all the staff and colleagues at the Electronic and Electrical Department who have helped me to manage my deadlines for my research, and who have always been courteous and friendly with regards to documentation and submissions.

Table of Contents

Abstract i

Acknowledgements ii

Figures ix

Tables xv

List of Publications xvii

Nomenclature xviii

Chapter 1. Introduction 21

1.1 Outline 21

1.2 Original Contribution 22

1.3 Background 23

1.3.1 Antenna Fundamentals 23

1.3.2 Field Region 23

1.3.3 Radiation Pattern of Antenna 25

1.3.4 Radiation Intensity 26

1.3.5 Beamwidth 27

1.3.6 Directivity 28

1.3.7 Antenna efficiency 29

1.3.8 Gain 31

1.3.9 Antenna input impedance 32

1.4 Fundamentals of Wireless Communication Systems 34

1.4.1 The basics of Wireless Channel 34

1.4.2 Aims of a cellular system 35

1.5 Basic Propagation Models 36

1.5.1 Definition of Path Loss 36

1.5.2 Noise Modelling 38

1.5.3 Free Space Loss 40

1.5.4 Link Budgets 41

1.6 Thesis Outline 41

Chapter 2. Literature Review 44

2.1 Reconfigurable Antenna Parts 44

2.2 Types of the reconfigurable antennas: 45

2.3 Fundamental theory and methods to achieve frequency reconfigurability 46

2.4 Fundamental theory and methods to achieve polarisation reconfigurability 47

2.5 Fundamental theory and methods to achieve radiation pattern reconfigurability 47

2.6 Fundamental theory and methods to achieve compound reconfigurable antennas 49

2.7 Applications 51

2.7.1 Reconfigurable antenna for software defined, cognitive radio systems 51

2.7.2 Reconfigurable antennas in MIMO systems 53

2.7.3 Reconfigurable antenna for space application 54

2.7.4 Reconfigurable antenna for street furniture applications 55

2.7.5 Reconfigurable antenna for base station applications 56

2.7.6 Reconfigurable antenna in Heterogeneous Networks 56

2.7.7 Reconfigurable antenna for 5G communication 58

2.8 Mobile network architecture in 4G 63

2.9 Mobile network architecture in 5G 64

Chapter 3. System Performance analysis of Cell and Edge Capacity in a Homogeneous Cellular Network 67

3.1 Introduction 67

3.2 Review of existing work 68

3.3 Research Contribution 70

3.4 Reconfigurable Network Concept 71

3.5 Reconfigurable antenna concept 72

3.6 System Simulator 75

3.6.1 Simulation Flow 76

3.6.2 System model 77

3.6.3 SINR Calculation 79

3.6.4 Tri-Sector Antenna Beamwidth Optimisation 82

3.6.5 SINR distribution 83

3.7 Cell edge detection 84

3.8 Network Performance Results 85

3.8.1 Optimum cell coverage and downtilt angle 86

3.8.2 Instantaneous cell edge performance assessment 89

3.8.3 Different path loss models verification for switching azimuth beamwidth from 60° to 110° for cell and edge capacity 93

3.8.4 Cell and edge region performances for different ISDs 98

3.8.5 Varying cell edge performance 103

3.8.6 Results summary for different ISDs 106

3.9 Summary 108

Chapter 4. Azimuth Beamwidth Reconfiguring Analysis on Homogeneous Cellular Network: Antenna Design 110

4.1 Introduction 110

4.2 Research Contribution 111

4.3 Pattern-reconfigurable antenna concept 111

4.4 Parametric Study for Single Pattern-Reconfigurable Antenna Design 113

4.4.1 Single vertical strip design with varying reconfigurable reflector length $\boldsymbol{La}$ 115

4.4.2 Single vertical strip design with varying solid metallic sheet length $\boldsymbol{Lpec}$ 118

4.4.3 Double vertical strip design with varying reconfigurable reflector length $\boldsymbol{La}$ 121

4.4.4 Double vertical strip design with varying solid metallic sheet length $\boldsymbol{Lpec}$ 124

4.4.5 Double vertical strip design with varying second vertical strip position $\boldsymbol{Lg}$ 127

4.4.6 Double vertical strip design with varying gap $\boldsymbol{Hg}$ between horizontal metallic strips 130

4.4.7 Double vertical strip design with varying vertical strip width $\boldsymbol{Ls}$ 133

4.4.8 Double vertical strip design with varying Height $\boldsymbol{Ha}$ of the antenna.....135

4.5 12-element pattern reconfigurable antenna array design and simulation.....138

4.6 System model performance comparisons.....142

4.7 Validation 145

4.7.1 60° to 110° pattern-reconfigurable antenna Test Case 145

4.7.2 60° to 90° pattern-reconfigurable antenna Test Case 149

4.8 Summary.....152

Chapter 5. Effect of Number of antenna elements on Cellular Network System 154

5.1 Introduction.....154

5.2 Review of existing Work.....155

5.3 Research Motivation 157

5.3.1 Background Technique Overview.....157

5.3.2 The effects of elevation radiation pattern for different number of antenna array elements on the system performances.....160

5.4 Array Pattern.....161

5.5 System Performance Analysis 163

5.6 Network Coverage Map with Different High Gain Antenna Configurations: 166

5.7 Summary.....169

Chapter 6. Antenna Elevation Beam Shaping for the System Performance Improvement in the cellular Mobile Network.....171

6.1 Introduction.....171

6.2 Review of existing work.....171

6.3 Research Motivation 172

6.4 Research Methodology 173

6.4.1 Antenna Downtilt Side Direction Verification 173

6.4.2 Testing Case 1: 176

6.4.3 Testing Case 2 178

6.4.4 Testing Case 3 179

6.4.5 Testing Case 4 181

6.4.6 Testing Case 5 182

6.5 Antenna Elevation Sidelobe Effects On Mobile Network Performances 184

6.6 Verification of Antenna Elevation Null filling effects on Mobile Network Performances 187

6.7 Antenna Elevation Beam Shaping Techniques in the original 12-element antenna array pattern 190

6.8 Using Taylor Beam Synthesis to achieve the first upper-side null filling without compensating the antenna gain loss. 195

6.9 Application of Antenna first upper-side null filling pattern in the mobile cellular network 201

6.9.1 Step 1: Cell edge detection 202

6.9.2 Step 2: Cell edge and cell capacity for central cell and surrounding 6 cells 202

6.9.3 Step 3: Statistical Results for cell edge and cell capacity for the cells in the first tier 205

6.10 Summary 213

Chapter 7. Conclusion and Future Work 215

7.1 Summary 215

7.2 Work Impact 217

7.3 Future Work 218

References 221

Appendix: Edge and cell capacity difference between two different scenarios 241

Figures

Figure 1: Graphic description of different regions 24

Figure 2: Antenna Coordinate System [7] 25

Figure 3: Omnidirectional antenna pattern [6] 26

Figure 4: Antenna parameters description on a directional radiation pattern 28

Figure 5: Antenna terminals (a) and losses (b) [6] 30

Figure 6: Transmitting antenna (a) and an equivalent circuit (b) 33

Figure 7: Communication system architecture 34

Figure 8: Components of wireless communication systems 37

Figure 9: Simplified two-port network system 38

Figure 10: Category of methods to achieve the reconfigurability of antenna [10] 45

Figure 11: Cognitive Radio Cycle 53

Figure 12: A pattern-reconfigurable antenna for MIMO application [10] 54

Figure 13: Deploying Helical Antennas in Progression [16] 55

Figure 14: Reconfigurable antenna with AMC unit cell [34] 55

Figure 15: 3D Multifunctional Reconfigurable Antenna. [48] 58

Figure 16: Proposed stacked microstrip patch reconfigurable antenna [49] 59

Figure 17: Parasitic layer based reconfigurable antenna [54] 60

Figure 18: Proposed multi-beam reconfigurable antenna [55] 61

Figure 19: Proposed T-shaped reconfigurable antenna [57] 62

Figure 20: Proposed Polarisation reconfigurable antenna [58] 62

Figure 21: Heterogeneous network architecture in 4G [64] 64

Figure 22: The proposed 5G HetNet with Massive MIMO and mmWave technology. [65] . 65

Figure 23: User cell distribution (a-left, b-right) 72

Figure 24: Antenna azimuth beamwidth changing from 60° to 110°. 72

Figure 25: Antenna model for reconfigurable azimuth beamwidth 74

Figure 26: Antenna azimuth (a) and elevation (b) vs. reflector length 75

Figure 27: Radiation pattern of reconfigurable antenna for 12 element antenna array 75

Figure 28: Simulation flow of mobile network system performance calculation 76

Figure 29: Cell deployment and observation area 77

Figure 30: Vertical (a) and Horizontal (b) angles 80

Figure 31: Cumulative Density Function of SINR for a range of antenna azimuth beamwidth 83

Figure 32: SINR distribution plot for; a) 60°; b) 75°; c) 90°; and d) 110° at a tilt of 1° and an ISD of 500m 83

Figure 33: Difference SINR distribution plot for; a) 60°-75°; b) 60°-90° and; c) 60°-110° at a tilt of 1° and an ISD of 500m 84

Figure 34: The detected edge of the central sector for; a) 60°; b) 75°; c) 90° and; d) 110° azimuth beamwidth at a tile of 1° and an ISD of 500m. 85

Figure 35: Average cell capacity for different azimuth beamwidth VS. Tilt angle for ISD of 500m 86

Figure 36: CDF distribution of SINR for 60° azimuth beamwidth at different tilt angles for ISD of 500m 87

Figure 37: CDF distribution of SINR for different azimuth beamwidth at tilt angle of 9° for ISD of 500m 88

Figure 38: Sector edge of the 60°azimuth beamwidth (a) superimposed on the SINR distribution plot of; b) 75°; c) 90° and; d) 100° azimuth beamwidth at a tilt angle of 1° and an ISD of 500m 89

Figure 39: Average cell edge SINR of 60° azimuth beamwidth superimposed on 75°, 90° and 110° azimuth beamwidth cell for an ISD of 500m 90

Figure 40: Average cell edge capacity of 60° azimuth beamwidth superimposed on 75°, 90° and 110° azimuth beamwidth cell for an ISD of 500m 91

Figure 41: Average cell edge SINR for different azimuth beamwidth vs tilt angle for an ISD of 500m 92

Figure 42: Average cell edge capacity for different azimuth beamwidths vs tilt angle for an ISD of 500m 92

Figure 43: Path loss vs distance, based on 3 different path loss models 95

Figure 44: Average instantaneous edge SINR of 60° and superimposed on 110° azimuth beamwidth vs tilt angles for different path loss models for an ISD of 500m 96

Figure 45: Average instantaneous edge capacity of 60° and superimposed on 110° azimuth beamwidth vs tilt angles for different path loss models for an ISD of 500m 96

Figure 46: Average cell SINR for 60° and 110° azimuth beamwidth vs tilt angles for different path loss models and an ISD of 500m 97

Figure 47: Average cell capacity for 60° and 110° azimuth beamwidth vs tilt angles for different path loss models and an ISD of 500m 98

Figure 48: Average cell edge SINR of 60° superimposed on 110° azimuth beamwidth for different ISDs vs tilt angles 99

Figure 49: Average cell edge capacity of 60° superimposed on 110° azimuth beamwidth for different ISDs vs tilt angles 99

Figure 50: Average cell SINR of 60° and 110° azimuth beamwidth for different ISDs vs tilt angles 100

Figure 51: Average cell capacity of 60° and 110° azimuth beamwidth for different ISDs vs tilt angles 101

Figure 52: Four different cell edge definitions 103

Figure 53: Detected cell edge for varying cell edge region; a) Original defined cell edge; b) Cell edge 2; c) Cell edge 3 and; d) cell edge 4 at an optimal tilt angle of 9° and an ISD of 500m 104

Figure 54: Varying cell edge capacity of 60° and superimposed on 110° azimuth beamwidth for ISD of 500m (Cell edge 1) 104

Figure 55: Varying cell edge capacity of 60° and superimposed on 110° azimuth beamwidth for ISD of 500m (Cell edge 2) 105

Figure 56: Varying cell edge capacity of 60° and superimposed on 110° azimuth beamwidth for ISD of 500m (Cell edge 3) 105

Figure 57: Varying cell edge capacity of 60° and superimposed on 110° azimuth beamwidth for ISD of 500m (Cell edge 4) 106

Figure 58: a) Geometry of the reflector antenna b) Schematic of 3-sector antenna 112

Figure 59: Unit cell illustration of reconfigurable reflector and dipole antenna 114

Figure 60: Equivalent Circuit for “On” and “Off” state for PIN diode 114

Figure 61: a) Reflection coefficient b) Azimuth Radiation Pattern for various La 117

Figure 62: a) Reflection coefficient b) Azimuth Radiation Pattern for various $Lpec$ 120

Figure 63: Double vertical strip reconfigurable reflector 122

Figure 64: a) Reflection coefficient b) Azimuth Radiation Pattern for various La.....123

Figure 65: a) Reflection coefficient b) Azimuth Radiation Pattern for various $Lpec$ 126

Figure 66: a) Reflection coefficient b) Azimuth Radiation Pattern for various Lg 129

Figure 67: a) Reflection coefficient b) Azimuth Radiation Pattern for various Hg 132

Figure 68: a) Reflection coefficient b) Azimuth Radiation Pattern for various Ls 134

Figure 69: a) Reflection coefficient b) Azimuth Radiation Pattern for various Ha 137

Figure 70: 12-element reconfigurable antenna array concept including "unit cell" element.138

Figure 71: Surface current distribution on a) "On State" b)"Off State" 140

Figure 72: a) Reflection Coefficient b) Radiation Pattern for 12-element reconfigurable antenna array 141

Figure 73: Radiation Pattern for Azimuth Plane between idealised metallic and novel pattern reconfigurable antenna array 142

Figure 74: Mean cell edge capacity for idealised and proposed reconfigurable antennas.....143

Figure 75: Mean Cell capacity for idealised and proposed reconfigurable antennas 143

Figure 76: Single element pattern-reconfigurable antenna model Simulated VS Manufactured 145

Figure 77: Antenna Simulation and Measurement reflection coefficient magnitude.....146

Figure 78: Anechoic Chamber.....148

Figure 79: Antenna Performance Test using test facility [117] 148

Figure 80: Antenna Horizontal Pattern for simulation and Measurement 149

Figure 81: Schematic of the pattern-reconfigurable antenna 150

Figure 82: Surface current for PIN diodes states a) "ON" b) "OFF" 151

Figure 83: Comparisons between measured and simulated azimuth radiation patterns 152

Figure 84: Antenna array for far-field observation.....155

Figure 85: Single Reflector Antenna Model 160

Figure 86: Vertically stacked antenna array elements 161

Figure 87: Various Antenna array Elevation Pattern.....162

Figure 88: Antenna Elevation Gain VS Antenna Vertical HPBW 163

Figure 89: Cell edge of central sector for 60° azimuth case 165

Figure 90: Antenna Downtilt for mobile network Coverage 165

Figure 91: Coverage of a three-sector 60° azimuth antenna with tilt of 6°: a) 6-element array b)12-element array, and c) 20-element array 166

Figure 92: a), b) Cell edge and cell capacity VS Antenna downtilt angle.....169

Figure 93: Antenna Radiation pattern for the 12-element array.....174

Figure 94: Elevation beam shaped pattern without sidelobes 175

Figure 95: SINR distribution plots at antenna downtilt of a)0° and b)15° 175

Figure 96: Five different elevation shaped beam pattern for tesing cases 176

Figure 97: Testing Elevation pattern 1.....177

Figure 98: SINR distribution plots at antenna downtilt of a) 14° and b) 15°.....177

Figure 99: Testing Elevation Pattern 2 178

Figure 100: SINR distribution plots at antenna downtilt of a)0°, b)15° and c) -15° 179

Figure 101: Testing Elevation Pattern 3 180

Figure 102: SINR distribution plots at antenna downtilt of a)0°, b)15° and c) -15° 181

Figure 103: Testing Elevation Pattern 4 181

Figure 104: SINR distribution plots at antenna downtilt of a)0° and b)10° 182

Figure 105: Testing Elevation Pattern 5 183

Figure 106: SINR distribution plots at antenna downtilt of a)0° and b)15° 183

Figure 107: Sidelobe shaped elevation pattern VS Original elevation pattern 185

Figure 108: a), b) Cell edge and Cell Capacity for Sidelobe shaped pattern VS Original pattern.....187

Figure 109: Different upper null filling elevation pattern.....188

Figure 110: a), b) Cell edge and Cell Capacity for different upper null filling patterns 189

Figure 111: Binominal shaped elevation pattern VS Original elevation pattern.....191

Figure 112: Chebychev shaped elevation pattern VS Original elevation pattern 195

Figure 113: a) Amplitude distribution b) Phase distribution VS Antenna Elements 198

Figure 114: Upper-side null filling patterns VS original elevation pattern 199

Figure 115: a), b) Edge and cell capacity for different upper-side null filling patterns 200

Figure 116: Cell edge detection for tilt angle of 0°, 6°, and 12° of 60° azimuth beamwidth case for ISD of 500m network.....202

Figure 117: a), b) Cell edge and Cell capacity VS Tilt angle for first upper-side null filling to 6dB pattern 204

Figure 118: a) cell edge and b) cell capacity for tilt angle of 7.5° at the centre cell only 207

Figure 119: a) cell edge and b) cell capacity for tilt angle of 7° at the centre cell only 207

Figure 120: a) cell edge and b) cell capacity for tilt angle of 6.5° at the centre cell only 208

Figure 121: a) cell edge and b) cell capacity for tilt angle of 6° at the centre cell only 208

Figure 122: a) cell edge and b) cell capacity for tilt angle of 5.5° at the centre cell only 209

Figure 123: a) cell edge and b) cell capacity for tilt angle of 5° at the centre cell only 209

Figure 124: a) cell edge and b) cell capacity for tilt angle of 4.5° at the centre cell only 210

Figure 125: a) cell edge and b) cell capacity for tilt angle of 4° at the centre cell only 210

Figure 126: a) cell edge and b) cell capacity for tilt angle of 3.5° at the centre cell only 211

Figure 127: a) cell edge and b) cell capacity for tilt angle of 3° at the centre cell only 211

Figure 128: a) cell edge and b) cell capacity for tilt angle of 2.5° at the centre cell only 212

Tables

Table 1: Comparison between different types of switches 50

Table 2: The properties of different types of electric and optical switches [10].....51

Table 3: System simulation parameters.....78

Table 4: Summaries of cell edge and cell capacity for different ISDs at an optimum tilt angle of
9°.....102

Table 5: Summaries of the varying cell edge capacity for different ISDs between 60° and 110° azimuth beamwidth at optimum tilt angle of
9°.....107

Table 6: Summary of antenna parameters.....115

Table 7: Antenna Parameters for Section 4.4.1.....116

Table 8: Reconfigurable reflector length VS. Antenna azimuth beamwidth.....118

Table 9: Antenna Parameters for Section 4.4.2.....119

Table 10: Solid metallic sheet length VS. Antenna azimuth beamwidth.....120

Table 11: Antenna Parameters for Section 4.4.3.....121

Table 12: Reconfigurable reflector length VS. Antenna azimuth beamwidth.....124

Table 13: Antenna Parameters for Section 4.4.4.....124

Table 14: Solid metallic sheet length VS. Antenna azimuth beamwidth.....126

Table 15: Antenna Parameters for Section 4.4.5.....127

Table 16: Second vertical strip position VS. Antenna azimuth beamwidth.....129

Table 17: Antenna Parameters for Section 4.4.6.....130

Table 18: The gap between horizontal metallic strips VS. Antenna azimuth beamwidth.....132

Table 19: Antenna Parameters for Section 4.4.7.....133

Table 20: The vertical strip width VS. Antenna azimuth beamwidth.....135

Table 21: Antenna Parameters for Section 4.4.8.....135

Table 22: Dimension of a single pattern-reconfigurable antenna element.....139

Table 23: Summaries of different cell edge and cell capacity for different ISDs at an optimum tilt angle of 9°.....144

Table 24: System Simulator Parameters.....164

Table 25: Calculated edge and cell capacity with different antenna array configurations (6-element, 12-element and 20-element with 60° azimuth beamwidth at antenna downtilt angle of 6°).....167

Table 26: Comparison between relative amplitude and the number of elements in an array.....191

Table 27: Statistical results for Edge and cell capacity difference between the two different scenarios for tilt of 7.5° applied to centre cell in Scenario 1.....206

List of Publications

1. Y. You, J. M. Rigelsford, K. L. Ford and T. O'Farrell, "A dynamic basestation antenna with reconfigurable azimuth beamwidth," The 8th European Conference on Antennas and Propagation (EuCAP 2014), The Hague, 2014, pp. 1889-1892.

2. Y. You, K. L. Ford, J. M. Rigelsford and T. O'Farrell, "Analysis of the use of beam reconfigurable antennas in a homogeneous cellular network deployment," 2014 Loughborough Antennas and Propagation Conference (LAPC), Loughborough, 2014, pp. 169-172.

3. Y. You, K. L. Ford, J. M. Rigelsford and T. O'Farrell, " Systems analysis of a pattern reconfigurable antenna for capacity improvement of cell edge users in cellular networks" submitted to IEEE Transactions on Vehicular Technology.

Nomenclature

SINR, γ	Signal to Noise and Interference Ratio
RAN	Radio Access Network
BS	Base Station
MS	Mobile Station
RNC	Radio Network Controller
GEO	Geographical Coverage
CoMP	Coordinated Multipoint
MIMO	Multiple Input Multiple Output
LTE	Long Term Evolution
ISD	Inter-Site Distance
EM	Electromagnetic
D_i	Largest dimension of the space surrounding an antenna
r	Distance from/between the antenna
λ	Wavelength
E (plane)	Electric field vector
H (plane)	Magnetic field vector
ϕ	Antenna azimuth angle
θ	Antenna elevation angle
E_θ	Component of elevation angle in the electric field
E_ϕ	Component of elevation angle in the magnetic field
η	Intrinsic Impedance of radiation medium
FNBW	First Null Beamwidth
HPBW	Half Power Beamwidth
SLL	Side Lobe Level
F/B	Front/Back (Ratio)
D	Directivity
D_0	Maximum value for Directivity
U	Radiation intensity
U_0	Radiation intensity from isotropic source
P_{rad}	Total radiated power from antenna
e_0	Total efficiency
e_r	Reflection efficiency
e_c	Conduction efficiency
e_d	Dielectric efficiency
Γ	Voltage reflection coefficient
Z_{in}	Antenna input impedance
Z_0	Transmission line impedance
VSWR	Voltage Standing Wave Ratio
e_{cd}	Radiation efficiency
P_{in}	Antenna input power
G	Antenna gain
G_{abs}	Absolute gain
$G_{o\ abs}$	Maximum absolute gain
Z_A	Antenna impedance at terminal a-b
R_A	Antenna resistance at terminal a-b

R_r	Radiation resistance
R_L	Loss resistance
X_A	Antenna reactance
R_g	Generator resistance
X_g	Generator reactance
BER	Bit Error Rate
P_T	Transmitter power
L	Path loss
L_T	Feeder loss at transmitter
G_T	Transmitter gain
G_R	Receiver gain
L_R	Feeder loss at receiver
P_R	Receiver power
EIRP, P_{TI}	Effective isotropic radiated power
EIPR, P_{RI}	Effective isotropic power received
L_{db}	Maximum acceptable path loss (dB)
F	Noise factor
T	Temperature
k	Boltzmann's constant
B	Effective bandwith
N_{in}	Input noise divided by gain
N_{out}	Output noise divided by gain
F_{db}	Noise power (decibels)
T_e	Equivalent input noise temperature
L_F	Propagation loss in free space
f	Frequency
L_{ex}	External system losses
RA	Reconfigurable Antennas
RF-MEMS	Radio Frequency Microelectromechanical System
FET	Field Effect Transistor
PIFA	Planar Inverted F-type Antenna
AMC	Artificial Magnetic Conductor
EBG	Electromagnetic Band Gap
WiMAX	WorldWide Interoperability for Microwave Access
TSA	Tapered Slot Antenna
CPW	Coplanar Waveguide
HSPA	High Speed Package Access
IoT	Internet of Things
RAT	Radio Access Technology
QoS	Quality of Service
FFR	Fractional Frequency Reuse
SFR	Soft Frequency Reuse
RB	Resource Block
OFDMA	Orthogonal Frequency-Division Multiple Access
DAS	Distributed Antenna Systems
CoMP	Coordinated Multipoint
ESPAR	Electrically Steerable Passive Array Radiator
L_a	Length of Antenna Reflector
H_a	Height of Antenna Reflector

d_p	Dipole-to-Reflector distance
BTS	Base Transceiver Station
A	Antenna Pattern
N	Number of BSs in RAN
M	Number of sections in BTS
AWGN/n_0	Additive White Gaussian Noise
n_{UE}	User noise figure
h	User antenna height
H	Basestation antenna height
θ_t	Antenna downtilt angle
α	Adjustment angle
I	Received power
Ci	Maximum throughput
CDF	Cumulative Density Function
C_{edge}	Total edge capacity of central sector of cell
C	Central sector edge capacity
NLOS	Non-Line of Sight
L_p	Path loss from Cost-231-Hata path loss model
L_{NLOS}	Path loss from Cost 231-Walfisch-Ikegami NLOS model
L_{FS}	Free Space Path Loss
L_{RTS}	Roof-to-Street loss
L_{ori}	Street Orientation Loss
L_{MSD}	Multi-Diffraction loss
CST	Computing simulation technology
$\Delta\varphi$	Phase of the wave radiated from dipole antenna
φ_r	Phase of the reflective wave
φ_t	Radiated wave from dipole antenna
h_s	Distance from the dipole antenna to the apex of the reflector
R_s	Equivalent diode resistance
L_d	Inductance of diode
R	Electrical Resistance
C_s	Shunted Capacitance of diode
L_a	Reconfigurable Reflector Length
H_1	Height between antenna bottom surface and PIN diode
H_2	Space between PIN diodes
H_g	Gap between antenna horizontal strips
L_{pec}	Solid Metallic Sheet Length
H_a	Recofigurable antenna height
L_g	Second strip vertical position
L_s	Antenna strip width
PCB	Printed Circuit Board
VNA	Vector Network Analyser
AUT	Antenna Under Test

Chapter 1. Introduction

1.1 Outline

As a result of exponential data growth in wireless communication systems coupled with increasing demanding for mobile data, spectrum shortage is becoming an increasingly prominent problem in current 4G mobile networks and is a recognised issue for the implementation of future 5G systems. The wireless industry is researching ways to serve their mobile users more efficiently and to a greater degree of cost effectiveness. The mobile users served by any wireless network need to have at least the required radio coverage to enable their required wireless network connectivity, and the offered network capacity needs to provide the maximum coverage footprint with the maximum application throughput. They also require a high signal to noise and interference ratio (SINR) within their mobile network, as this results in better service across the radio access network (RAN), which in turn results in more revenue and greater customer satisfaction.

Today, in the first phase of base station deployment, mobile network operators use radio network planning tools to provide coverage for a typical geographical area that a base station (or cells) needs to cover. These tools are critical in accurately simulating coverage and interference, taking into account the transmitter and receiver parameters of Base Stations (BS's) and Mobile Stations (MS's) in a particular coverage area, as well as the formation of typical link-budgets. The main problem with these techniques is the fact that they do not take into account the performance aspects of the BS-MS radio links (i.e. planning for mobile and changing traffic demands). It is obvious that attempting to simulating future mobile traffic is a very complicated task (if not impossible) with the available system and tools a mobile network operator has to hand: it is not yet possible to predict radio traffic in real time, nor to respond effectively to changing demand from mobile users within the Radio Network Controller (RNC) system.

To tackle this problem, dynamic radio planning techniques need to be enforced: The term 'dynamic' here refers to the fact that since usage and traffic in a cell's Geographical Coverage (GEO) area can change constantly, network coverage should therefore also be able to respond rapidly match these changing needs. An example of a dynamic radio planning technique is deploying a cognitive and reconfigurable network, which has the ability and capacity to identify an optimum radio strategy which would best meet customer data

demands, and then change the network structure to suit this strategy. These networks have the ability to change fundamental system properties on-demand, such as the system frequency, the beam pattern and polarisation: they do this by analysing the feedback from both channel estimations and from the signal quality [1]. Other possible solutions such as deployed device-to-device communication around cell edge of a macro cell, coordinated multipoint (CoMP) Multiple Input Multiple Output (MIMO) techniques and beamforming have also been suggested as dynamic radio planning techniques as they all have the potential to improve cell edge coverage and throughput ([2] to [5]).

Specific to this research, reconfigurable antennas have been studied to analyse their potential to achieve greater network flexibility and solve the challenges which modern mobile networks face. These have been chosen due to their inherent advantages in their ability to change network characteristics simply and flexibly without applying complicated feeding network systems. To address specific challenges which current and future systems are facing, considering both the azimuth plane from the direction of beam travel and the vertical plane, a novel pattern-reconfigurable antenna is proposed.

1.2 Original Contribution

The original contribution of this thesis is summarised as follows:

a) A novel pattern-reconfigurable antenna is designed and tested here for a mobile network system which can switch its azimuth automatically by using PIN diode switches. The simulated reflection coefficient and radiation pattern from this antenna match closely from measured results from the test of a prototype.

b) The application of this 12-element pattern-reconfigurable antenna array for the dynamic azimuth planning in a homogeneous cellular network is investigated, combined with the effects of antenna downtilt angle, different Inter-Site Distances (ISDs), Path loss models and the effect of the vicinity of the cell edge on antenna performance. It is found that a typical capacity increase of 20% is achievable by switching the azimuth beamwidth of the base station antenna from 60° to 110°. This capability provides the potential to trade off overall cell capacity against cell edge user capacity and is applicable for a range of cell sizes.

c) Antenna elevation beam shaping, which is achieved by filling the first upper side null, is applied for the proposed pattern-reconfigurable antenna array. It is found to improve the network coverage performance at a large antenna downtilt angle. The application of this beam shaped pattern is in optimising a particular cell which has below-network average performances, by choosing a proper downtilt angle for it whilst still keeping the optimum tilt angle for the other surrounding cells.

d) The effect of the number of elements for this pattern-reconfigurable antenna array is investigated on the cell edge and overall cell coverage and capacity. By increasing the number of antenna elements in the system, performance at both the cell edge and for the overall network can be improved along with its optimum angle, due to the increased antenna gain. This finding suggests that this high-gain antenna array in a homogenous mobile network can be used for large-site separations and fewer installations.

1.3 Background

1.3.1 Antenna Fundamentals

Antennas are devices which transmit and receive low frequency electromagnetic (EM) waves. Transmitting antenna operate by converting electrical currents in conductors into an EM field in free space, whereas receiving antennas operate in the opposite fashion. It is necessary to use different parameters in order to analyse how an antenna performs as part of a telecommunication network. These can be correlated amongst each other, and specific parameters can be used to evaluate an antenna's performance under different environmental conditions. This section describes antenna parameters which are most often used to evaluate performance in antenna systems. [6]

1.3.2 Field Region

The characteristics of the EM fields emitted by an antenna can vary, and depend on the distance between an observer and the antenna in question. The space surrounding an antenna, with a largest dimension of D_i, is customarily classified into three categories: [6]

a) The reactive near field region;

b) The radiating near field (Fresnel) region, and;

c) The far field (Fraunhofer) region

These are shown in Figure 1. In the reactive near-field region EM energy is stored, and the electric and magnetic fields generated by the antenna are out of phase. In the radiating near field (Fresnel) region part of the EM energy is radiated out from the antenna, although there are still strong magnetic and electric fields present: move away from this region and it would be seen that a constant pattern of EM radiation begins to dominate the total energy which an antenna emits [6].

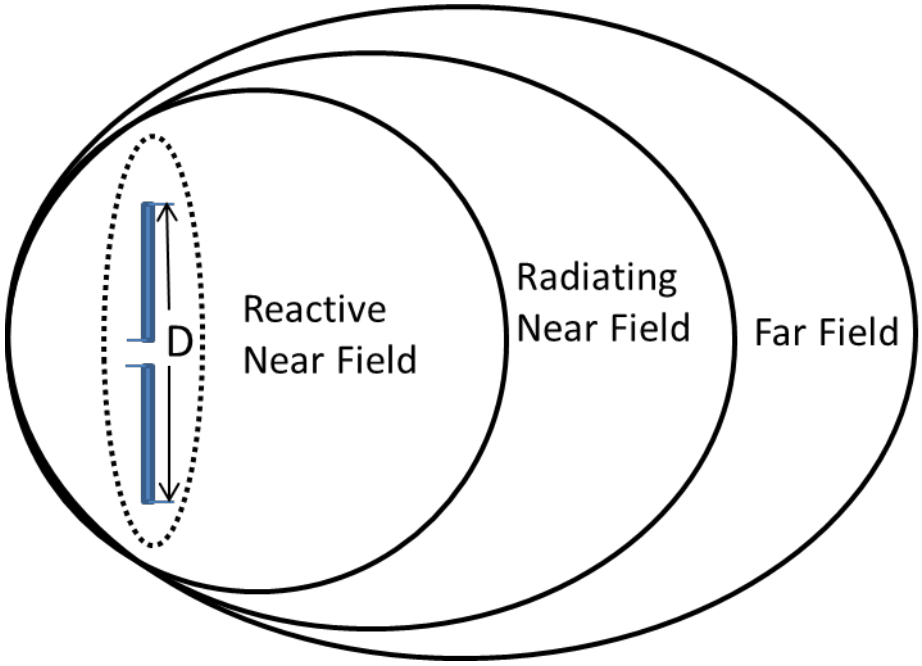

Figure 1: Graphic description of different regions

To numerically identify the boundary between different regions, both the antenna size and wavelength of the transmitted EM energy need to be considered. Equations (1.1), (1.2) and (1.3) compare the relationship between the antenna size and field wavelength for these three key antenna regions:

Reactive near-field region: $$r_1 < 0.62\sqrt{\frac{{D_i}^3}{\lambda}} \quad (1.1)$$

Radiating near-field region: $$0.62\sqrt{\frac{{D_i}^3}{\lambda}} \leq r_2 < \frac{2{D_i}^2}{\lambda} \quad (1.2)$$

Far Field region: $$r_3 \geq \frac{2{D_i}^2}{\lambda} \quad (1.3)$$

Here r is the distance from the antenna, D_i is a representation of the largest dimension of the antenna and λ is the wavelength of the radiation produced by the antenna.

1.3.3 Radiation Pattern of Antenna

The behaviour of the radiation emitted in the antenna into the surrounding space is complicated, and necessitate accurate graphical descriptions in terms of special coordinates (or alternatively through mathematical functions). EM radiation dominates the energy emitted in the far field region of an antenna, as outlined previously: the strength (or amplitude) of the radiation emitted will vary across a constant radius, drawn outwards from the antenna. This is shown in Figure 2 using a spherical coordinate system (r, θ, φ), for an antenna which it is located at or near a system's origin [6].

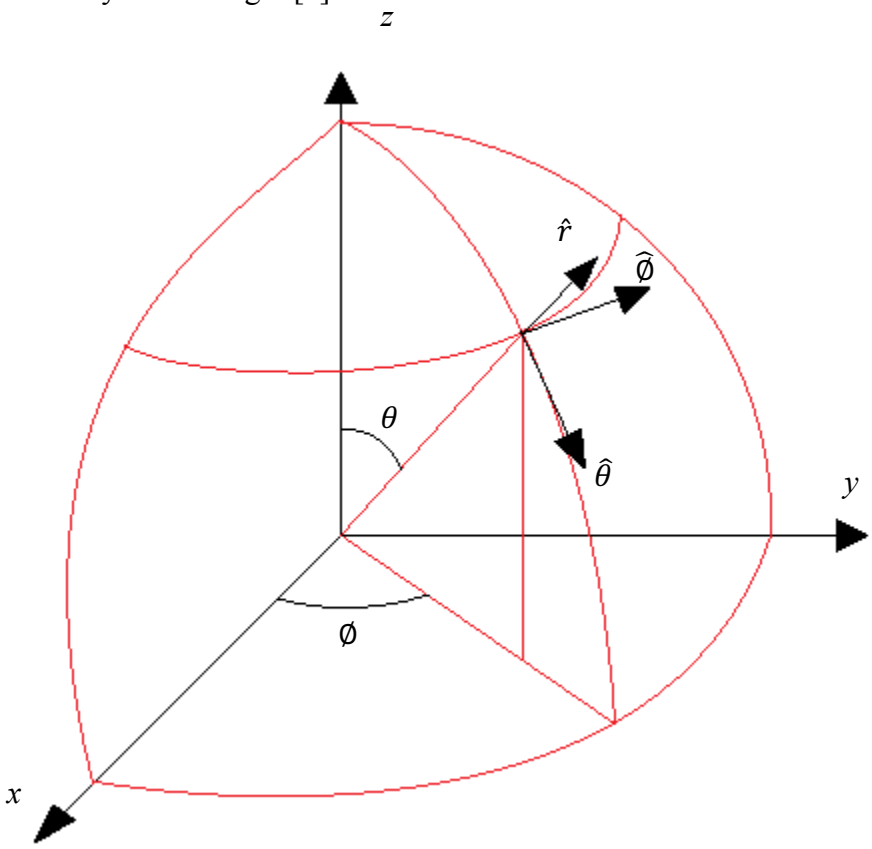

Figure 2: Antenna Coordinate System [7]

The performance of an antenna within this coordinate system is often represented in terms of electric and magnetic field vectors, also known as the E and H plane respectively. These two

planes lie perpendicular to each other and are known as the Principal planes. Within Figure 2, ϕ represents the azimuth angle of the antenna and θ represents the corresponding antenna elevation angle. These are mathematical expressions which are used to describe how an antenna performs within the two Principal planes.

The cutting procedures shown in Figure 3 demonstrate two 2D cuts of an omnidirectional radiation pattern, and show the relationship between the magnetic and electric field generated by an antenna.

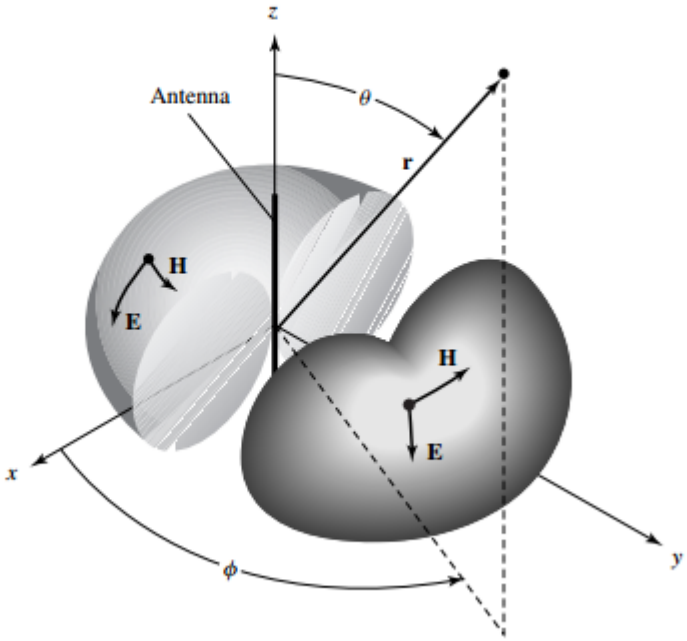

Figure 3: Omnidirectional antenna pattern [6]

1.3.4 Radiation Intensity

As alluded to in Section 1.3.2, assuming a large distance from an observer to the antenna, the pattern of the EM radiation which the antenna emits stays constant in its far field region. As a result, the intensity of the pattern from an antenna can be expressed as a normalised EM power density function, which does not contain terms for the distance between the antenna and observer: usually it is described as the angular distribution of power. A mathematical expression of this is outlined in equation (1.4). [6]

$$U(\theta,\varphi)=\frac{r^2}{2\eta}\left|E(r,\theta,\varphi)\right|^2\cong\frac{r^2}{2\eta}\left[\left|E_\theta(r,\theta,\varphi)\right|^2+\left|E_\varphi(r,\theta,\varphi)\right|^2\right]$$
$$\cong\frac{1}{2\eta}\left[\left|E_\theta^o(r,\theta,\varphi)\right|^2+\left|E_\varphi^o(r,\theta,\varphi)\right|^2\right] \quad (1.4)$$

Here $E(r,\theta,\varphi)$ is the intensity of the electric field emitted from the antenna in the far field region, and is further evaluated in equation (1.5):

$$E(r,\theta,\varphi)=E^o(\theta,\varphi)\frac{e^{-jkr}}{r} \quad (1.5)$$

Here E_θ and E_φ represent the components of the electric field of the antenna in its far field range in terms of the azimuth and elevation angle, while η is the intrinsic impedance of the medium through which the radiation travels.

1.3.5 Beamwidth

Another parameter associated with the antenna radiation pattern is beamwidth. The basic antenna beamwidth is defined as the width (in angles) of the opposite sides of the radiation pattern. There are a number of mathematical definitions of beamwidth, however one which is commonly used is the angular difference between two beams, both of which have a radiation intensity which is half that of the main beam. This is called the Half-Power Beamwidth (HPBW). Alternatively, a different definition is the difference in angles between the first troughs (or 'nulls') of the radiation interference fringes, which is commonly referred to as the First-Null Beamwidth (FNBW). Both of these definitions are shown graphically in Figure 4. [6].

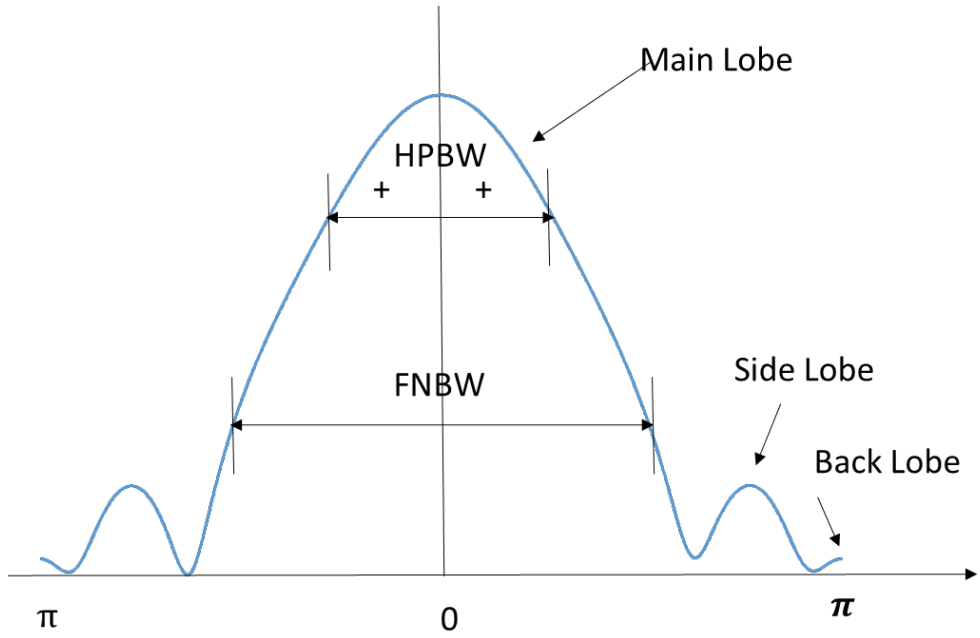

Figure 4: Antenna parameters description on a directional radiation pattern

Figure 4 also shows the parameters 'side lobe' and 'back lobe'. The Side Lobe Level (SLL) is defined as the power difference between the main lobe and the maximum power experienced in the side lobe direction, in decibels (dB). A high side lobe value is not desired as this indicates that the antenna is transmitting a large proportion of its radiation outside of the antenna main lobe direction, whereas for a directional antenna it is desired that the majority of radiation is transmitted in a controlled direction. The other parameter is called Back Lobe, which is defined as power which is emitted from the 'rear' of the antenna (i.e. the direction which is the opposite of the main beam). It is often used as part of a parameter called Front/Back Ratio (F/B Ratio), as the difference (in decibels) between the power emitted in the direction of main lobe and the direction from the back of the antenna.

1.3.6 Directivity

Directivity of the antenna can be defined as the ratio between the intensity of the radiation emitted in a desired direction and the average radiated power which is emitted in all directions from the antenna. This is related to the average radiation intensity from an antenna which, given the spherical terms adopted for the radiation emitted, can be calculated as the total power radiated by the antenna divided by 4π. A simplification of the relationship between directivity and average radiation intensity can be derived by understanding that the degree of directivity of a non-isotropic source (i.e. a source which has clear directional

properties) is equal to the ratio of the radiation intensity in a given direction (from the directional antenna in question) to the radiation intensity from an isotropic source. The directivity of a directional antenna is shown in equation (1.6). [6]

$$D = \frac{U}{U_0} = \frac{4\pi U}{P_{rad}} \tag{1.6}$$

If an antenna's direction is left unspecified, a value for maximum directivity can be calculated using equation (1.7).

$$D_{\max} = D_0 = \frac{U|_{\max}}{U_0} = \frac{U_{\max}}{U_0} = \frac{4\pi U_{\max}}{P_{rad}} \tag{1.7}$$

Here D represents directivity in a given direction (which is dimensionless), D_0 is the maximum value for directivity (dimensionless), U is the radiation intensity (Watts (W)/unit solid angle), U_{max} is the maximum radiation intensity, U_0 is the intensity of the radiation from an isotropic source and P_{rad} is the total radiated power from an antenna in Watts (W).

1.3.7 Antenna efficiency

As the power delivered to the antenna cannot all be converted to useful radiation, there are losses at the antenna's terminal and within the antenna structure. Figure 5 shows that antenna losses can be a result of reflection (i.e. mismatches in electrical impedance between the antenna and its transmission line), electrical conduction within the antenna and as a result of dielectric loss (I^2R).

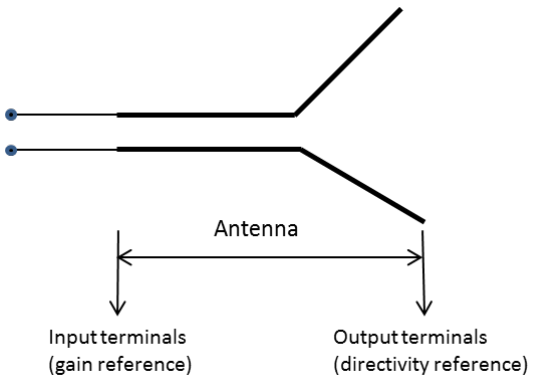

a)

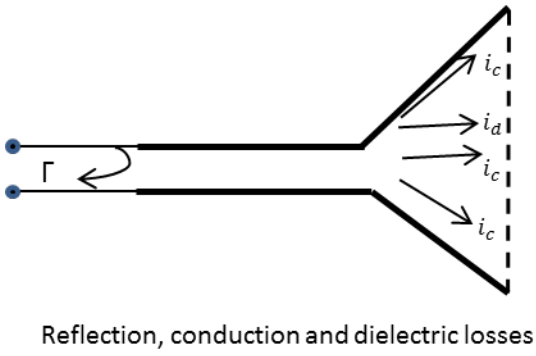

b)

Figure 5: Antenna terminals (a) and losses (b) [6]

Losses in an antenna can alternatively be expressed as a number of different antenna efficiencies, where there total efficiency e_0 takes into account all of the losses which an antenna experiences (as shown in Figure 5 (b)). Total efficiency is expressed mathematically in equation (1.8). [6]

$$e_o = e_r e_c e_d \tag{1.8}$$

Where e_r , e_c and e_d represent the reflection, conduction and dielectric efficiency respectively. The reflection efficiency can be further defined as:

$$e_r = 1 - |\Gamma|^2 \tag{1.9}$$

In equation (1.9), Γ is called the voltage reflection coefficient, and applies at the input terminals of the antenna. This term is equal to the following expression:

$$\Gamma = \frac{(Z_{in} - Z_o)}{(Z_{in} + Z_o)} \tag{1.10}$$

Here Z_{in} and Z_0 represent the antenna input impedance and the transmission line characteristic impedance respectively. Related to this is the Voltage Standing Wave Ratio (VSWR), which is:

$$VSWR = \frac{1+|\Gamma|}{1-|\Gamma|} \tag{1.11}$$

Usually e_c and e_d are experimentally determined: however it is more common to write the total antenna efficiency in terms of the antenna radiation efficiency e_{cd}, as shown in equation (1.12):

$$e_o = e_r e_{cd} = e_{cd}(1-|\Gamma|^2) \tag{1.12}$$

The antenna radiation efficiency is dependent on the antenna gain and directivity: a definition of antenna gain is outlined below.

1.3.8 Gain

The antenna gain is closely relevant to antenna directivity: however, whereas the directivity of the antenna does not consider antenna efficiency, antenna gain takes both the antenna directivity and efficiency into account. Antenna gain is the ratio of the intensity of emitted radiation in a known direction compared to the intensity radiated if the antenna was an isotropic source (which is equal to the antenna input power divided by 4π). A mathematical expression for this is shown in equation (1.13). [6]

$$G = 4\pi \frac{radiation\ intensity}{total\ input\ (accepted)\ power} = 4\pi \frac{U(\theta,\varphi)}{P_{in}} \tag{1.13}$$

In most situations the term relative gain is used, which is the ratio between a given direction antenna gain to that of a reference antenna in an arbitrary reference direction. Usually, the reference antenna is of a type where their gain is known or can be calculated, such as dipoles or horns.

As antenna gain is closely related to both efficiency and directivity, the total power which is radiated from the antenna P_{rad} must also be related to the power input P_{in} into the antenna as shown in equation (1.14). [6]

$$P_{rad} = e_{cd} P_{in} \tag{1.14}$$

In order to take the reflection and mismatch losses from the antenna into account, the term absolute gain is used. The mathematical expression for this is shown in equation (1.15). [6]

$$G_{abs}(\theta,\varphi) = e_r G(\theta,\varphi) = (1-|\Gamma|^2)G(\theta,\varphi)$$
$$= e_r e_{cd} D(\theta,\varphi) = \mathrm{e}_o\, D(\theta,\varphi) \tag{1.15}$$

Where e_0 is the overall efficiency defined in equation (1.12). Similarly, the maximum absolute gain can be correlated to the maximum directivity and the mathematical expression is shown in equation (1.16).

$$G_{o\,abs} = G_{abs}(\theta,\varphi)\big|_{max} = e_r G(\theta,\varphi)\big|_{max} = (1-|\Gamma|^2)G(\theta,\varphi)\big|_{max}$$
$$= e_r e_{cd} D(\theta,\varphi)\big|_{max} = e_o D(\theta,\varphi)\big|_{max} = e_o D_o \tag{1.16}$$

1.3.9 Antenna input impedance

The input impedance of the antenna is the ratio of input voltage to current at the antenna's terminals, or alternatively as the ratio between the electric and magnetic fields at the terminals. Figure 6 shows a diagram of an antenna and its representative circuit [6].

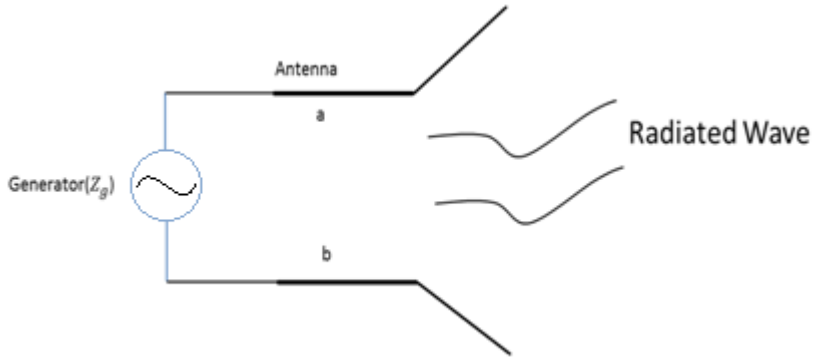

a)

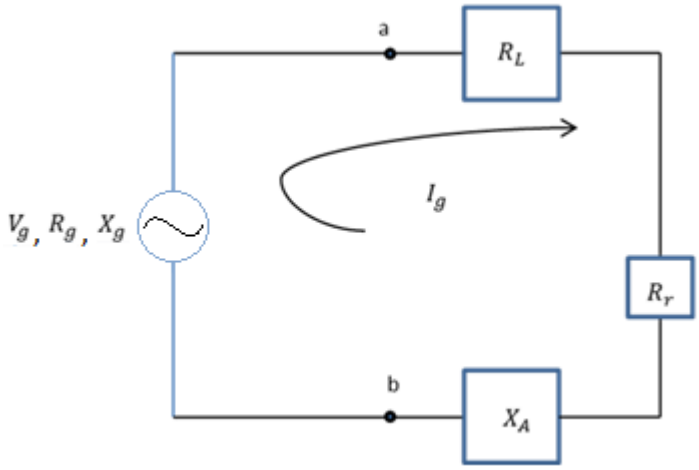

b)

Figure 6: Transmitting antenna (a) and an equivalent circuit (b)

The impedance of the antenna can be expresses in equation (1.17). [6]

$$Z_A = R_A + jX_A \tag{1.17}$$

Here Z_A represents the impedance of the antenna at terminal a-b, whereas R_A is the resistance of the antenna at terminal a-b. Consequently, X_A is the corresponding reactance of the antenna. All of these terms are measured in Ohms (Ω). The resistance of the antenna is comprised of two terms called radiation resistance (R_r) and loss resistance (R_L), as shown in equation (1.18).

$$R_A = R_r + R_L \tag{1.18}$$

Assuming that the generator is used in the antenna transmitting side, the internal impedance of the generator can be expressed in equation (1.19)

$$Z_g = R_g + jX_g \tag{1.19}$$

Where R_g and X_g are the resistance and reactance of the generator respectively. Please note that both these terms are also measured in Ohms. As EM power moves through the antenna via transmission lines or waveguides, some power is lost due to reflection and/or attenuation. In order to maximise the power delivered to the antenna, the impedance at the antenna input

must be matched with transmission line impedance (which is usually in the order of 50 ohms). The mathematical equation for this situation is shown in (1.20). [6]

$$R_r + R_L = R_g$$
$$X_A = -X_g \tag{1.20}$$

1.4 Fundamentals of Wireless Communication Systems

1.4.1 The basics of Wireless Channel

An understanding of wireless channels is necessary to effectively operate, design and analyse any wireless system. A generic wireless communication system is shown in Figure 7. Here an information source attempts to send a signal from a transmitter/receiver unit through a communication channel: however, as it does this the signal is subjected to interference and distortion due to noise, thus changing fundamental signal characteristics such as amplitude or phase. This means that the final received signal may be illegible or distorted, and so the receiver needs to be able to overcome common signal distortions with as few errors as possible [7].

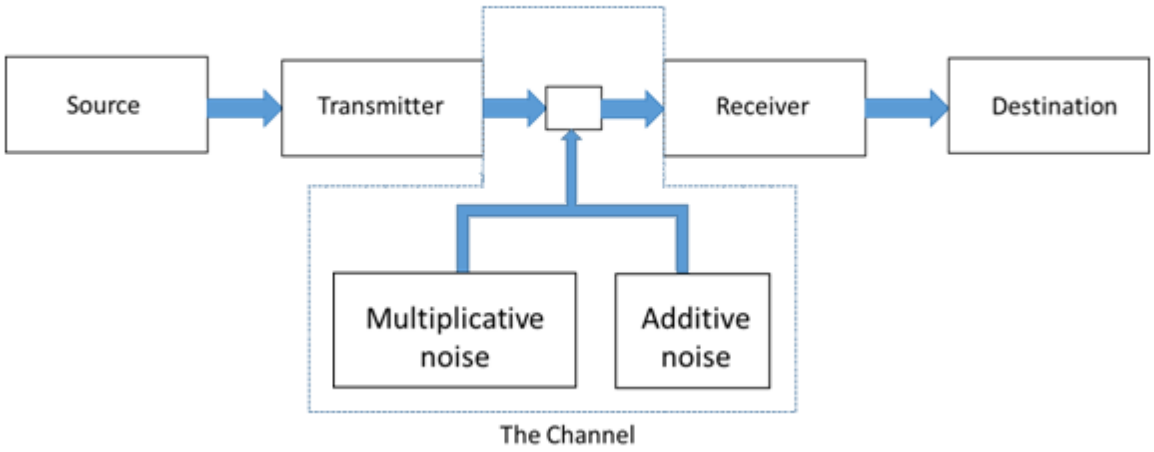

Figure 7: Communication system architecture

In any wireless system, noise can be classified into multiplicative and additive categories, as shown in Figure 7. Additive noise comes from sources which are both internal and external to the antenna, such as thermal noise, shot noise, cosmic radiation interference and local changes in the atmospheric. It can also be a result of interference from other transmitters, a

phenomenon which it is important to control carefully especially when reusing the number channels in the system to maximise capacity. Alternatively, multiplicative noise can arise when the transmitted the signal encounters objects as it travels from the transmitter to the receiver. This noise can result from:

- Directional properties (which are inherent to transmitters and receivers)
- Reflection of the signal from 'smooth' surfaces including walls, buildings and hills
- Absorption from features such as buildings, and from the atmosphere
- Scattering of the signal across rough edges
- Refraction resulting from different atmospheric layers and certain types of materials

Multiplicative noise in the wireless channel can be further divided into three different time-varying types known as path loss, shadowing (slow fading) and fast fading (also known as multipath fading). These three types of fading are due to the relative position change and objects or materials between the transmitter and receiver.

1.4.2 Aims of a cellular system

The complexity of the system has the most significance on the network design. It can influence the parameters of channel. So, the cellular system has the three key aims: [7]

- Coverage and Mobility: Cellular systems need to maximise coverage for users in all positions and areas, both indoors and outdoors. The system also needs to provide mobility to users, which allows them to access resources at different locations as well as allows for interworking between different signal standards.
- Capacity: Due to the increasing number of mobile devices and an increasing demand for high data rate services in cellular systems, there is a need for an increasing spectrum of resources as well as techniques such as channel reuse among cells, which ensures that the system has the capacity to meet this growing demand.
- Quality: Within a mobile cellular system, the service quality for mobile users should be as high as possible. This includes the quality of received voice speech as well as common cellular system features such as Bit Error Rate (BER) and throughput.

1.5 Basic Propagation Models

Within this section different methods are presented which can be used to calculate the range of a wireless communication system, as well as predict system features such as interference and antenna efficiency. They are approximate in nature and rely on idealised assumptions: however, they are useful for the development of scoping calculations and, to understand how a particular antenna system will perform in practice. They also demonstrate the principles of coverage distribution in a cellular network [7].

1.5.1 Definition of Path Loss

Section 1.4.1 outlined how losses can form for the signal between a transmitting antenna and receiving antenna, and stated that one type of multiplicative noise is known as path loss. Path loss is strictly defined as the ratio of transmitted power over the received power of a system, and it is usually measured in decibels. It can include all of the losses associated with the transceiver components and the interacting objects for the propagation waves between the transmitter and receiver. It is usually difficult to measure the path loss directly, as this term incorporates many different specific types of losses and takes into account the complex behaviour of the transmitted radiation as it interacts with objects in its transfer medium. The elements involved in a communication system are shown in Figure 8. A realistic approach to describe the power which is received at thee input port of the receiver terminal is [7] shown in equation (1.21):

$$P_R = \frac{P_T G_T G_R}{L_T L L_R} \tag{1.21}$$

The parameters used in this equation are presented in Figure 8: all gains and losses are expressed here as power ratios, and all power is expressed in Watts (W).

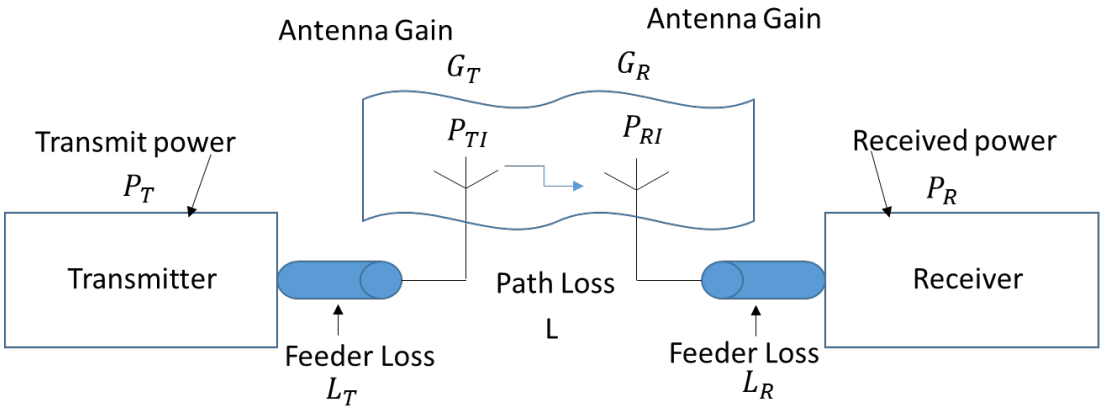

Figure 8: Components of wireless communication systems

As outlined previously, the antenna gain is expressed with reference to an ideal isotropic antenna. The Effective Isotropic Radiated Power (EIRP) from an isotropic antenna is:

$$EIRP = \frac{P_T G_T}{L_T} = P_{TI} \tag{1.22}$$

Similarly, the Effective Isotropic Power Received (EIPR) is:

$$EIPR = \frac{P_R L_R}{G_R} = P_{RI} \tag{1.23}$$

It is convenient to express power in terms of EIPR as this means that path loss, L, can be added to the system independently. This allows for different path loss models to be implemented for different simulations easily. Path loss is defined here as the ratio of the transmitted EIRP over received EIPR. In an ideal system, where there are no antenna feeder losses and all antennas are assumed to be isotropic (i.e. where $G_{R,T} = L_{R,T} = 1$), path loss is therefore:

$$L = \frac{P_{TI}}{P_{RI}} = \frac{P_T G_T G_R}{P_R L_T L_R} \tag{1.24}$$

The propagation loss from the system, which effectively outlines how the EM from the antenna behaves in the propagation medium, is usually independent of the system gains and losses: however, in practice it can vary depending on the antenna radiation pattern properties, which result from changes in the angle of arrivals of radiation at the receiver. This variance can be ignored for many systems, especially for highly directional antennas where scattering effects from outside the antenna's main beam are negligible.

The purpose of developing different path loss models is to attempt to predict path loss as accurately as possible, as this means that the range and performance of a communication system can be simulated as accurately as possible. The maximum range which a particular antenna system can achieve is defined as the range at which the received power drops below an acceptable communication quality level. This level can be set by technical limits or by operating standards regarding signal quality, and it is referred to as the receiver sensitivity. The maximum acceptable path loss described in dB is:

$$L_{dB} = 10\log\left(\frac{P_{TI}}{P_{RI}}\right) \tag{1.25}$$

Due to the theorem of reciprocity, the definition of the path loss is unchanged when analysing signals either from the transmitting antenna or to the receiving antenna: However, the actual acceptable quality level can be different in two directions, due to the different losses and sensitivities over the transmitter and receiver.

1.5.2 Noise Modelling

The performance of a communication system is largely determined by the SINR, and as a result modelling the noise within the system is necessary. The majority of noise in a system is a result of the receiver, although there are external sources of noise which can affect system performance. For any communication system, the total noise can be calculated by analysing a simplified two-port network as demonstrated in Figure 9, which is comprised of a single input and single output. As outlined in Section 1.3.8, networks have a parameter called gain, G: however they also have a parameter called noise factor, F, which is the ratio of the element output noise divided by G (i.e. referred to the input) over that at the input [7].

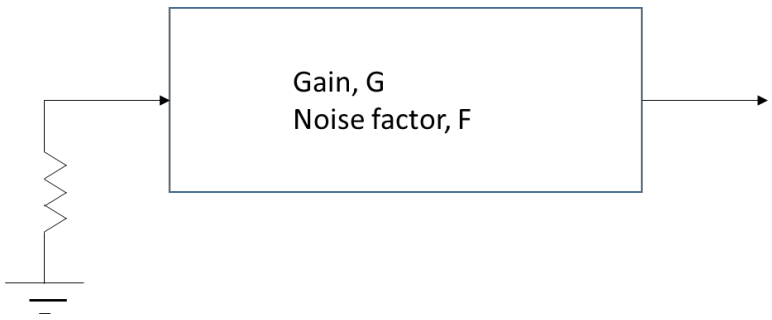

Figure 9: Simplified two-port network system

The noise power at the input of this system, which has a resistor at temperature T (290 Kelvin, K, or (23°C)) is:

$$P_N = kTB \tag{1.26}$$

Here k is Boltzmann's constant, which is equal to 1.379x10^{-23} W$Hz^{-1}K^{-1}$ whereas B is the effective bandwidth of the system in Hz. Assuming that the impedance and resistance of the network are matched to the resistance, the noise factor F can be expressed as:

$$F = \frac{N_{out}}{N_{in}} = \frac{N_{out}}{kTB} \tag{1.27}$$

Where N_{out} is an expression of the output noise power of the element referred to the input, (i.e. the actual output noise power divided by G). The noise factor figure for the system, in decibels, can be calculated using equation (1.28):

$$F_{dB} = 10log_{10}F \tag{1.28}$$

Noise power can be expressed numerically (in dBW) using:

$$N_{out|dBW} = F_{dB} - 204 + 10logB \tag{1.29}$$

The equivalent noise power in dBm is:

$$N_{out|dBm} = F_{dB} - 174 + 10logB \tag{1.30}$$

An alternative way to characterise output noise power is by modifying equation (1.26) to consider an equivalent noise temperature T_e at the input. This is the temperature of an arbitrary source of noise at the input. If the network is noiseless, the equivalent noise power can be expressed as:

$$N_{out} = kTB + kT_eB = k(T + T_e)B \tag{1.31}$$

Thus:

$$F = \frac{N_{out}}{N_{in}} = \frac{k(T+T_e)B}{kTB} = 1 + \frac{T_e}{T} \tag{1.32}$$

Where B is usually the intermediate frequency (IF) bandwidth of the receiver.

1.5.3 Free Space Loss

The analysis of free space loss must begin with the Friis transmission formula, which is: [7]

$$\frac{P_r}{P_t} = G_T G_R (\frac{\lambda}{4\pi r})^2 \quad (1.33)$$

Where G_T and G_R represent the gain of the terminal antennas (i.e. the transmitting and receiving antennas), r represents the distance between the transceivers and λ is the system wavelength. This formula can be thought of as an expression of the power which is propagating over the sphere surface with a radius r at the centre of the antenna. This means that the power within the sphere surface area increases as r^2 increases, while the received power at the receiving antenna of fixed aperture decreases in proportion to r^2. The propagation loss from the communication system in free space, L_F, can be expressed as:

$$L_F = \frac{P_t G_a G_b}{P_r} = (\frac{4\pi r}{\lambda})^2 = (\frac{4\pi r f}{c})^2 \quad (1.34)$$

L_F is also dependent frequency and distance and follows are 'square law' relationship as outlined above. It can be expressed in decibels as:

$$L_{F(dB)} = 32.4 + 20logR + 20logf_{MHz} \quad (1.35)$$

Where the frequency is in MHz and the distance R is in kilometres. By doubling the frequency or distance in the system, the free space loss can therefore be increased by 6dB. Cases where the loss between two antenna terminals is less than the free space loss are rare and so only occur in highly abnormal propagation conditions: for example, when the propagation is confined to some guided structure, such as waveguide. In most situations, the received power is usually smaller than the free space loss and this is a result of loss from other sources (i.e. free space loss is not the defining loss within most antenna systems).This means that the total loss in the system can be defined as:

$$L = L_F + L_{ex} \quad (1.36)$$

Where L_{ex} represent external system losses.

1.5.4 Link Budgets

The link budget is essentially a complete assessment of the signal powers, noise power and SINR within a communication system, and it is necessary in order to complete any accurate communication system design. By providing accurate assumptions for each of the individual elements of a link budget, the overall performance of a system can be derived. This is related to the maximum acceptable path loss in the system, which is usually divided into two parts: a path loss model which is dependent on distance, such as the free space loss, and a fade margin which provides resilience against signal fading beyond the model's predicted values. The overall acceptable propagation loss can therefore be expressed as: [7]

$$Maximum\ acceptable\ propgation\ loss[dB] = Predicted\ loss + Fade\ margin \quad (1.37)$$

If the system has a large margin, is usually has a higher reliability and single quality. However, a large margin may constrain the system maximum range. In practice, by knowing the propagation loss, the corresponding desired range of the system and other system parameters such as antenna height can be estimated by using the system link budgets. The uplink and downlink budgets are usually balanced by improving the base station receiver using a low noise figure or some diversity gain.

1.6 Thesis Outline

An overall introduction to this thesis is as follows:

Chapter 2 summarises the different type of Reconfigurable Antennas (RA), techniques to modify of key antenna parameters including frequency, radiation pattern and polarisation by using the Reconfigurable Antennas. The various applications of RAs in current and future wireless communication system are introduced and described. In addition, the overview of the current cellular system and future 5G network architecture is demonstrated.

Chapter 3 demonstrates how pattern reconfigurable antenna arrays can be implemented in a homogeneous network system. In this chapter it shows that the proposed azimuth beamwidth switching concept can help dynamic network planning needs, in which the users can be in-homogeneously distributed in the geographical coverage of the cell. Numerical system analysis is presented for a hexagonal homogeneous cellular network to evaluate how the reconfigurable antenna can be used to trade-off the mean and cell edge capacity, through

reconfiguring the azimuth beamwidth from 60° to 75°, 90° and 110°. The systems analysis show that by switching the beamwidth from 60° to 110°, the cell edge capacity can be improved for most of the original 60° azimuth cell and this improvement is consistent for cell sizes ranging from 500m to 1500m. Also, the influence of mechanical tilt, inter site distance, path loss model and vicinity of cell edge are described.

Chapter 4 introduces a new reconfigurable antenna model which can change its azimuth beamwidth from 60° to 110°. In this chapter, the proposed pattern-reconfigurable antenna design mechanisms and details are demonstrated and explained. It is capable of achieving the required system performance, and two prototype antenna models are demonstrated through simulations and measurements.

Chapter 5 shows the effects of number of reflector antenna elements for the antenna array on the network coverage/capacity. It is shown that by increasing the number of antenna elements in the elevation direction, the network capacity can be increased as well at its optimum tilt angle. This suggests that a high gain antenna array in a cellular mobile network can be potential for large site deployment and fewer installations.

Chapter 6 shows the antenna elevation beam shaping technique can help improve the network coverage at large antenna downtilt angles. After evaluating and analysing different elevation beam shaping techniques, it was found that the first upper side null filling for the pattern-reconfigurable antenna array can be used to enhance both the cell edge and overall network coverage/capacity for large antenna downtilt cases. The application of this elevation beam shaped pattern is demonstrated for optimising a specific cell where the network performance is below network average in a homogenous cellular network. By choosing a proper antenna downtilt angle for this specific cell while keep the optimum tilt angle of other cells in the network, the cell's capacity can be improved without deteriorating other surrounding cells' performance.

Lastly, **Chapter 7** summarises this project and outlines future work on this topic.

This page is intentionally blank.

Chapter 2. Literature Review

2.1 Reconfigurable Antenna Parts

Antennas play a key role in developing dynamic communication systems [8], and making antennas reconfigurable has becoming a major research topic in recent years. [9] Since the characteristics of traditional antennas are fixed, they may in turn limit the overall performance of the communication systems such as capacity, energy efficiency and data rate. In this situation, making the behaviour of the antenna reconfigurable to adapt to the required system and new environment can improve the capacity gain, data rate and additional functionality of the system ([8], [9], [11] and [12]). In [8], [10] and [13], by alternating and rearranging the currents on the body of the antenna, the electromagnetic fields surrounding this device can also be changed, which achieves reconfigurability in an antenna's operating characteristics. These include the frequency and polarisation of the radiation from the antenna, as well as the overall radiation pattern. Current rearrangement on the body of an antenna can be achieved through electrical, optical, physical and material change techniques.

An antenna working as a transceiver makes a link between the circuits of the system and wave propagation. This means that achieving reconfigurability for an antenna's particular radiation pattern may in turn change other characteristics, such as the frequency response. Reconfigurability can also be applied in multiple resonant modes, in which the antenna can achieve different radiation patterns over different frequency bands for different communication standards. This greatly increases the operating flexibility of these types of antennas. In contrast, for a system in which the requirements of the antenna's characteristics need to be separate, the reconfigurable antenna can be used in such a way as the operating characteristics can just adjust the system to adapt to the linkage or make the linkage suitable for the required system. ([8] and [14]).

The main techniques to achieve the reconfigurability of the antenna are divided into four categories as follows.

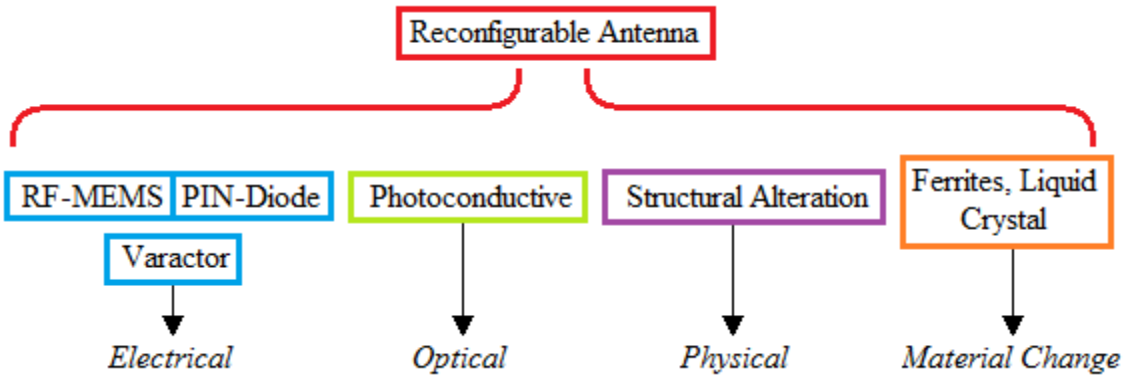

Figure 10: Category of methods to achieve the reconfigurability of antenna [10]

2.2 Types of the reconfigurable antennas:

Different designs of reconfigurable antenna are described below: ([8], [10], [15] and [16])

1) **Frequency reconfigurable antennas:** These devices occur in two distinct forms. For example, continuous reconfigurable antennas are those where the transitions between different frequency bands are smooth and no immediate switching of different frequency bands occurs. In contrast, in switchable reconfigurable antennas changes between different frequency bands are distinct.
2) **Polarisation reconfigurable antennas:** The reconfigurability in antennas' polarisation can provide immunity to interfering signals, which can subsequently be filtered out. This technique can also improve the link quality of an antenna.
3) **Radiation pattern reconfigurable antennas:** In this arrangement a set of techniques is used to change an antenna's radiation pattern in terms of the shape, beamwidth and gain according to different requirements of the system.
4) **Compound reconfigurable antennas:** These reconfigurable antennas combine the previous three reconfigurable antennas and can separate and select the impedance, bandwidth, operating frequency bands, radiation pattern and polarisation. This means that the antenna can achieve frequency reconfigurability as well as pattern reconfigurability at the same time.

2.3 Fundamental theory and methods to achieve frequency reconfigurability

In accordance with antenna theory, the operating frequency of an antenna is mainly dependent on the antenna's effective electrical length. As a result, changing the electrical length of the antenna will therefore result in a new operating frequency. The mechanisms used to modify this electrical length can be summarised as follows: ([8] and [19])

1) **Switches:** To achieve a distinct 'switch' in the operating frequency, electronic components such as PIN diodes, optical switches, and Field Effect Transistors (FET)s are used to modify electrical pathways on an antennas surface, and thus change the electrical length of the antenna. Switching may also be achieved using radio frequency microelectromechanical system (RF-MEMS) switches.
2) **Variable Reactive loading:** The main difference between reactive loading and electronic switches is that the reactive loading method has the ability to change the effective electrical length of the antenna continuously, in order to achieve smooth tuning over different frequency bands. Some researchers have found that using varactor diodes can achieve continuous frequency switching along with reactive FETs and integrated RF-MEMS capacitors.
3) **Mechanical/Structural changes:** Changing the antenna's physical structure using actuation mechanisms (such as piezoelectric actuator systems or magnetically actuators) can achieve large frequency shifts. However, structure changes can also cause other characteristics of the antenna to be altered, which may compromise the antenna's performance.
4) **Material changes:** It has been found that changes in material characteristics, particularly relative permittivity and permeability, will in turn change the antenna's effective electrical length and resulting frequency. For example, ferroelectric and ferrite materials have a high relative permittivity and permeability, and so can greatly reduce the antenna's size and switch frequency bands. However, due to their high conductivity, they can decrease the antenna's efficiency.

2.4 Fundamental theory and methods to achieve polarisation reconfigurability

The direction of the current flowing on the surface of an antenna determines the polarisation of the radiation, since it changes the antenna's electric field in its far field domain. To achieve polarisation reconfigurability, the structures of antennas, material properties, and feed configurations of antennas need to be changed properly to allow the current flow on the antenna to be modified. Polarisation reconfigurability is usually subdivided into linear polarisations, left hand- and right hand- circular polarisations. The mechanisms to achieve the polarisation reconfigurability are similar compared with frequency reconfigurability antennas. ([8] and [20]) and are as follows:

1) **Switches:** Research on the capability of switches indicates that the polarisation of several antennas can be reconfigured among different forms. For example, one method which is currently under development is the use of slot antennas equipped with PIN diodes to switch from linear polarisation to circular polarisation, or to switch between different types of circular polarisations. An alternative method is using a MEMS actuator or piezoelectric transducer inserted in a microstrip antenna.
2) **Material changes:** Some researchers have found that using a ferrite film on a microstrip antenna to bias its magnetism can achieve reconfigurable polarisations between cross-polarisation and a set of elliptical polarisations. In addition, altering and improving the configuration of feed points as well as changing the properties of the ferrite material can achieve purely linear polarisation and circular polarisations within the antenna.

2.5 Fundamental theory and methods to achieve radiation pattern reconfigurability

Altering the arrangement or distribution of the current (electric or magnetic) on the structure of an antenna can reconfigure the pattern of the radiation coming from the antenna. Establishing links between source currents and the antenna's radiation pattern also provides an option of achieving pattern reconfigurability without affecting the operating frequency significantly. Using a tuneable circuit or some specific types of antennas (i.e. reflector antennas or parasitically coupled antennas) can eliminate changes in operating frequency

whilst still achieving radiation pattern reconfigurability. ([8] and [21]) Several methods which have been found to achieve radiation pattern reconfigurability are as follows:

1) **Structural/Mechanical changes:** It has been shown that physically removing or changing the reflective surface of a reflector antenna by isolating it from its feed point can reconfigure the radiation pattern whilst keeping the operating frequency unchanged. One application of this is altering the structure of reflectors in an antenna to achieve a reshaped beam and then adding a motor or actuator to acquire automatic radiation pattern reconfiguration. In addition, adopting surfaces which have a high-impedance can also achieve this effect. One example of this is a mechanical tuning reconfigurable leaky-wave antenna: through tuning the moveable top capacitance surface mechanically (which in turn changes the capacitance values of the surface), the radiation pattern reflected from the surface can be steered in elevation plane. The actuation mechanisms and micromachined components used in a trough waveguide and in hornlike antennas respectively can also provide radiation pattern reconfigurability whilst preserving the original bandwidth of the antenna.
2) **Electrical changes:** Using electrical changes to alter the structure of the antenna has been found to be a feasible method to change its radiation pattern. One example of this is the annular slot antenna, which use PIN diodes around its slot to alter the nulls of the antenna's radiation interference pattern.
3) **Parasitic Tuning:** The use of parasitic elements in an antenna is a very effective method to achieve radiation pattern reconfigurability. This is because they exploit mutual coupling effects between the driven and tuned elements on antenna to change source currents on the antenna surface, this resulting in the antenna beam being tilted or steered. Examples using parasitic tuning have been developed in parasitic dipole array, waveguide array and micro-strip antennas. They can also be combined with PIN diode switches or similar devices, which gives an antenna operator the ability to change the magnitude and phase of the parasitic elements compared with the driven elements.
4) **Array tuning:** Another method to achieve the beam tilting is using phase shifters in array elements. One example of this is a phased-tuned reflect array micro-strip patch antenna equipped with two varactor diodes. By changing the states of the two varactors, the reflection phase can be altered over 360 degrees, which can achieve beam tilts of up to 40 degrees.

5) **Material changes:** Ferrite and ferroelectric materials have been found to achieve reconfigured radiation patterns as well as reconfigured frequency patterns. By changing the characteristics of these materials, the resonant current distribution around the antenna can be altered which results in the beam being tilted and propagation speeds being altered. One example of this is the use of ferroelectric superstrates with a resonant slot-antenna, which allow an antenna's permittivity to be tuned and the beam direction changed. The other example is the reconfigurable leaky-wave antennas integrated with phasing shifts and ferroelectric materials inserted into feeding waveguide, which can tune the antenna beam up to 60 degrees from the broadside.

2.6 Fundamental theory and methods to achieve compound reconfigurable antennas

Compound reconfigurable antennas are in theory very similar in design to those which can only reconfigure one particular antenna characteristic. However, the design and control of these devices is in practice much more complex. In most cases, a compound reconfigurable antenna changes characteristics individually, without considering the 'interplay' between different characteristics. However, for reconfigurable apertures, the operating frequency and radiation pattern characteristics need to be considered together. Research suggests that a pixel-based method could divide an aperture into small parts, to allow for changes to the current or field distribution. Overall, compound reconfigurability is achieved through **Electronic reconfiguration mechanisms** which utilise switches such as MEMS, pin diodes or solid states on reconfigurable apertures to achieve reconfigurability. Another method is the use of semiconductor plasmas integrated with silicon-based. ([8], [17] and [18])

Table 1 compares the key features of different types of switches. Table 2 shows the different operating parameters for these switches from "Reconfigurable Antennas for Wireless and Space Applications," [10].

Table 1: Comparison between different types of switches [8]

Type of Switch	Switch Characteristics
RF-MEMS	These operate through mechanical movements which close and open circuits in the current path of an antenna. Mechanical movements can be activated by actuators.
PIN Diodes	Uses on and off states to tune the circuits of the antenna. The on state is achieved by forward biasing and the off state is not biased.
Varactors	These are made up of a p-n junction diode, and have capacitances which can change from tens to hundreds of picofarads.
Photoconductive	These are activated using laser diodes, which cause the flow of electrons from valence bands on the switch to the conduction bands and thus change current paths on the antenna..

Table 2: The properties of different types of electric and optical switches [10]

Electrical Property	Type of Switch		
	RF-MEMS	PIN Diode	Optical Switch (Si)
Voltage (V)	20-100	3-5	1.8-1.9
Current (mA)	0	3-20	0-87
Power Consumption (mW)	0.05-0.1	5-100	0-50
Switching speed	1-200 µsec	1-100 nsec	3-9µsec
Isolation (1 – 10 GHz)	Very high	High	High
Loss (1 – 10 GHz) (dB)	0.05-0.2	0.3-1.2	0.5-1.5

Table 2 shows that RF-MEMS switches have the lowest loss and power consumption of the different types of switches, although PIN diodes have the fastest switching speeds. For optical switches, due to their linear behaviours they can reduce intermodulation distortion and they do not need biasing lines to integrate into the antenna, which therefore decreases unwanted interferences and radiation pattern distortion. However, they also require complex activation mechanisms. [10]

2.7 Applications

2.7.1 Reconfigurable antenna for software defined, cognitive radio systems

It has been shown that reconfigurable antennas have applications in a wide range of different wireless communication systems, all of which need the ability to react dynamically to

changes in user demand and capacity, and that these devices have distinct advantages such as a reduced physical size and improved system performance. In [14], a new approach which combines wideband and reconfigurable narrow band antennas is developed, which can be utilised for military application and software defined or cognitive radio.

Cognitive radio systems, such as those shown in Figure 11, also have the advantages of significantly improved throughput and system efficiency. To achieve a cognitive operation cycle, a typical system first starts with channel activity observation through the use of a 'sensing' antenna. Once observation is complete, a cognitive network identifies a suitable spectrum for wireless communication. Following that, a processor sends a command to the communicating antenna to make it act (i.e. switch its properties) to suit a required communication mode. In the last step, the system feeds back data from the new arrangement and begins the whole process again to obtain further system improvements. ([16] and [23]) An example of this is: through the monitoring the unused frequency spectrum (white spaces), tuning the transceivers' characteristics to the unused frequency bands can overcome the interferences from other wireless communication systems and thus improve the overall signal quality.

Two methods have been identified to implement cognitive radio systems. One uses a modified planar inverted-F antenna, which utilises RF-MEMS switches, to achieve frequency reconfigurability. The advantage of this is due to its low loss features, more frequency bands can be covered by an antenna of relatively small size. The other method uses two self-duplexing Planar Inverted F-type Antennas (PIFA)s combined with an antenna interface module consisting of different devices such as switches. [22] An actual reconfigurable cognitive antenna can be implemented in practice by combining two 'sensing' antennas as well as two reconfigurable filtering antennas ('Filtennas') on the same substrate. The frequency reconfigurability of this antenna is achieved by using the PIN diodes, and the subsequent wideband sensing ability of this device gives it the ability to react to the observed channel environment in a cognitive radio setting. [24]

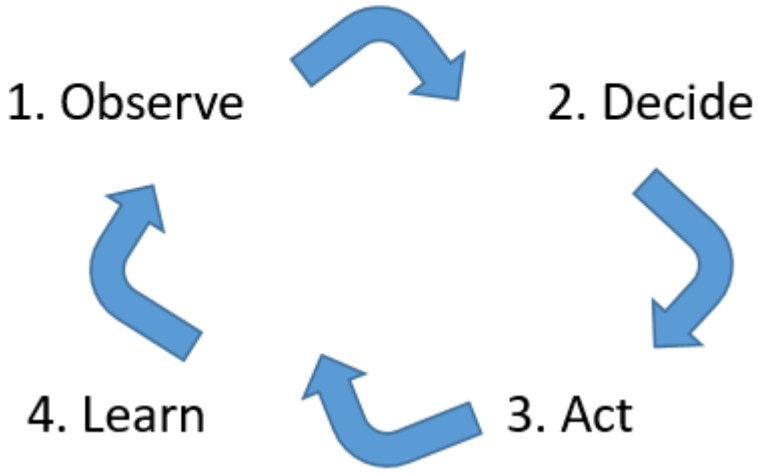

Figure 11: Cognitive Radio Cycle

2.7.2 Reconfigurable antennas in MIMO systems

Recently pattern reconfigurable antennas have found use as part of MIMO systems, where there are many antennas deployed as both transmitters and receivers to provide diversity in a fading channel. Multiple transmitted and received signals from antennas can form many independent channels, combined with advanced signal processing techniques (such as space-time coded modulation) and MIMO processing. The combination of these different features means that the capacity and efficiency of the communication system in question can be improved significantly using these antennas. In [25] and [26], pattern reconfigurable antenna arrays are used as part of a MIMO system to maximize the channel link capacity. An example of a design for a reconfigurable antenna in this setting is shown in Figure 12: this is made from two microstrip dipoles and a quarter wavelength microstrip balun. With two PIN diodes inserted into the dipole arms, the length of the dipoles can be changed which therefore results in pattern reconfiguration. Through altering the length of the microstrip dipole arms, the inter-element spacing of the antenna array can be changed as well. Thus, this design can decrease the spatial channel correlation in MIMO systems, which improves their spectrum efficiency. ([10], [27] and [28])

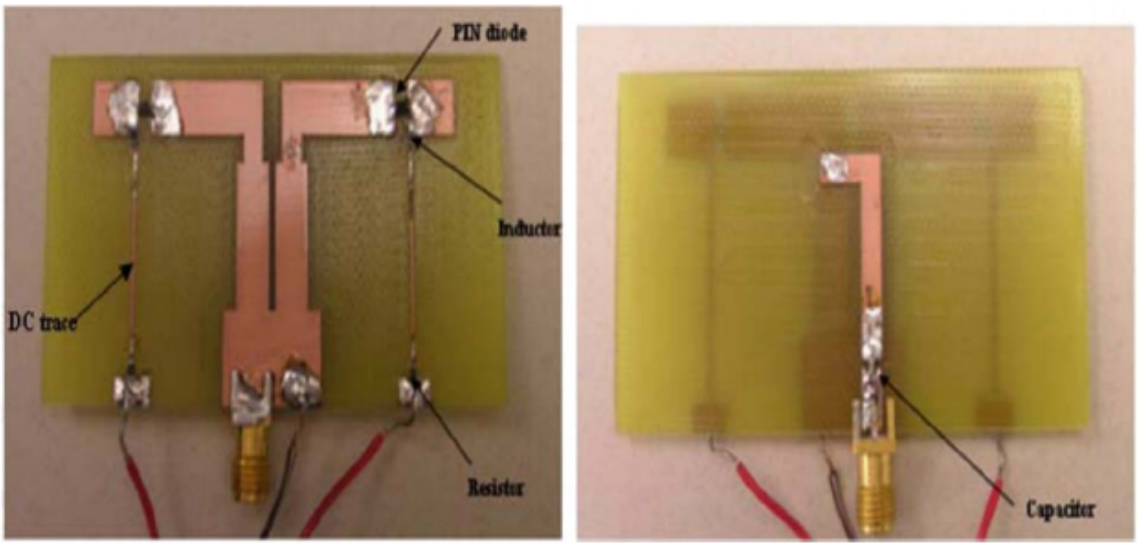

Figure 12: A pattern-reconfigurable antenna for MIMO application [10]

2.7.3 Reconfigurable antenna for space application

Today there is a trend towards implementing dynamic space applications which deploy reconfigurable antennas in satellite communication. The reconfigurable antennas used in these applications provide pattern reconfigurable to provide signal cover over a new range, reduce the fading loss in some areas and keep the high data rate in all frequency bands. One example of this is a reconfigurable antenna with an 85cm aperture and using rotational and zooming method to produce an elliptical beam and tune the radiated beam from a small to a large ellipse. It has been found that changing the size of the antenna's aperture can achieve high antenna gain and directivity and be reconfigured to cover several frequency bands of operation. [10] Alternatively the antenna may be deployed in stages as shown in Figure 13. Sequentially deploying the helical antenna to the actuators allows the antenna frequency to be gradually 'tuned' to suit a particular application since the only part of the antenna which radiates (and therefore produces a signal) is that part which is been deployed out of the ground. ([16] and [29] to [33])

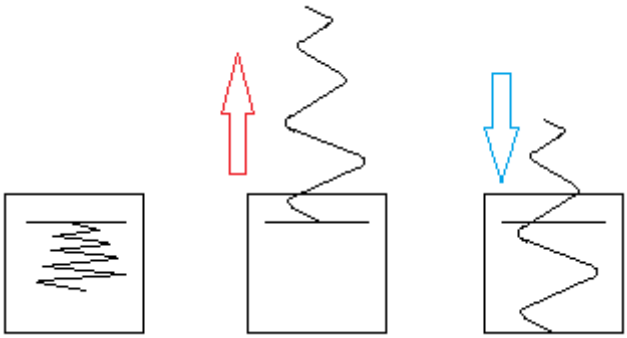

Figure 13: Deploying Helical Antennas in Progression [16]

2.7.4 Reconfigurable antenna for street furniture applications

Recently, beam steering reconfigurable antennas have been used for street furniture and base station. In [8], it is shown that a high impedance surface can be used to achieve radiation pattern reconfigurability. Active Artificial Magnetic Conductor (AMC) and Electromagnetic Band Gap (EBG) surfaces have also been implemented in several antenna designs to steer the main radiation direction as well as provide a low antenna profile. Street furniture antennas are mainly used in challenging urban environments, where they can be mounted on the walls of buildings. As shown in Figure 14, a dipole antenna which is spaced a- quarter wavelength away from the active AMC surface has been shown to steer its main beam from the boresight to 65 degrees. [34] It has also been shown that using active AMC surfaces with integrated phase shifters gives the array antennas the ability to radiate energy as close to endfire as possible, through changing the values of the capacitances between the two elements. This design has been used in mobile phone communications which can improve the network coverage. ([35], [36] and [37])

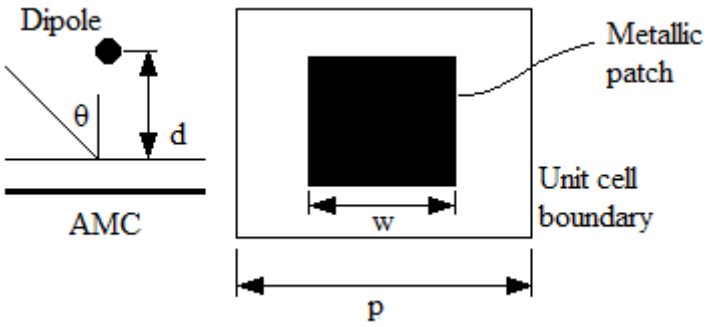

Figure 14: Reconfigurable antenna with AMC unit cell [34]

2.7.5 Reconfigurable antenna for base station applications

Due to growing demand for data volume and high energy consumption, most of the available relevant antenna research has been focused on low energy consumption and high demand data volume in information and communication technology [38]. For example, a dynamic base station concept has been proposed which allows for the adjustment of active sectors in real time to match the load from users. This can be implemented using a reconfigurable antenna with reflector sectors to tune the azimuth beamwidth. A design using a radiating dipole and a folded metallic reflector with a series of PIN diodes has been shown to achieve beamwidth adjustment: the sectors act as reflectors alongside the conducting PIN diodes to provide directional beam steering in the azimuth plane. When the PIN diodes are non-conducting, the partial transparent sectors provide the Omni-directional beam pattern in the azimuth plane. This novel design has made a contribution to energy and cost efficient mobile communication systems [38].

In order to reduce the high insertion loss, power handling capacity and structural fragility, a dual-band reconfigurable base station antenna can be designed without using the switch components such as PIN diodes, RF-MEMS. This antenna consists of two square patches for two different operating bands. Patch 1 is made up of metal plate and patch 2 is designed under the cylindrical cavity of patch 1. Two probe feeding cables are used to feed the two patches respectively to achieve a symmetric radiation pattern. Thus, the dual-band reconfigurable antennas are designed to support two operating frequency bands for cellular and WorldWide Interoperability for Microwave Access (WiMAX) services, respectively ([39] and [40] to [43]).

2.7.6 Reconfigurable antenna in Heterogeneous Networks

Recently, heterogeneous networks have been developed to meet increasing data rates and traffic, and thus enhance mobile network capacity. A heterogeneous network can connect different devices and computers together through different operating systems and protocols. [44] Expanding network capacity can be achieved by adding femto cells, pico cells and other low power nodes into macro cell sites. As a single base station in a wireless cellular network has achieved its optimal performance according to theoretic capacity limits, by densifying and complementing the macro-cell base stations the spectral efficiency per unit area can be

improved. [45] In some articles, it has been found that using multi-antennas in relay nodes within a heterogeneous network reduces the total number of required relay nodes, along with system cost and signal processing complexity. [46] In order to manage the interference in a two-tier heterogeneous network, orthogonal frequency planning, power control schemes, and antenna techniques can be implemented. In addition, femto-cell access control plays an important role in decreasing the cross-tier interference. It has been shown that once the interference occurs, the femto cell base station can reconfigure the radiation pattern to overcome signal interference. Thus, these systems can achieve spectrum sharing in both the time and space domain. [47]

Multi-functional reconfigurable antennas have been the focus of significant interest as part of wireless communication systems. As they can reconfigure operating frequencies to support multi-mode, multi-standard wireless systems (as well as use beam pattern to suppress co-site interferences and polarisation between the linear and circular) they can greatly improve the performance of a communication system at both the transmitting and receiving ends. Multi-functional reconfigurable antennas can also reduce the overall system size and reduce cost compared with a single functional antenna. They achieve reconfigurability through a combination of electrical, optical, mechanical and material techniques. It is predicted that in future wireless communication networks, smart reconfigurable antennas will also be deployed with new software which can precisely detect changes in the RF environment, in order to maximise their effectiveness.

Figure 15 shows an example of a 3D Multifunctional Reconfigurable antenna. It has the capability of steering its main beam into 3 different directions, as well as reconfigure its polarisation status from linear to circular. It comprised up of a driven microstrip patch along with a reconfigurable parasitic layer, and its pixel surface can be altered through mutual coupling from the driven patch to the upper surface of the parasitic layer and by connecting or disconnecting the adjacent pixels using switches [48].

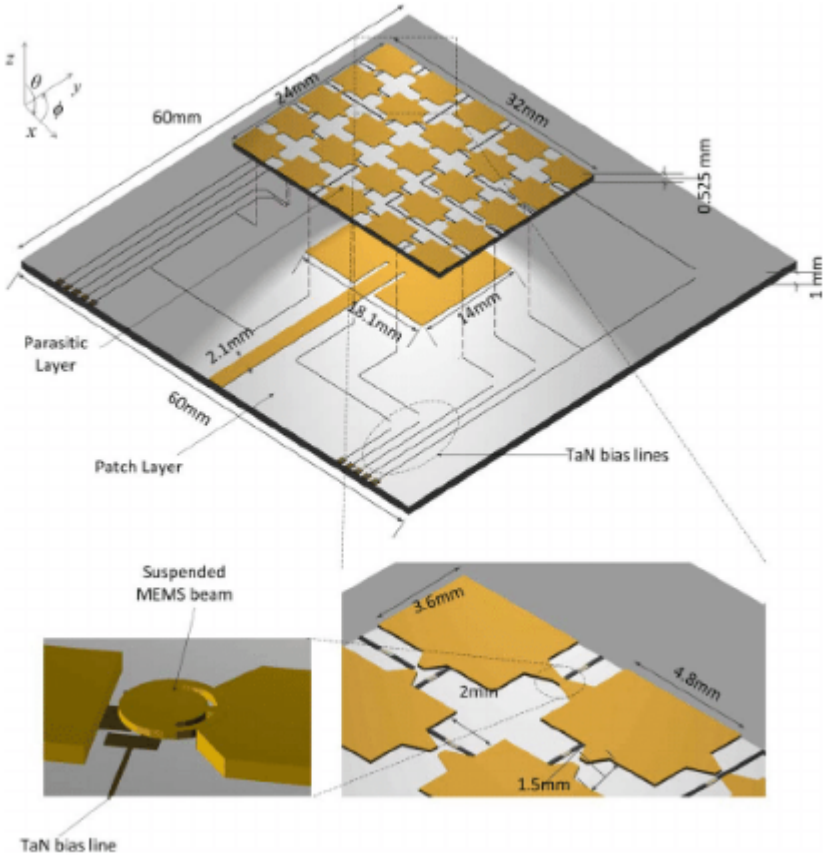

Figure 15: 3D Multifunctional Reconfigurable Antenna. [48]

2.7.7 Reconfigurable antenna for 5G communication

A reaction to the growth in mobile traffic demand is the development of a new type of communication system which attempts to balance capacity frequency spectrum requirements. The 5G communication system is this new development, and it is aiming for high data rate, seamless connectivity and ultra-low latency. In order to meet 5G requirements which are low power, low cost and complexity deigns, significant challenges must be overcome when using MIMO system with multiple antenna elements. ([50] and [51]) As outlined previously a single reconfigurable antenna can achieve multiple antenna characteristics such as frequency, radiation pattern and polarisation reconfigurability through changing the antenna's properties. Thus, in 5G communication systems it is desirable to use a single reconfigurable antenna to replace multiple antenna elements to achieve the same antenna performance. In [49], [52] and [53] a reconfigurable stacked microstrip patch antenna is proposed for high data rate transmission at 60GHz. As can be seen from Figure 16, this pattern reconfigurable antenna is comprised of 3 layers. Both the top and bottom layers use the substrate of Taconic TLY-5

and the middle layer has the bonding film of Arlon Cuclad. The microstrip line at the bottom layer feeds the microstrip patch through the slot. The electromagnetic wave is then coupled to the nine closely parasitic patches by the microstrip patch antenna. Instead of using the electrical switches here, the parasitic patches are interconnected by metal strips to reduce the effects on the antenna performances. Two groups of shorting pins achieve beam shifting in horizontal plane (A, B, C, D) and vertical plane (W, X, Y, Z) respectively.

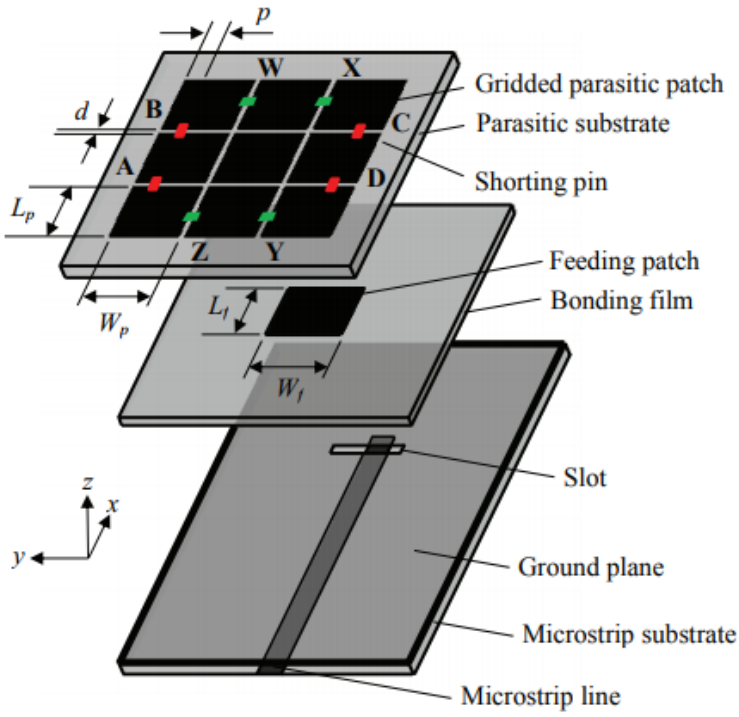

Figure 16: Proposed stacked microstrip patch reconfigurable antenna [49]

In addition another application for 5G pattern reconfigurable antenna is in ultra-dense small cell deployment. These scenarios require antennas with high capacity and low cost access points, with coverage improvement achieved through using 3D beam-steering features. Figure 17 shows a single reconfigurable antenna which is composed of a driven dipole antenna and surrounding 3D parasitic layers. The upper and lower layers are formed by identical hexagonal domes and the six side faces are made up of rectangular planes. The surfaces of the faces are composed of electrically small pixels, with adjacent pixels connected by PIN diodes. The radiation pattern reconfigurability over the horizontal plane is controlled by the intermediate part, while electric beam tilting in the elevation plane is controlled by the top and bottom pixels. Thus, through changing the electrical length of the connect pixels by

PIN diode switches, the 3D parasitic layer can work either as reflector or director to achieve the different radiation patterns. [54]

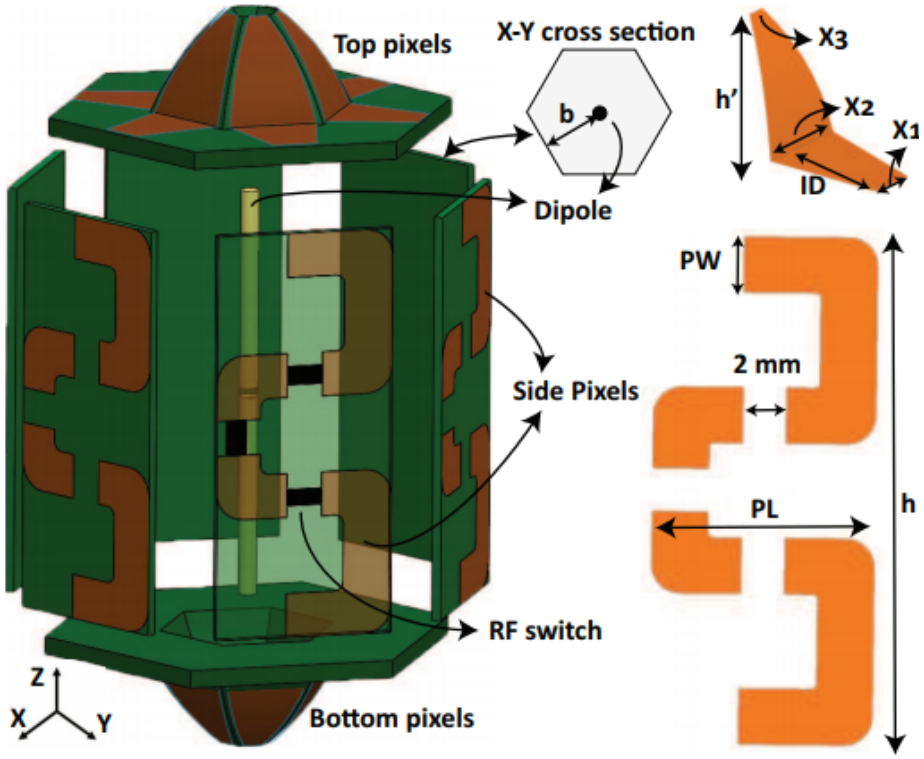

Figure 17: Parasitic layer based reconfigurable antenna [54]

5G communication systems are expected to use the millimetre wave (mmWave) frequency band, and one of the potential benefits of this arrangement is a wide bandwidth. However, the signal from these systems can suffer poor radiation characteristics due to the large path loss at the mmWave frequency band. Reconfigurable antennas therefore have the potential to be used with 5G systems as they are inherently able to support beam adaptability and diversity across complex networks.

In [55], a new mmWave MIMO system is proposed which uses a new class of reconfigurable antennas to improve a low rank MIMO system and leads to capacity enhancements at the mmWave frequency band. As can be seen in Figure 18, the proposed reconfigurable mmWave MIMO antenna is composed of a spherical lens with multiple Tapered Slot Antennas (TSAs). These TSAs only require a single radiofrequency Transceiver Chain.: through the selection of TSA feeds with the spherical dielectric lens antenna a highly

directive beam in the far field can be generated. Since each TSA can generate a beam in the far field, this system essentially is comprised of a multi-beam antenna in which each beam can be independently controlled to achieve the desired signal in a given direction. Thus, this design can support the multi-stream data transmission in a MIMO system to achieve a high capacity performance.

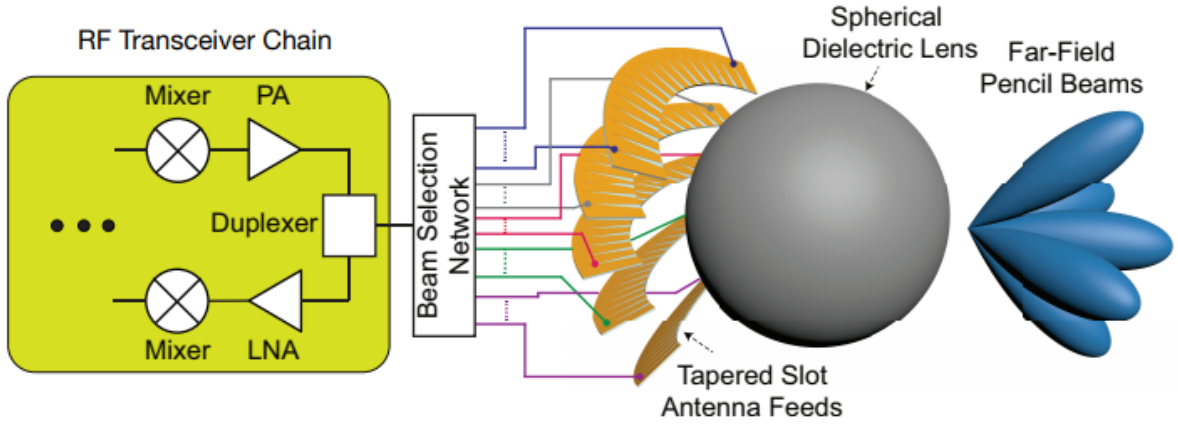

Figure 18: Proposed multi-beam reconfigurable antenna [55]

Since mmWave frequency reconfigurable antennas are a candidate for the next generation of communication systems due to their wide bandwidth capability, different frequency reconfigurable antennas are proposed for communication at the mmWave frequency band. An optically reconfigurable slotted waveguide antenna array is proposed in [56] which can reconfigure the frequency band at 28GHz and 38GHz for a future mobile backhaul system. This slotted waveguide antenna array is composed of two waveguide slots at different lengths as well as two optical switches. By using an 808nm laser to illuminate the two optical switches, the frequency band of the antenna can be remotely controlled.

A Coplanar Waveguide (CPW) fed T-shaped frequency reconfigurable antenna is proposed in [57] which can work at the mmWave frequency band from 23-29GHz. This antenna is shown in Figure 19. The T-shaped structure has been chosen due to its wideband and multiband characteristics. The CPW feeding has the advantage of providing consistent values for characteristic impedance over a wide range of bandwidths. By connecting the stubs and ground plane using two variable resistors, the frequency of the antenna can be reconfigured.

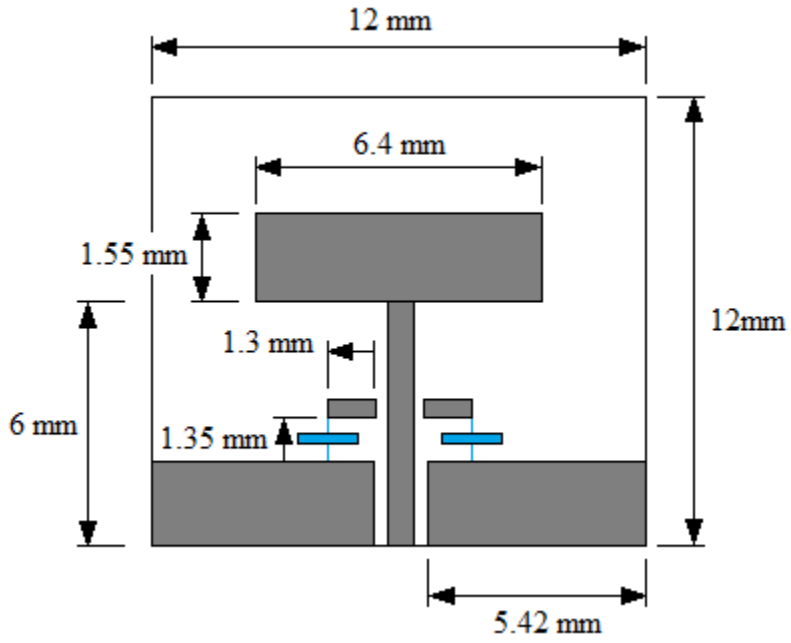

Figure 19: Proposed T-shaped reconfigurable antenna [57]

Since mobile signals can suffer multipath effects in a rich scattering environment, which can deteriorate signal quality, a polarised reconfigurable antenna is popular for next generation 5G communication systems as well. An example of this is shown in [58]. Figure 20 shows the proposed polarised reconfigurable antenna, which is comprised of a single aperture feed source and a rotatable cylindrical polariser. The circular polarizer is made up of several dielectric slabs and air slabs. By rotating the polariser at a different angle of φ, right hand circular, left hand circular and linear polarisation can all be achieved.

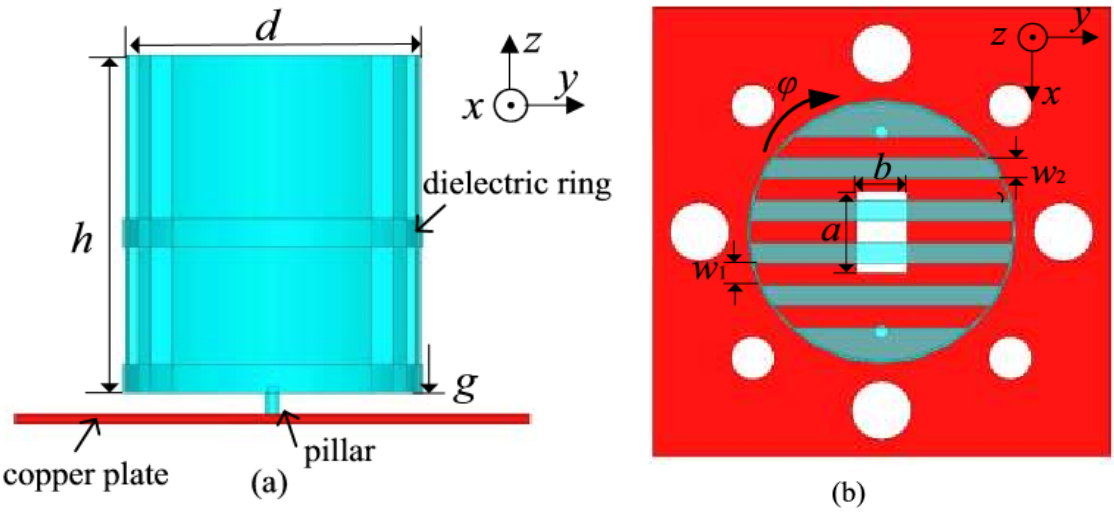

Figure 20: Proposed Polarisation reconfigurable antenna [58]

2.8 Mobile network architecture in 4G

Research suggests that the increasing number of smart phones, tablets and similar devices is overwhelming the wireless mobile network capacity. [59] As a result, this demand must be effectively managed through densifying and enhancing the High Speed Package Access (HSPA)/LTE multi-standard macro cellular network. Research suggests that in order to improve the network capacity, several options can be adopted for communication systems such as changing the macro layer through quality improvements, densification and populating the macro layer with low power nodes. Among these, adding low power nodes like small cells to the macro cells can offload the traffic from central cells to the unlicensed bands. Hence the concept of a heterogeneous network has been given to expanding the network capacity and fulfilling the requirements of the customers. [60]

LTE as a new global communication standard has been adopted in for modern wireless communication networks. As a 4G mobile network standard, it satisfies bandwidth requirements ranging on average from 50 to 100 MB/s. [59] Nowadays; heterogeneous networks are seen as a significant and cost-effective method for LTE mobile network to improve system capacity. Macro-cellular base stations can also extend system coverage, with lower power nodes placed close to areas of high demand to provide extra signal. [61] Figure 21 shows a heterogeneous network architecture in a 4G mobile network. The heterogeneous network architecture consists of different layers, from the macro cell to the pico cell or even smaller. All these cells can share the same spectrum and use different radio access technologies such as WiMax and WiFi within both licensed and off-license bands. [62]

To achieve heterogeneous network deployment, several stages need to be adopted. The first step is to ensure mobile broadband coverage which can be achieved by extending existing macro base stations through adding low frequency bands. The second step is to increase the network capacity by using additional spectrum, high sectorization, and additional numbers of macro base stations. This can be combined with site renewal through upgrading active antenna systems to reduce site acquisition costs. After these two steps, outdoor and indoor small cells can be deployed in congested places such as hot zones and commercial or residential areas. [63]

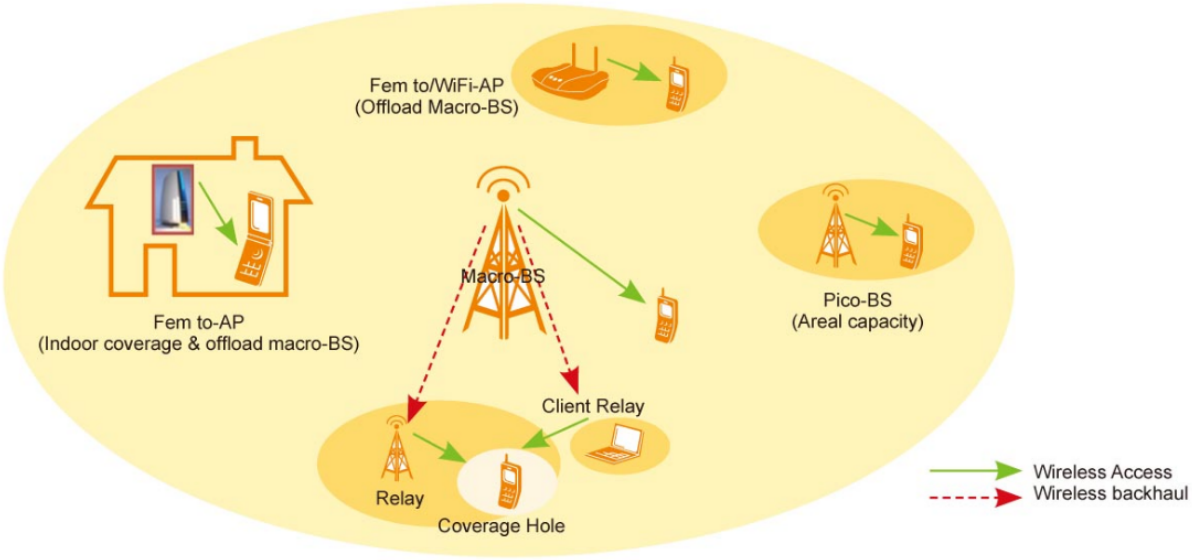

Figure 21: Heterogeneous network architecture in 4G [64]

2.9 Mobile network architecture in 5G

Another proposed solution to high mobile traffic growth and increasing numbers of wireless connections is the implantation of fifth-generation 5G and the deployment of super-dense heterogeneous network of small cells, as well as by developing massive MIMO technologies and utilizing higher frequencies (particularly mmWave frequencies). Although, 5G has not yet been standardised, certain requirements for 5G communication have already been accepted by industry and academia. In order to support different types of communication in 5G system such as massive machine to machine type communication, Internet of Things (IoT) and driverless car communication, these requirements are defined as follows: To achieve the seamless connectivity in 5G, these systems need to support connectivity anytime and anywhere with the minimum user-experience data rate of 1Gbit/s. To reduce the latency in 5G mobile network, the data delivered to the end needs to be on the order of 1-5ms. To support the multi Radio Access Technology (RAT) in 5G communication, 5G communication systems needs to integrate existing communication technologies into a unified system. Lastly, the cost and energy efficiency in 5G system needs to be significantly improved, with a cost reduction to 1$/b required alongside a 1000-fold increase in energy efficiency compared to the current wireless technologies. ([65] and [66] to [68])

Figure 22 suggests that massive MIMO and mmWave technologies are able to solve many technical challenges in the future 5G HetNet system. The deployment of massive MIMO in

the transmitter and receiver side of a communication system can significantly improve energy and spectral efficiency, especially in a rich scattering environment, and through the using the beamforming at the transceiver for massive MIMO, it is possible to achieve a high performance gain. In addition, there is an unexploited mmWave frequency band from 30-300GHz which can provide a huge amount of bandwidth to boost overstrained network capacity. The ability to implement massive MIMO technology at the transmitter and receiver end of a system is due to key features of 5G communications: namely, the short wavelength at mmWave frequency.

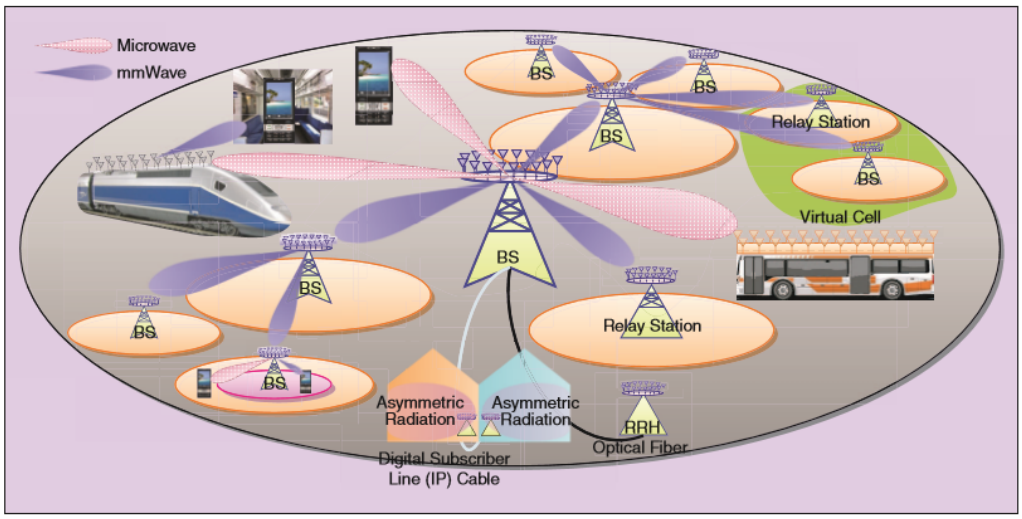

Figure 22: The proposed 5G HetNet with Massive MIMO and mmWave technology. [65]

This page is intentionally blank.

Chapter 3. System Performance analysis of Cell and Edge Capacity in a Homogeneous Cellular Network

3.1 Introduction

As outlined in Chapter 2, enhancing cellular Quality of Service (QoS) beyond 4G is of global interest to both industry and academia. There is a growing demand for high mobile data rates coupled with a need to give all mobile users the best network capacity possible, for both uploads and downloads. It has also been seen that a possible solution to these challenges is to develop dynamic networks. There has already been significant research into these systems areas and has been shown that a dynamic network deployment can be rapidly adapted to changes or user distribution across a sector in the underlying network architecture [69]. They do this by changing the size and shape of the cells within these dynamic networks such that data is shifted from overloaded sector users to underutilized sectors. This clearly helps to fill the coverage loss and improve capacity within the system ([70], [71]).

There is the potential for reconfigurable antennas to become an essential part of dynamic networks. These antennas have the freedom to alter their characteristics in frequency, polarization and radiation pattern dynamically, thus allowing operators to continuously optimise their network's performance [72] Chapter 2 suggests that they can be used as part of MIMO systems, digital home applications and Transceiver base stations ([73] to [76]). These devices operate by altering the current flow within the antenna, which can be achieved via mechanical movement, phase shifters, PIN/varactor diodes, MEMS and active materials,([77], [78], [79]). These have all been demonstrated on a range of different types of antenna including dipoles, monopoles and patch antennas. Pattern reconfigurable antennas have been proposed as a possible solution capable of balancing network traffic, improving network capacity, increasing system gain and security, reducing noise, reducing traffic jamming and improving energy efficiency by altering or steering its radiation pattern ([80] to [90]).

Once particular problem which reconfigurable antennas address is the uncertainty of the distribution of mobile users. Users which are concentrated around the edges of a cell causes uneven distribution of data across the network and research is presented which investigates how to increase the minimum data capacity that a user within a sector might have available.

By using a novel pattern-reconfigurable antenna which can switch its azimuth beamwidth from narrow to wide, it is possible to balance the need to:

a) Increase the available capacity for cell edge users.

b) Maximise the average user capacity.

This Section aims to show that by combining novel antenna design with current mobile network, the system performances in cell and edge capacity can be optimised. Section 3.2 presents an overview of the available research concerning reconfigurable antennas, while Section 3.3 discusses how this work contributes to the existing literature. A reconfigurable network and antenna concept is presented in Section 3.4 and 3.5 respectively, while Section 3.6 summarises the methodology taken to analyse these concepts. Section 3.7 introduces a novel method to analyse the performance of the network through cell edge detection. Lastly, the results of the analysis are shown in Section 3.8, and the chapter is summarised in Section 3.9.

3.2 Review of existing work

The majority of available literature regarding dynamic networks and reconfigurable antennas focuses on the issue of increasing mobile data traffic and designing a 5G paradigm with lower latency, higher data rates and energy efficiency. It is also clear from the literature that meeting capacity challenges, both as an average across a cell and at the edges of a cell, has become an urgent issue in wireless mobile networks: In areas of high demand and especially at cell edges, performances are severely reduced due to high path-loss effects and inter-cell interferences. It has been recognised that one possible way to improve this issue is to introduce a heterogeneous network, which is formed by adding small cells containing low power to the existing macro-cell base stations. This resultant heterogeneous network can be used to improve the bitrates per unit area. [91] Through the deployment of smaller cells, and by using device-to-device communication around the edges of macro base stations, the cell-edge mobile users can be served and the network coverage and capacity can be increased [92].

The existing literature also suggests that base station cooperation can also improve data rates of cell edge users, through methods including cooperative MIMO, simple cooperation, selective cooperation and cooperative with 1-bit phase feedback [93]. In these systems

Orthogonal frequency division multiple access (OFDMA) is used as the transmission scheme, along with frequency reuse techniques (which have the potential to improve cell edge throughput). Flexible frequency ruse techniques such as Fractional and Soft Frequency Reuse (FFR/SFR) have also been used to attempt to optimise the cell edge user data rate. [94] In single-cell networks, numerous Resource Block (RB) allocation algorithms have also been suggested to reduce user delay and increase user data rates New methods have also been proposed which combine the beamforming technique with smart user scheduling to improve the cell edge user performance in Orthogonal Frequency-Division Multiple Access (OFDMA) networks and reduce cell interface with MIMO antennas. [95]. These use a flexible 3-dimensional (3D) beamforming technique to control the radiation pattern in both horizontal and vertical planes dynamically, thus improving service coverage of non-uniform mobile users. Research in this area has shown that 3D beamforming adaption for User specific equipment can improve user's performance compared with traditional sectorization and fixed downtilt scheme ([96] and [97]).

Several papers suggest that small cell deployments and outdoor Distributed Antenna Systems (DAS) can be used as part of improvements to the data rates of networks. However, outdoor DAS may be the better of these techniques as has better interference management, which allows improved cell edge capacity compared with small cell deployments [98]. Coordinated Multipoint (CoMP) MIMO techniques based on unlimited backhaul capacity assumption have also been shown to be effective in improving system performance ([99] and [100]) although for limited backhaul capacity cellular networks, a joint scheme combined user scheduling with power control has been proposed. This would improve the sum-rate of users at the cell edges without degrading too much of cell centre users' data rate. [101]

Research focused on developing advanced antenna systems for improving network performances mainly in capacity has also been conducted in the available literature. The conventional adaptive and smart antenna systems have been found to be able to improve the network performances through steering or adjusting the beam pattern. However, the complex beamforming systems required for these antennas can result in increased capital costs. [102] Instead, the majority of literature focuses on pattern-reconfigurable antennas, which steer their main beams in different directions by exciting four different ports. It has been shown that these designs can be integrated with a Wi-Fi system to address multipath fading in a complex electromagnetic environment. [103] and that performance improvement can be

achieved by using these antennas in combination with MIMO systems [104] One particular study focussed on a loop-and-dipole MIMO antenna for mobile devices. This antenna was shown to have the ability to generate orthogonally directional radiation patterns in three different directions, as well as having a high isolation and a low-correlation coefficient. [105] A modified pattern-reconfigurable antenna based on a conventional Electrically Steerable Passive Array Radiator (ESPAR) antenna was also evaluated within the existing literature for mobile relay stations. By switching and steering antenna's beam electronically, the improvement of SINR performance at cell boundary and handover success rate was achieved. [106]

3.3 Research Contribution

As can be seen from the current literature, several techniques have the potential to improve communication system coverage, capacity and QoS. These techniques are based on network system deployment and optimisation, as well as through the use of antenna placement, orientation and beamwidth. Deploying electrical or mechanical tilt with directional antennas in the elevation plane can reduce interference from neighbouring cells while still meeting the required coverage area. Antenna arrays which use adaptive algorithms in their processing networks can employ multiple beam positions, sizes and directions in their operation. [107] However the literature suggests that while directional antennas are effective at improving network performance adding new cells or infrastructure should be avoided as this can increase electricity, transmission and rental costs.

Different types of reconfigurable antennas haven been proposed as methods to optimise system capacity through leveraging antenna parameters. The majority of literature discuss the fact that reconfigurable antennas change operating characteristics through various different techniques [108], as outlined in Chapter 2: however, most literature also focuses on design and related technological issues, whereas research on how these devices are used in real communication systems is still very limited. If reconfigurable antennas are to become a fixed part of current and future systems, then this area of research must be expanded upon to prove that these systems are not only able to improve the user's throughput in the close region of base station but also to give all mobile users equal data rates homogeneously over the whole cell area.

All of the available literature highlight the challenge of improving a mobile user's capacity at the cell edge, and also suggest that there are different ways to improve the cell edge capacity in a cellular network system. These techniques include deploying small cells, Inter-cell interference cancellation and device-to-device communication. In this chapter we are specifically interested in balancing network capacity in terms of both users distributed evenly across a sector and users distributed towards the edge of a cell in the downlink communication. However, this reconfigurable antenna concept can also be extended for the uplink communication. In this case, Mobile users (MU) are the transmitting sides and the Base station (BS) is the receiving end. In order to achieve the maximum received SINR at the BS, reconfigurable antennas which can dynamically change its radiation pattern for optimized signal reception can be implemented at the BS. By using this dynamic reconfigurable antenna, the main lobe of the antenna can be steered to the desired users while the nulls of the antenna can be pointed to the interfering users. As a result, the uplink SINR at the BS for the desired mobile users can be improved. The other possible scenario for uplink communication is when the mobile terminals are equipped with a pattern-reconfigurable antenna. By directing the main beam of the MUs through a reconfigurable radiation pattern antenna towards the receiving BS, the received SINR at the BS end can be maximized. Also, compared with the omni-type equipped antennas for MUs, the interference between mobile users during the uplink communication can be reduced by using this pattern-reconfigurable antenna.

A topic for the downlink reconfigurable network scenario which is expanded upon in Section **3.4.** A new concept for a reconfigurable antenna with the capability to achieve advanced system performance is then presented, and a prototype antenna is demonstrated through simulations and measurements.

3.4 Reconfigurable Network Concept

This section illustrates how the distribution of the users can change within the network cell, as well as how a reconfigurable antenna can improve the capacity for users about that edge. Figure 23 (a) shows the different distribution of users within a hexagonal cell. An assumption has been made that users would be uniformly distributed and as such the radiation pattern should maximize the average capacity across the cell. Figure 23 (b) shows a situation where users may be distributed towards the edges of the cell, where significantly lower capacity is available compared with the average. The principle behind the antenna concept in this

situation is to instantaneously switch the beamwidth of the basestation antenna to a wider beamwidth, producing the situation shown in Figure 24. The users are located in the same physical location but are now further away from the edge of the new wide beamwidth cell, i.e. in a location where the capacity may be higher. Using this concept the network providers could then choose whether to offer maximum average capacity or improved edge capacity.

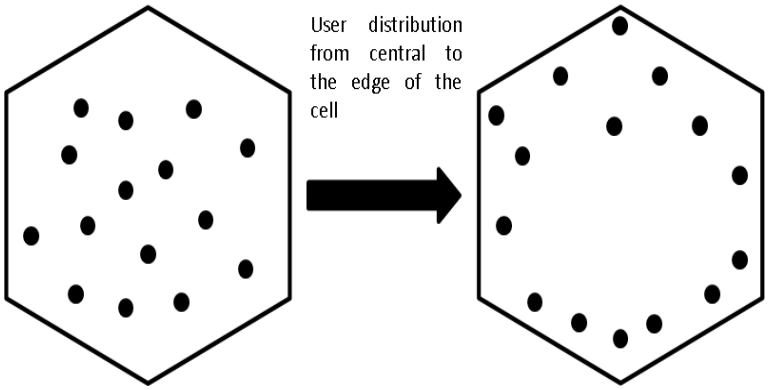

Figure 23: User cell distribution (a-left, b-right)

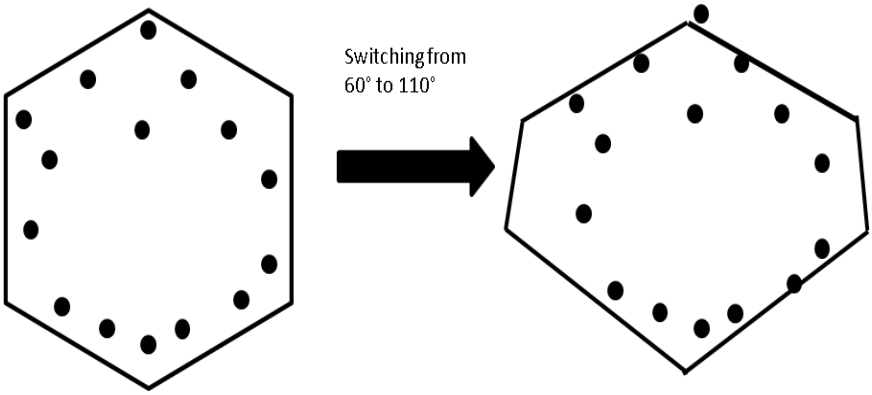

Figure 24: Antenna azimuth beamwidth changing from 60° to 110°.

3.5 Reconfigurable antenna concept

Figure 25 shows an illustration of a proposed reconfigurable antenna device (plan view) which consists of three radiating elements (dipoles in this case) spaced a distance, d, away from the centre of the base station. Three metallic reflectors of length, L_a, and height, H_a, extend from the centre of the base station with an angle of 120° between each reflector as illustrated in Figure 25. This configuration is suitable for a three sector cellular deployment. To provide beamwidth reconfigurability the length of the reflectors can be varied. As the

reflector length tends to zero each dipole will have an omni-direction pattern whereas for longer lengths of reflector the beamwidth will reduce to a minimum beamwidth limit.

Since the antenna azimuth beamwidth is related to the length of metal reflectors, in order to assess the range of available beamwidths which this antenna can achieve initial simulations were carried out through the use of Computing Simulation Technology (CST) Microwave Studio computer simulation software, which is based on full EM wave modelling by using a finite difference time domain technique [114]. Simulations were carried out using a printed dipole with two folded metallic reflectors formed by an angle of 120° (i.e. a single sector antenna). By changing the length of the reflector, L_a, different azimuth beamwidths can be obtained. As can be seen from Figure 26 a), by increasing the length of the metal reflectors, the corresponding azimuth beamwidth can be reduced and the relationship between the beamwidth and reflector length for beamwidth varying between 50° and 180° can be estimated using equation (3.1).

$$\varphi_{3dB} = 170e^{\frac{-4L_a}{\lambda}} + 48 \tag{3.1}$$

Here λ is the transmission wavelength and L_a is the length of the reflector. In order to achieve an antenna gain that represents real cellular network deployments (~17.5 dB for 3GPP standard, [109]), a 12-element vertical antenna array was modelled and the azimuth and elevation radiation patterns for 60° and 110° azimuth beamwidths were simulated. The gains for these two beamwidths are shown in Figure 27. The simulations were carried out at 1.9GHz with dimensions as follows, dipole-to-reflector distance d_p=39.5mm, H_a=1000mm and L_a= 39.7mm and 105mm for 110° and 60° respectively.

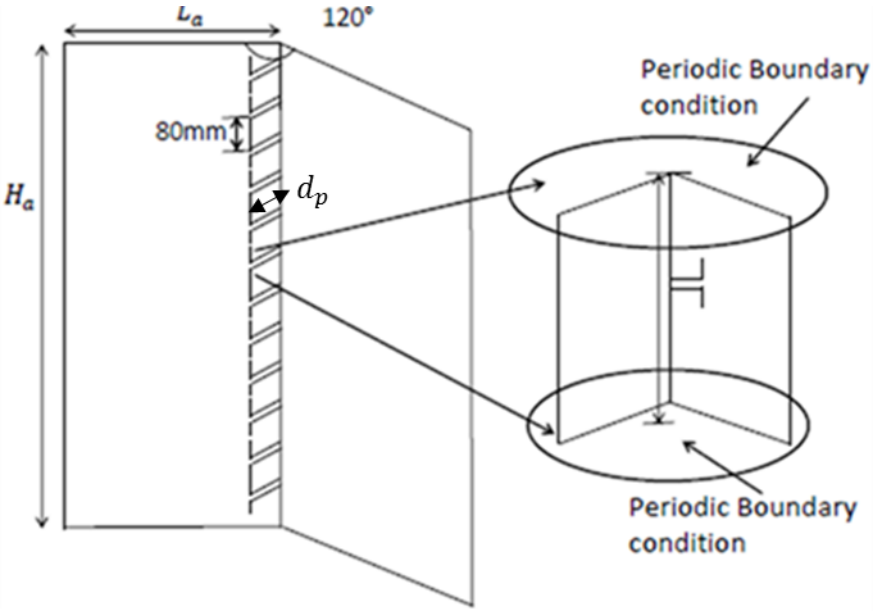

Figure 25: Antenna model for reconfigurable azimuth beamwidth

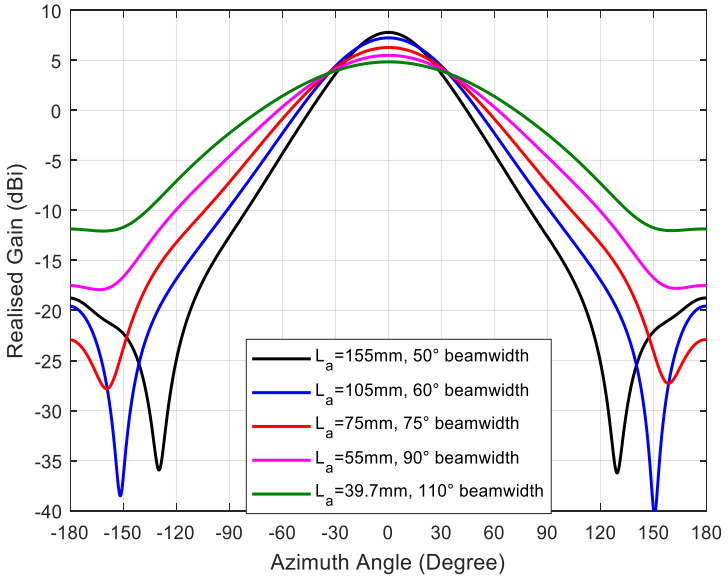

a)

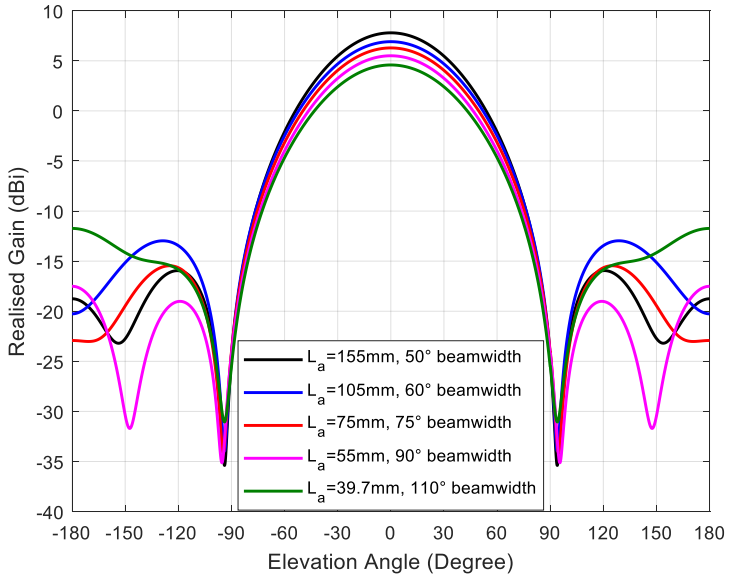

b)

Figure 26: Antenna azimuth (a) and elevation (b) vs. reflector length

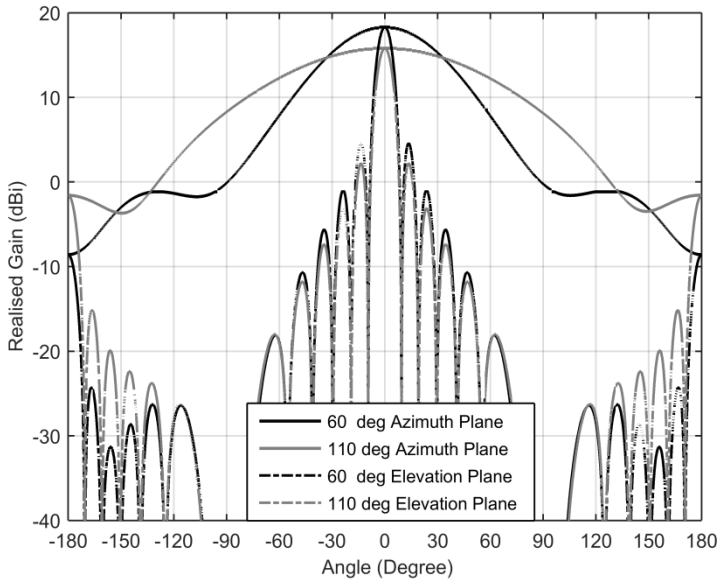

Figure 27: Radiation pattern of reconfigurable antenna for 12 element antenna array

3.6 System Simulator

Based on the pattern-reconfigurable antenna model, a system simulator was used to simulate the system performance in terms of the mobile network coverage and capacity. The dynamic

system level simulator introduced here is a new proprietary RAN simulator to measure and test solutions. It evaluates network performance in terms of conventional metrics such as capacity and outage [108]. This simulator has been designed to simulator downlink network performances in multi-cell multi-users environments taking into account BS planning, antenna configurations, path loss models and interference.

3.6.1 Simulation Flow

The following section defines the process steps which were taken to complete each simulation. Initially the simulation area was defined and fixed before the antenna radiation pattern configuration, ISD of base stations, access network deployment model and path loss models were defined. Users were then placed in square pixels across the whole network. Before scheduling, the propagation channel between users and base station was defined along with the received SINR. Lastly, the numerical and graphical output results in terms of coverage and capacity were then evaluated.

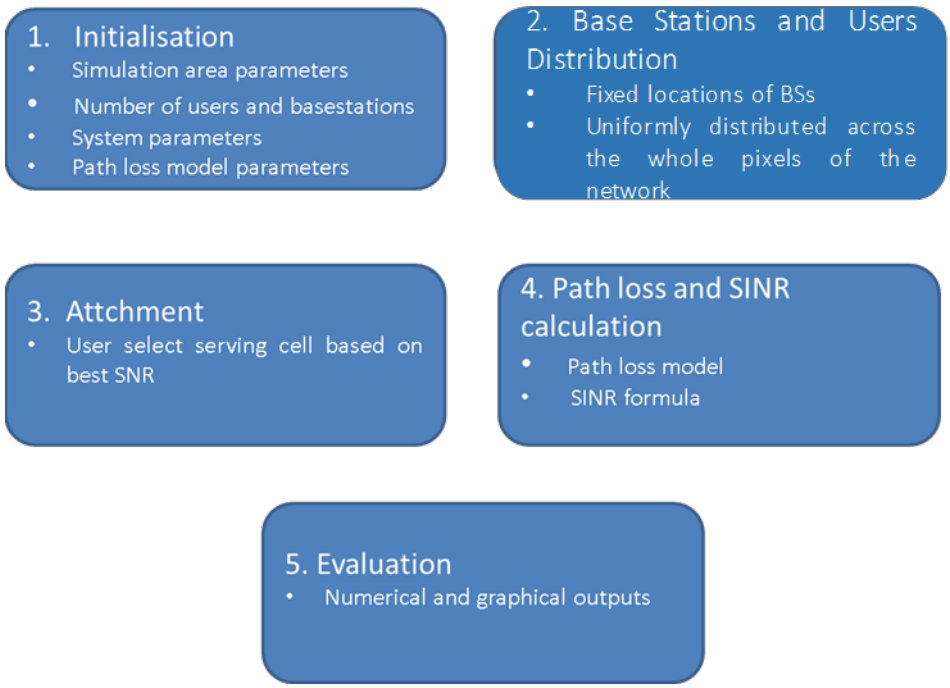

Figure 28: Simulation flow of mobile network system performance calculation

3.6.2 System model

The system model used to simulate the network performance in terms of coverage and capacity with applied pattern-reconfigurable antenna parameters is based on the simulation flow shown in Figure 28.

Figure 29 illustrates a homogeneous Base Transceiver Station (BTS) deployment made up of 19 stations, where each BTS is on a hexagonal lattice and is separated by a defined ISD. As previously mentioned each BTS has 3 antennas (and so the system therefore has 3 tier deployments). Figure 29 also shows the defined observation area for the analysis, which covers the central BTS site as well as the adjacent 6 BTS sites. This was used to calculate the system performance. The observation area is discretized, using a Cartesian coordinate system (X, Y) where each pixel is 10m by 10m. The central BTS is allocated the pixel (0, 0). The aim of the system model was to calculate the SINR for each pixel, which in turn gives the pixel's available capacity. The SINR and capacity data were then analysed to provide cell edge and cell average performance for the sector denoted "1" in Figure 29. The BTS antenna radiation patterns shown in Figure 27 were employed in this model. The ability to mechanically tilt the antenna's elevation was introduced into the model and a range of 0 – 15 degrees was analysed. One of the aims of this paper is to evaluate how system performance varies depending on the size of the cellular deployment; as a result, the ISD was varied from 500m to 1500m in order to represent small to large macrocell deployments.

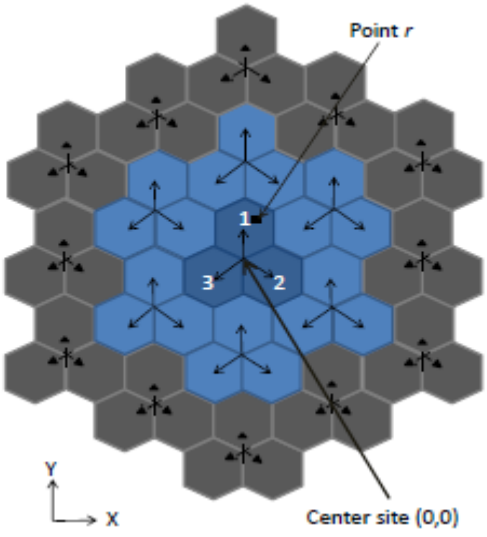

Figure 29: Cell deployment and observation area

Table 3 provides the input parameters used in the system model. These represent typical values presented in similar simulations. The focus of this research was antenna deployment in urban deployments and as such the WINNER II path loss model has been used throughout the simulations. It has been assumed that as the ISD increases the BTS antenna height, H, also increases as represented by the empirical calculation H=ISD/45.

Table 3: System simulation parameters

	Parameter	**Value**
	Transmission Scheme	SISO
	Cell Deployment	Homogeneous Hexagonal Deployment (Figure 29)
	Antenna Pattern	$A(\theta,\emptyset)$
	Antenna Gain	$G(\theta,\emptyset)$
$\boldsymbol{P}$	Transmit Power	40W
$\boldsymbol{f}$	Operating frequency	1.9GHz
B	Bandwidth	20MHz
$\boldsymbol{N}$	Number of BSs in RAN	19
$\boldsymbol{M}$	Number of sectors in BTS	3
$\boldsymbol{n_0}$	Additive White Gaussian Noise (AWGN)	$6X10^{-17}$ W/Hz
$\boldsymbol{n_{UE}}$	User noise figure	8dB (6.31W)
$\boldsymbol{G_r}$	Received Antenna Gain	-1dB
$\boldsymbol{L}$	Path Loss model	WINNER II
$\boldsymbol{H}$	User antenna height	1.5m
$\boldsymbol{H}$	Base-station Antenna Height	11-33m

Table 3: System simulation parameters		
	Parameter	**Value**
$\boldsymbol{\theta_t}$	Antenna downtilt angle	0-15degrees
ISD	Inter-site Distance	500-1500m

3.6.3 SINR Calculation

As mentioned in Section 3.6.2 the centre cell site is located at the origin (0, 0) of a Cartesian coordinate system. We used the term $n_{(x,y)}$to identify the position (x, y) of cell site n. As each cell site is composed of 3 sectors, $n_{m(x,y)}$is identified to the sector m, 1≤M≤3, of the site n. Let n= {1,…,N}, the set of n basestations in the mobile network. Consider a point r in the observation area which is denoted as position (x_r,y_r): The received power at this point from the antenna at n^{th} basestation and the m^{th} sector can be given in equation (3.2).

$$P_{n_m,r} = 10\log_{10} P + G\left(\theta_{n_m,r}, \emptyset_{n_m,r}\right) - L_{n_m,r} + G_r \tag{3.2}$$

Here P is the antenna transmitting power. Terms G($\theta_{n_m,r}$) and G($\emptyset_{n_m,r}$) are the azimuth and elevation gain based on the position of point r from the main beam of the basestation antenna in cell sector m. $L_{n_m,r}$ is the path loss between point r and the sector m of cell site N. G_r is the gain of the received antenna and assumed to be isotropic. G ($\theta_{n_m,r,}\emptyset_{n_m,r}$) is the antenna gain in dB at the point r from the transmitting antenna of the basestation in sector m of cell site n. The 3D pattern of the antenna is combined by both the azimuth and elevation patterns given in equation (3.3).

$$G\left(\theta_{n_m,r}, \emptyset_{N_m,r}\right) = G\left(\theta_{n_m,r}\right) + G\left(\emptyset_{n_m,r}\right) \tag{3.3}$$

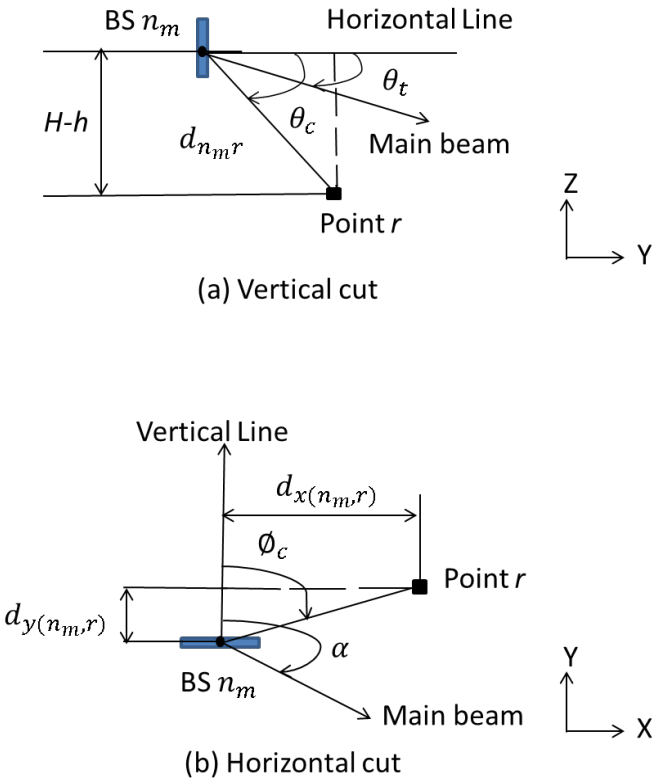

Figure 30: Vertical (a) and Horizontal (b) angles

As shown in Figure 30, the angle $\theta_{n_m,r}$ is dependent on the antenna tilt angle θ_t sitting from the main beam to the horizontal line. The lower part of Figure 30 (b) shows that $\emptyset_{n_m,r}$ is related to the horizontal angle α, which is the angle between the vertical line and antenna main lobe direction. According to Figure 30, angles θ_c and $\emptyset_c$ from the antenna at basestation n_m for point r can be calculated in equation (3.4) and (3.5).

$$\theta_c = |\sin^{-1}(\frac{H-h}{d_{n_m,r}})| \tag{3.4}$$

$$\emptyset_c = \tan^{-1}\frac{|x_r - x|}{|y_r - y|} \tag{3.5}$$

$$d_{n_m,r} = \sqrt{(x_r - x)^2 + (y_r - y)^2 + (H - h)^2} \tag{3.6}$$

Here H represents the height of basestation antenna n_m, h is the height of the point r above the origin and $d_{n_m,r}$ is the distance (m) from the point r to the basestation antenna in sector n_m. Thus, the corresponding elevation and azimuth angle of the point r from

basestation antenna in sector $n_m$can be calculated in equation (3.7) and (3.8) according to Figure 30 (b).

$$\theta_{n_m,r} = |\theta_c - \theta_t| \tag{3.7}$$

$$\emptyset_{n_m,r} = |\emptyset_c - \alpha| (\alpha = 0°, 120°, 240°, when\ m = 1,2,3) \tag{3.8}$$

As mentioned previously the path loss model used in LTE simulator is Winner Dense Urban Micro NLOS model, which is expressed in equation (3.9):

$$L_{n_m,r} = 26 \log_{10} f + 22.7 + 36.7 \log_{10}(d_{n_m,r}) \tag{3.9}$$

Where $L_{n_m,r}$ is the path loss (dB) between the basestation n_m and point r, f is the transmission frequency of the antenna (GHz) and $d_{n_m,r}$ is the separation distance between the basestation n_m and the center of the point r.

Assuming the UEs connects to the sectors with the maximum received power, thus for the received power at r^{th} point from the m^{th}sector at the n^{th} basestation can be provided by searching for the maximum received power. As shadowing and fading are not considered in our case, the serving sector n_m can be simplified mathematically to the following expression:

$$P_{n_m,r} = max(P_{1,r}, P_{2,r}, ., P_{N_M,r}) \tag{3.10}$$

The received power from the remaining of the sectors is treated as the interference for the point r at the sector n_m. This is shown in equation (3.11)

$$I_{n_m,r} = \sum_{n=1,n' \neq N'}^{N} \sum_{m=1,m' \neq M}^{3} P_{n'_{m'},r} \tag{3.11}$$

Where $n'_{m'}$ are the remaining sectors except for the sector n_m in the mobile network. The sum of the received power $P_{n'_{m'}}$ for the point r is treated as the interference here. The noise power for the user is shown in equation (3.12):

$$P_n = B n_o n_{UE} \tag{3.12}$$

Where B is the bandwidth of the network in (Hz), n_o represents the Additive White Gaussian Noise and n_{UE} is the noise figure shown in Table 1.

The SINR received by point r and issued from sector n_m can be calculated using equation (3.13):

$$\gamma_{n_m,r} = \frac{P_{n_m,r}}{I_{n_m,r}+P_n} \tag{3.13}$$

The quality of throughput is dependent on the coverage and interference conditions. Thus, the maximum throughput Ci at the r^{th} pixel can be set by Shannon capacity as follows:

$$Ci_{n_m,r} = B \cdot \log_2(1+\gamma_{n_m,r}) \tag{3.14}$$

3.6.4 Tri-Sector Antenna Beamwidth Optimisation

One of the key metrics for network deployment is the sector downlink throughput, which is related to the SINR that a user is subjected to. Before considering the reconfigurability of the antenna concept we first needed to decide what the optimum antenna beamwidth should be for a given network deployment. Based on the reconfigurable antenna concept, the antenna azimuth beamwidth was be obtained from 50° to 180° by changing the length of antenna metal reflectors. To address this, the SINR coverage is calculated for various azimuth beamwidth based on the uniform hexagonal deployment model with an ISD of 500m and 5° antenna tilt. This is demonstrated in Section 3.6.2 and the system parameters used are shown in Table 3.

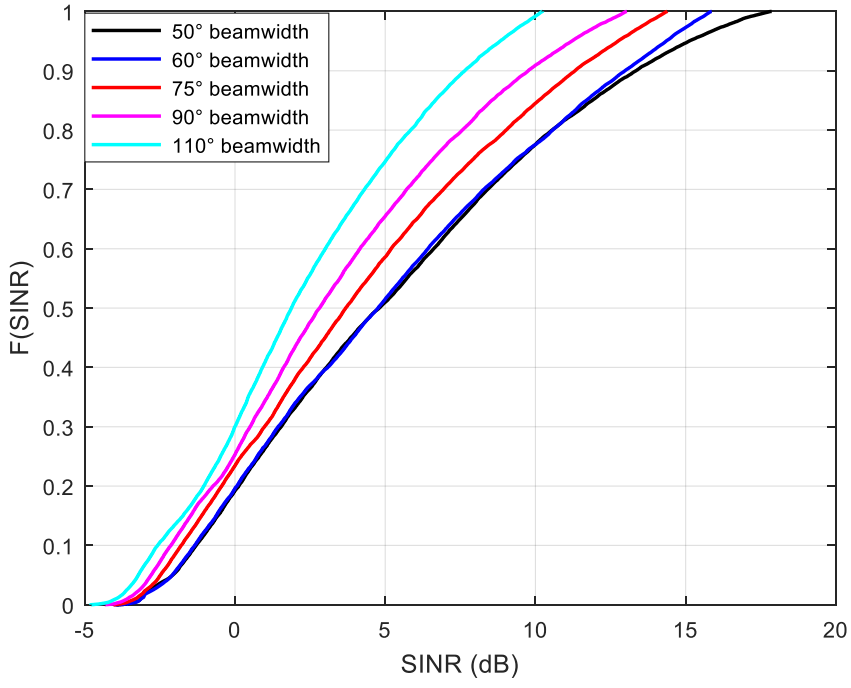

Figure 31: Cumulative Density Function of SINR for a range of antenna azimuth beamwidth

Figure 31 illustrates how the beamwidth can change the network coverage, however, to decide on which beamwidth is optimum a Cumulative Density Function (CDF) of the SINR in the whole deployed BTS cells was used. Figure 31 shows the CDF for a range of antenna beamwidths. It can be seen that there are diminishing returns for the SINR as the beamwidth is reduced. It was decided that the 60° beamwidth was optimum as this gives good SINR over the entire cell. The 50° was not chosen as the network becomes noise limited rather than interference limited which would not be appropriate for a network deployment.

3.6.5 SINR distribution

Having chosen the "optimum" antenna beamwidth for this deployment the potential of reconfiguring the antenna beamwidth is addressed. In this study we are interested in users who may be close to the edge of the optimum cell. In this case the benefit of reconfiguring to an alternative beamwidth which may have a higher SINR is assessed.

Figure 32 shows the received SINR distribution across the whole network. This shows SINR distribution across the whole network for an antenna azimuth beamwidth of 60°, 75°, 90° and 110° respectively, with a tilt angle of 1° and an ISD of 500m. It can be seen that the cell centre region has a higher SINR value compared with the cell edge area for different azimuth beamwidths, with the 60° azimuth beamwidth cell having the highest SINR value around the centre part of the cell (10-15 dB).

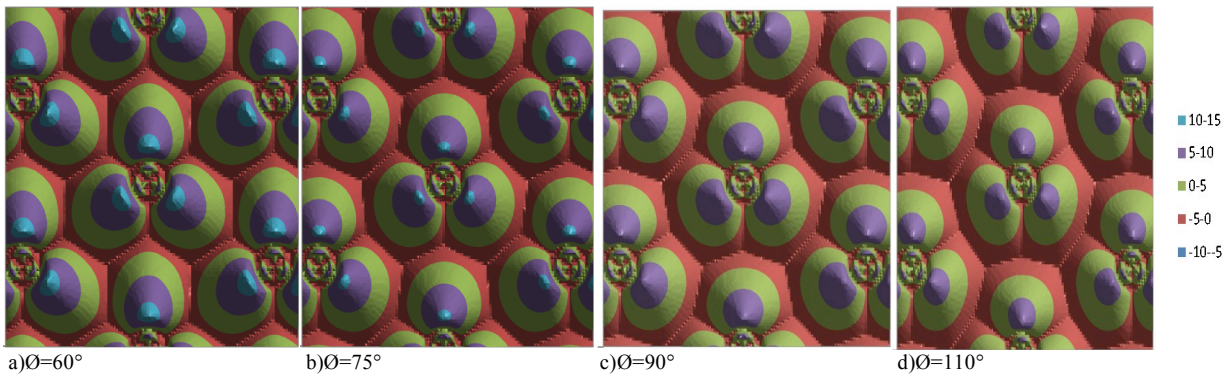

Figure 32: SINR distribution plot for; a) 60°; b) 75°; c) 90°; and d) 110° at a tilt of 1° and an ISD of 500m

Based on the assumption introduced in Section 3.4, it is claimed that through switching the azimuth beamwidth from narrow to wide, the cell edge capacity of narrow azimuth beamwidth can be improved. In order to investigate this claim and compare the differences between cell edge SINR performance among different azimuth beamwidths, a subtraction of the SINR values was carried out, denoted as $SINR_{60} - SINR_{\theta}$ where θ is the azimuth beamwidth of the reconfigurable antenna.

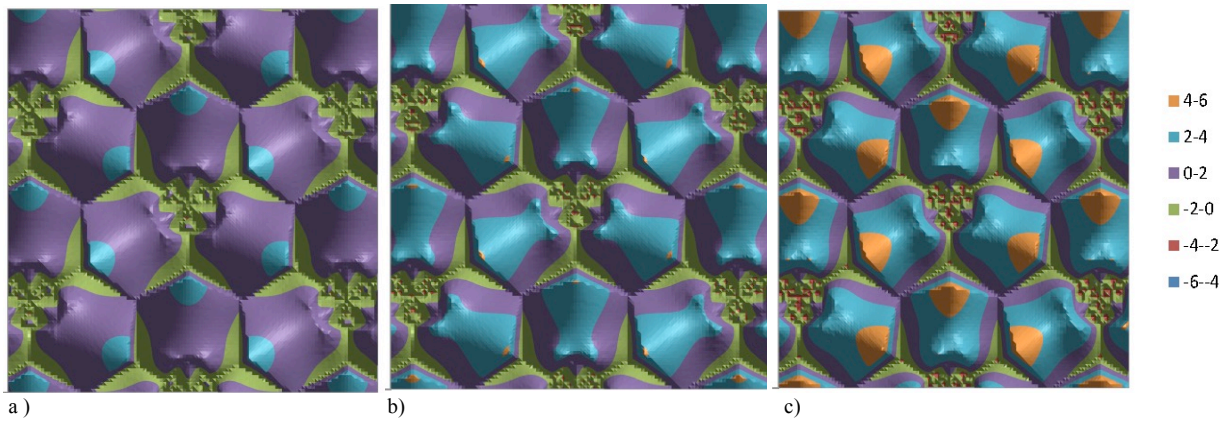

Figure 33: Difference SINR distribution plot for; a) 60°-75°; b) 60°-90° and; c) 60°-110° at a tilt of 1° and an ISD of 500m

As can be seen in Figure 33, the cell edge region of 60° azimuth beamwidth can achieve higher SINR performance through switching the azimuth beamwidth from narrow 60° to wider azimuth beamwidths. In order to investigate the improvement of cell edge capacity of 60° azimuth beamwidth by switching the azimuth beamwidth of the antenna, a novel cell edge detection technique was developed. This is introduced in Section 3.7.

3.7 Cell edge detection

As part of the calculation of cell edge capacity, a cell edge detection algorithm has been applied which determines the physical position of the edge and its throughput. The targeted sector is chosen as the central sector labelled as 1 in Figure 29. The detected cell edge is comprised of the minimum SINR value based on the cell edge definition.

The first part of this algorithm detects the local minimum SINR value around the central section by comparing the gradient in SINR in the x and y direction. Based on this local minimum, the edge of central sector can be detected. An example of this for different cell

shapes is shown in Figure 34, which clearly shows the detected edge of the central section within each SINR plot.

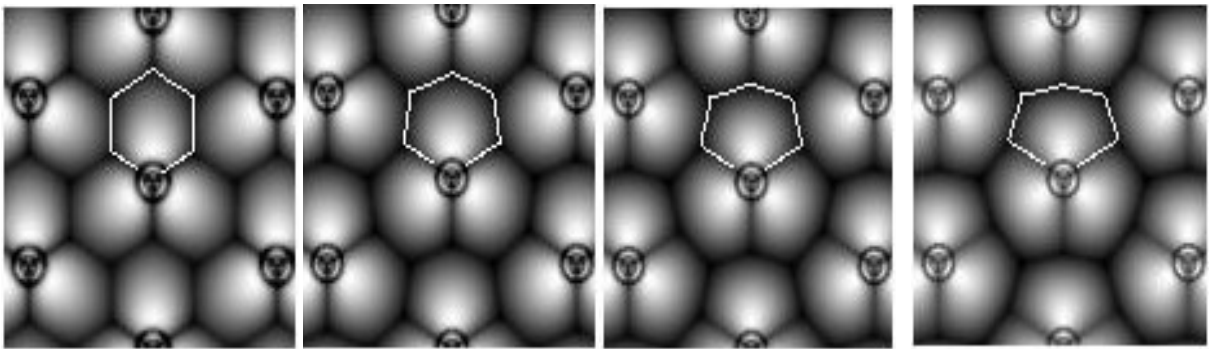

Figure 34: The detected edge of the central sector for; a) 60°; b) 75°; c) 90° and; d) 110° azimuth beamwidth at a tile of 1° and an ISD of 500m.

Following on from the SINR calculation, the capacity of each pixel can be calculated using equation (3.14). In order to calculate the capacity of the edge of the central sector, the capacity value of each pixel in the edge of the sector must be added together. Thus the total edge capacity of the central sector can be found using equation (3.15):

$$C_{\ edge} = \sum_{j=1}^{E} C_{b,j} \tag{3.15}$$

E represents the number of the pixels in the edge of central sector. The average edge capacity is derived by dividing the total edge capacity C_{edge} by the number of pixels in the cell edge E. The total central sector's capacity can be calculated using a similar expression from the calculation of the central sector's edge capacity (equation (3.16)):

$$C = \sum_{j=1}^{D} C_{b,j} \tag{3.16}$$

Here D is the number of the pixels in the central sector (rather than the edge). A value for average cell capacity at the central sector is C divided by total number of pixels in the sector D.

3.8 Network Performance Results

In the following section, network cell coverage and capacity is investigated and analysed, and the optimum cell coverage and downtilt angle is discovered. The instantaneous cell edge

improvement is also assessed and different path loss models are used to verify the cell edge performances. Lastly, the varying cell edge is defined and its performances are analysed before the results of cell and cell edge performances for different ISDs are summarised.

3.8.1 Optimum cell coverage and downtilt angle

In this section, the optimum cell coverage and antenna downtilt angle are investigated through comparing different azimuth beamwidths. The average cell capacity for beamwidths of 60°, 75°, 90° and 110° was derived for a tilt angle range of 0° to 15°. The ISD was kept at a constant 500m. The average cell capacity for the different tilt angle is compared in Figure 35

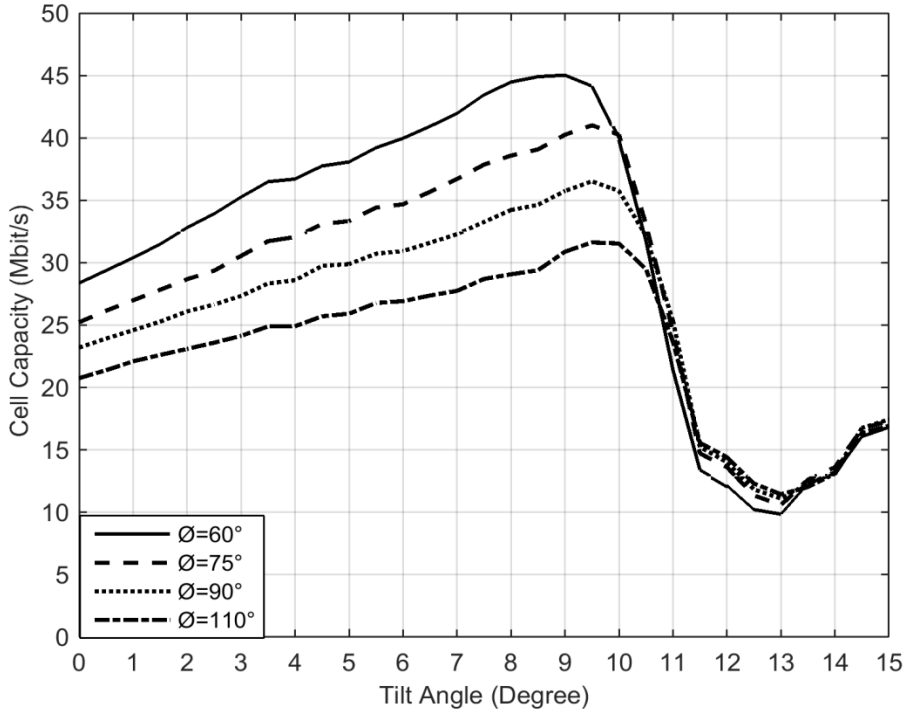

Figure 35: Average cell capacity for different azimuth beamwidth VS. Tilt angle for ISD of 500m

Figure 35 shows that the cell capacity for a beamwidth of 60° is higher than the other azimuth beamwidths for a tilt angle range of 0° up to 10°. The optimum tilt angle for all azimuth beamwidths is 9°. Between this range of tilt angles, the cell capacity decreases with increasing azimuth beamwidth. Past a tilt angle of 9°, the cell capacity sharply drops for all azimuth beamwidths. The lowest value within this range is experienced with the 60°

beamwidth at a tilt angle of around 13°: however, in practice we are not concerned with the extreme tilt angle performance of the beams as their cell capacities are unfeasibly low, and so the 60° azimuth beamwidth is considered to be the most optimal choice for the indicated tilt angle range.

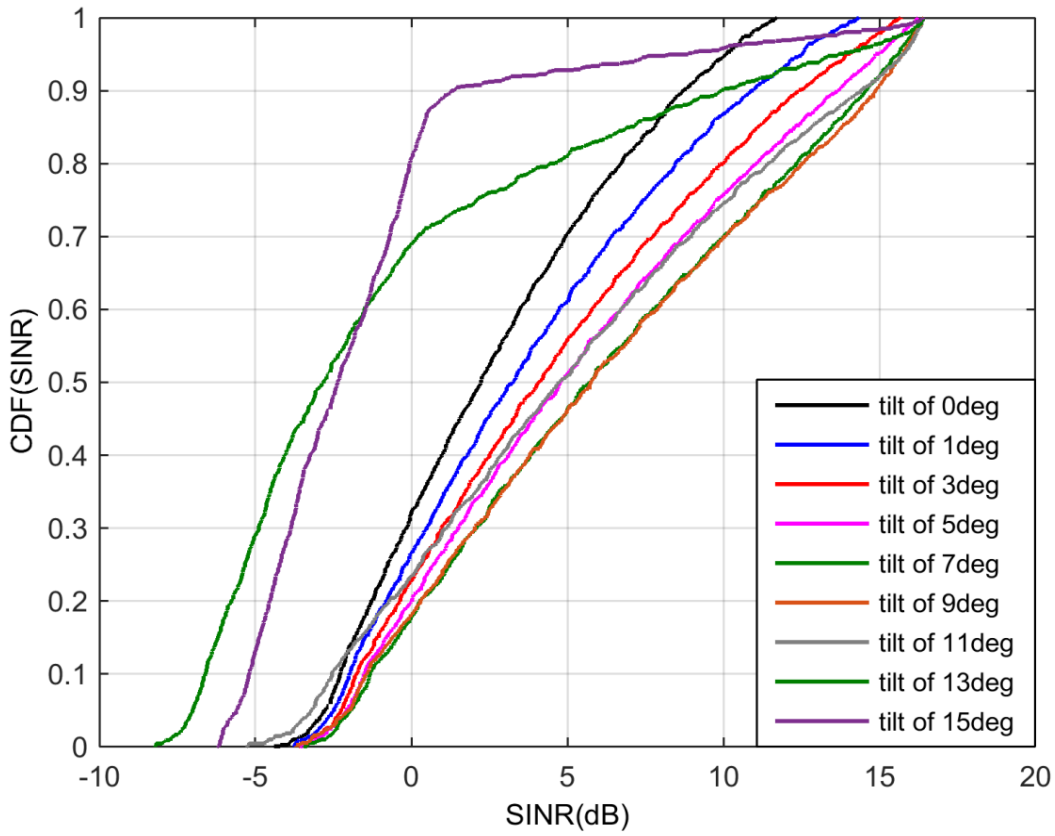

Figure 36: CDF distribution of SINR for 60° azimuth beamwidth at different tilt angles for ISD of 500m

In Figure 36 at a tilt angle of 9°, the cell SINR reaches the maximum value. However, from statistical point of view, for the high tilt angle the data is more skewed as the antenna's radiation pattern is pointed more towards the basestation side. It can reduce the interference in certain outliers but only by sacrificing with the coverage.

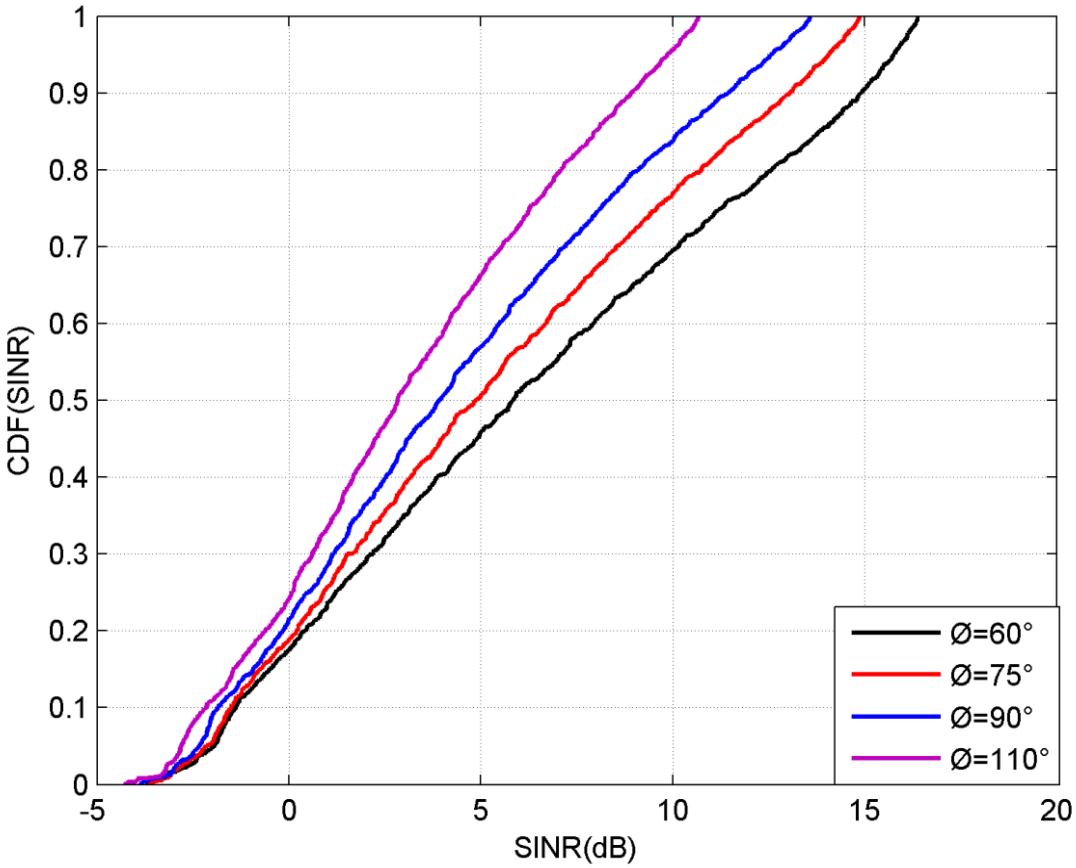

Figure 37: CDF distribution of SINR for different azimuth beamwidth at tilt angle of 9° for ISD of 500m

Figure 37 shows the CDF distribution of SINR for different azimuth beamwidth at the optimum tilt angle of 9° for ISD of 500m. It can be seen that at the optimum tilt angle of 9°, the 60° azimuth beamwidth cell shows the best cell performance.

Section 3.8.2 compares the effect of switching the azimuth beamwidth from 60° to 75°, 90° and 110° in an attempt to improve cell edge capacity rather than the average cell capacity. The real cell edge performance of different azimuth beamwidth is also compared; and an explanation of the method used to compare the effect of switching the azimuth beamwidth is outlined in this Section.

3.8.2 Instantaneous cell edge performance assessment

In the assumption outlined in Section 3.5, the methodology for improving the capacity of cell edge users was to widen the antenna's azimuth beamwidth, thus shifting the relative position of the edge users towards the centre of the cell. As a result, the cell capacity of these users can be improved.

The 60° beamwidth was chosen as the reference case as it displayed the most optimal cell capacity of the beamwidths studied for a reasonable tilt angle range. In order to compare the results in a concise way, it was decided that the original sector edge plot for the 60° beamwidth should be superimposed on top of the new sector edge plot from the switched beamwidth. The original 60° beamwidth sector edge is shown as a white border within the greyscale image of the new sector edge plot. This is shown in Figure 38, with the 60° sector edge superimposed on the SINR distribution plot for the chosen azimuth beamwidth range.

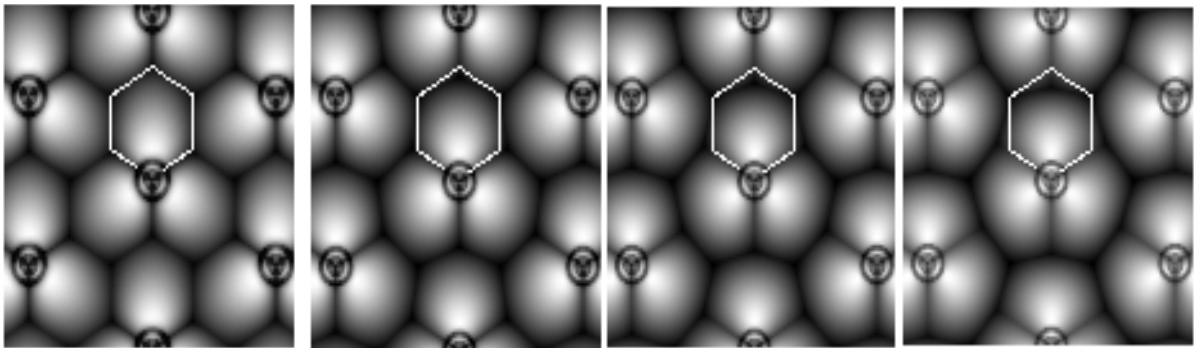

Figure 38: Sector edge of the 60°azimuth beamwidth (a) superimposed on the SINR distribution plot of; b) 75°; c) 90° and; d) 100° azimuth beamwidth at a tilt angle of 1° and an ISD of 500m

Figure 38 shows that the actual shape of the cell for the higher beamwidths is very different compared to the original 60° instantaneous cell. Following on from this analysis, the average cell edge capacity for the instantaneous 60° white cell was calculated for the new beamwidths of 75°, 90° and 110°. This was completed by calculating the cell edge capacity for each pixel in the white instantaneous cell shown in Figure 38, and then taking the average of these results, for each chosen azimuth beamwidth. Results were taken for a tilt angle range of 0° to

15° and an ISD of 500m. The results are shown in Figure 39 and Figure 40, the instantaneous cell edge SINR and Capacity.

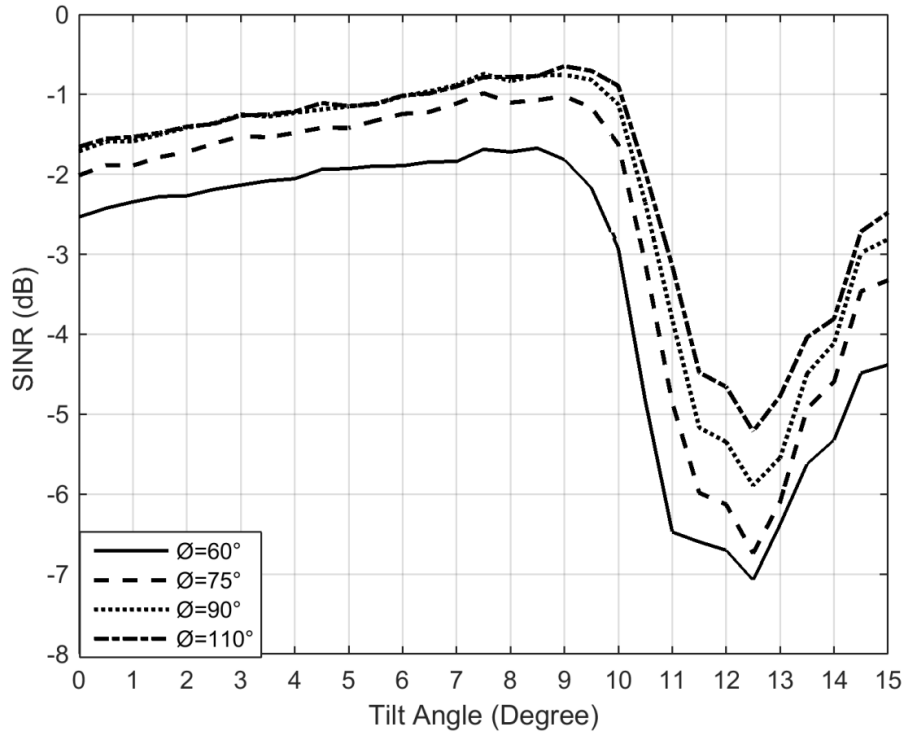

Figure 39: Average cell edge SINR of 60° azimuth beamwidth superimposed on 75°, 90° and 110° azimuth beamwidth cell for an ISD of 500m

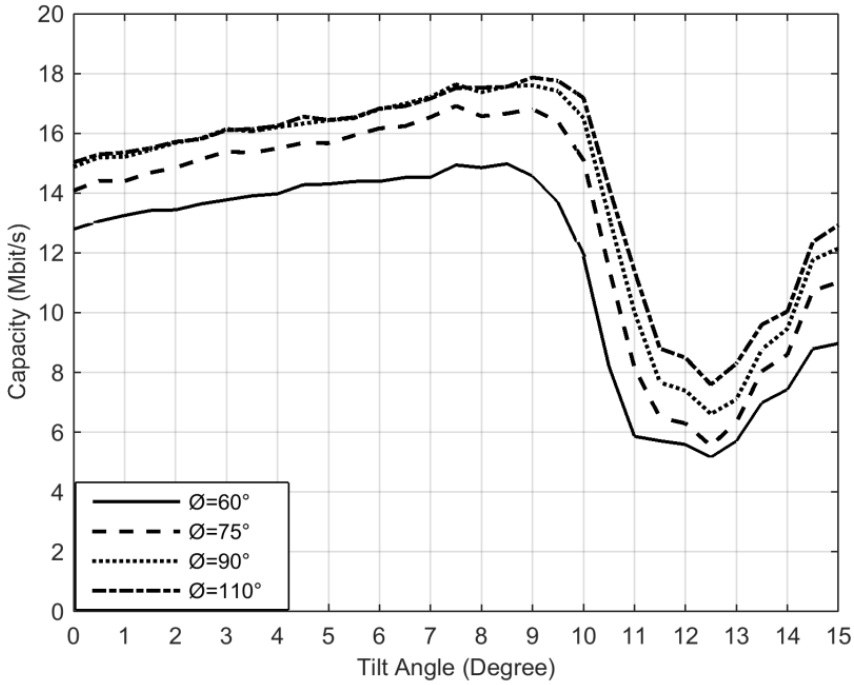

Figure 40: Average cell edge capacity of 60° azimuth beamwidth superimposed on 75°, 90° and 110° azimuth beamwidth cell for an ISD of 500m

Both the instantaneous cell edge SINR and capacity shown in Figure 39 and Figure 40 show a similar trend. It can be seen that the cell edge capacity of 60° azimuth beamwidth can be improved the most by switching the azimuth beamwidth from 60° to 110°. At a tilt angle of 9°, the cell edge capacity of the 60° azimuth beamwidth can be improved by around 3.3Mbit/s by switching to 110°. It has already been discussed that the downside to this method is that average cell capacity decreases: for example, Figure 40 shows that at a tilt angle of 9° the difference in average cell capacity between the widest and narrowest beams is 14.15Mbit/s. This is still enough capacity to support most communications; however, it shows that there is a trade-off between cell capacity and cell edge capacity by switching the antenna's azimuth beamwidth.

The results in Figure 41 were derived by calculating the average capacity around the white edge of the instantaneous 60° cell for each different azimuth beamwidth. This was then compared with the real cell edge performance for each of the azimuth beamwidths, in order to show the advantages of employing beam switching rather than keeping the beamwidths fixed in terms of cell edge performance. The real edges of the cells for the 60°, 75°, 90° and 110° beamwidths are shown as white borders in Figure 38. The cell edge capacity for these cells is shown in Figure 42, for the same tilt angle range and ISD.

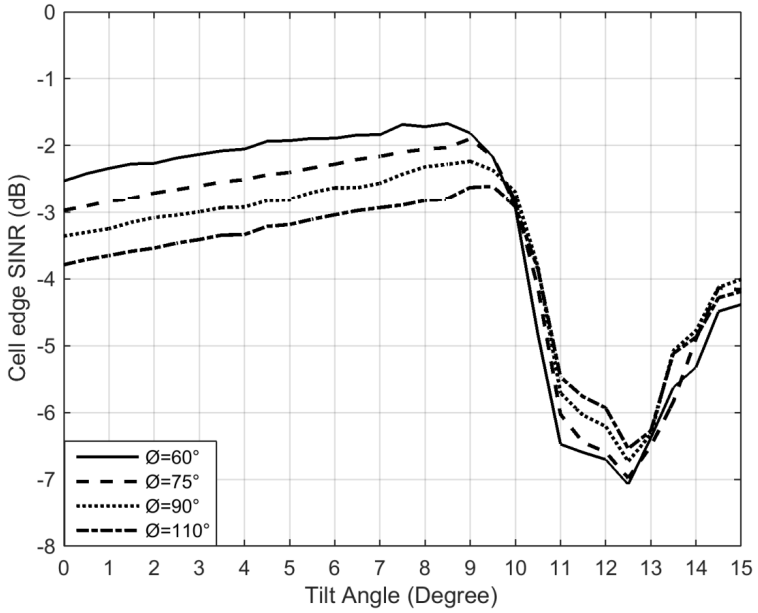

Figure 41: Average cell edge SINR for different azimuth beamwidth vs tilt angle for an ISD of 500m

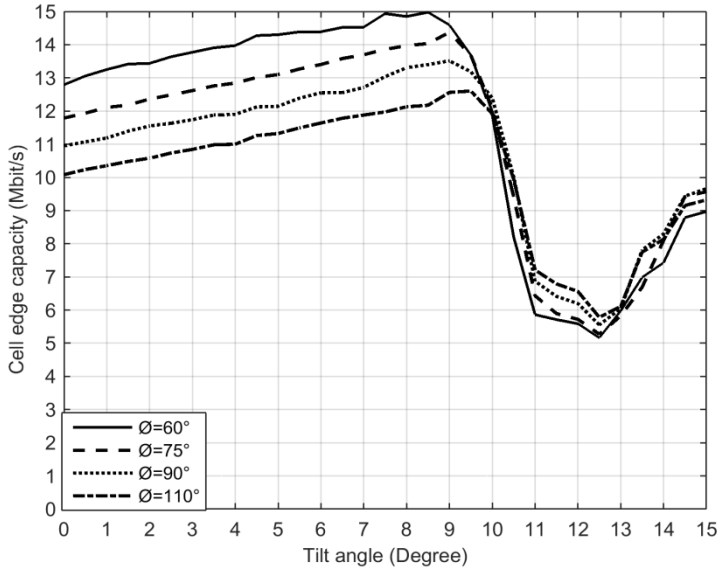

Figure 42: Average cell edge capacity for different azimuth beamwidths vs tilt angle for an ISD of 500m

Both Figure 41 and Figure 42 show the similar trend of the cell edge performance in terms of SINR and capacity for different azimuth beamwidth. Figure 42 also shows a similar trend between average cell edge capacity and the average cell capacity for the different beamwidths. The 60° beamwidth cell shows the greatest cell edge capacity between a tilt angle of 0° and 9°. The maximum value for this beam is 15 Mbit/s: however, Figure 35 shows a maximum cell edge capacity of 18Mbit/s at the same tilt angle. This means that for users gathered at the

edge of the instantaneous 60° cell, switching the beamwidth from 60° to 110° can bring an improvement of 3 Mbit/s to the cell edge capacity, this demonstrating the potential of employing beamwidth switching schemes.

3.8.3 Different path loss models verification for switching azimuth beamwidth from 60° to 110° for cell and edge capacity

As a way to verify these improvements, different path loss models have been applied to compare performances for different boundary equations. The path loss models chosen are; Winner II, which is 3GPP defined and implemented in our system simulator; Cost-231- Hata, which is an empirical path loss model used in medium to small cities; and Cost 231 Non-Line-of site (NLOS), which is a semi-empirical path loss model taking the characteristics of the city structure into account. As shown in Section 3.8.2, by switching the antenna's azimuth beamwidth from 60° to 110°, the cell edge capacity of 60° azimuth beamwidth can be improved by around 3.3 Mbit/s at an optimum tilt angle of 9° and an ISD of 500m. The cell capacity of 60° azimuth beamwidth will however drop by around 14Mbit/s as a trade-off through widening the antenna's azimuth beamwidth using the Winner II path loss model.

The Winner II Dense Urban path loss model is expressed as in equation (3.17):

$$L_{(dB)} = 26\log_{10} f + 22.7 + 36.7\log_{10}(d_m) \tag{3.17}$$

The Cost-231-Hata model [111] is used here to verify the system performances. The mathematical expression of this path loss model is shown in equation (3.18):

$$L_p\,(dB) = A + B log_{10}(d) + C \tag{3.18}$$

Where:

$$A = 46.3 + 33.9\, log_{10}\,(f_c) - 13.28\, log_{10}\,(h_b) - a\,(h_m) \tag{3.19}$$

$$B = 44.9 - 6.55 log_{10}(h_b) \tag{3.20}$$

$$C = \begin{Bmatrix} 0, for\ medium\ city\ and\ surburban\ areas \\ 3, for\ metropolitan\ areas \end{Bmatrix} \tag{3.21}$$

The Cost 231-Walfisch-Ikegami Non-line of sight (NLOS) ([112] and [113]) can be expressed as follows:

$$L_{NLOS}(\text{dB}) = L_{FS} + L_{rts}\,(w_r, f, \Delta h_{Mobile}\,, \emptyset\,) + L_{MSD}\,(\Delta h_{Base}\,, h_{Base}\,, d, f, b_s\,) \quad (3.22)$$

Where:

$$L_{FS} = Free\ Space\ Path\ Loss = 32.4 + 20log_{10}(d[km]) + 20log_{10}(f[MHz]) \quad (3.23)$$

$$L_{rts} = Roof - to - Street\ loss \quad (3.24)$$

$$= -8.8 + 10log_{10}(f[MHz]) + 20log_{10}(\Delta hMobile\,[m]) - 10log_{10}(w[m]) + L_{ori}$$

$$L_{ori} = Street\ orientation\ function \quad (3.25)$$

$$= \begin{Bmatrix} 10 + 0.35\phi & 0 \le \phi \le 35° \\ 2.5 + 0.075(\phi - 35) & 35° \le \phi \le 55° \\ 4.0 - 0.114(\phi - 55) & 55° \le \phi \le 90° \end{Bmatrix}$$

$$L_{MSD} = Multi - diffraction\ loss \quad (3.26)$$

$$= L_{bsh} + k_a + k_d log_{10}(d[km]) + k_f log_{10}(f[MHz]) - 9log_{10}(b)$$

$$L_{bsh} = \begin{Bmatrix} 18log_{10}(1 + \Delta h_{Base}) & h_{Base} > h_{Roof} \\ 0 & h_{Base} \le h_{Roof} \end{Bmatrix} \quad (3.27)$$

The specific type of Cost 231 Walfish-Ikegami NLOS model used here is called microcell NLOS pathloss: this is a variant of the Cost 231 where the antenna height at the basestation is set to 11.11 m and the height of the surrounding buildings are 12m. The interspacing between buildings is 50 and the width of each surrounding street is 25m. Each mobile station antenna has a height of 1.5m, and the tilt of each antenna is 25°. The operating frequency of the system is 1900 MHz. With these parameters, the following simplification can be made:

$$L_{NLOS}(dB) = 148.48 + 39.11log_{10}\left(\frac{d}{1000}\right) + 1.424\left(\frac{d}{1000}\right) \quad (3.28)$$

Based on these 3 different path loss models, the path loss VS distance results are shown in Figure 43.

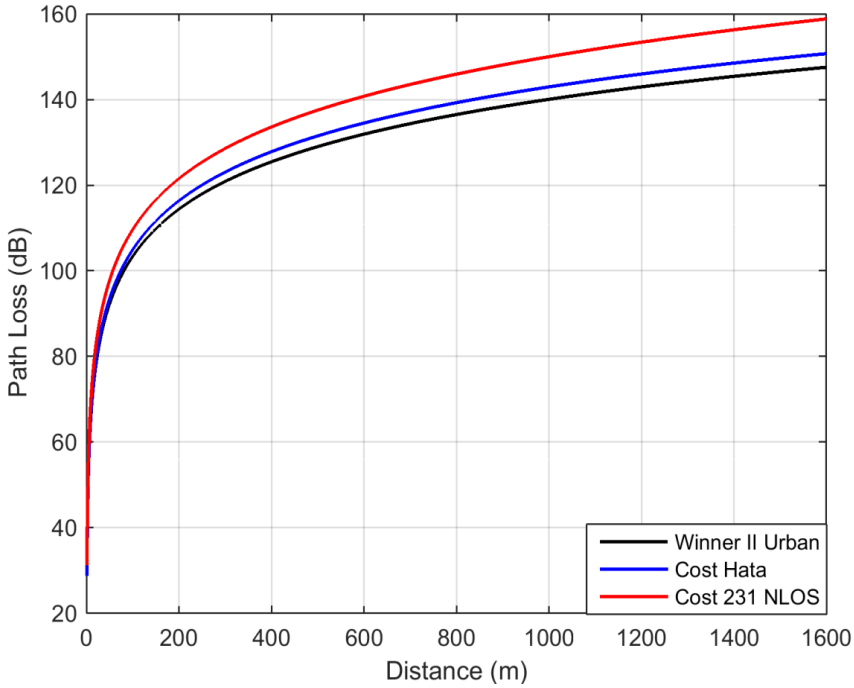

Figure 43: Path loss vs distance, based on 3 different path loss models

Figure 43.shows that the difference between the Winner II Urban and Cost Hata path loss model is small (1 to 3dB) for an ISD above 200m, and that the difference between Cost 231 NLOS and the other two path loss models is between 3 to 9dB. Both the Winner II Urban and Cost Hata Path loss models are empirical ones and the Cost 231 NLOS is a semi-empirical model based on the real city structures.

The average cell capacity and instantaneous cell edge improvement by switching antenna's azimuth beamwidth from 60° to wide 110° using these 3 different path loss models are shown below:

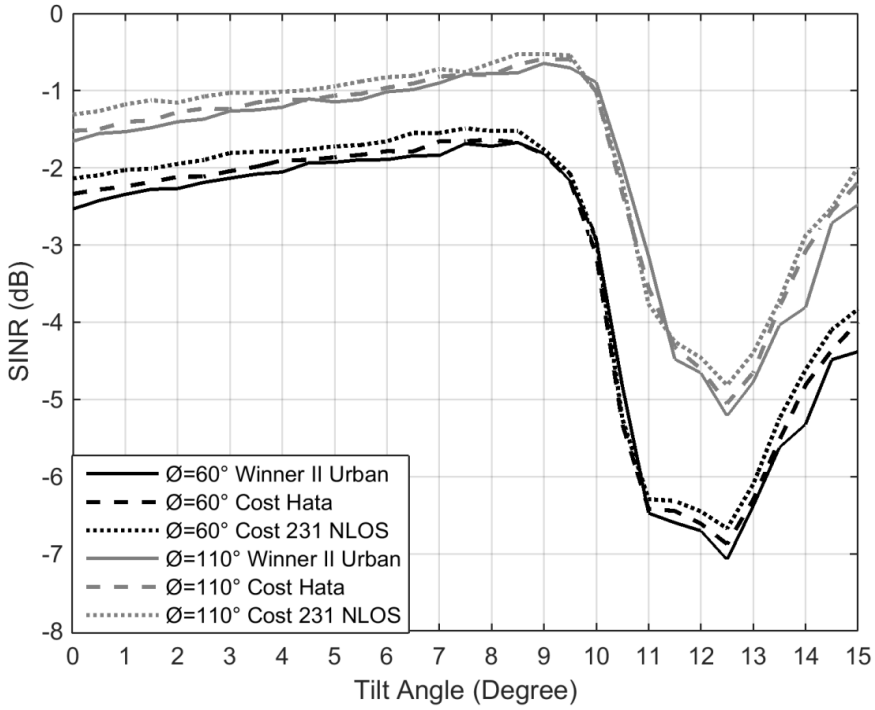

Figure 44: Average instantaneous edge SINR of 60° and superimposed on 110° azimuth beamwidth vs tilt angles for different path loss models for an ISD of 500m

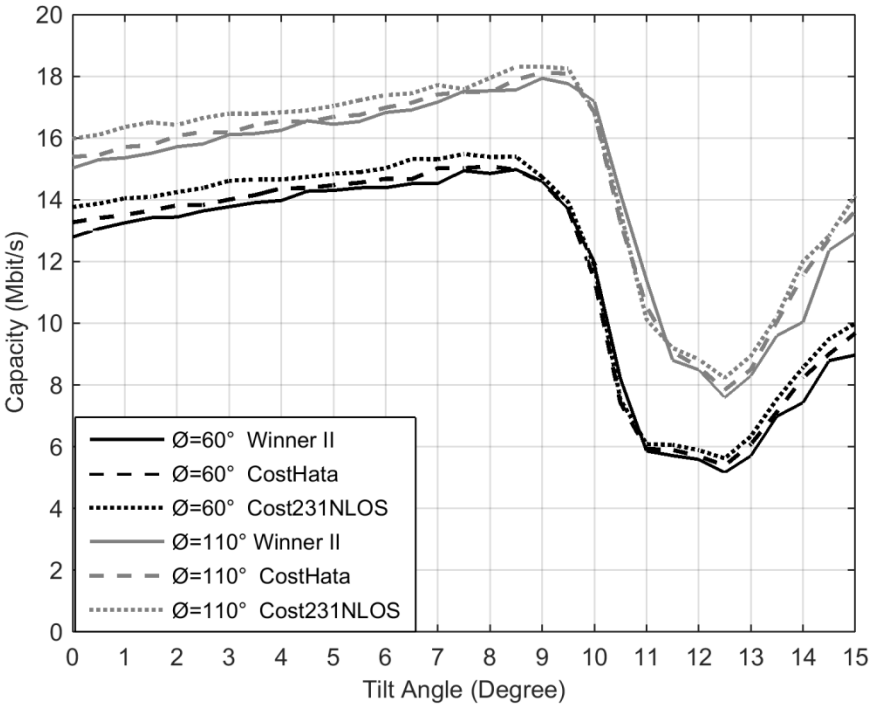

Figure 45: Average instantaneous edge capacity of 60° and superimposed on 110° azimuth beamwidth vs tilt angles for different path loss models for an ISD of 500m

It can be seen from Figure 45 that the cell edge capacity of 60° and 110° azimuth beamwidth follow the same trend for different tilt angles. The different between each path loss model is within 1Mbit/s. As each of the different path loss models show the same trend and similar results, this investigation verifies that the by switching this antenna's azimuth beamwidth from 60° to 110°, the cell edge capacity of 60° azimuth beamwidth can be improved.

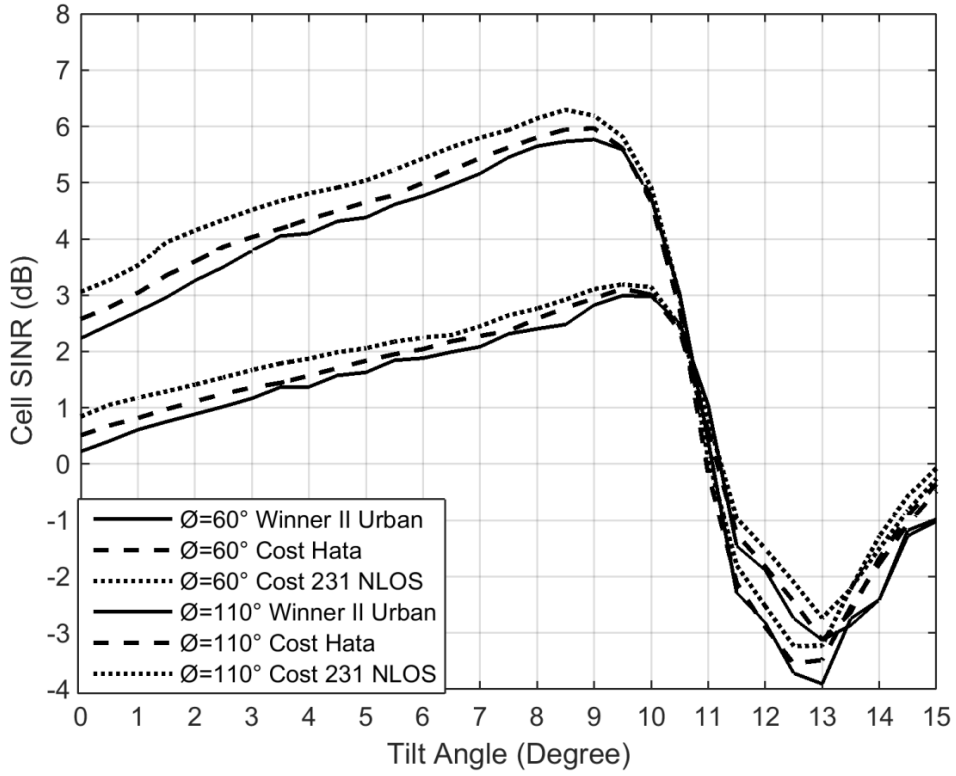

Figure 46: Average cell SINR for 60° and 110° azimuth beamwidth vs tilt angles for different path loss models and an ISD of 500m

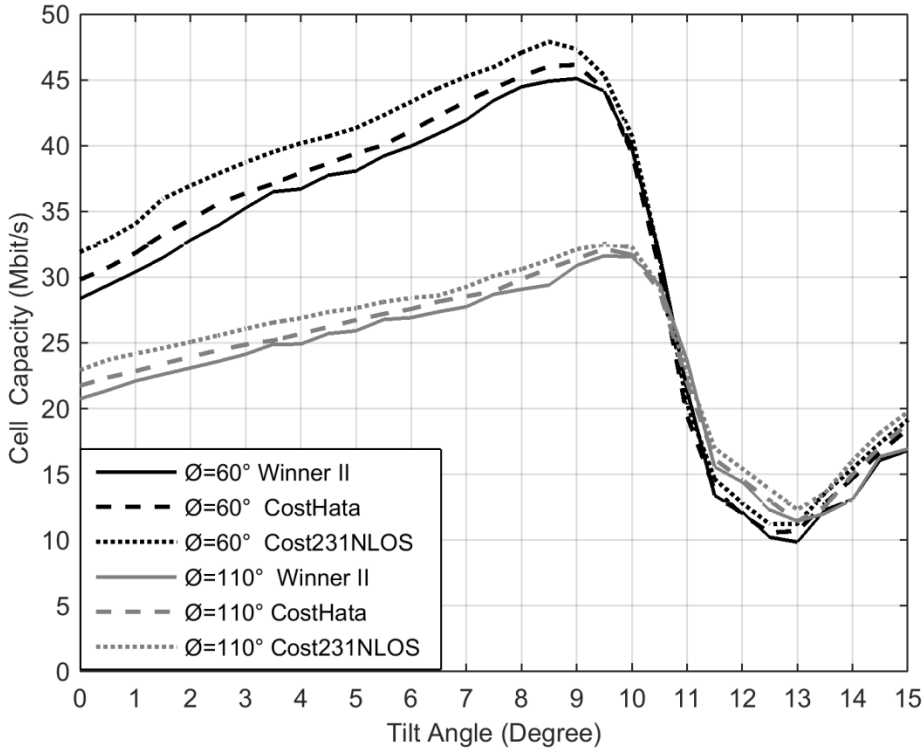

Figure 47: Average cell capacity for 60° and 110° azimuth beamwidth vs tilt angles for different path loss models and an ISD of 500m

Both Figure 46 and Figure 47 show the Instantaneous cell edge and cell performance in terms of SINR and capacity with different tilt angles for ISD of 500m. Comparing these with Figure 42 shows that the average cell capacity of 60° and 110° azimuth beamwidth follows the same trend for different path loss models within the range of tilt angle from 0° to 15°, when the antenna's azimuth beamwidth is switched from 60° to 110° for ISD of 500m.

3.8.4 Cell and edge region performances for different ISDs

Based on the same system model and parameters, different ISDs from 500m to 1500m are investigated here to further compare the effect of switching the antenna's azimuth beamwidth from 60° to 110°. The figures below show the effect of changing the ISD and tilt angle on the average cell SINR and the average cell capacity.

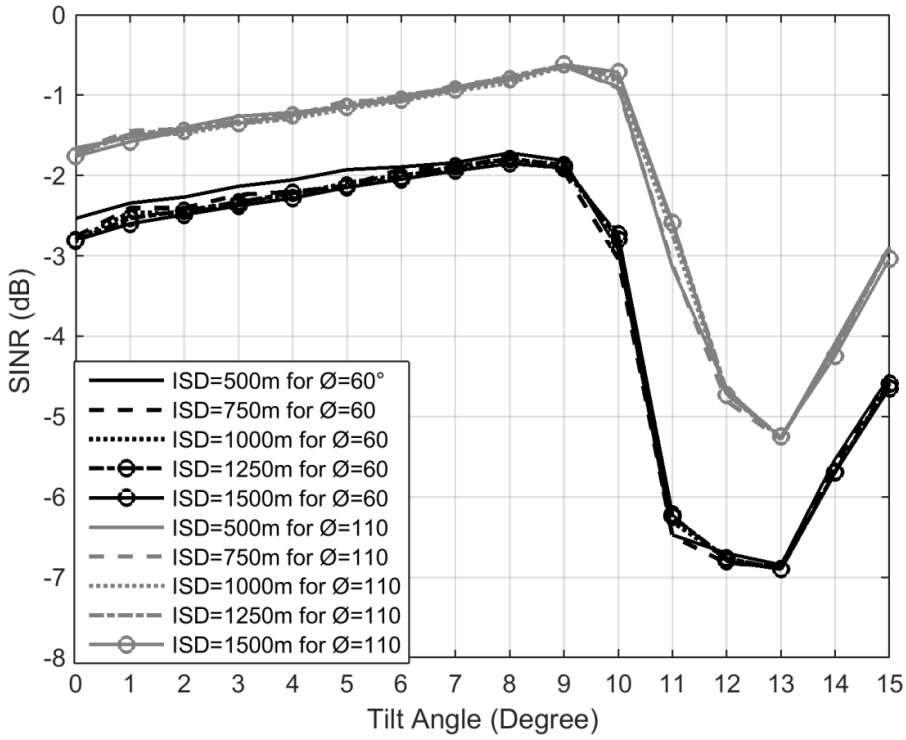

Figure 48: Average cell edge SINR of 60° superimposed on 110° azimuth beamwidth for different ISDs vs tilt angles

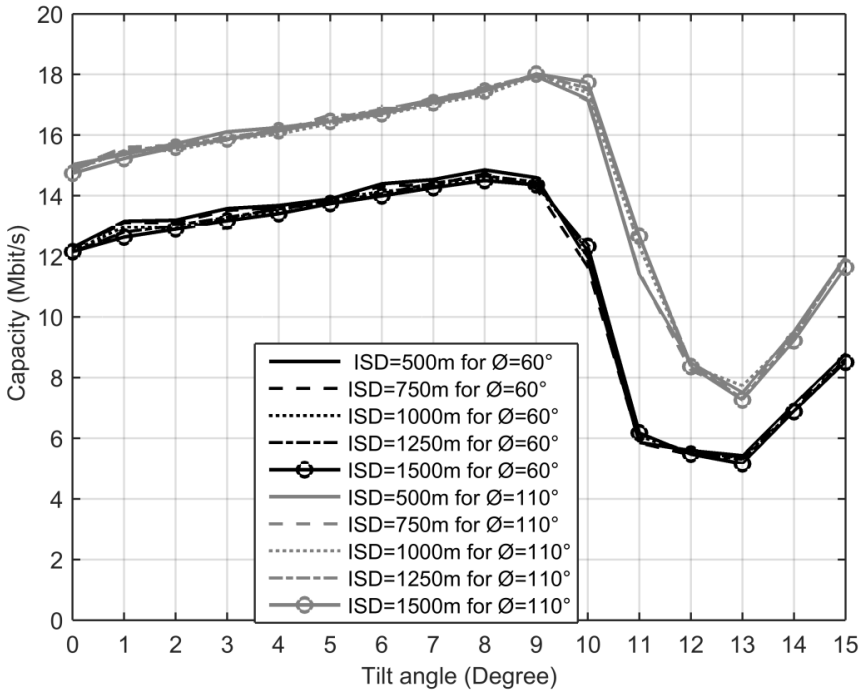

Figure 49: Average cell edge capacity of 60° superimposed on 110° azimuth beamwidth for different ISDs vs tilt angles

Figure 48 and Figure 49 show that there is improvement of cell edge SINR and capacity of 60° azimuth beamwidth by switching the antenna's azimuth beamwidth from 60° to 110° , and that the SINR and average cell capacities follow the same trend for different ISDs from 500m to 1500m within the tilt angle range of 0° to 15°.

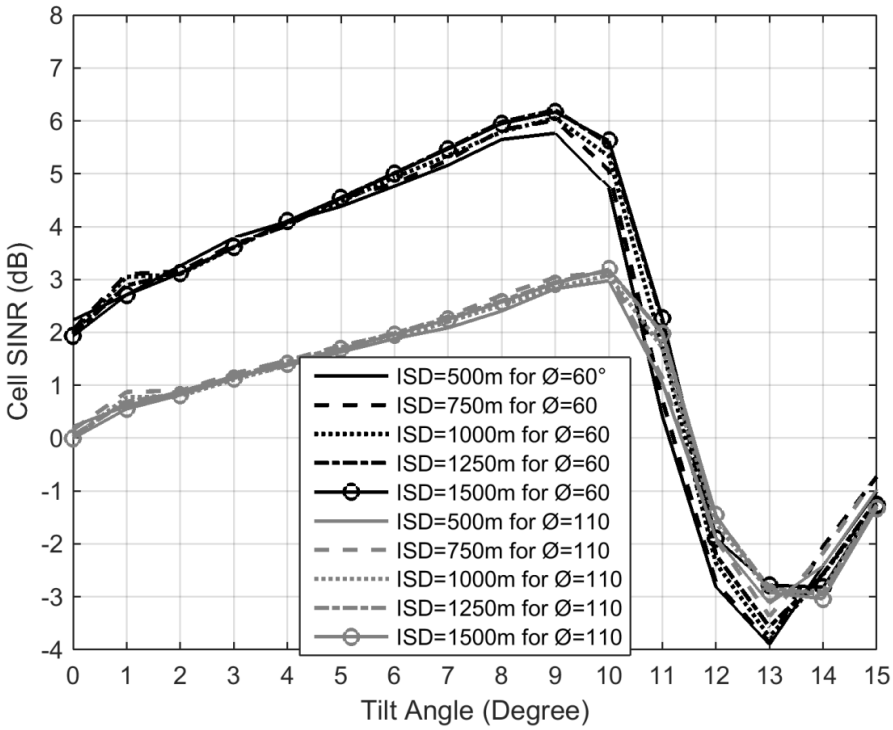

Figure 50: Average cell SINR of 60° and 110° azimuth beamwidth for different ISDs vs tilt angles

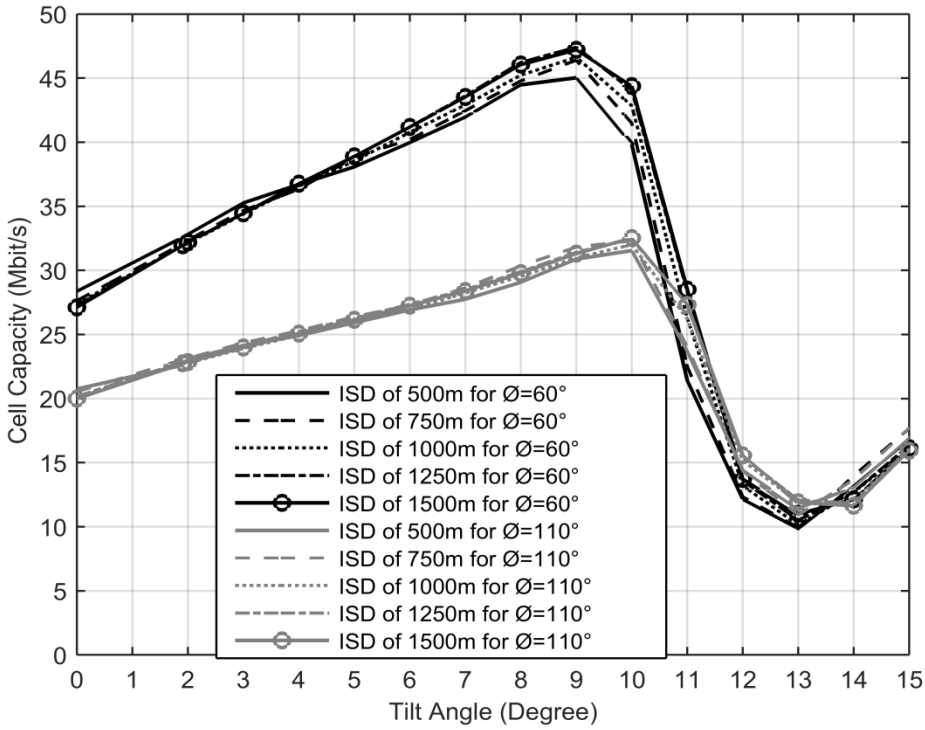

Figure 51: Average cell capacity of 60° and 110° azimuth beamwidth for different ISDs vs tilt angles

Figure 50 and Figure 51 show that the average cell SINR and capacity of the azimuth beamwidth for 60° and 110° follows the same trend with tilt angle varying from 0° to 15° for different ISDs from 500m to 1500m. The table below summaries the average cell capacity and the improvement of cell edge capacity for 60 ° azimuth beamwidth through switching the antenna's azimuth beamwidth from 60° to 110° at optimum tilt angle of 9° for ISDs from 500m to 1500m.

Table 4: Summaries of cell edge and cell capacity for different ISDs at an optimum tilt angle of 9°

ISD (m)	Azimuth Beamwidth (°)		% Change
	Cell edge capacity (Mbit/s) (Cell capacity (Mbit/s))		
	60°	110°	
500	14.6 (45.0)	17.9 (30.9)	22.6 (-31.3)
750	14.2 (46.4)	18.0 (31.0)	26.8 (-33.2)
1000	14.4 (46.6)	17.9 (31.2)	24.3 (-33.0)
1250	14.5 (47.4)	18.0 (31.4)	24.1 (-33.8)
1500	14.4 (47.2)	18.0 (31.3)	25.0 (-33.7)

It can be seen that there is a trade-off between average cell capacity and cell edge capacity by switching the antenna's azimuth beamwidth from 60° to 110° in that at the wider azimuth beamwidth the cell edge capacity increases while the cell capacity decreases. For example, by switching the beamwidth from 60° to 110° for an ISD of 500m and a tilt angle of 9° the cell edge capacity increases by 22.6% (14.6 Mbit/s to 17.9 Mbit/s) while the cell capacity decreases by 31.3% (45 Mbit/s to 30.9 Mbit/s). And, for different ISDs, they follow the same

trend as with the case for ISD of 500m. Overall, the cell edge capacity of 60° azimuth beamwidth can be improved by around 3.5 Mbit/s for different ISDs. However, there is a decrease in average cell capacity by around 15Mbit/s through switching the azimuth beamwidth from 60° to 110°.

3.8.5 Varying cell edge performance

The following section demonstrates the varying cell edge concept. To compare the improvement of cell edge capacity of 60° azimuth beamwidth by superimposing it on 110° azimuth beamwidth cell within varying cell edge area, four different cell edge regions are defined to analysis the user capacity. Basically, the cell edge is defined as the minimum SINR value and detected by the image processing technique stated in Section 3.8.2.

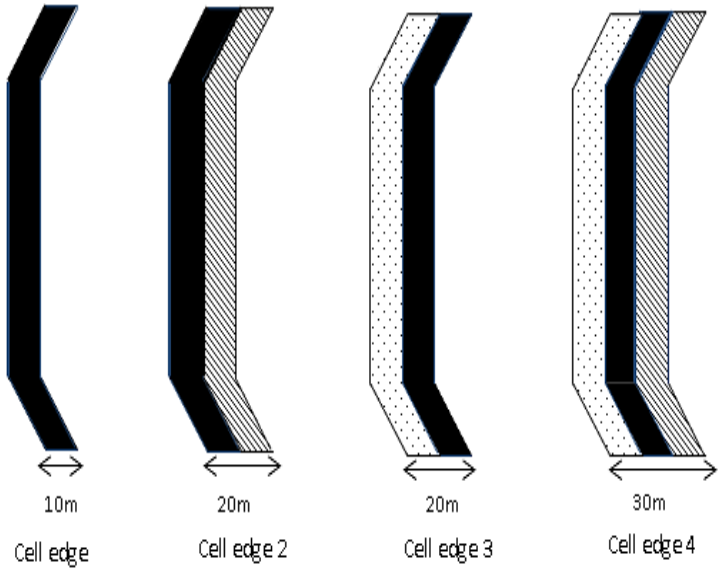

Figure 52: Four different cell edge definitions

The different cell edge definition is shown in Figure 52. The original cell edge is defined by 1 pixel width, which is around 10m. The second cell edge is the original edge region plus 1 pixel width into the cell and the total cell edge width is 20m. The third cell edge is the original cell edge region plus 1 pixel width out from the cell and the total cell edge width is 20m. The fourth cell edge is the original cell edge region plus 1 pixel width in the cell and 1 pixel width out from the cell and the total cell edge width becomes 30m.

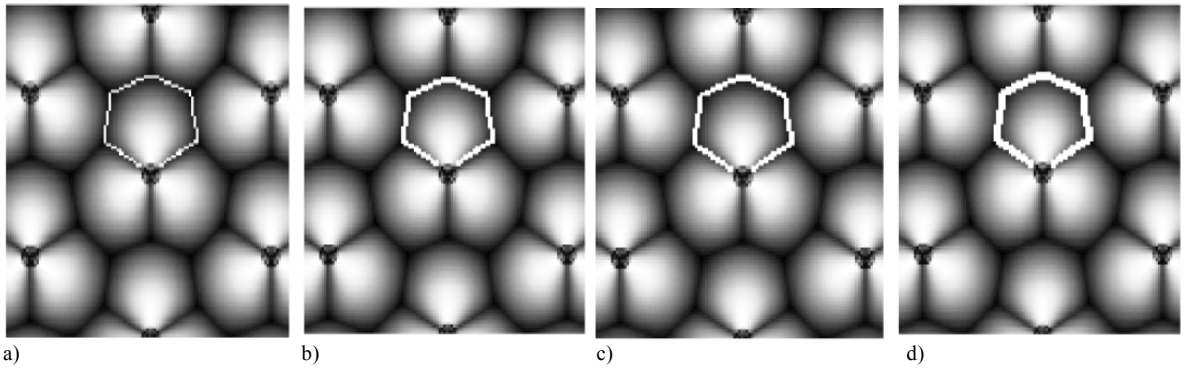

Figure 53: Detected cell edge for varying cell edge region; a) Original defined cell edge; b) Cell edge 2; c) Cell edge 3 and; d) cell edge 4 at an optimal tilt angle of 9° and an ISD of 500m

Figure 53 shows the four different cell edge regions which can be detected using the cell edge detection technique. It can be seen that the thickness of the cell edge changes depending on how this edge is defined. Figure 53 a) to d) shows how the capacity of each of the cell edge definitions varies depending on the tilt and the azimuth beamwidth.

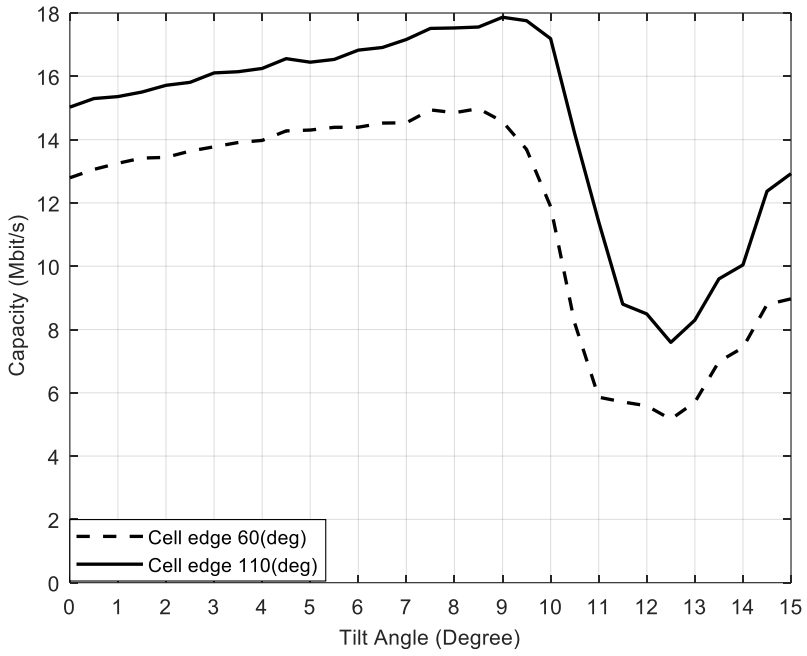

Figure 54: Varying cell edge capacity of 60° and superimposed on 110° azimuth beamwidth for ISD of 500m (Cell edge 1)

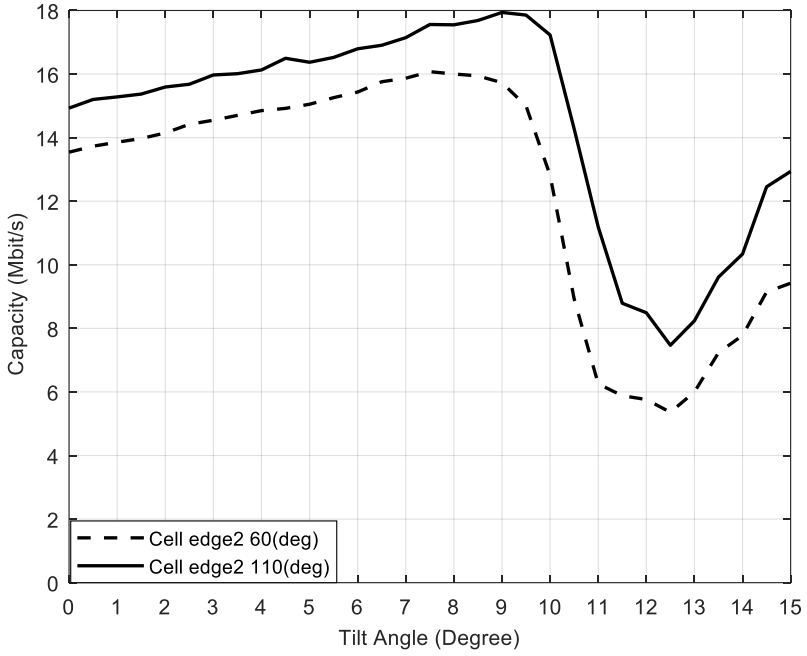

Figure 55: Varying cell edge capacity of 60° and superimposed on 110° azimuth beamwidth for ISD of 500m (Cell edge 2)

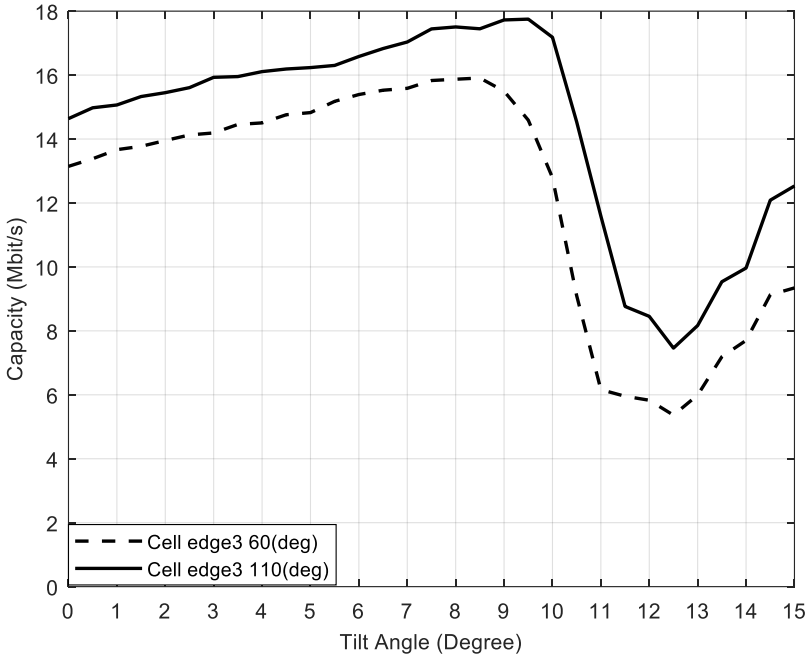

Figure 56: Varying cell edge capacity of 60° and superimposed on 110° azimuth beamwidth for ISD of 500m (Cell edge 3)

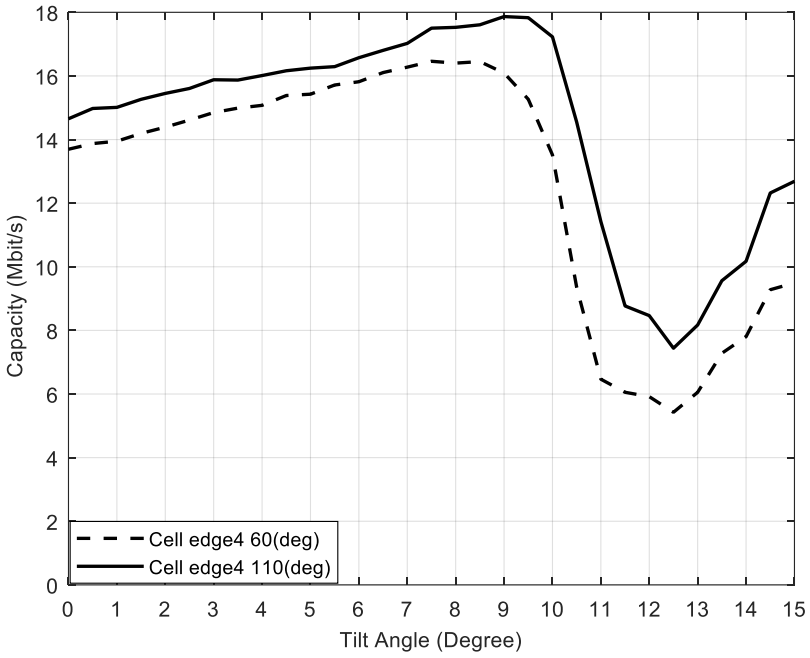

Figure 57: Varying cell edge capacity of 60° and superimposed on 110° azimuth beamwidth for ISD of 500m (Cell edge 4)

It can be seen from Figure 54 to Figure 57 that at the optimum tilt angle of 9°, by switching the antenna's azimuth beamwidth from 60° to 110°, the original cell edge region of 60° azimuth beamwidth can be improved by around 3.3Mbit/s. This trend is mirrored by cell edge region 2 and cell edge region 3, which can both be improved by around 2.2Mbit/s. For the wide cell edge region 4, the cell edge capacity can be improved by around 1Mbit/s. The varying cell edge capacity confirms that the original cell edge capacity of 60° azimuth beamwidth can be improved most by superimposing the cell edge on 110° azimuth beamwidth cell through switching the azimuth beamwidth from 60° to 110°.

3.8.6 Results summary for different ISDs

Table 5 summarizes the varying cell edge capacity at optimum tilt angle of 9° for different ISDs. There are four cell edge region capacity comparisons obtained by using 60° azimuth beamwidth cell edge and superimposing it on 110° azimuth beamwidth cell for different ISDs.

Table 5: Summaries of the varying cell edge capacity for different ISDs between 60° and 110° azimuth beamwidth at optimum tilt angle of 9°

ISD (m)	**Cell edge capacity (Mbit/s) (Cell capacity (Mbit/s))**							
	Edge Region 1		**Edge Region 2**		**Edge Region 3**		**Edge Region 4**	
	60°	**110°**	**60°**	**110°**	**60°**	**110°**	**60°**	**110°**
500m	14.6 (45.5)	17.9 (30.9)	15.7 (45.5)	17.9 (30.9)	15.5 (43.3)	17.8 (29.3)	16.1 (43.3)	17.8 (29.3)
750m	14.2 (46.4)	18.0 (31.0)	14.9 (46.4)	18.0 (31.0)	14.8 (44.0)	17.9 (29.9)	15.3 (44.0)	17.7 (29.9)
1000m	14.4 (46.6)	17.9 (31.2)	14.8 (46.6)	17.8 (31.2)	14.8 (44.9)	17.8 (29.8)	15.1 (44.9)	17.8 (29.8)
1250m	14.5 (47.4)	18.0 (31.4)	14.8 (47.4)	17.9 (31.4)	14.7 (45.3)	17.9 (30.4)	15.0 (45.3)	17.8 (30.4)
1500m	14.4 (47.2)	18.0 (31.3)	14.7 (47.2)	17.9 (31.3)	14.6 (45.7)	17.8 (30.5)	14.8 (45.7)	17.8 (30.5)

Table 5 shows that the improvement in varied cell edge capacity for different cell edge region is between around 1Mbit/s and 3Mbit/s for an ISD range of 500 m to 1500 m. For all ISDs the improvement in cell edge capacity is compensated for by a reduced cell capacity, which decreased in the range of 14 Mbit/s to 16 Mbit/s.

3.9 Summary

A novel approach has been suggested here to instantaneously improve the cell edge capacity of antennas. This used an advanced beam switching antenna system rather than through a method described in the existing literature. Through switching the azimuth beamwidth of the antenna from narrow 60° to wide 110°, the cell edge capacity of 60° azimuth beamwidth cell can be improved instantaneously by around 3 Mbit/s. In addition, the antenna downtilt angle (from 0° to 15°) effects on mobile network performances, in terms of cell coverage and capacity with different ISDs (from 500m to 1500m), has been investigated. It is shown that for different cell sizes and different ISDs, the instantaneous cell edge and cell capacity has a similar trend in that switching the beamwidth in this way increases the cell edge capacity but decreases the average cell capacity. It also shows that with the tilt angle of antenna increases, the cell performances of the mobile network can be improved up to an optimum tilt angle of 9°, at which point the cell performances quickly worsen.

This page is intentionally blank.

Chapter 4. Azimuth Beamwidth Reconfiguring Analysis on Homogeneous Cellular Network: Antenna Design

4.1 Introduction

Following on the discussion on system performance analysis in a homogeneous cellular network by using azimuth beamwidth switching antenna, a 12-element pattern-reconfigurable antenna array is designed and demonstrated which is applicable for the cellular mobile system. Due to the increasing adoption of pattern-reconfigurable antennas in wireless communication, different pattern-reconfigurable models have been developed such as reconfigurable microstrip parasitic array antenna, planar electronically reconfigurable Wi-Fi band antenna and reconfigurable microstrip circular patch antenna. [115] As outlined previously there are many different mechanisms which can be employed for these types of systems, however they all rely on changing the way the current flows across the antenna, be this through a mechanical or electrical technique, thus leading to pattern reconfiguration. In addition, parasitic tuning and array tuning have been used to achieve the radiation pattern reconfigurability as well, and through material changes such as Ferrites, ferroelectric materials and frequency selective surface etc., the resonant current distribution on the antenna surface can be changed which results in controlled radiation pattern changes. [116]

Based on the assumption in network concepts, through switching the antenna azimuth beamwidth from 60° to 110°, the cell edge capacity can be improved instantaneously. Unlike the Base station antenna radiation pattern used for each sector in 3-sector cell sites in 3GPP network [164] which has a fixed azimuth beamwidth of 65° and its azimuth pattern is given by the formula shown in equation 4.1. Here, the type of a novel pattern-reconfigurable antenna chosen is based on the corner reflector antennas which can be used for 3-sector basestation transceivers. The 12-element pattern reconfigurable antenna array is designed and demonstrated. Also, two single element type of pattern-reconfigurable antenna models are designed and tested for validation purpose here.

$$A(\theta) = -min\left[12\left(\frac{\theta}{\theta_{3dB}}\right)^2, A_m\right] \; where -180 \leq \theta \leq 180, \tag{4.1}$$

θ_{3dB} is the 3dB beam width which corresponds to 65 degrees, and $A_m = 20dB$ is the maximum attenuation.

4.2 Research Contribution

In order to achieve the pattern reconfigurability in the azimuth plane, a 12-element pattern-reconfigurable antenna model which can switch its azimuth beamwidth from narrow 60° to wide 110° is designed which can be suitable for using in the cellular mobile system to achieve the required system performance. In contrast to other traditional array antennas, in order to change the pattern reconfigurability or directionality this novel design achieves pattern reconfigurability through the use of PIN diodes. The switching of the beamwidth from narrow one to wide ones is achieved by changing the PIN diodes states on the antenna reflectors, which in turn modifies the flow of current on the antenna and causes changes in the radiation pattern. This differs from traditional array antenna systems, which instead operate by changing the amplitude and phase of the elements of the array.

The performance of the antenna was simulated with CST Microwave Studio. Simulations of the realised antenna gain patterns were carried out for a 12 element array, which was found to provide the required antenna gain.

4.3 Pattern-reconfigurable antenna concept

Based on the idealised corner reflector antenna concept [6], in order to achieve the directive, low sidelobe/backlobe radiation pattern, the reflected wave from the side metallic sheet needs to be in phase with the transmitted wave from the radiating dipole. In this design, there is a crucial point where the reflected wave from the dipole is parallel to its apex as shown in Figure 58 a). Thus, to capture most of the energy radiated from the dipole antenna, the side metallic sheet length L_a needs to be chosen large enough to obtain it. Since, this idealised reflector antenna used here is composed of two reflectors formed 120° apart, the side metallic sheet length to achieve the parallel reflected wave to its apex from dipole is about $2h_s$. In order to achieve a directive radiation pattern by using this corner reflector antenna, the reflected wave needs to be in phase with the wave radiated from the dipole antenna which can be express as:

$$\Delta\varphi = \varphi_r - \varphi_t = 2n\pi, n = 0,1,2 \ldots \tag{4.2}$$

Where φ_r is the phase of the reflected wave which can be express as:

$$\varphi_r = 2h_s \times (\frac{2\pi}{\lambda}) \tag{4.3}$$

φ_t is the radiated wave from the dipole antenna which can be given as:

$$\varphi_t = -\pi \tag{4.4}$$

Thus, the distance from the dipole antenna to the apex of the reflector can be shows as:

$$h_s = \frac{(-1-2n)\lambda}{4} \tag{4.5}$$

So, the minimum distance to acquire the in-phase relationship between the radiating wave from the dipole and the reflected wave from the reflectors is $\frac{1}{4}\lambda$.

Based on the reflector antenna shown in Figure 58 a), it is possible to see that a completed 3-sector antenna would contain another two dipoles which are set 120° apart. It would also contain an additional reflector, as shown in Figure 58 b).

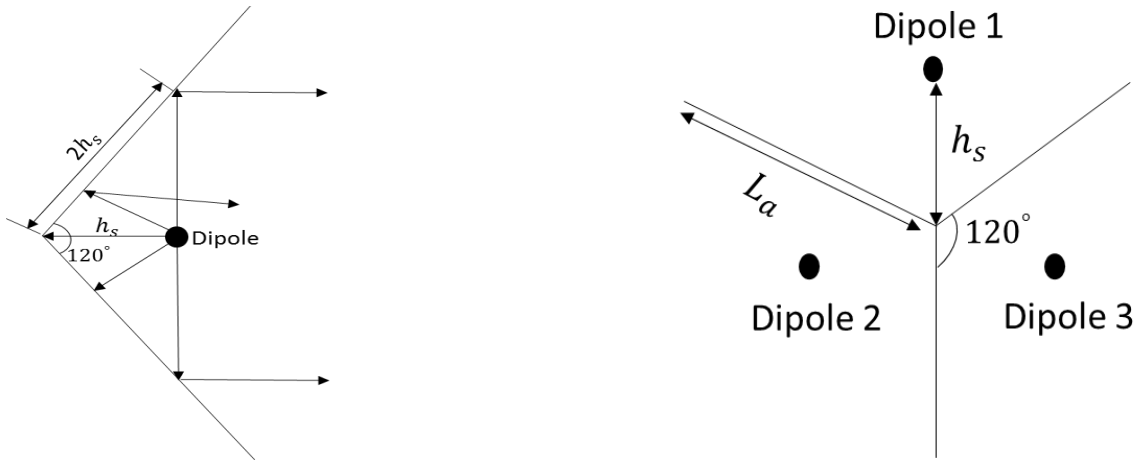

a) b)

Figure 58: a) Geometry of the reflector antenna b) Schematic of 3-sector antenna

The following sections define the full design of a novel active azimuth controlled antenna, used for a 3-sector Base station but with the potential of being extended into use as part of a multi-sector system based on the previous work [38]. It is comprised of a radiating dipole antenna which is located about $\frac{1}{4}\lambda$ away from the reflectors and folded reflectors to provide the antenna reconfigurability in the azimuth plane. The reflector is comprised of an array of horizontal metallic strips, vertical strips and a solid metallic strip. The capacitors between the solid reflector and horizontal metallic strips act as DC blockers. The PIN diodes connected in series in these two vertical strips can provide the antenna reconfigurability in the azimuth plane:

- With the diodes in the 'ON' state, the short spacing between the horizontal metallic strips is electrically small compared to the single wavelength which can provide a directional narrow beamwidth in the azimuth plane
- With the diodes in the 'OFF 'state, the reflectors behave as a partially transparent surface, which provides a wider azimuth beamwidth.

4.4 Parametric Study for Single Pattern-Reconfigurable Antenna Design

Now, to fully study the pattern-reconfigurable antenna operation mechanism and its acceptable parameters to get the switched azimuth beamwidth from narrow 60° to wide 110°, a single pattern-reconfigurable antenna is designed for the parametric studying. The schematic structure of the reconfigurable reflector and radiating dipole for the pattern-reconfigurable antenna is shown in Figure 59.

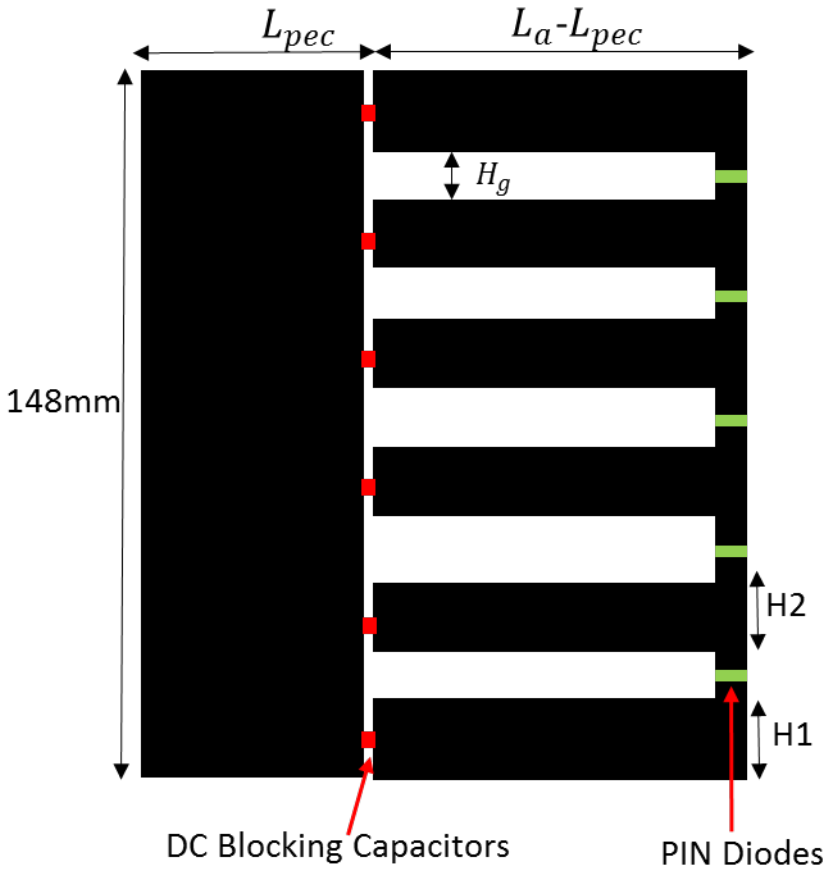

a) Half of the reconfigurable Reflector

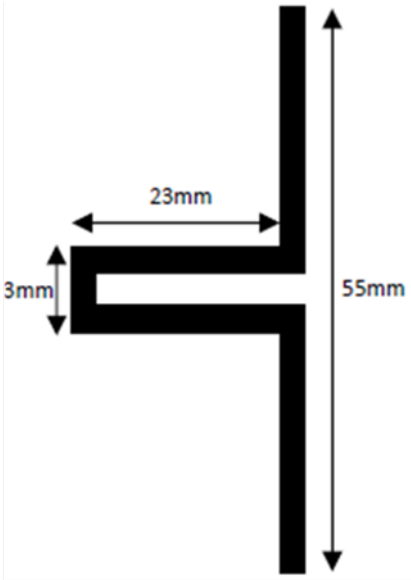

b) Dipole Antenna

Figure 59: Unit cell illustration of reconfigurable reflector and dipole antenna

The PIN diodes were modelled using the equivalent circuit shown in Figure 60 to match the real PIN diode model from the datasheet. The diode parameters were approximated as having an equivalent series circuit where the resistance, $R_s = 1\Omega$, and inductance, $L_d = 0.6nH$. The shunted capacitance was $C_s = 0.12pF$. The resistance, R, is varied from 0.1Ω (ON state) to 5000Ω (OFF state).

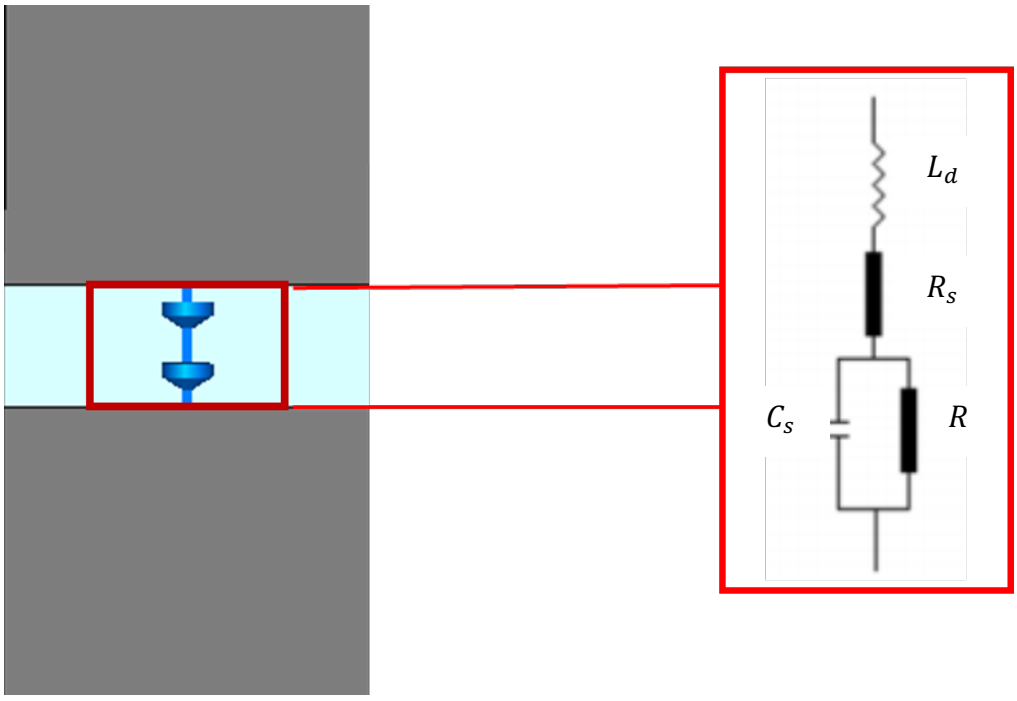

Figure 60: Equivalent Circuit for "ON" and "OFF" state for PIN diode

Table 6: Summary of antenna parameters	
Term	**Value (Units)**
L_s	0.6 (nH)
R_s	1 (Ω)
C_s	0.12 (pF)
R (Forward Biased)	0.1 (Ω)
R (Reverse Biased)	5000 (Ω)

The electromagnetic simulation of the antenna was carried out using CST Microwave Studio. Simulations of the realised antenna gain patterns were carried out for this single pattern-reconfigurable antenna.

4.4.1 Single vertical strip design with varying reconfigurable reflector length L_a

Based on an idealised reconfigurable antenna design concept, the length of reflectors could be altered to achieve a range of azimuth beamwidths. Thus, the first parameter we used here to achieve its azimuth reconfigurability is the reconfigurable reflector length L_a. Figure 59 shows one half of the symmetric reconfigurable reflector used to vary the antenna's azimuthal beamwidth. The antenna height of the single element is chosen as 148mm high and as such is approximately λ at the chosen design frequency of 1.9GHz. Each conducting strip has a PIN diode at its centre. The six horizontal elements are connected to a rectangular metallic reflector via 1nF capacitors which act as DC blocks. The reconfigurable reflector has two modes of operation, the first being when diodes are conducting (i.e. they are in the 'ON' state): Here the diodes are biased by applying a voltage across the top and bottom of the horizontal conductors and the capacitors are in place to act as DC blocks, but are designed such that the RF currents are not impeded. In this state these components have a low impedance and the reflector can be approximated as a continuous conductor. This assumption can be made as the separation of the vertical conducting strips is electrically small compared

with λ. The forward bias case then provides desired narrow beamwidth. However, in contract when the PIN diodes are in the 'OFF' state (i.e. they are reverse biased) the diodes have high impedance and the horizontal conducting elements can be approximated as being semi-transparent. In this case a wide azimuth beamwidth is produced by the continuous central rectangular reflector. The reflector comprises a 1.6mm thick FR4 substrate which itself consists of six horizontal conducting elements connected by thin (3mm) vertical conducting strips, as illustrated in Figure 59. The radiating dipole is a printed dipole antenna of length 55mm which is on a 1.6mm FR4 substrate (Ɛ=4.3, tan(δ)=0.025, not shown in the figure for clarity). The dipole includes a narrow band balun with the feed at the centre of the dipole.

Since, the purpose of this pattern-reconfigurable antenna design is to achieve its azimuth beamwidth reconfigurability from narrow 60° to wide 110°, in order to study the effects of reconfigurable reflector length L_a on antenna's performances effects, the antenna dimensions for other parameters including the solid metallic sheet length L_{pec} are shown below

Table 7: Antenna Parameters for Section 4.4.1

Term	**Value (mm)**
L_{pec}	39.5
H_1	15.5
H_2	15.5
H_g	11

Figure 61 shows the single pattern-reconfigurable antenna reflection coefficient and radiation pattern in azimuth plane by switching PIN diodes states. The solid metallic sheet length L_{pec} chosen of 39.5mm is because in idealised corner reflector antenna, this length can provide a directive azimuth pattern with around 60° beamwidth. As can be seen from it that the working frequency for the pattern-reconfigurable antenna is at around 1.9GHz for both "ON" and "OFF" states across the whole range of selected reconfigurable reflector lengths. Towards the azimuth radiation pattern, it can be seen that when the reconfigurable reflector length L_a increases, there is an energy loss in the antenna azimuth pattern.

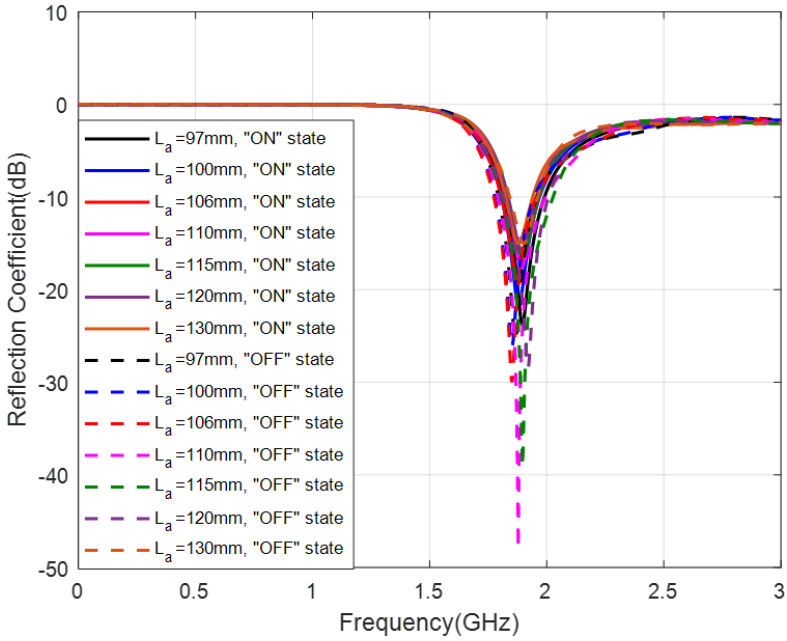

a)

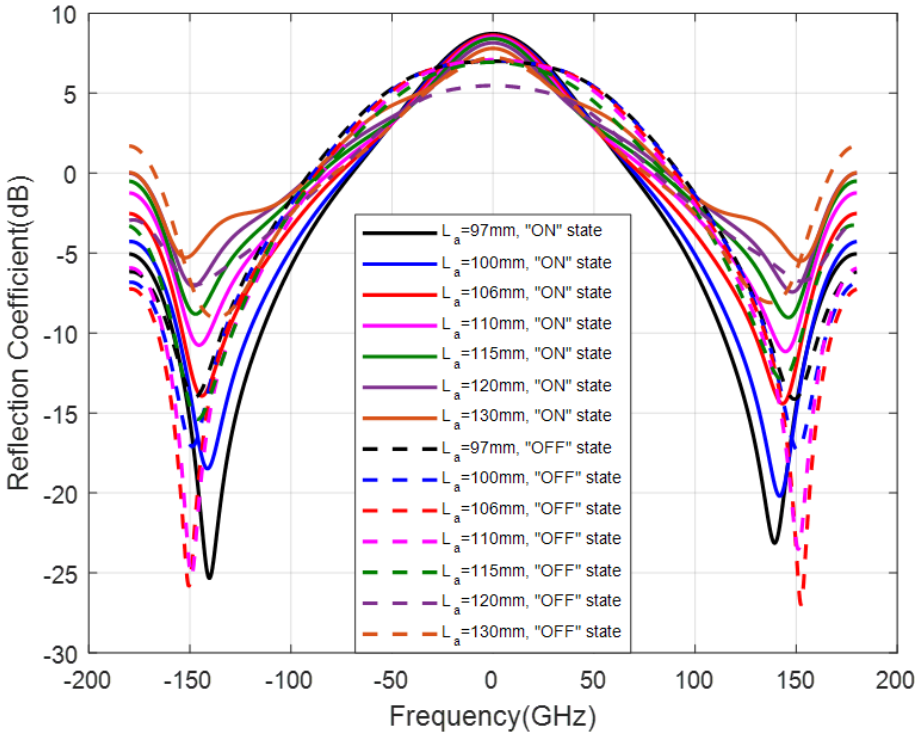

b)

Figure 61: a) Reflection coefficient b) Azimuth Radiation Pattern for various L_a

Table 8: Reconfigurable reflector length VS. Antenna azimuth beamwidth		
Reflector Length L_a (mm)	φ_{3dB} "On State"	φ_{3dB} "Off State"
97	67.4°	126.8°
100	67.1	124.3°
106	64.5°	121.6°
110	62.7°	116.2°
115	61.6°	110°
120	62.8°	117.5°
130	75.4°	80.4°

Table 8 summarises the relationship between the selected reconfigurable reflector lengths and the antenna azimuth beamwidth for both "ON" and "OFF" diode states. It can be seen that in order to achieve the reconfigurability of antenna azimuth beamwidth from 60° to 110° without much energy loss, the acceptable reconfigurable reflector length L_a can be within $0.65\lambda < L_a < 0.76\lambda$.

4.4.2 Single vertical strip design with varying solid metallic sheet length L_{pec}

After studying the reconfigurable reflector length L_a, the solid metallic sheet length L_{pec} is chosen here now to study its effects on achieving azimuth beamwidth reconfigurability. The antenna dimensions for other parameters are shown in Table 9.

Table 9: Antenna Parameters for Section 4.4.2	
Term	**Value (mm)**
L_a	106
H_1	15.5
H_2	15.5
H_g	11

Figure 62 demonstrates the single pattern-reconfigurable antenna refelction coefficient and azimuth radiation pattern for both "ON" and "OFF" diode states across the whole range of the selelcted solid metallic sheet length L_{pec}. The reconfigruable reflector length L_a chosen here is based on the lower bound of the acceptable range for this antenna design from section A. It can be seen that the working frequency for this pattern-reconfigurable antenna is at around 1.9GHz for both "ON" and "OFF" diode states within the selected solid metallic sheet length. As can be seen from Figure 62 b) that when the solid metallic sheet length L_{pec} increases, the reconfigruable refelctor becomes more reflective which can provide a more directive radition pattern in the azimuth plane.

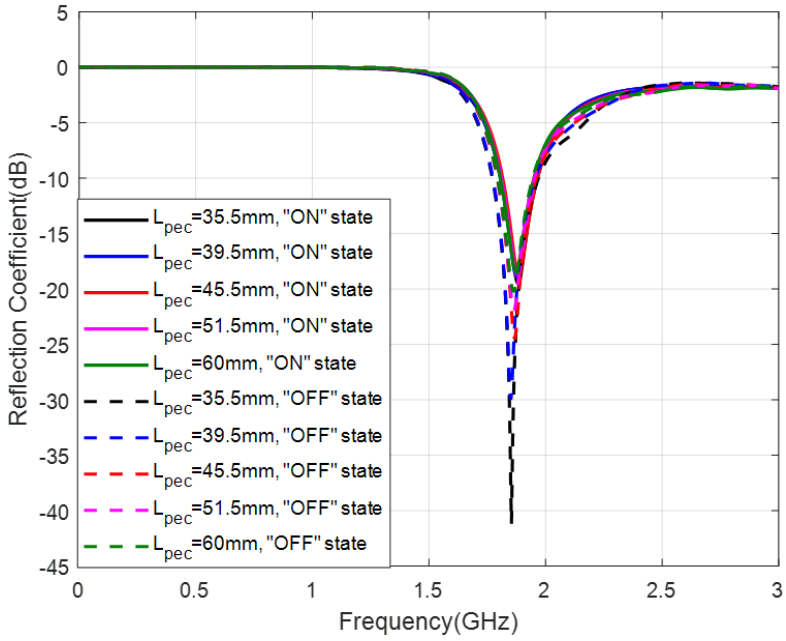

a)

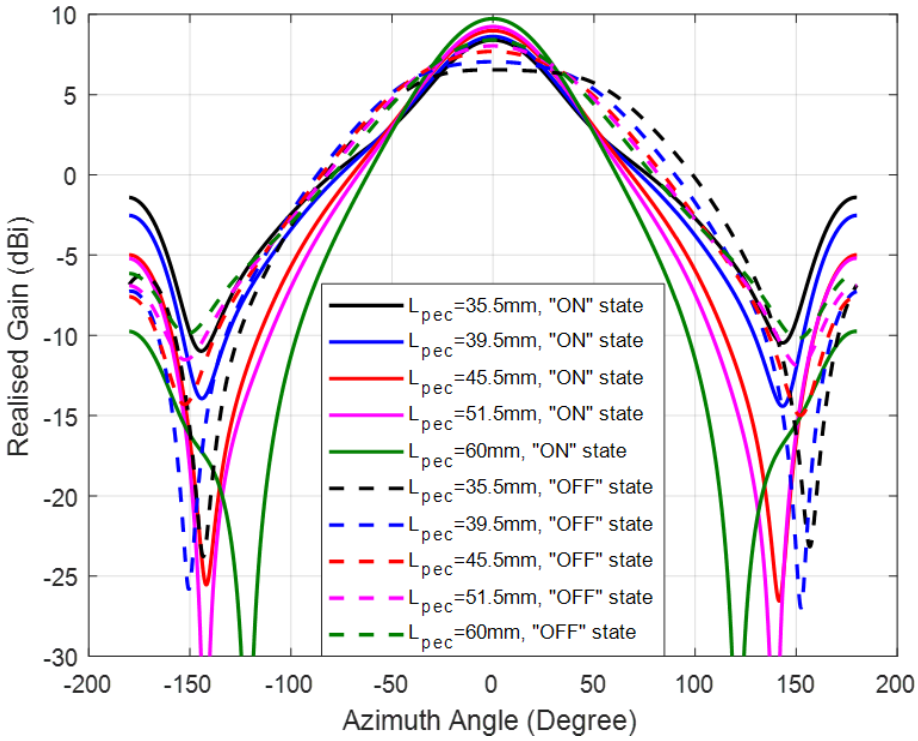

b)

Figure 62: a) Reflection coefficient b) Azimuth Radiation Pattern for various L_{pec}

Table 10: Solid metallic sheet length VS. Antenna azimuth beamwidth

Solid Metallic Strip Length L_{pec} (mm)	φ_{3dB} "On State"	φ_{3dB} "Off State"
35.5	64.1°	132.7°
39.5	64.5°	121.6°
45.5	63.3°	112.7°
52.5	62.4°	94.9°

Table 10: Solid metallic sheet length VS. Antenna azimuth beamwidth		
Solid Metallic Strip Length L_{pec} (mm)	φ_{3dB} "On State"	φ_{3dB} "Off State"
60	60.7°	84.6°

Table 10 summarises the relationship between the solid metallic strip length L_{pec} and antenna azimuth beamwidth for both "ON" and "OFF" diode states. It can be seen that the acceptable solid metallic sheet length to achieve the azimuth beamwidth reconfigurability from 60° to 110° can be within $0.2\lambda < L_{pec} < 0.35\lambda$.

4.4.3 Double vertical strip design with varying reconfigurable reflector length L_a

As can be seen from Section 4.4.1 that, with the reconfigurable reflector length L_a increasing, there is a generally energy loss in the antenna radiation pattern in the azimuth plane. So, in order to improve this issue, a double vertical strip reconfigurable antenna is proposed as shown in Figure 63. The radiation dipole dimension is kept the same as shown in Figure 59 b). Now, to study the effects of reconfigurable reflector length L_a using this double vertical strip reflector design on the antenna performances, especially to compare with the effects by using single vertical strip design shown in Section 4.4.1, the antenna dimension for other parameters are:

Table 11: Antenna Parameters for Section 4.4.3	
Term	**Value (mm)**
L_s	3
L_{pec}	39.5
H_a	148
H_g	11

Table 11: Antenna Parameters for Section 4.4.3	
Term	**Value (mm)**
H_1	15.5
H_2	15.5
L_g	$(L_a - L_{pec})/2$

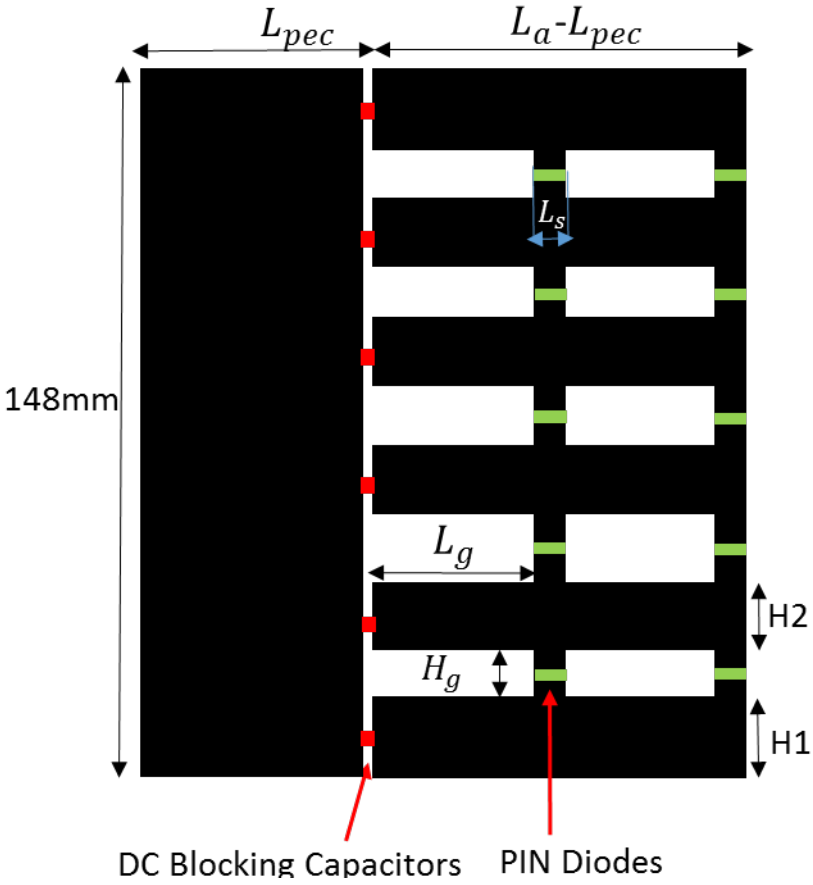

Figure 63: Double vertical strip reconfigurable reflector

Figure 64 shows that the working frequency for this double vertical strip reconfigurable antenna is at around 1.9GHz for both "ON" and "OFF" diode states across the selected reconfigurable reflector length L_a which is within the band of interest for our application in mobile network system. Figure 64 b) shows that by using the double vertical strip design in the antenna reflector surface, the gain of the antenna azimuth pattern for the "ON" diode

states can be improved by at least 1 dBi compared with the single vertical strip design shown in Figure 59 a). However, for the "OFF" diode states, the radiation pattern in the azimuth plane can be spread out which provides a much wider azimuth beamwidth in this case.

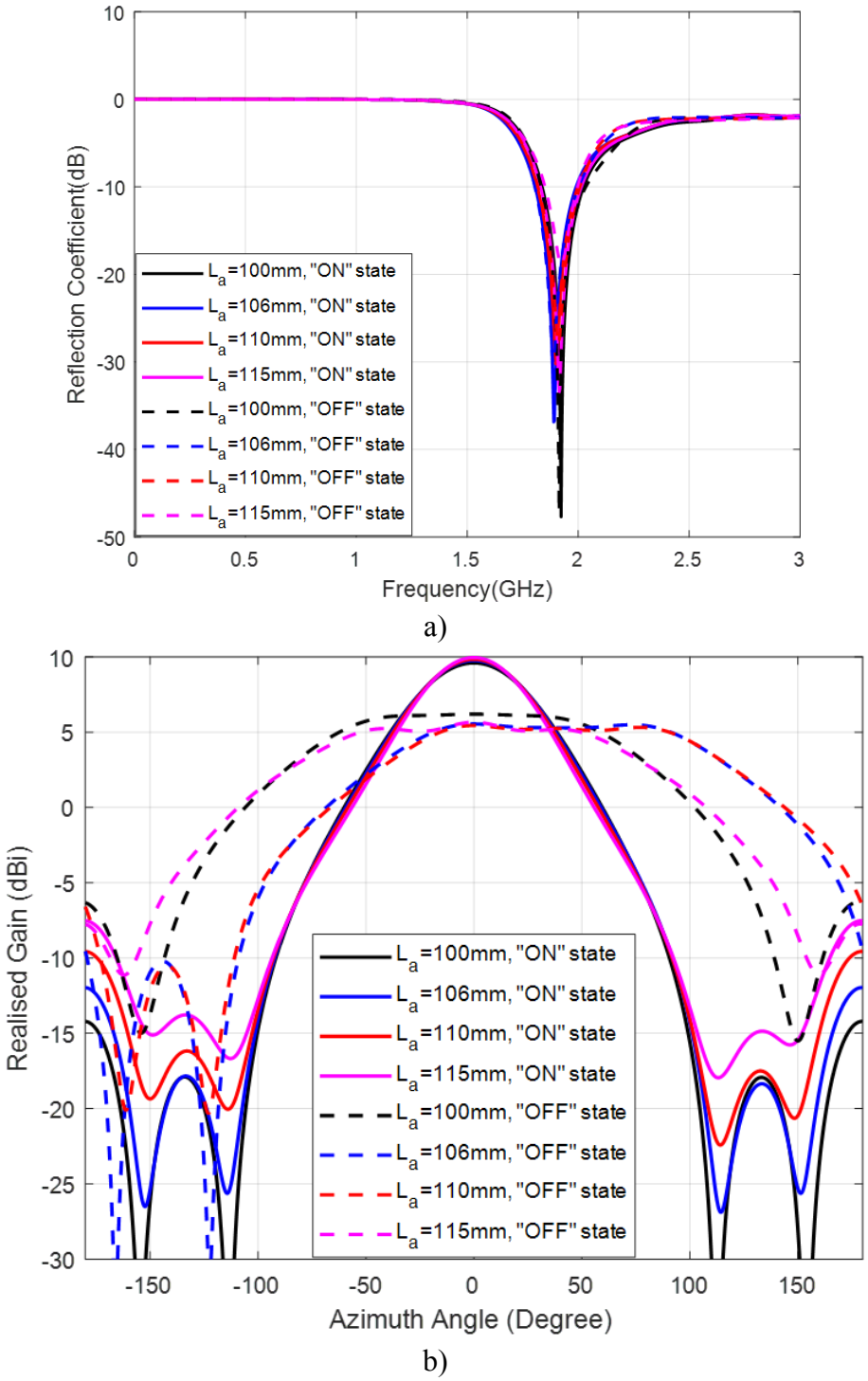

Figure 64: a) Reflection coefficient b) Azimuth Radiation Pattern for various L_a

Table 12: Reconfigurable reflector length VS. Antenna azimuth beamwidth		
Reflector Length L_a (mm)	φ_{3dB} "On State"	φ_{3dB} "Off State"
100	61.0°	158.9°
106	58.8°	166.7°
110	56.9°	166.2°
115	53.9°	166.6°

Table 12 summarises the relationship between the reconfigurable reflector length L_a and the antenna azimuth beamwidth by using this double vertical strip reflector design for both "ON" and "OFF" diode states. It can be seen that for the "ON" diode states, it can meet our requirements for 60° azimuth beamwidth. However, for the "OFF" diode states, the reflector becomes more transparent which has a much wider azimuth beamwidth compared with the design shown in Section 4.4.1.

4.4.4 Double vertical strip design with varying solid metallic sheet length L_{pec}

To study the effects of solid metallic sheet length L_{pec} on the antenna performances and compare with the case by using single vertical strip reflector design shown in Section 4.4.2.All other parameters used for this simulation are shown in Table 13.

Table 13: Antenna Parameters for Section 4.4.4	
Term	**Value (mm)**
L_s	3
L_a	106
H_a	148

Table 13: Antenna Parameters for Section 4.4.4	
Term	**Value (mm)**
H_g	11
H_1	15.5
H_2	15.5
L_g	$(L_a - L_{pec})/2$

It can be seen from Figure 65 a) that the working frequency for this pattern-reconfigurable antenna is at around 1.9GHz for both "ON" and "OFF" diode states across the whole selected solid metallic sheet length L_{pec}. The azimuth radiation pattern shown in Figure 65 b) shows that for the "ON" diode states by using this double vertical strip reflector design, the antenna gain can be improved by above 1 dBi compared with the single vertical strip reflector case demonstrated in Section B especially for a shorter metallic sheet length L_{pec} of 35.5mm and 39.5mm. For the "OFF" diode states, the radiation pattern in azimuth plane at metallic sheet length L_{pec} of 35.5mm and 39.5mm can be spread out more compared with the single vertical strip reflector case.

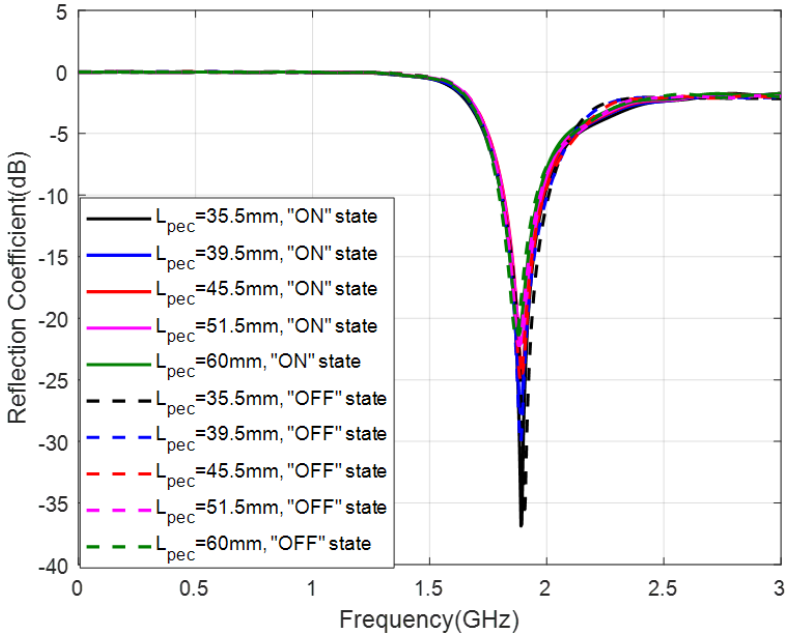

a)

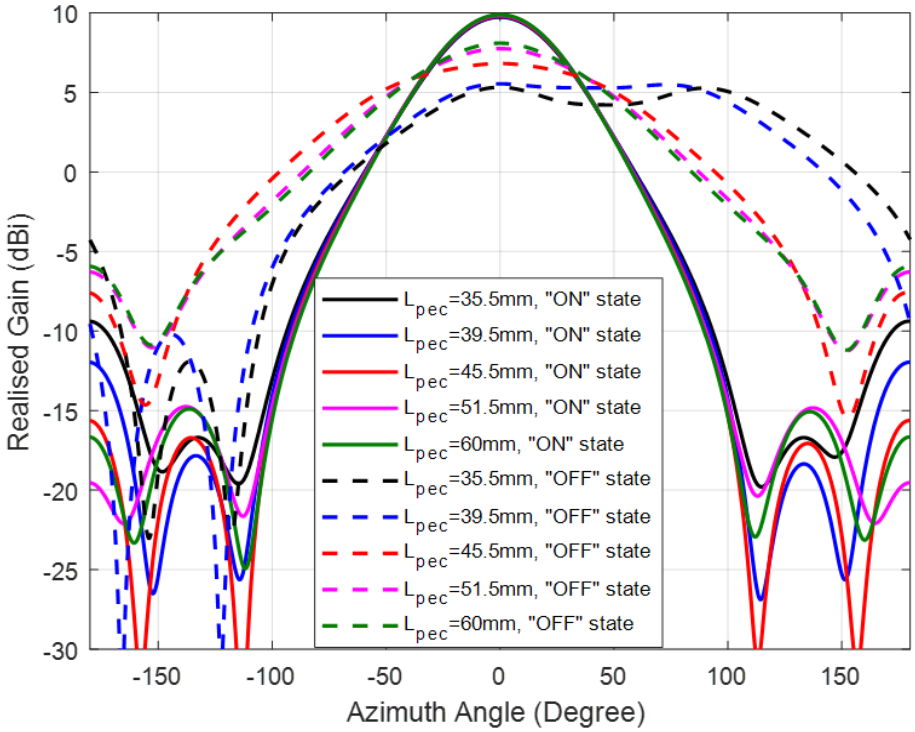

b)

Figure 65: a) Reflection coefficient b) Azimuth Radiation Pattern for various L_{pec}

Table 14: Solid metallic sheet length VS. Antenna azimuth beamwidth		
Solid Metallic Strip Length L_{pec} (mm)	φ_{3dB} "On State"	φ_{3dB} "Off State"
35.5	58.6°	179.8°
39.5	58.8°	166.7°
45.5	58.8°	114.4°
51.5	58.9°	99.8°
60	58.4	91.2°

Table 14 summarises the relationship between the solid metallic sheet length and the antenna azimuth beamwidth for both "ON" and "OFF" diodes states. It can be seen that by using this

double vertical strip reflector design, the antenna gain can be improved in the diode "ON" states. In order to achieve the azimuth beamwidth reconfigurability from 60° to 110°, the acceptable solid metallic sheet length L_{pec} can be within $0.25\lambda < L_{pec} < 0.35\lambda$.

4.4.5 Double vertical strip design with varying second vertical strip position L_g

After studying the parameters of reconfigurable reflector length L_a and solid metallic sheet length L_{pec}, it shows that by using this double vertical strip reflector design, for the "ON" diode states case, the antenna gain can be improve by above 1 dBi compared with the single vertical strip reflector design. Thus, it is important to study the effects of the second vertical position L_g shown in Figure 63 on the antenna performances. The varying the second vertical position L_g here, the antenna dimensions for the other parameters are shown in Table 15, both the reconfigurable reflector length L_a and the solid metallic length L_{pec} are chosen within the acceptable range for antenna azimuth reconfigurability requirements.

Table 15: Antenna Parameters for Section 4.4.5

Term	Value (mm)
L_s	3
L_a	106
H_a	148
H_g	11
H_1	15.5
H_2	15.5
L_{pec}	51.5

It can be seen from Figure 66 a) that the antenna working frequency for both diodes “ON” and “OFF” states is at around 1.9GHz across the whole range of second vertical position L_g. Figure 66 b) shows that by moving the second vertical strip towards the edge vertical strip (L_g increasing), the reconfigurable reflector becomes more reflective which can provide a more directive radiation pattern in the azimuth plane.

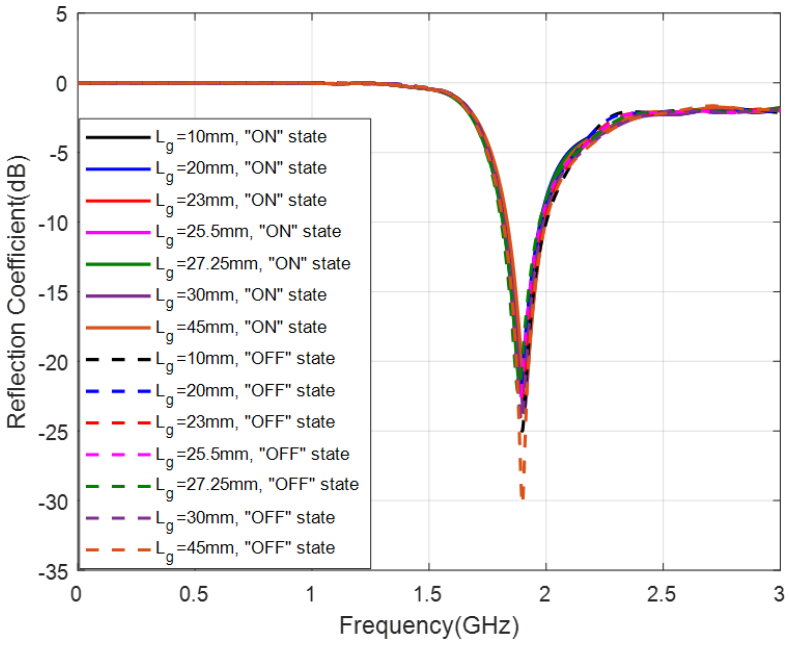

a)

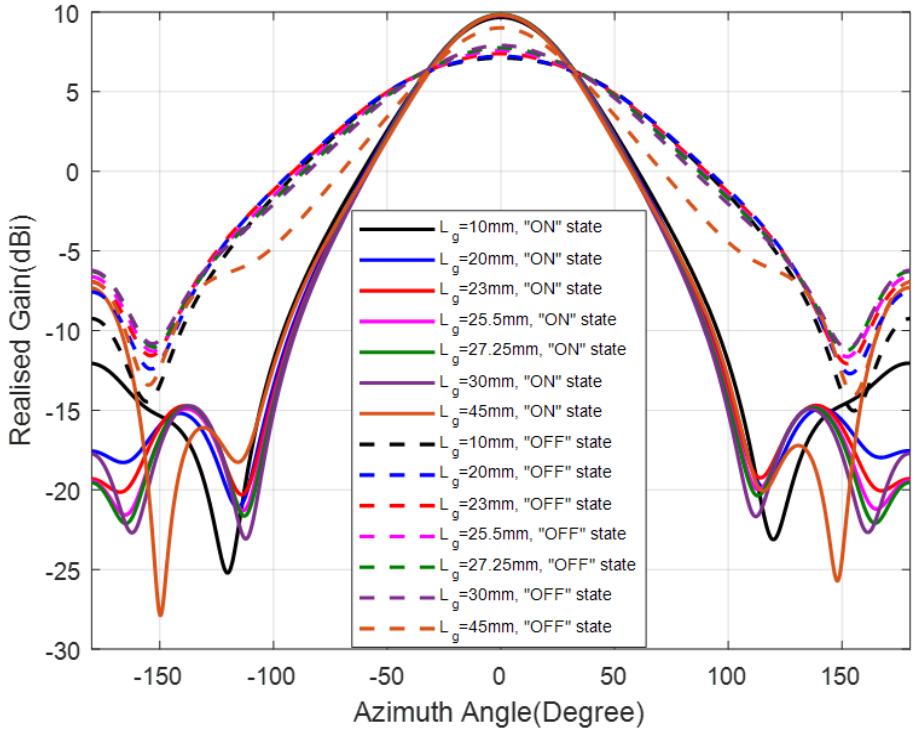

b)

Figure 66: a) Reflection coefficient b) Azimuth Radiation Pattern for various L_g

Table 16: Second vertical strip position VS. Antenna azimuth beamwidth		
Second Strip Position L_g (mm)	φ_{3dB} "On State"	φ_{3dB} "Off State"
10	60.7°	116.1°
20	59.7°	114.8°
23	59.4°	110.4°
25.5	59.1°	104.2°
27.25	58.9°	99.8°
30	58.5°	94.7°
45	56.9°	68.1°

Table 16 summarises the relationship between the second vertical strip position L_g and the antenna azimuth beamwidth for both "ON" and "OFF" diode states. It can be seen that when the second vertical strip distance L_g increases (moving towards the edge vertical strip), the reconfigurable reflector becomes more reflective which can provide a more directive radiation pattern in the azimuth plane. To fulfil the azimuth beamwidth reconfigurability requirements, the acceptable second vertical strip position L_g can be within $0.06\lambda < L_g < 0.19\lambda$.

4.4.6 Double vertical strip design with varying gap H_g between horizontal metallic strips

In this section, the gap H_g between 6 horizontal metallic strips shown in Figure 63 is investigated to compare its effects on the antenna performances. To varying the gap H_g, the antenna dimension for the other parameters are summarised as below. The parameters chosen for L_a, L_{pec}, L_g are within the acceptable range for achieving the azimuth beamwidth reconfigurability. Now, in order to vary the gap H_g from 5mm, 11mm, 15mm to 20mm, the height of both H1 and H2 are changed from 20.5mm, 15.5mm, 12.5mm to 8mm corresponding0 This is shown in Table 17.

Table 17: Antenna Parameters for Section 4.4.6

Term	Value (mm)
L_s	3
L_a	106
H_a	148
L_g	23
H_1	8-20.5
H_2	8-20.5

Table 17: Antenna Parameters for Section 4.4.6	
Term	**Value (mm)**
L_{pec}	51.5

It can be seen from Figure 67 that the antenna working frequency for both “ON” and “OFF” diode states, for the gap range specified, is at around 1.9GHz. However, there is an energy loss in the antenna main beam direction in the azimuth plane for the diodes “OFF” states with the gap H_g increasing which can lead to a high front to back lobe ratio.

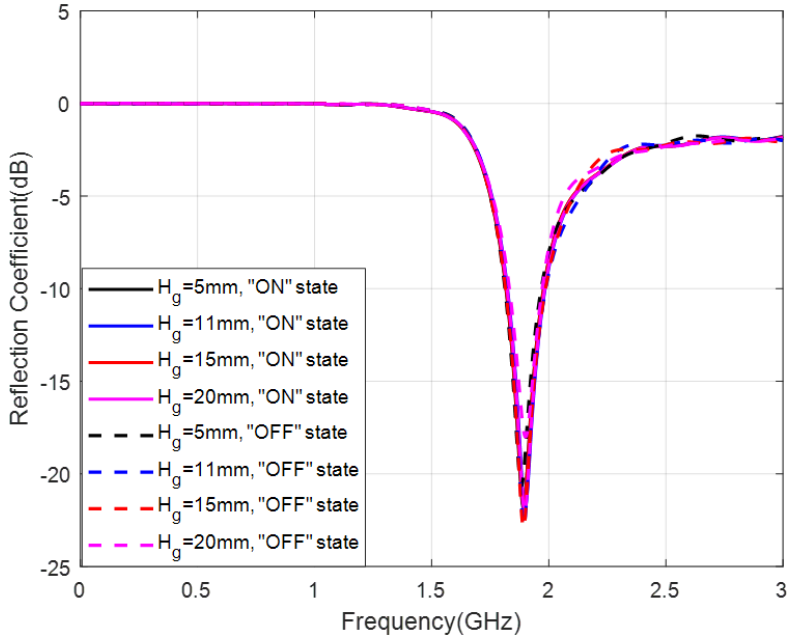

a)

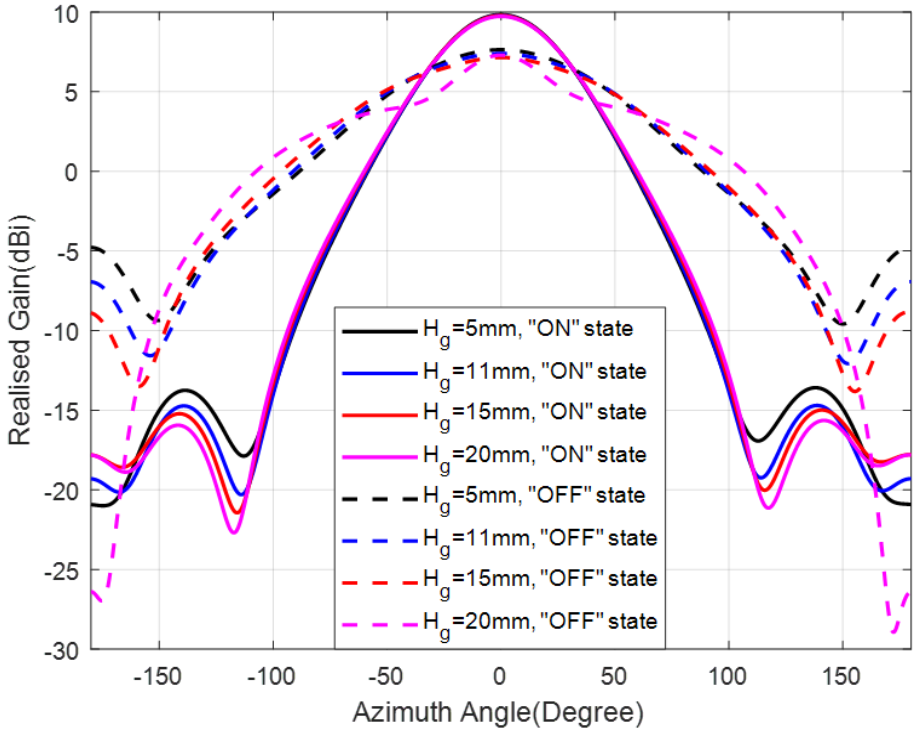

b)

Figure 67: a) Reflection coefficient b) Azimuth Radiation Pattern for various H_g

Table 18: The gap between horizontal metallic strips VS. Antenna azimuth beamwidth		
Gap between horizontal strips H_g (mm)	φ_{3dB} "On State"	φ_{3dB} "Off State"
5	59.1°	102.5°
11	59.4°	110.4°
15	59.9°	118.1°
20	60.3°	77.7°

Table 18 summarises the relationship between the gap H_g and the antenna azimuth beamwidth for both diodes "ON" and "OFF" states. It can be seen that with the smaller gap H_g, the reconfigurable reflector can provide a more directive pattern in the antenna main lobe which reduces the energy loss. The acceptable gap H_g to fulfil the antenna azimuth beamwidth reconfigurability can be within $0.03\lambda < H_g < 0.095\lambda$.

4.4.7 Double vertical strip design with varying vertical strip width L_s

In this section, the parameter of antenna vertical strip width L_s shown in Figure 63 is studied for the antenna performances. The antenna dimensions for other parameters which can fulfil our requirement to achieve the azimuth pattern reconfigurability are shown in Table 19.

Table 19: Antenna Parameters for Section 4.4.7

Term	**Value (mm)**
H_g	11
L_a	106
H_a	148
L_g	23
H_1	15.5
H_2	15.5
L_{pec}	51.5

It can be seen from Figure 68 that the antenna working frequency for the selected vertical strip width is at around 1.9GHz for both "ON" and "OFF" diodes states. The radiation pattern in azimuth plane for both diodes states can fulfil our requirements with various vertical strip width L_s.

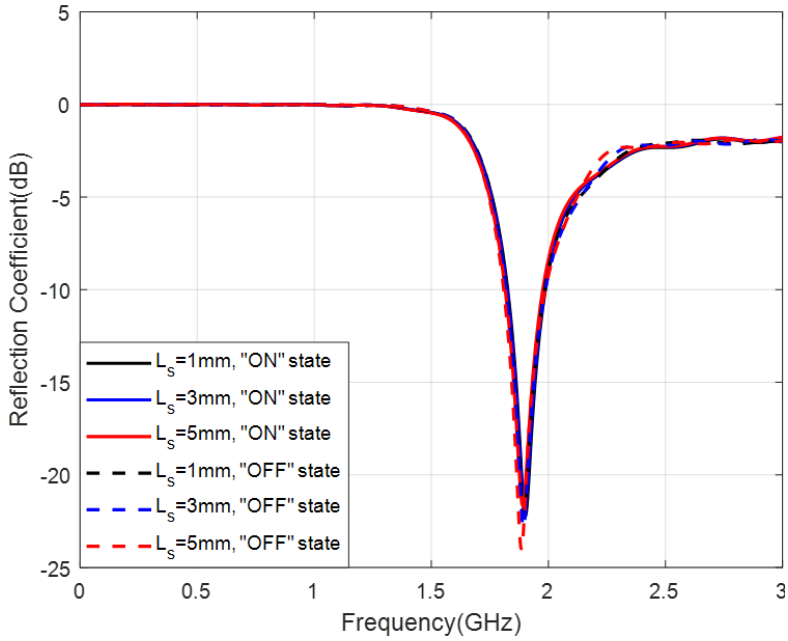

a)

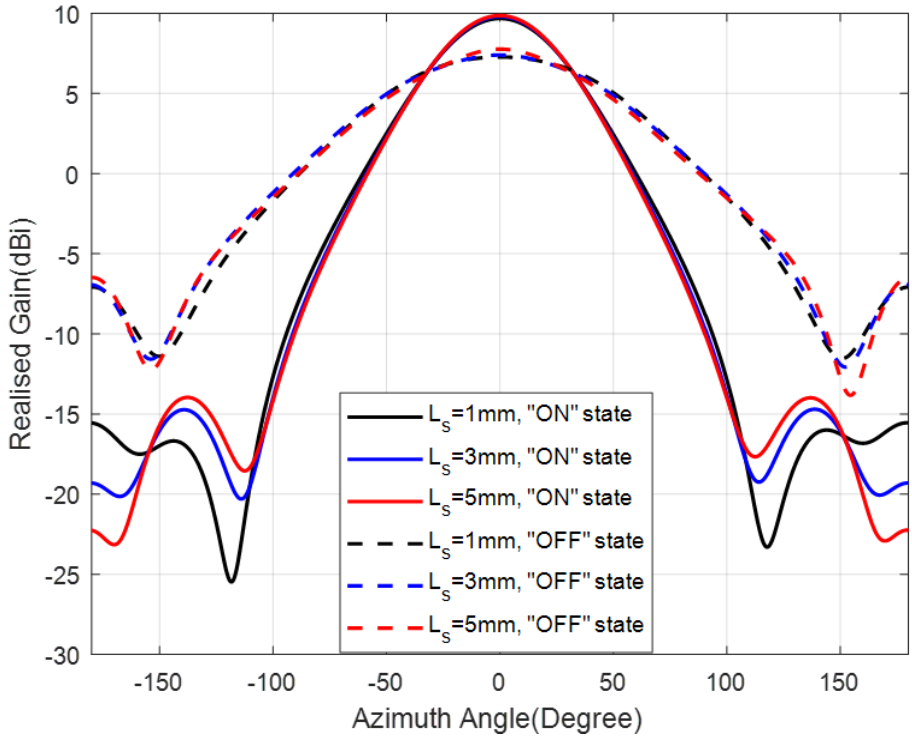

b)

Figure 68: a) Reflection coefficient b) Azimuth Radiation Pattern for various L_s

Table 20: The vertical strip width VS. Antenna azimuth beamwidth		
Vertical strip width L_s (mm)	φ_{3dB} "On State"	φ_{3dB} "Off State"
1	60.6°	113.3°
3	59.4°	110.4°
5	58.9°	97.9°

Table 20 summarises the relationship between the vertical strip width L_s and antenna azimuth beamwidth. It can be noticed that when the vertical strip width increases, the reconfigurable reflector becomes more reflective which can provide a more directive pattern in the azimuth plane for both diodes states.

4.4.8 Double vertical strip design with varying Height H_a of the antenna

In this section, the vertical height H_a of the reconfigurable antenna shown in Figure 63 is investigated on antenna performances. To make a fairy comparison by varying the antenna height H_a only, the antenna dimension for other parameters is shown as below. Here, by varying antenna vertical Height H_a, we essentially just add or reduce the number of horizontal strips and keep the other chosen parameters same. All the other parameters chosen here are within the acceptable range to achieve the pattern reconfigurability in the azimuth plane.

Table 21: Antenna Parameters for Section 4.4.8	
Term	**Value (mm)**
H_g	11
L_a	106
L_s	3

Table 21: Antenna Parameters for Section 4.4.8	
Term	**Value (mm)**
L_g	23
H_1	15.5
H_2	15.5
L_{pec}	51.5

It can be seen from Figure 69 that the working frequency for this single pattern-reconfigurable antenna design is at around 1.9GHz for both "ON" and "OFF" diode states with various antenna Height H_a which is the band of interest for our application in the mobile network system. For the radiation pattern in the azimuth plane, it can be seen that with a lower antenna height the antenna gain decreases in the main lobe regardless of whether or not the diodes are 'ON' or 'OFF'. Here with a reduction of H_a from 1.27λ to 0.5λ, antenna gain changes to 1.5 dBi for diodes in the 'ON' state and 1 dBi for diodes in the 'OFF' state. The energy loss resulting from reduced antenna height is mainly due to the energy leakage from the top and bottom of the antenna which means the antenna reflector is electrically small compared with the radiation dipole antenna size (0.35λ).

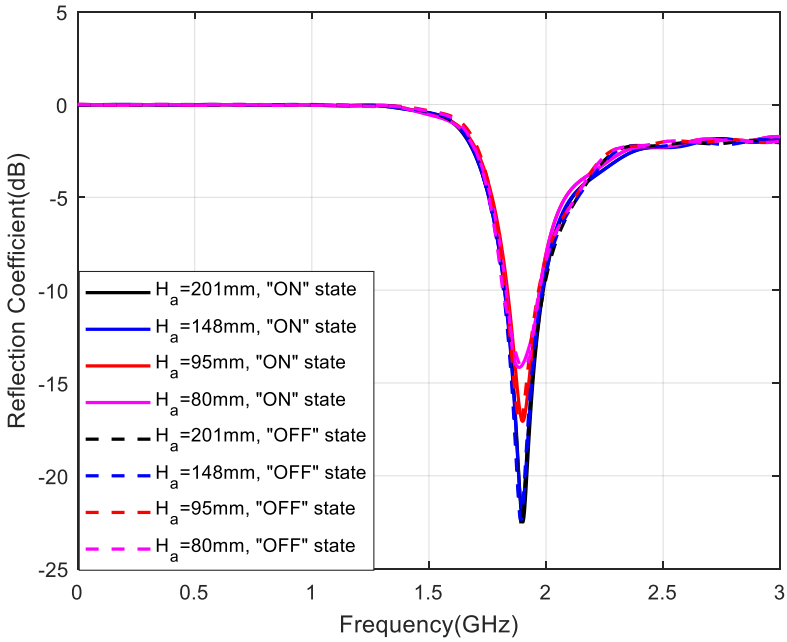

a)

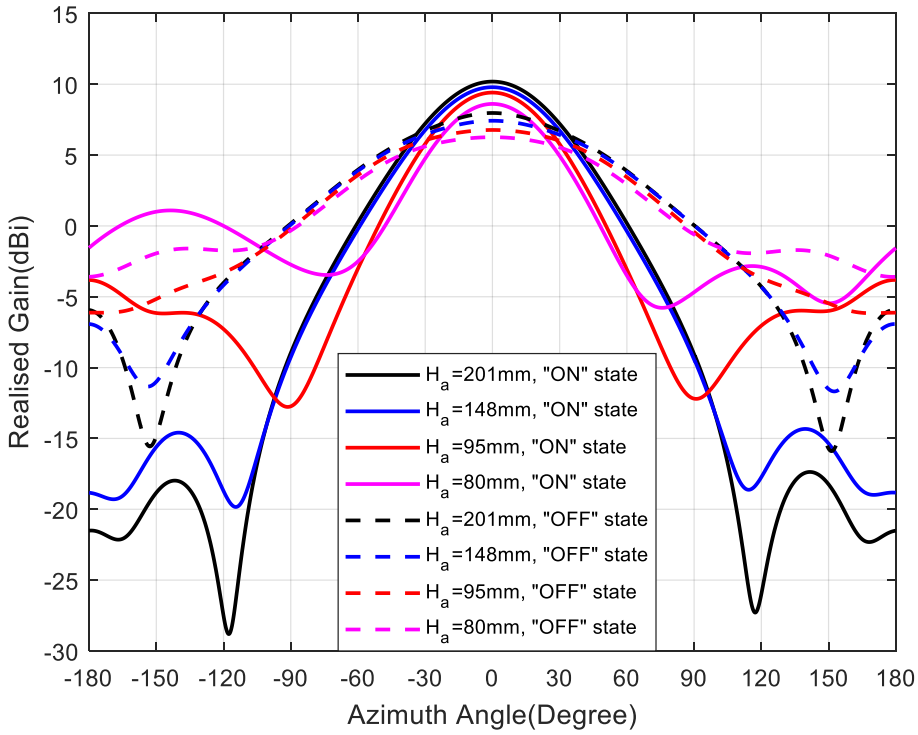

b)

Figure 69: a) Reflection coefficient b) Azimuth Radiation Pattern for various H_a

4.5 12-element pattern reconfigurable antenna array design and simulation

In order to design and simulate a 12-element pattern reconfigurable antenna array which can achieve the same performance gain in the cellular network by using the idealised reflector antenna, a 12-element antenna concept and a single element is shown in Figure 70 for clarify. To model the whole antenna array electromagnetically, a single unit cell can be considered with periodic boundary conditions applied to the upper and lower extremities of the unit cell. The periodic boundary conditions ensure that the effects of mutual coupling are considered without the high computational requirements of simulating a full array.

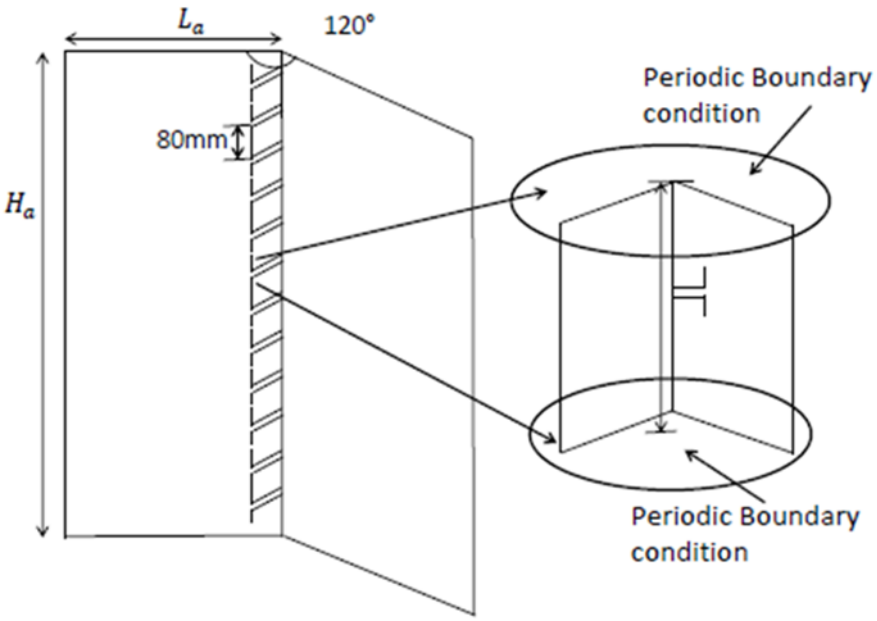

Figure 70: 12-element reconfigurable antenna array concept including "unit cell" element

Since the antenna element spacing chosen here in our application is 1/2λ about 80mm, to effectively achieve the antenna array performance by using this element distance, the single antenna element model selected here is the 80mm height one. The radiating dipole dimension is the same as shown in Figure 59 b). After all the parametric study for the single element pattern-reconfigurable antenna design, to achieve the required azimuth beamwidth reconfigurability to meet the requirements for our application in a cellular mobile network, the resultant final dimension for the single antenna element model is shown in Table 22.

Table 22: Dimension of a single pattern-reconfigurable antenna element	
Term	**Value (mm)**
H_g	11
L_a	106
L_s	3
L_g	23
H_1	7.75
H_2	15.5
L_{pec}	51.5

Here the reconfigurability in the azimuth plane is achieved by controlling the PIN diodes states in the two vertical strips. The surface current distribution in linear scale shown in Figure 71 demonstrates the two operation modes of the reconfigurability. As can be seen from Figure 71 a) that when the diodes are forward biased, the currents can flow to both of the vertical strip lines which means the separation of the vertical conducting strips are electrically small in comparison to the wavelength of the signal. So, in this case, it can provide the narrow azimuth beamwidth. When the diodes are reverse biased as shown in Figure 71 b), the surface current is disconnected along the vertical strip lines which means the reconfigurable reflectors can be seen as semi-transparent. Thus, in this case, it can provide a wide azimuth beamwidth from the solid rectangular metal strip.

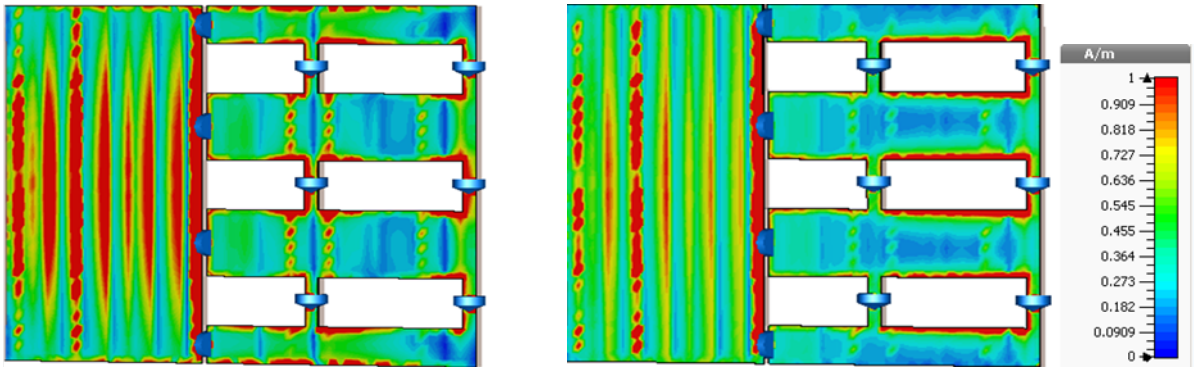

a) b)

Figure 71: Surface current distribution on a) “On State” b)”Off State”

The simulated reflection coefficient and radiation pattern for the azimuth and elevation plane for the two cases are shown in Figure 72. It can be seen that the reconfigurable antenna array for both “ON” and “OFF” states can work at around 1.9GHz which is the desired working frequency for the cellular system. When a narrow mode of operation is specified the azimuth and elevation of the -3dB beamwidth is around 60° and 7.9°, and the antenna gain is around 17dBi. In the wide directional mode of operation, the azimuth and elevation beamwidth is around 110° and 8.3° with a gain of around 15.5dBi.

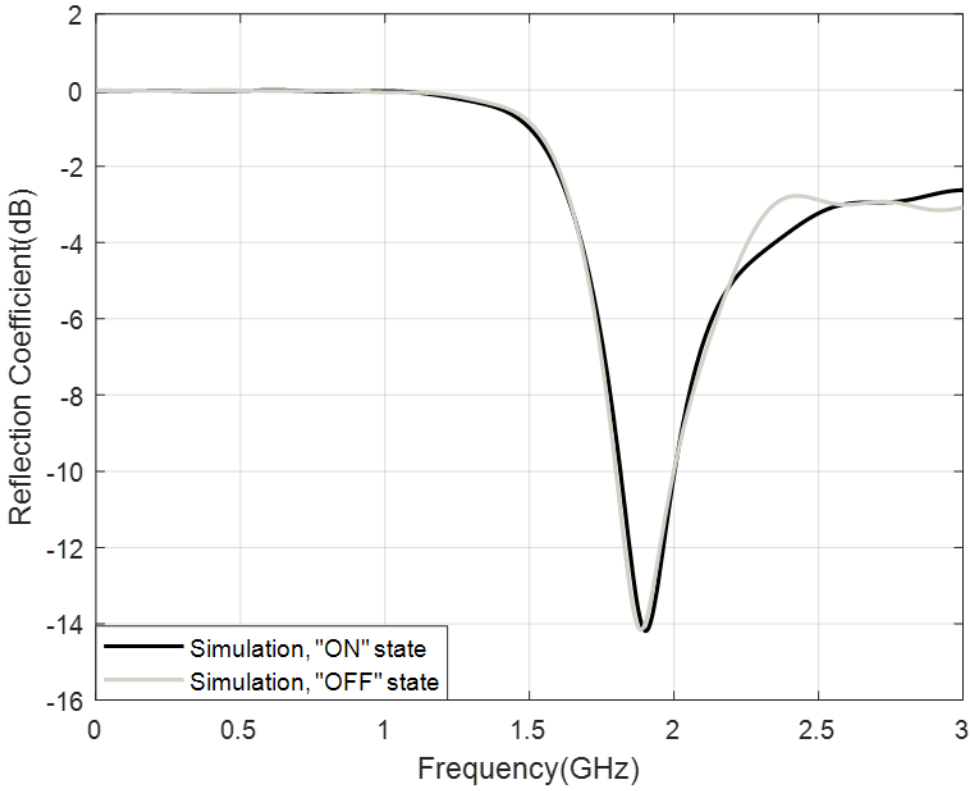

a)

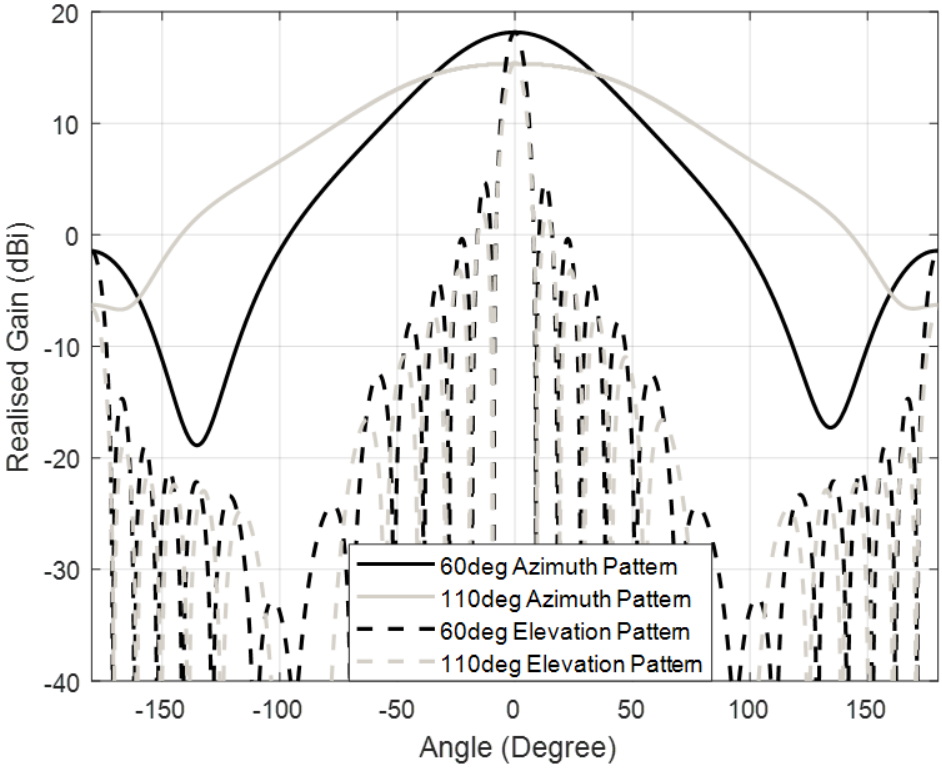

b)

Figure 72: a) Reflection Coefficient b) Radiation Pattern for 12-element reconfigurable antenna array

A comparison between the simulated realised gain of the idealised and proposed novel antenna array, versus azimuth angles, is shown in Figure 73. The results show a good comparison with a maximum gain of 18dBi and 17dBi for the idealised and proposed antenna respectively for a beamwidth of 60 °. For the 110° beamwidth case the maximum realised gain is approximately 16dBi and 15.5dBi for the idealised and proposed antenna respectively. The differences in gain are due uncertainties in the PIN diode model and other manufacturing tolerances.

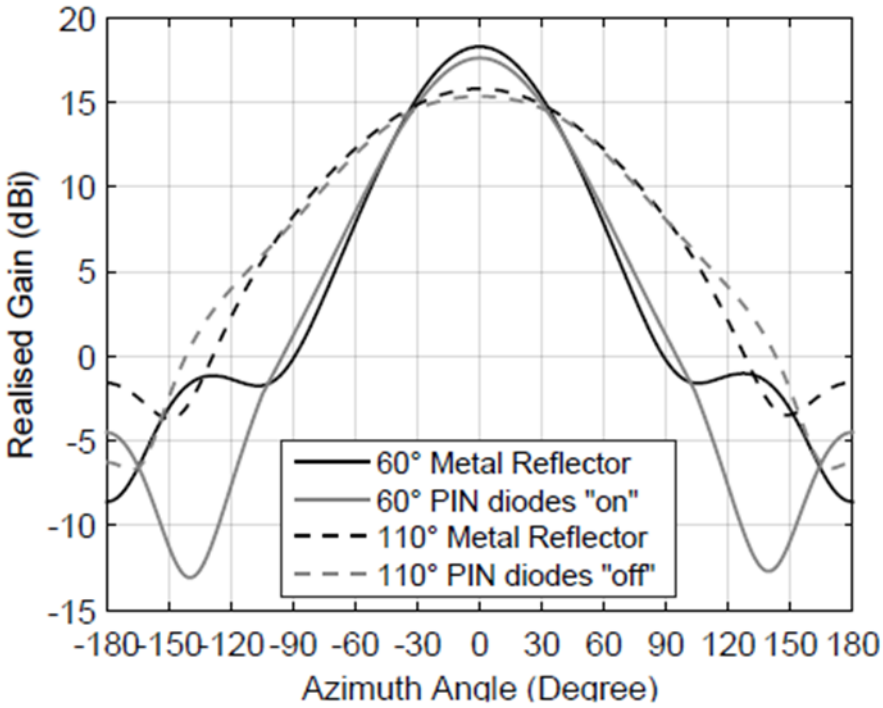

Figure 73: Radiation Pattern for Azimuth Plane between idealised metallic and novel pattern reconfigurable antenna array

4.6 System model performance comparisons

In order to evaluate system performance using the reconfigurable antenna a tri-sector antenna gain pattern was simulated and embedded into the system model described in Chapter 3. Figure 74 shows the capacity for edge users who are situated around the perimeter of the 60° sector and the subsequent improvement for those users when the antenna is switched to a 110° beamwidth. Here the selected antenna downtilt angle is from 0° to 15° in a homogeneous network with an ISD of 500m as mentioned in Chapter 3. It can be seen that the capacity is similar between the idealised and proposed antenna designs. Figure 75 shows the overall mean cell capacity for the idealised and proposed antennas and again they compare well.

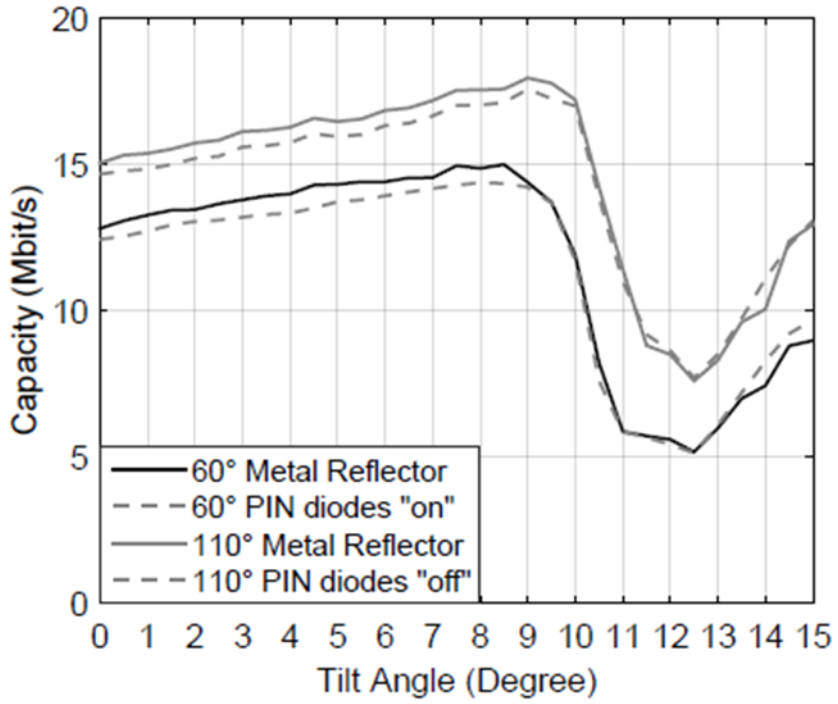

Figure 74: Mean cell edge capacity for idealised and proposed reconfigurable antennas

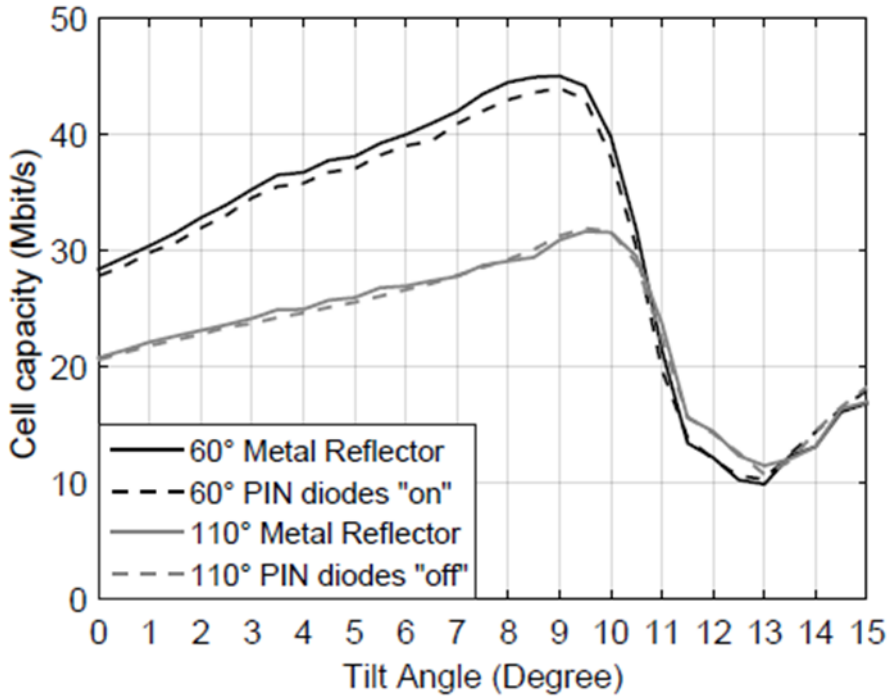

Figure 75: Mean Cell capacity for idealised and proposed reconfigurable antennas

Figure 74 and Figure 75 show that the cell and edge capacity of 60° and 110° azimuth beamwidth between proposed pattern-reconfigurable antenna model and idealised antenna model are similar. The difference of cell and edge capacity between using these two antenna models is within around 1Mbit/s. Thus, it shows that the novel pattern-reconfigurable antenna

can have a good match with the original theoretical antenna model. Table 23 shows the difference in edge and cell capacity when the antenna's azimuth beamwidth is switched from 60° to 110° for different ISDs (500m, 750m, 1000m, 1250m and 1500m) at optimum tilt angle of 9°.

Table 23: Summaries of different cell edge and cell capacity for different ISDs at an optimum tilt angle of 9°

ISD (m)	Azimuth Beamwidth (°)	
	Difference in Cell edge capacity (Mbit/s) (Cell capacity (Mbit/s))	
	60	110
500m	0.16 (1.00)	0.38 (0.18)
750m	0.18 (0.99)	0.36 (0.16)
1000m	0.16 (0.98)	0.37 (0.19)
1250m	0.17 (1.01)	0.35 (0.14)
1500m	0.14 (1.00)	0.31 (0.17)

It can be seen from Table 23 that, the difference of cell and edge capacity at tilt angle of 9° for different ISDs between novel antenna model and theoretical antenna model is very small (within 1 Mbit/s), with a lowest value of 0.14. This demonstrates that the proposed double-strip pattern-reconfigurable antenna can match the results well with the theoretical antenna model used before across a range of different ISDs.

4.7 Validation

4.7.1 60° to 110° pattern-reconfigurable antenna Test Case

To provide some confidence in the proposed reconfigurable antenna design and instead of making a full 12-element antenna array a single antenna element was designed and manufactured using standard Printed Circuit Board (PCB) etching techniques. The PIN diodes and DC blocking capacitors were manually soldered.

Figure 76 shows the simulated and manufactured single antenna model. It can be seen that the single element pattern-reconfigurable antenna model's height is made of length of 148mm which is about one wavelength of the antenna working frequency. The reconfigurable reflector is made up of 6 horizontal strips, which prevent signal leakage from different sides of the antenna (especially from its top and bottom surfaces). The reflection coefficient and radiation pattern for the azimuth plane are measured respectively in order to verify the performances of the real antenna model with the simulated model.

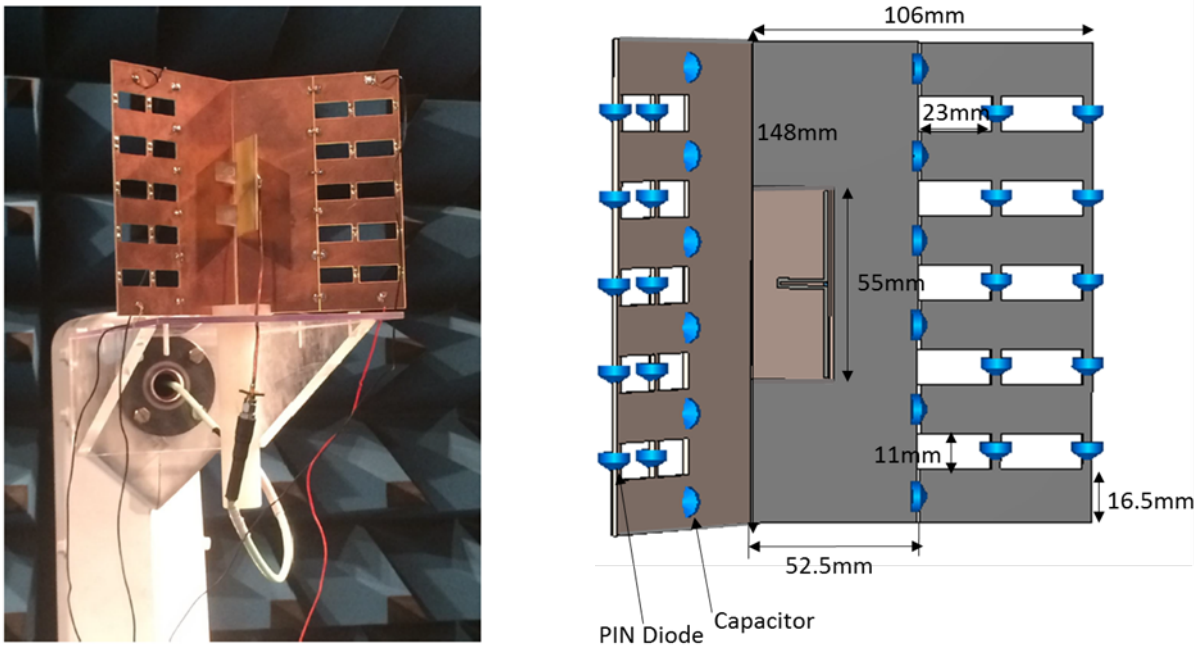

Figure 76: Single element pattern-reconfigurable antenna model Simulated VS Manufactured

1) **Antenna Reflection Coefficient Measurement**

In the very first step, we used the network analyser to measure the antenna's reflection coefficient. As can be seen from Figure 76, the pattern reconfigurable antenna is formed from a radiating dipole and two reconfigurable reflectors. To measure the reflection coefficient of

this design, we needed to make sure the network analyser could work over antenna's working frequency range. Here our frequency range was chosen from 1-3GHz. Then, we started calibrating the network analyser. We used a cable connected the network analyser to the antenna as the transmission line (the effect of the cable was calibrated out of the final results). The Vector Network Analyser (VNA) was supplied with a "Cal kit" which has a matched load of 50 Ω, as well as both an open circuit and a short circuit load. By applying the supplied loads to the end of the cable, the calibration was completed. After the calibration procedure, we connected the network analyser to the antenna under test and set the desired working frequency (1-3GHz). The network analyser transmitted a small amount of power around 0dBm to the antenna and measured how much power is reflected back to the network analyser, which allows for the calculation of the reflection coefficient.

A comparison of the reflection coefficient, derived from both measured data and from simulations with diodes in different states, is shown in Figure 77. Both 'ON' and 'OFF' diodes have a resonant frequency of approximately 1.9GHz. The majority of the differences shown in bandwidth between the different results are a result of inherent uncertainty in the diode model and typical measurement uncertainties, and these are not significant over the band of interest.

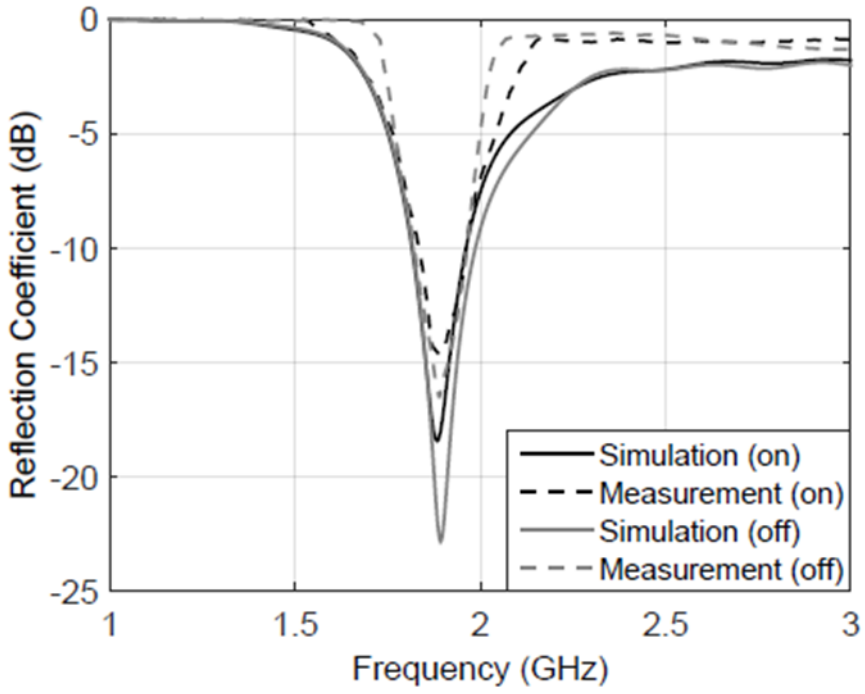

Figure 77: Antenna Simulation and Measurement reflection coefficient magnitude

2) **Antenna Radiation Pattern Measurement in Azimuth Plane**

A measurement process for the pattern-reconfigurable antenna, which analyses the radiation pattern in the azimuth plane from this design, is carried out in an anechoic chamber in order to validate its performance. This chamber is shown in Figure 78, and it can be seen that all internal surfaces are covered in absorber material to minimise beam reflection and diffraction. This material is composed of a series of wedges with certain height and width. After the incident wave impinges the wedge, the energy gets dissipated gradually inside it. In addition, with the use of the foam material to fabricate the wedge, another energy dissipation of the wave occurs between the wall and wave interaction.

Figure 78 shows the novel antenna design, which for testing purposes is called the Antenna Under Test (AUT), mounted opposite the source antenna. They are set at a distance d as $\frac{2D^2}{\lambda}$ between each other, which allows for measurement of the radiation pattern in the far-field region. Here a wideband horn antenna, with a known polarization and gain is used as the source, and it transmits EM waves in a specific direction to the AUT (these EM waves are assumed to be plane wave in the far field region). Assuming the received power comes from direction (Θ, Ø) = (0°,0°), rotating the AUT allows for measurement of the "cuts" of the radiation pattern such as those in the E or H-plane.

It is worth mentioning that the polarisation of the resulting radiation pattern also needed to be matched with the source antenna. The controller and analysis equipment are located outside the chamber, and a schematic of their arrangement is shown in Figure 79. This system consists of an antenna ranger controller, a beam controller, a work station and a network analyser (which here is an Aglient E5071C ENA). This arrangement can evaluate the frequency of antenna up to 20 GHz [117].

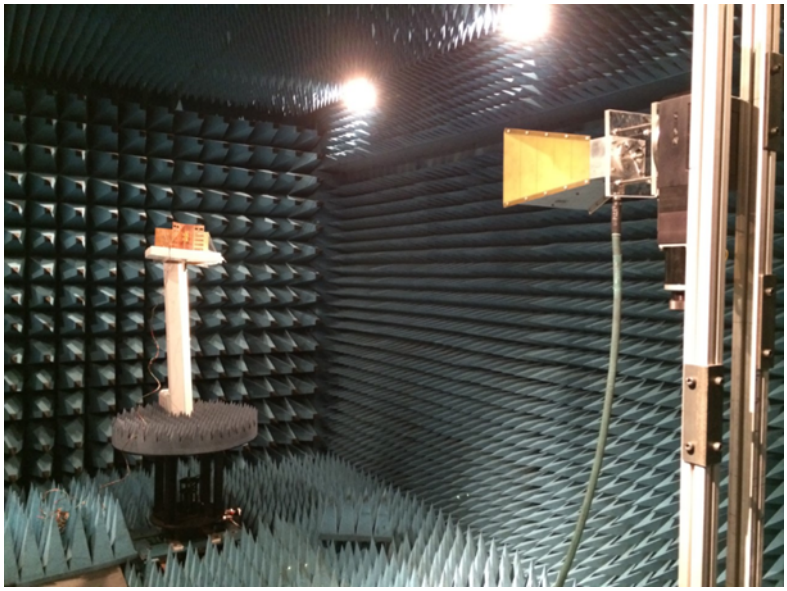

Figure 78: Anechoic Chamber

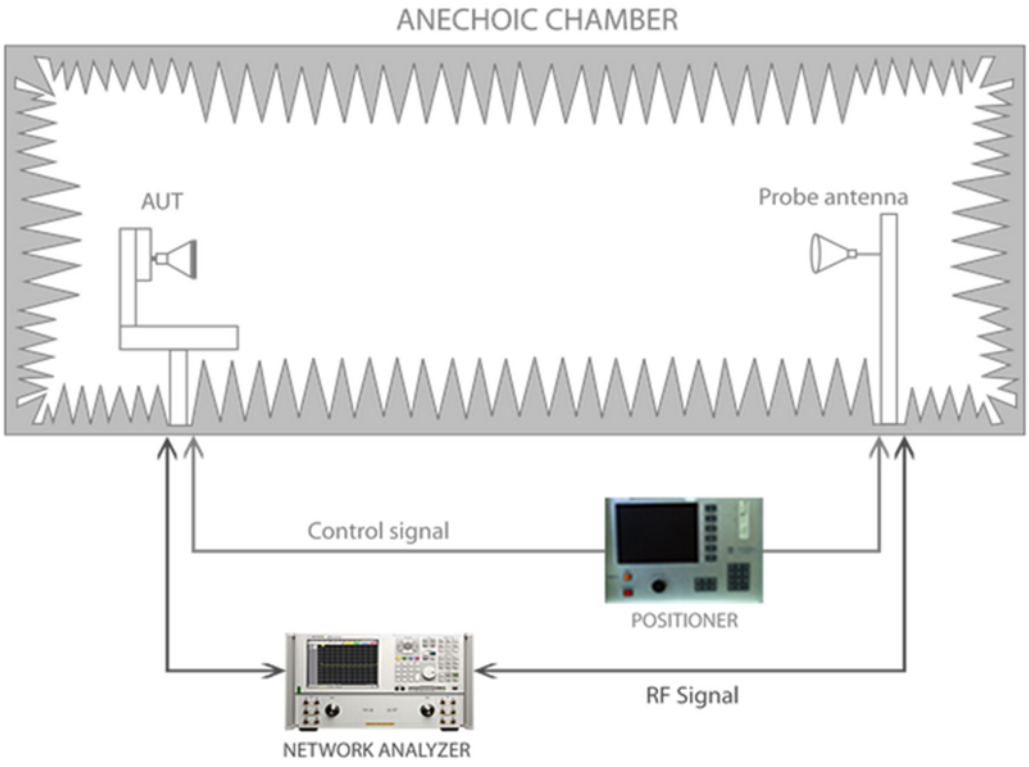

Figure 79: Antenna Performance Test using test facility [117]

Measurement data for the novel design's *H*-plane radiation pattern was then compared with corresponding simulation data for diodes in both the 'ON' and 'OFF' state. Gain measurements and simulations are shown in Figure 80 versus azimuth angle; the results show the measured and simulated on state gain is 9.4dBi and 9.8dBi respectively, and the beamwidth in both cases is approximately 59° When the diodes are in the "off" state the gain

is 7.4dBi for both the measured and simulated data with a beamwidth of 110° approximately. The measurement results therefore show that the measured and simulated results are closely matched at an azimuth beamwidth of both 60° and 110°, particularly for an azimuth angle between approximately -120° and 120°. Poor matching between the simulated and measured results is as a result of real-life antenna beam issues such as scattering around the experiment assembly and losses within the antenna itself and are not a concern to us at this point.

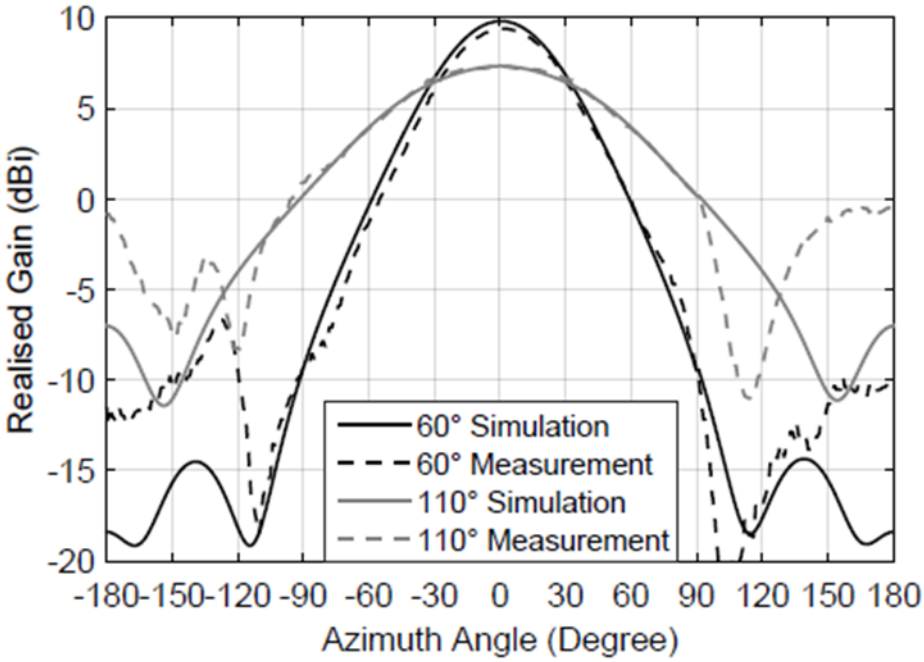

Figure 80: Antenna Horizontal Pattern for simulation and Measurement

4.7.2 60° to 90° pattern-reconfigurable antenna Test Case

Another single pattern-reconfigurable antenna test model is designed which can switch its azimuth beamwidth from 60° to 90°. In this testing case, the antenna model is designed with a single vertical strip which is shown in Figure 81, the azimuth beamwidth reconfigurability can be achieved by controlling the PIN diode states. It can be seen from Figure 81 that the single pattern-reconfigurable antenna has the same height as the test model shown in Figure 19. It is comprised of 6 horizontal metallic strips and a solid vertical metallic strip is positioned at the inner/proximal end at each half of the reflector. The horizontal strips are individually isolated from the central portion of the reflector with capacitors. Reconfigurability is provided via an array of 5 PIN diodes connected in a vertical series, joining the distal ends of the horizontal stripes on each half of the reflector. The DC block

capacitor value and the PIN diodes model chosen here is the same as designed antenna model for the 60° to 110° case.

Figure 82 shows the current surface distribution amplitude in linear in the single element pattern-reconfigurable antenna for both "ON" and "OFF" diode states. It can be seen that when the diodes are conducting, reconfigurable reflector has strong surface current flowing through it which means the separation of the reconfigurable reflector is electrically small compared to the wavelength of the signal. So, it can provide a narrow azimuth beamwidth. When the diodes are non-conducting, the reconfigurable reflector has weaker surface current flowing through it which means the separation of the reconfigurable reflector is electrically large and the reflector becomes semi-transparent. Thus, in this case, it can provide a wide azimuth beamwidth.

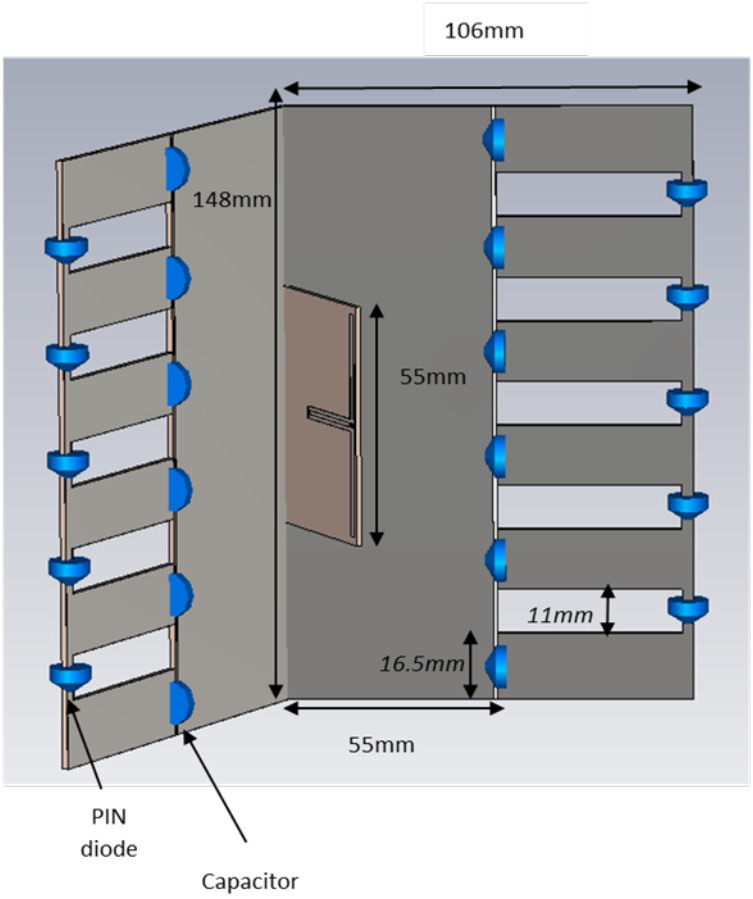

Figure 81: Schematic of the pattern-reconfigurable antenna

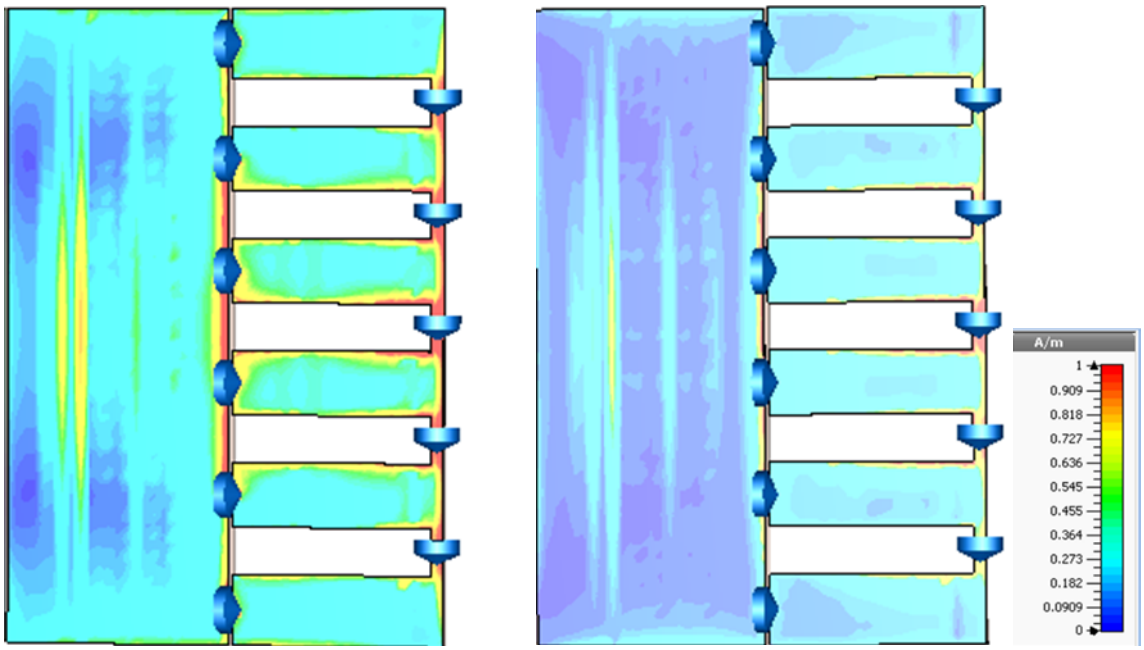

a) b)

Figure 82: Surface current for PIN diodes states a) “ON” b) “OFF”

In order to compare the simulated and measured radiation pattern in the azimuth plane for both “ON” and “OFF” diodes states for this particular designed model, a real antenna model was manufactured. The same testing procedures for the antenna radiation pattern measurement was operated here in anechoic chamber. After antenna performance measurement, a comparison between measured and simulated azimuth radiation patterns is shown in Figure 83. It can be seen that the azimuth beamwidth can be switched from 60° to 90° for “on” and “off” PIN diode states respectively. It also shows the measured azimuth beamwidth for the “on” state of PIN diodes is 59° with a gain of 7.3dBi and for the “off” state; the azimuth beamwidth is 87° with a gain of 7.3dBi. The simulated results show that the azimuth beamwidth is 60° with a gain of 9.2dBi for the “on” state and 90° with 8.0dBi gain for the “off” state. The 2 dB difference between the measured and simulated gain for the “on” state shown in Figure 83 can be attributed to inaccuracies in the simulated diode resistance, R_s , which was obtained from the manufacturer’s data sheet.

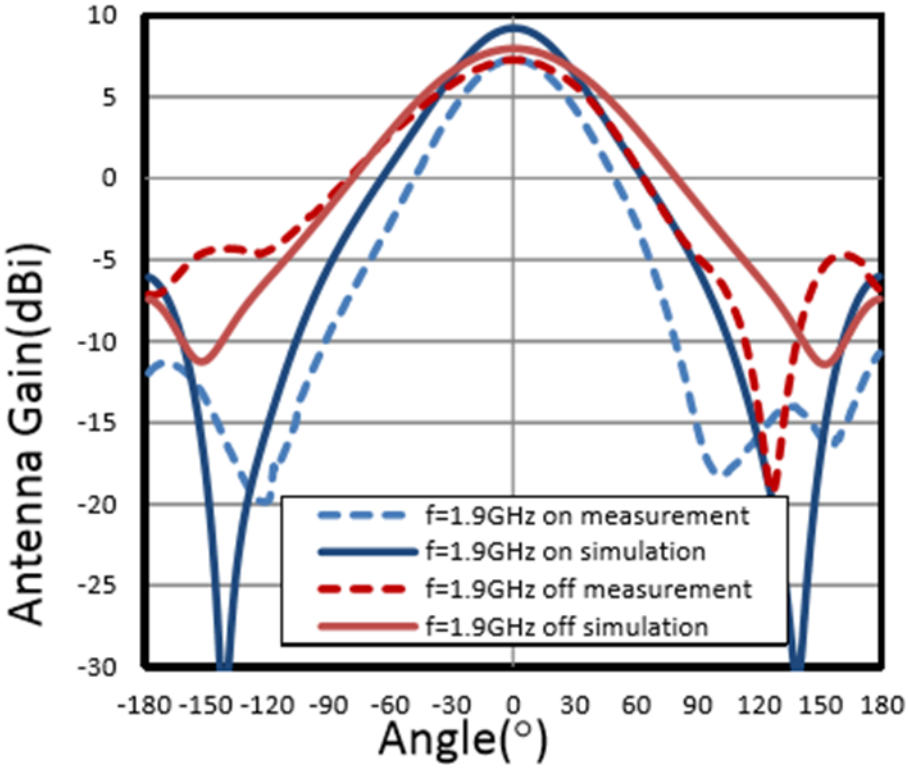

Figure 83: Comparisons between measured and simulated azimuth radiation patterns

4.8 Summary

A novel proposed basestation antenna employing PIN diodes has been proposed to achieve antenna reconfigurability. Simulations of a homogeneous three sector network have shown that a typical capacity increase of 20% is achievable by switching the azimuth beamwidth of the basestation antenna from 60° to 110°. This capability provides the potential to trade off overall cell capacity against cell edge user capacity and is applicable for a range of cell sizes. Validation of the antenna concept against measurements has also been presented for a single antenna element where excellent agreement between measurements and simulations was found.

This page is intentionally blank.

Chapter 5. Effect of Number of antenna elements on Cellular Network System

5.1 Introduction

This chapter investigates the effect of changing antenna downtilt angle and number of antenna array elements on the edge and cell capacity on reconfigurable antenna performance. This is for a homogeneous cellular network within an ISD of 500m. The research in this chapter is part of continuing attempts to improve spectral efficiency and capacity of the antenna, as this will continue to be an important issue as wireless communication data traffic increases for 5G systems.

The traditional way to improve the network performances can be achieved by cell splitting, or adding new cell sites. However, building new cell site infrastructure can be costly and is restricted by zoning [117]. Other alternative methods are deploying heterogeneous networks with low power nodes and distributed antenna systems ([119] to [121]). The performance impact of electrical downtilt in a 3D heterogeneous network systems was discussed in ([117], [122], [123] and [124]). However, these analysis is either focused on fixed number of array elements or using simple array element (dipole) or 3GPP standard antenna pattern. Here, in order to model the network performances more realistically, a 3-sector reflector antenna model is used for performance analysis as shown in Figure 84. This reflector antenna is designed to have a fixed azimuth beamwidth of 60° which matches with the most practical 3-sector antenna azimuth beamwidth applied in the field.

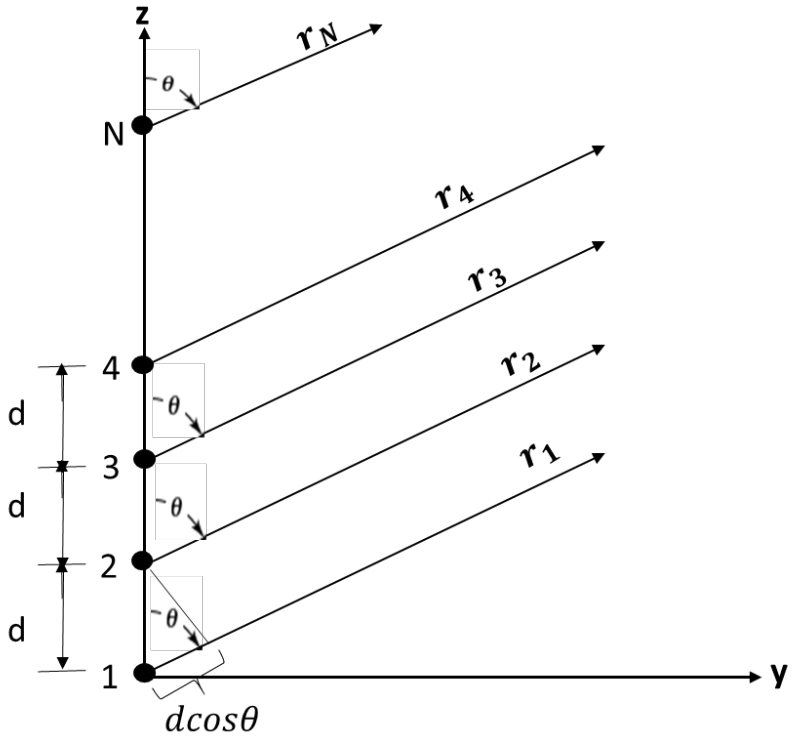

Figure 84: Antenna array for far-field observation

Based on this, we investigate the impact of the various elevation half-power beamwidth (HPBW) and antenna downtilt angle by using this 3-sector reflector antenna pattern on the cell edge and cell capacity in a homogeneous mobile network system. As demonstrated, with narrower elevation beamwidth and optimum antenna downtilt angle, both the cell edge and cell capacity in the system can be higher. Also, from this investigation, it shows that when the number of antenna elements reaches 40, it can get the saturate cell capacity in the network system.

5.2 Review of existing Work

Due to the ever-growing number of mobile devices in the current and future mobile system, antenna arrays have been used to overcome the issues of mobile systems in terms of limited channel bandwidth, channel capacity, reducing interference and multipath fading effects ([127] and [128]). MIMO systems, which utilise large numbers of elements, have the potential to achieve the large spectral and energy efficiency which makes it the strong candidate for 5G communication system. However, most of literature focused on using the omni-directional type of antenna element in the massive MIMO system. Recent studies show that by using the directional antenna type in the 120° sector massive MIMO cellular system, the lower bound achievable data rate can be obtained ([131] to [133]). However, in this study,

the directional antenna type used in the system analysis is a simplified theoretical antenna model only containing the main lobe and back lobe. Recently, Massive MIMO operation has been studied extensively focusing on omnidirectional profiles and homogeneous arrays [160-162]. However, most of these studies neglect the impact of the directional array gain pattern on the massive MIMO system performance. These assumptions can overestimate for realistic scenarios with compact antenna arrays. These feature a finite-number of antennas that can be closely spaced to each other (typically half a wavelength distance) and experience significant mutual coupling. In the existing literature, there are no guidelines of how to select a basic element for a massive MIMO antenna array and it becomes a crucial aspect of a massive MIMO array and system. One thing that is known from the basic MIMO theory is that it is always better if an antenna element in such an array receives as much multipath from all directions as possible. Hence, it has often been assumed that using a quasi-omnidirectional dipole is always better than the more directive patch element. However, the study of how these realized gain variations (a problem more understood in the antenna and propagation community) impact system-level performance (a problem formulation approach typically used in the massive MIMO signal processing community) is novel to both communities. In [163], the active antenna gain pattern variation of individual antenna elements in a large massive MIMO array, caused by the mutual coupling between closely spaced antenna elements and the edge effects in finite arrays is studied. Both the dipole type antenna element and patch antenna element are considered and evaluated in the simulation environment and real-life experiments. It has been found that in a finite array, there is a strong variation in the gain pattern of the different antenna elements. The gain variation is larger in a dipole array, which makes it more sensitive to angle of arrival than a patch array consisting of directional elements.

Other studies in [129], [130], [134] and [135] have investigated the antenna parameters impacts on the cellular system capacity which includes antenna topology, antenna azimuth, elevation HPBW and antenna downtilt angles. However, these studies demonstrated the effects of all antenna parameters on the system performances only on a limited number of antenna elements up to 10 now.

5.3 Research Motivation

Since Mobile communication today and beyond are exploring the high number of antenna elements for Base Stations, this can enable the new technologies such as Massive MIMO, antenna beamforming for different deployment scenarios to improve the system capacity ([125] and [126]). After investigating the antenna horizontal parameters (Azimuth Beamwidth) on the cellular network performances in the previous chapters, the vertical antenna parameters (Elevation Beamwidth) are discussed here on cellular network capacity. Based on the metal reflector antenna model developed in Chapter 3, the effects of increasing the antenna elements on the cellular network performance are studied. By combining with antenna downtilt angle, the effects of number of antenna elements on both cell edge and cell capacity are discussed in a homogeneous cellular network. It can indicate us by choosing the proper number of antenna elements and tilt angle, both the cell edge and cell capacity can benefit most from it.

5.3.1 Background Technique Overview

As a single antenna element usually has wider radiation pattern characteristics, it is difficult to meet requirements for high directivity. In addition, in many systems, it is also necessary to provide a high antenna gain to meet coverage requirements. In order to get a high directivity of the antenna, the electrical size of a single antenna element has to be increased. To avoid enlarging the dimension of a single element of the antenna, it is instead proposed that the relative electrical size of a single element can be increased by combing a number of smaller elements together. [6] This means that the antenna dimensions can be increased while still keeping electrical losses in the system to a minimum. The multi elements system is referred to as an antenna array and has been widely used as part of communication systems. [6].

The overall pattern of this array is dependent on adding the vector field of each element in the array. There are in general five ways to achieve the overall radiation pattern of the antenna array:

1) Using different geometrical radiating elements for the array
2) Changing the antenna element spacing
3) Changing the antenna element amplitude distribution
4) Changing the antenna element phase distribution

5) Changing the relative pattern of each element

Assuming there is a N-element antenna array which is uniformly located with the equal amplitude excitation, then the method for determining the array factor of N uniformally located elements along the z axis can be generalised. This method assumes that each element has the same amplitude and a progressive phase called β which leads the current excitation relative to the preceding one. A uniform array is defined here as an array of identical elements with the same magnitude but a progressive phase. Thus, the array factor for a uniform N-element linear array can be obtained by considering the elements to be point sources: [123]

$$AF = 1 + e^{j(kdcos\theta+\beta)} + e^{j2(kdcos\theta+\beta)} + \cdots + e^{j(N-1)(kdcos\theta+\beta)} \quad (5.1)$$

$$AF = \sum_{n=1}^{N} e^{j(n-1)(kdcos\theta+\beta)}$$

Here N is the number of array elements, k is the wave number, d is the antenna element spacing which is half-wavelength here and θ is the elevation angle. This expression can be written as:

$$AF = \sum_{n=1}^{N} e^{j(n-1)\psi} \quad (5.2)$$

$$\text{Where } \psi = kd\cos\theta + \beta$$

In order to simplify the array factor in equation (5.2), an alternate form of the antenna array factor can be derived to make the functions and distributions more recognizable. The derivation can be acieved by multiplying both sides of $e^{j\psi}$ expressed as follows:

$$(AF)e^{j\psi} = e^{j\psi} + e^{j2\psi} + \cdots + e^{j(N-1)\psi} + e^{jN\psi} \quad (5.3)$$

Substracting 5.2 from 5.3 derives the following expression:

$$AF\left(e^{j\psi} - 1\right) = (-1 + e^{jN\psi}) \quad (5.4)$$

This can also be written as:

$$AF = \left[\frac{e^{jN\psi}-1}{e^{j\psi}-1}\right] = e^{j\left(\frac{N-1}{2}\right)\psi}\left[\frac{e^{j\left(\frac{N}{2}\right)\psi}-e^{-j\left(\frac{N}{2}\right)\psi}}{e^{j\left(\frac{1}{2}\right)\psi}-e^{-j\left(\frac{1}{2}\right)\psi}}\right] = e^{j\left(\frac{N-1}{2}\right)\psi}\left[\frac{\sin\left(\frac{N\psi}{2}\right)}{\sin\left(\frac{\psi}{2}\right)}\right] \quad (5.5)$$

For an antenna array with a reference point at the physical center of the antenna, the array factor can be reduced to:

$$AF = \left[\frac{\sin\left(\frac{N\psi}{2}\right)}{\sin\left(\frac{\psi}{2}\right)}\right] \tag{5.6}$$

Equation (5.7) shows an approximation for equation (5.6) when assuming values of ψ:

$$AF \cong \left[\frac{\sin\left(\frac{N\psi}{2}\right)}{\left(\frac{\psi}{2}\right)}\right] \tag{5.7}$$

The normalised array factor is defined as the maximum value of each element, when these values are equal to unity. It is defined as:

$$(AF)_n = \frac{1}{N}\left[\frac{\sin\left(\frac{N\psi}{2}\right)}{\sin\left(\frac{\psi}{2}\right)}\right] \tag{5.8}$$

This can be approximated to:

$$(AF)_n \cong \left[\frac{\sin\left(\frac{N\psi}{2}\right)}{\left(\frac{N\psi}{2}\right)}\right] \tag{5.9}$$

To find the null of the array, equation (5.4) and (5.5) can be set to 0, which results in:

$$\sin\left(\frac{N\psi}{2}\right) = 0 \Rightarrow \frac{N\psi}{2}\Big|_{\theta=\theta_n} = \pm n\pi \Rightarrow \theta_n = cos^{-1}(\theta)\left(\frac{\lambda}{2\pi d}\right)\left(-\beta \pm \frac{2n\pi}{N}\right) \tag{5.10}$$

Here $n = 0, 1, 2, 3$ ... and $n \neq N, 2N, 3N,$ etc.

The value of n determines the order of the null in the antenna array. Equation (5.11) is used here to find the maximum values of the antenna array:

$$\frac{\psi}{2} = \frac{1}{2}(kd\cos\theta + \beta)\Big|_{\theta=\theta_m} = \pm m\pi \rightarrow \theta_m = \cos^{-1}\left[\frac{\lambda}{2\pi d}(-\beta \pm 2m\pi)\right] \tag{5.11}$$

Where $m = 0, 1, 2$ ... (etc). The array factor has only one maximum value and it happens only when $m = 0$ in equation (1.7).

$$\theta_m = \cos^{-1}\left(\frac{\lambda\beta}{2\pi d}\right) \tag{5.12}$$

This means that when $m = 0$ the observation angle ψ is 0 as well.

5.3.2 The effects of elevation radiation pattern for different number of antenna array elements on the system performances

This section outlines an investigation on how the antenna elevation pattern for different numbers of array elements has an effect on cell and cell edge capacity. Here the number of elements chosen has varied from 2 to 44. The antenna model selected here is a 60° azimuth beamwidth reflector antenna as mentioned in Chapter 3, and Figure 85 shows the single model of this reflector antenna. The dimensions for this single reflector antenna are the same as those used in Chapter 3. The reflector is 106mm wide and 79.5mm high as such is approximately λ/2 at the chosen designed frequency of 1.9GHz.

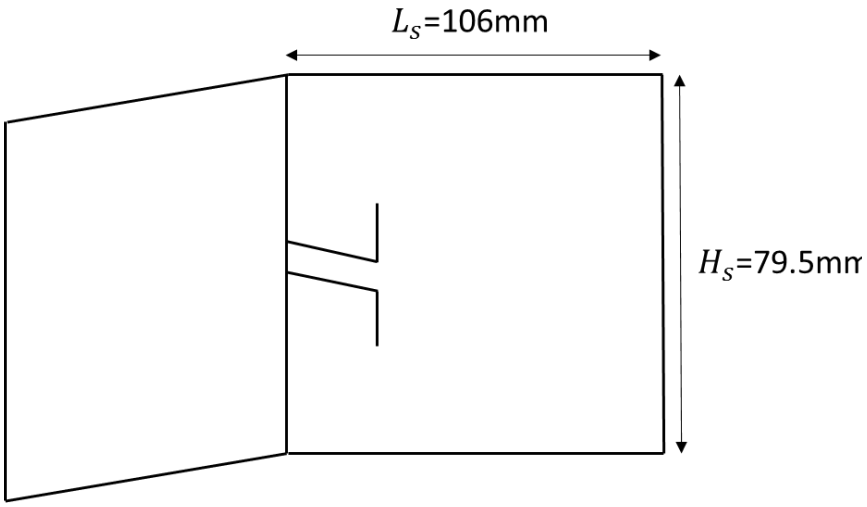

Figure 85: Single Reflector Antenna Model

The different number of single reflector antenna element is stacked on top of each other composing the antenna array elements as shown in Figure 86.

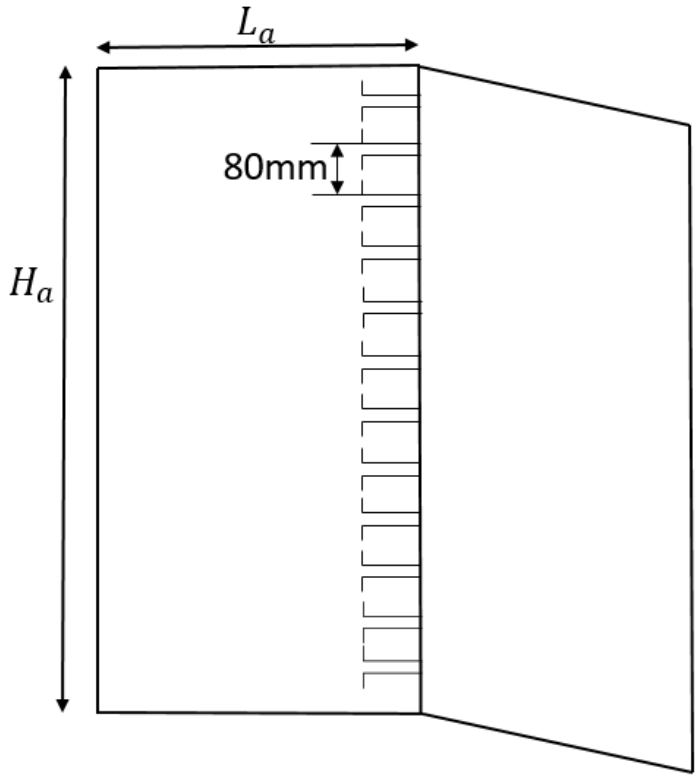

Figure 86: Vertically stacked antenna array elements

5.4 Array Pattern

Based on antenna array theory, if the single element has a pattern of $g_m(\theta, \varphi)$ then the antenna array pattern in the elevation plane can be expressed as [6]

$$E(t) = E\begin{pmatrix} single\ element \\ at\ reference\ point \end{pmatrix} * [array\ factor] * [mutual\ coupling] \qquad (5.13)$$

$$= g_m(\theta) * AF_{(n)} * C$$

Where $g_m(\theta)$ is the single element radiation pattern in the elevation plane Here, the mutual coupling between the antenna elements in the array can be expressed as a coupling matrix C as shown in equation (5.14):

$$E(t) = g_m(\theta) \cdot \begin{vmatrix} 1 \\ e^{j\pi cos\theta} \\ e^{2j\pi cos\theta} \\ \vdots \\ e^{j(n-1)\pi cos\theta} \end{vmatrix} \cdot C \qquad (5.14)$$

Figure 87 shows the simulation results for the array patterns in the elevation plane.

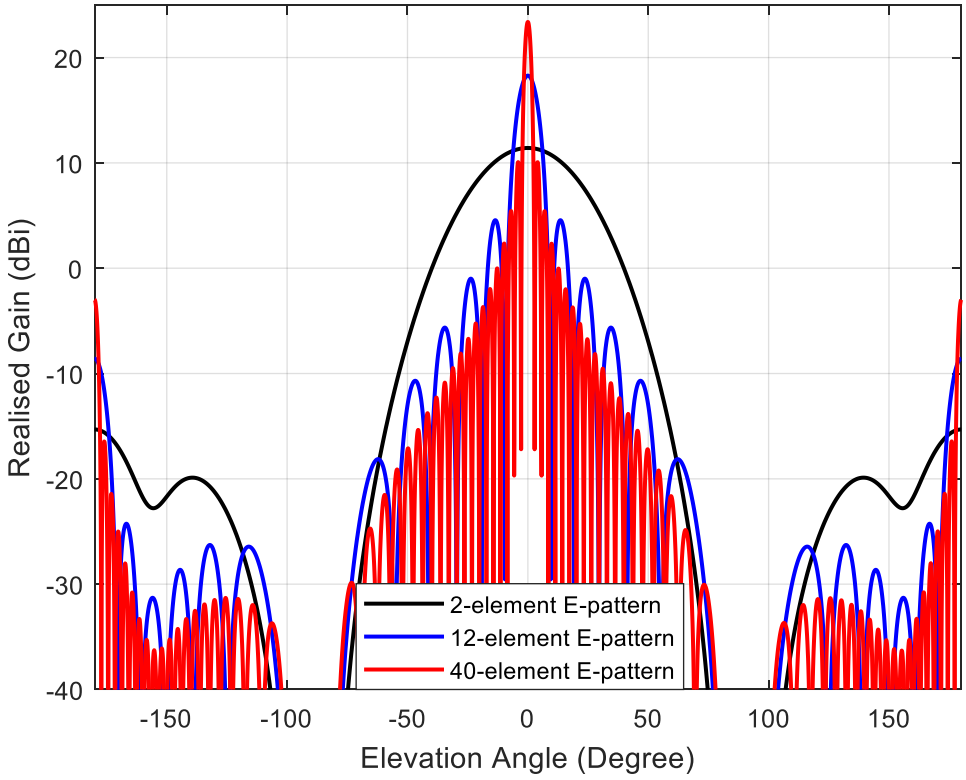

Figure 87: Various Antenna array Elevation Pattern

Figure 87 shows that the antenna array is comprised of vertically stacked single antenna element with the dimensions shown in Figure 86. Antenna array theory suggests that the gain of the antenna array increases as the number of elements increases. Here, by feeding the antenna element with power at an equal phase and amplitude, the corresponding gain of the antenna array can be achieved.

Figure 88 shows that as the number of antenna array elements increases from 2 to 44, the corresponding antenna array gain increases from 10.3dBi to 23.7dBi. However, the vertical beamwidth of the antenna array decreases as the gain increases, and as a result there is a trade-off in this system between gain and antenna vertical beamwidth which requires careful management.

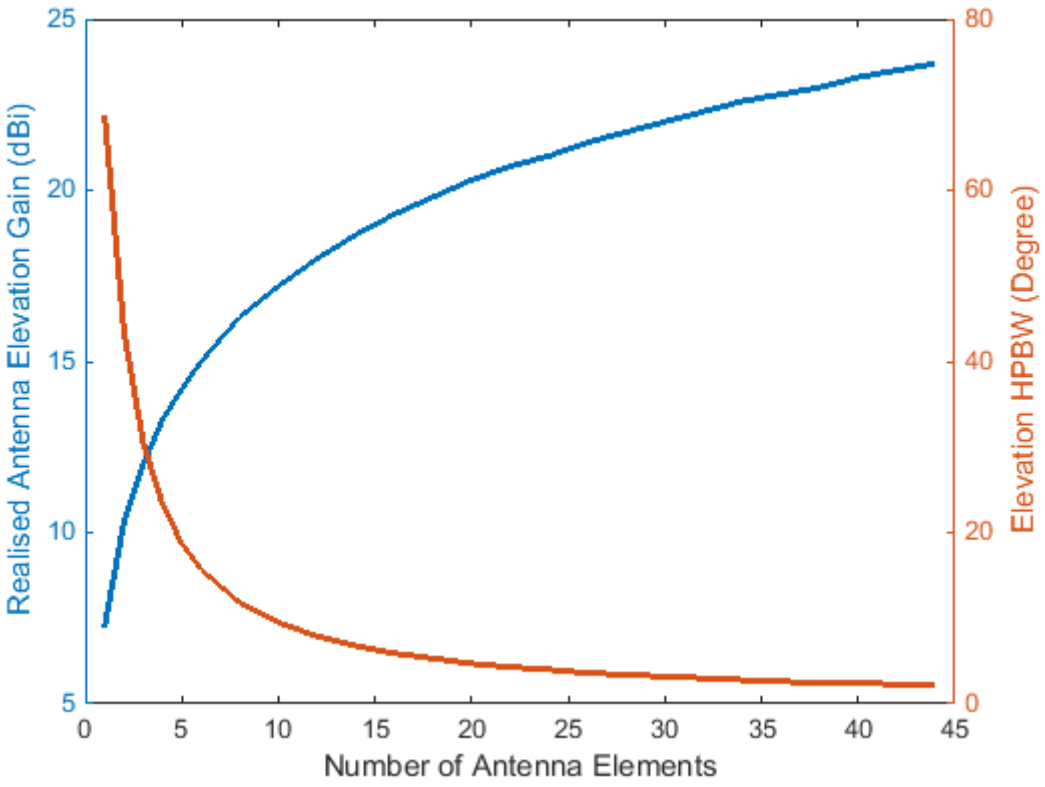

Figure 88: Antenna Elevation Gain VS Antenna Vertical HPBW

Figure 88 shows that as the number of antenna elements increases from 1 to 5, the Elevation HPBW of the antenna array drops sharply from 68.8° to 18.7°. However, for the gain of the antenna array, it can be increased gradually with the number of antenna elements increasing.

5.5 System Performance Analysis

The mobile network simulator used in Chapter 3 has been used again to analyse the effects of different elevation beam patterns, combined with changing the antenna array elements, on the edge and cell capacity in a homogenous mobile network system, the mobile network simulator used here is the same as mentioned in Chapter 3. The parameters chosen for the system performance evaluation are shown in Table 24.

Table 24: System Simulator Parameters		
Symbol	**Parameter**	**Value (units)**
P	Transmit Power	40 (W)
F	Operating frequency	1.9 (GHz)
B	Bandwidth	20 (MHz)
N	Number of Basestations in RAN	19
M	Number of sectors in BTS	3
$n0$	AWGN noise	$6x10^{-17}$ (W/Hz)
nUE	User Noise figure	8 (dB)
G_r	Received Antenna Gain	-1 (dB)
L	Path Loss Model	Winner II
H	User Antenna Height	1.5 (m)
H_a	Base-station Antenna Height	11 (m)
$ø_t$	Antenna Downtilt Angle	0-15 (°)
ISD	Inter-site Distance	500 (m)
N_m	Antenna Array Elements	2-44

To evaluate the effect of different elevation beam pattern of the $60°$ azimuth antenna array on edge and cell capacity for an ISD of 500m homogeneous mobile network, the true edge of the $60°$ beamwidth case is used here as shown in Figure 89. The cell capacity is evaluated by counting the mean value of all the pixels inside the cell edge boundary for the central sector.

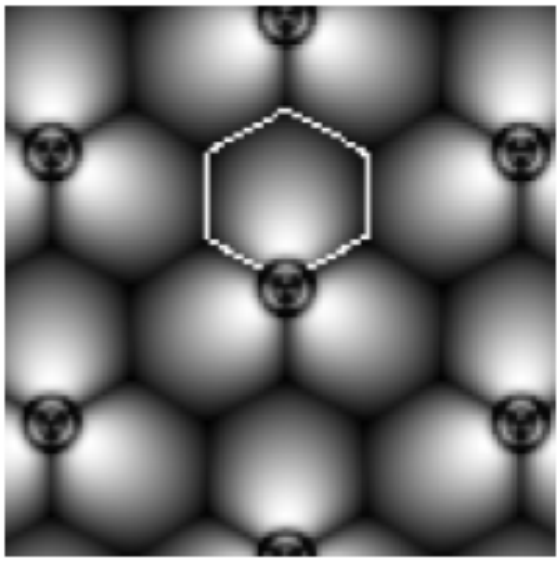

Figure 89: Cell edge of central sector for 60° azimuth case

A description of the Antenna downtilt angle analysis for the mobile network coverage is shown in Figure 90:

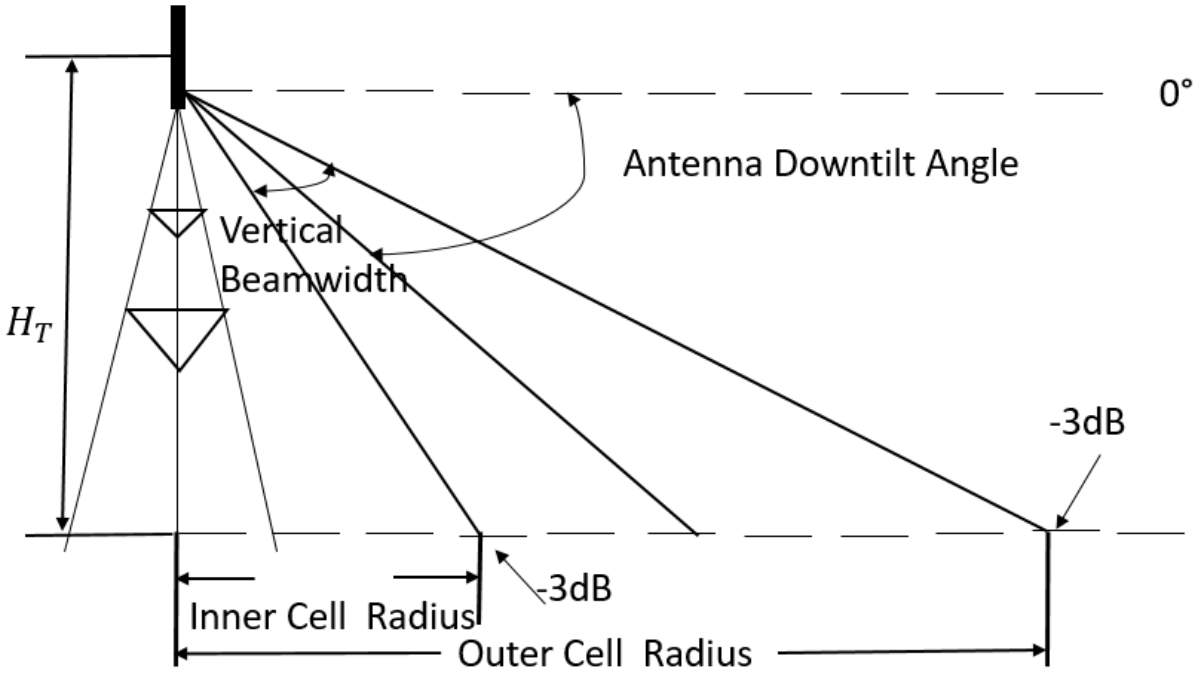

Figure 90: Antenna Downtilt for mobile network Coverage

Figure 90 shows that by changing the antenna downtilt angle, the mobile network coverage can be varied as well. The relationship between the antenna downtilt angle and mobile network coverage is shown in equation (5.15) and (5.16):

$$Inner\ Cell\ Radius = \frac{H_T}{\tan\left(\theta_t + BW/2\right)} \tag{5.15}$$

$$Outer\ Cell\ Radius = \frac{H_T}{\tan\left(\theta_t - \frac{BW}{2}\right)} \quad (5.16)$$

In equation (5.15) and (5.16), θ_t is the antenna downtilt angle, H_T is the basestation antenna height and BW is the elevation half-power beamwidth. So, from the antenna downtilt coverage figure, it is not difficult to find that the main mobile cellular network coverage is between the boundary of the Inner Cell Radius and Outer Cell Radius.

5.6 Network Coverage Map with Different High Gain Antenna Configurations:

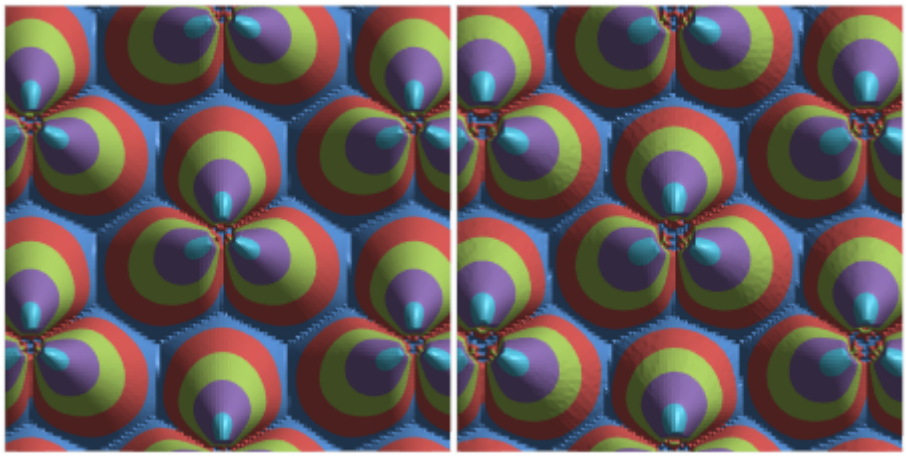

a) b)

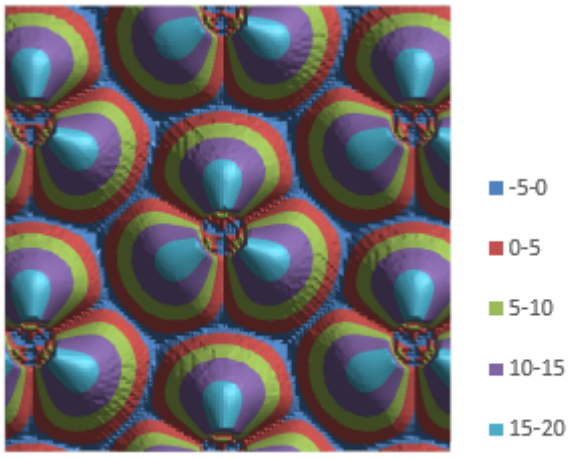

c)

Figure 91: Coverage of a three-sector 60° azimuth antenna with tilt of 6°: a) 6-element array b)12-element array, and c) 20-element array

Plots of network coverage for three different antenna array installations over an ISD of 500m homogeneous mobile network is shown in Figure 91. The coverage for a standard 12-element

antenna array with 7.9° elevation half-power beamwidth is compared with two different vertically stacked antenna arrays which have 6 elements and 20 elements respectively. This generates gain reduces of 3dB and increases of 2dB relative to the standard 12-element antenna array. Also, from the edge and cell capacity plot in Figure 91, with the antenna gain increasing, the cell capacity increases as well. It can be seen from Table 25 that, the average cell capacity can be increased by 13.3% and 43% with the antenna gain increased by 3dB and 5 dB respectively.

Table 25: Calculated edge and cell capacity with different antenna array configurations (6-element, 12-element and 20-element with 60° azimuth beamwidth at antenna downtilt angle of 6°)

Antenna Gain (dBi)	**Edge Capacity (Mbit/s)**	**Cell Capacity (Mbit/s)**	**Elevation HPBW (°)**
15 (6 element)	13.60	35.27	15.7
18 (12 element)	14.40	39.97	7.9
20 (20 element)	15.85	50.43	4.7

Figure 91 shows the cell edge and cell capacity in an ISD of 500m homogeneous mobile network for the antenna elements from 2 to 44 with the antenna downtilt angle from 0° to 15°. It shows that increasing number of elements in the elevation plane also increases the cell edge and cell capacity. However, once again there is a balance which must be met between the antenna gain and the elevation HPBW, as increasing the number of elements will cause elevation HPBW to decrease.

Since the users who located outside the antenna's -3dB beamwidth can suffer from 50% up to 90% less signal strength than the mobile users who are located inside the antenna's -3dB beamwidth, here when the number of the array elements reaches the number 40, the cell capacity gets the maximum value of around 54.3Mbit/s at the antenna downtilt angle of around 4°. However, if we keep downtilting the antenna angle beyond the optimal one, the network coverage can be deteriorated significantly due to this narrow HPBW of elevation pattern and for the large antenna downtilt angles, with the expense of cell radius, the mobile network can suffer from the coverage reduction which means the mobile network system can

become noise limited rather than interference limited. Thus the elevation beamwidth can affect the satisfying coverage region.

Since, in reality, antennas cannot work perfectly, it is better to choose the wider elevation beamwidth in the interference limited cases to avoid implementation errors. It is worth mentioning that although the narrow elevation beamwidth array can provide high capacity at its optimum tilt angle, the wrong tilt angle in this case can easily lead to significant capacity dropping compared with the wider elevation beamwidth case. The high-gain antenna array concept for providing link budget improvement over a homogeneous mobile cellular network indicates the potential for large site separations and fewer installations.

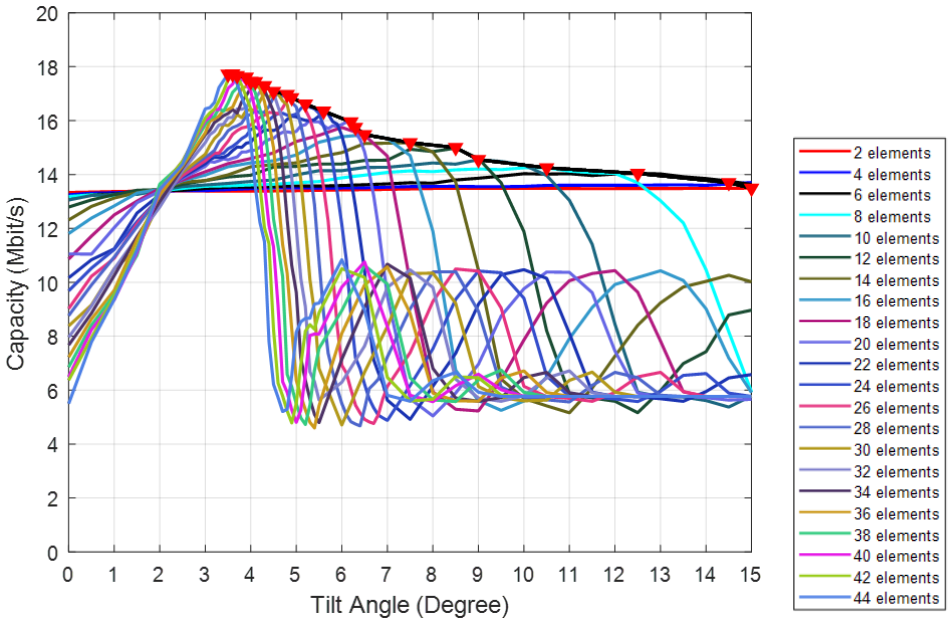

a)

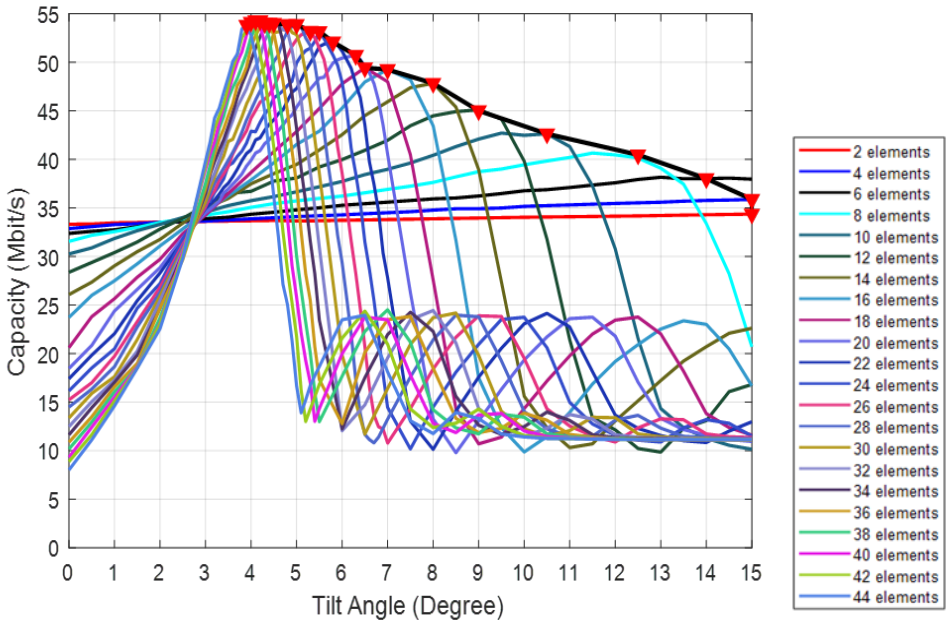

b)

Figure 92: a), b) Cell edge and cell capacity VS Antenna downtilt angle

5.7 Summary

In this chapter, we investigate the effects of number of antenna array elements combined with antenna downtilt angle on cell edge and cell capacity in a homogeneous mobile network. It has been shown that system performance is improved with an increasing number of antenna elements in the array, in terms of edge and cell capacity. However, this requires careful management as this results in a decrease in elevation HPBW along with a shift in the optimum downtilt angle. When the number of antenna array elements increased to 40, the system can get its saturate cell capacity of around 54.3Mbit/s at its optimum tilt angle of 4°. For, this high-gain antenna system, it is good to be used in a low traffic density network, while the coverage is priority.

This page is intentionally blank.

Chapter 6. Antenna Elevation Beam Shaping for the System Performance Improvement in the cellular Mobile Network

6.1 Introduction

In this Chapter, in order to address the low coverage performance at large antenna downtilt angles in the same ISD of 500m homogeneous cellular network as discussed in Chapter 3 for tilt angle from 10° to 15°, the elevation beam shaping techniques such as null filling, sidelobe level suppression have been discussed to get the corresponding shaped elevation beam pattern. In addition, the antenna elevation beam shaping for the 12-element array with 60° azimuth beamwidth is applied into the homogeneous mobile network to investigate the scenario on varying the downtilt angle from 0° to 15° for a typical cell in the mobile network, while keeping the optimum downtilt angle for the other surrounding cells in the same network. The detected cell edge and cell capacity in this scenario is then evaluated for comparison with the scenario where the variation of tilt angle from 0° to 15° is applied to all cells in the cellular network. This application can indicate us for the situation when the specific cell/cluster has the capacity below the whole network average, then optimising this cell/cluster capacity by using the antenna downtilt and elevation beam shaping can help improve its performances.

6.2 Review of existing work

Since antenna arrays have the ability to meet stringent communication system requirements, research on them has focused on developing new radiating elements such as using high refractive-index metamaterial unit cells, a quasi-planar reflector antenna, a shaped hourglass reflector antenna and the omnidirectional polyrod shaped beam antenna ([141]-[144]) have demonstrated its ability to shape the antenna beam pattern in the desired requirements for providing the improved antenna gain, bandwidth, electrical tilt or radiation efficiency. Majority research have shown that by combing using the array architecture with tapered amplitude or phase distribution for the array elements, the beam shaping, polarization diversity, multiple beam in azimuth can be achieved. It has been suggested that by applying these adaptive shaped beam pattern into the mobile system, the co-channel interference can be reduced and the capacity can be improved. [139], [140]

Recently, research in [145] and [146] have shown that using multilevel, 3D beamforming and proactive cell shaping can help support very high data rates and reduced energy consumption

in MIMO systems with large antenna arrays. However, these techniques may need large amount of feedback from users to choose the optimum beam. Other methods such as using beamforming combined with hybrid Particle Swarm Optimization and Gravitational Search Algorithm (PSOGSA) approach, 2D electronic beam steering with analogy phase shifters and adaptive digital beamforming have also shown their ability to achieve the desired pattern for supporting interference reduction, point to multi point communication and high-density observations in the elevation ([147]-[151])

Different antenna synthesis principles have been studied on achieving the required antenna beam pattern for the communication systems. The Orchard-Elliott technique and Taylor synthesis are the two popular synthesis methods to obtain the required beam pattern ([152] and [153]) Research in [154] to [159] have shown that by using antenna synthesis methods with genetic algorithm or different antenna array architectures such as interleaving array, linear edge slot array, dual planar reflector array and micro strip array can acquire the required beam pattern for sidelobe suppressing, null filling or both. Also, research in [136] has applied the synthesised beam pattern in the communication system to demonstrate its ability to reduce interference and extend coverage in a homogenous system compared to commercial antennas.

6.3 Research Motivation

Antenna arrays can achieve user-defined radiation patterns through the management of lots of complex radiating elements. By feeding the elements energy at a corresponding amplitude and phase, it is possible to 'tune' the beam pattern until a desired pattern is achieved [136] However, due to the changing environment in the current and future mobile network system such as dynamic mobile traffic, it is difficult to predict the mobile network behaviour and radiation pattern needed to achieve the optimal network performance (i.e. high coverage, low interference and better throughput). Due to this difficulty, most of the techniques in achieving the antenna optimisation are mainly focused on the antenna structure configuration, placement of the antenna and azimuth shaping.([137] and [138]) However, elevation beam shaping techniques such as sidelobe suppression and null filling have been identified as achieving a better radiation pattern and overcoming the low network capacity for a homogeneous mobile network at large antenna downtilt angles. As discovered in Chapter 3 that, the edge and cell capacity can be deteriorated beyond the cellular optimal downtilt angle.

In order to overcome this drawback or at least improve the network capacity at these high downtilt angles, the elevation beam pattern shaping is used here to design an antenna array which is capable of delivering the improved system performance compared with the original antenna array. As can be seen from Chapter 2, an elevation beam pattern is composed of one main lobe and several sidelobes and nulls. Thus, to improve the system capacity at large downtilt angles for this antenna array, sidelobe and null shaping techniques can be discussed here. The antenna elevation beam shaping combined with the antenna downtilt angle is also applied into a homogeneous mobile network to investigate the system performances. This specific application has indicated that by choosing the proper antenna downtilt angle for the specific cell/cluster with elevation beam shaping technique, the cell/cluster performances in terms of capacity can be improved without sacrificing too much performance of the other surrounding cells.

6.4 Research Methodology

In this Chapter, antenna elevation beam shaping methods and their application in a homogeneous cellular mobile network is discussed. In order to investigate how antenna elevation beam pattern influences cellular network performances, the antenna downtilt side direction, sidelobe effects and null effects of the 12-element antenna array are outlined. The different antenna elevation beam shaping methods including "binominal distribution", "Dolph-Tschebyscheff distribution" and "Taylor Beam Synthesis" are investigated in section D. Lastly, in section E the shaped elevation beam pattern is applied into a homogeneous mobile network to optimise the specific cell/cluster's coverage by choosing the proper downtilt angle for the specific cell only.

6.4.1 Antenna Downtilt Side Direction Verification

The antenna array configuration selected here is the standard 12-element metal reflector dipole array with 60° and 7.9° azimuth and elevation HPBW respectively. As shown in Figure 93, it illustrates the antenna azimuth and elevation pattern of the 12-element array which can have a gain of 18.3dBi.

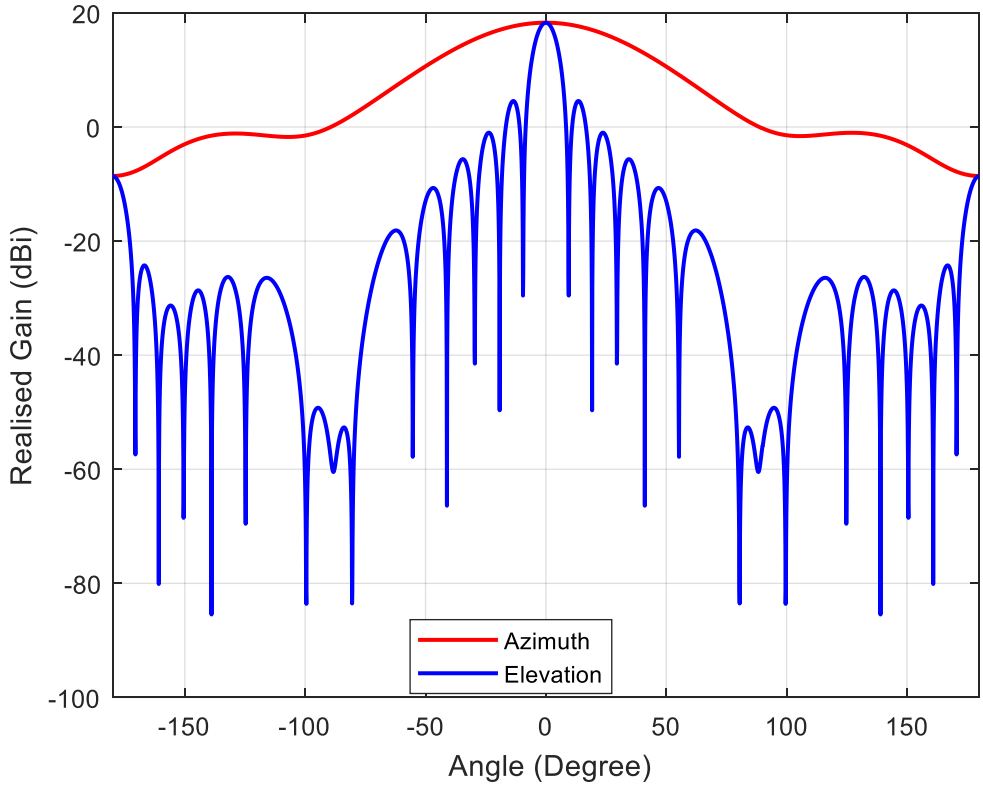

Figure 93: Antenna Radiation pattern for the 12-element array

Now, in order to investigate the antenna elevation beam pattern shaping on cellular mobile network performances with large antenna downtilt angles, the mobile network is chosen as a 3-sector cell sites with an ISD of 500m homogeneous system.

As antenna downtilt angle can vary the network coverage footprint especially at large antenna downtilt case, for the 12-element antenna array configuration, the edge and cell capacity can be dropped significantly beyond 10° tilt. In order to investigate the elevation beam shaping effects on the system performance more effectively, the downtilting side of the antenna array needs to be defined first. As can be seen from Figure 93, the downtilting side can be either lower half-side (the left half one) or the upper half-side (the right half one). In order to define the antenna downtilting side, a simplified single elevation pattern with constant sidelobe level is used here for testing purpose. As it is known that a real antenna elevation pattern can be made up of a main lobe, several sidelobes and antenna nulls. Here, to simplify the verification process for elevation beam shaping, a simple elevation pattern is used for this purpose based on the original 12-element array elevation pattern. The simplified elevation beam pattern can be started with only a single main lobe of the original elevation HPBW of 7.9° without sidelobes. The elevation shaped beam pattern can now be shown in Figure 94.

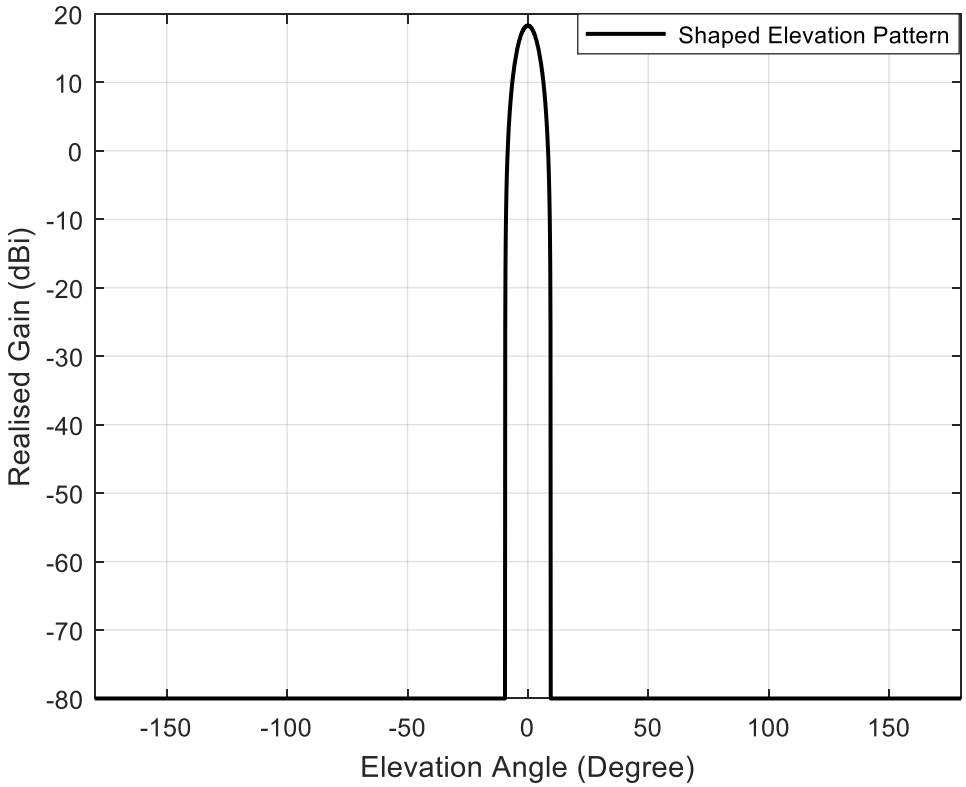

Figure 94: Elevation beam shaped pattern without sidelobes

Since the shaped beam pattern only contains the single main lobe, it is expected to have poor network coverage at high antenna downtilt angles. The system parameters to calculate the network coverage is shown in Chapter 5. Table 24. Figure 95 shows that at a downtilt angle of 0°, the network achieves good coverage from the main beam of the antenna. However, at the downtilt angle of 15° case, due to the very low power level (-80dB) from the antenna sidelobes, the network becomes noise limited system.

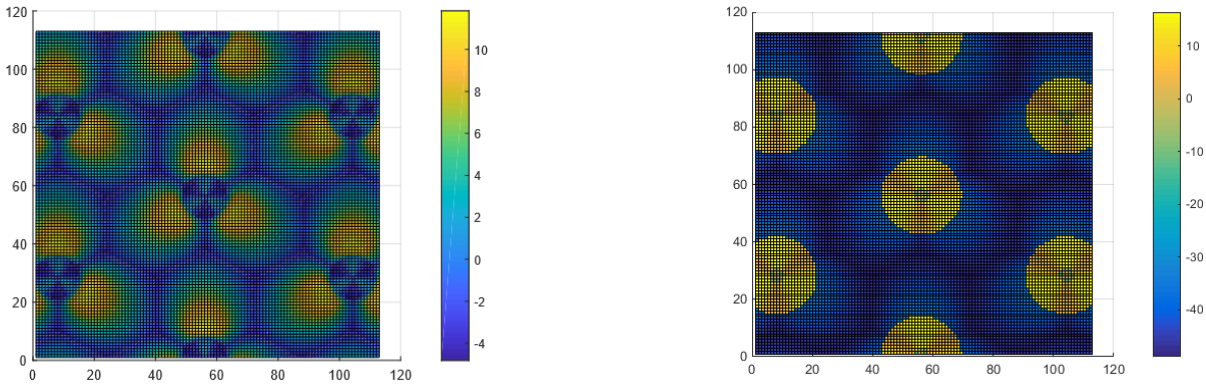

a) b)

Figure 95: SINR distribution plots at antenna downtilt of a)0° and b)15°

Thus, in order to verify the antenna downtilt side direction, five different elevation shaped beam pattern shown in Figure 96 based on the simplified pattern above is discovered here. The SINR distribution plots at certain antenna downtilt angles are shown to confirm the different assumptions.

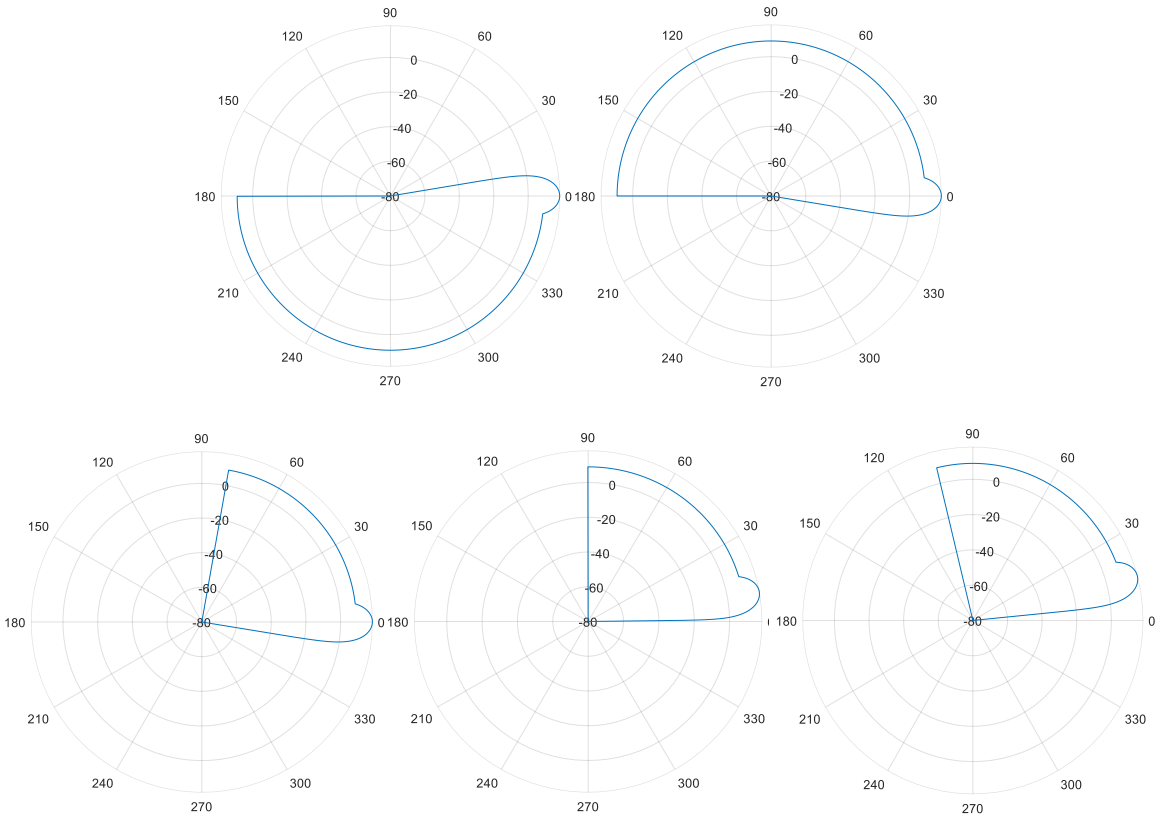

Figure 96: Five different elevation shaped beam pattern for testing cases

6.4.2 Testing Case 1:

The testing 12-element elevation pattern based on the original one is shown in Figure 97 consisting of a main lobe with elevation HPBW of 7.9° with constant lower half sidelobe level of +9dB and constant upper half sidelobe level of -80dB. In order to better understand the testing pattern effects on the mobile network performances, the polar plot is shown in Figure 96 (upper side left corner). Now, the SINR distribution plots for the different antenna downtilt angles are discovered here in an ISD of 500m homogeneous network.

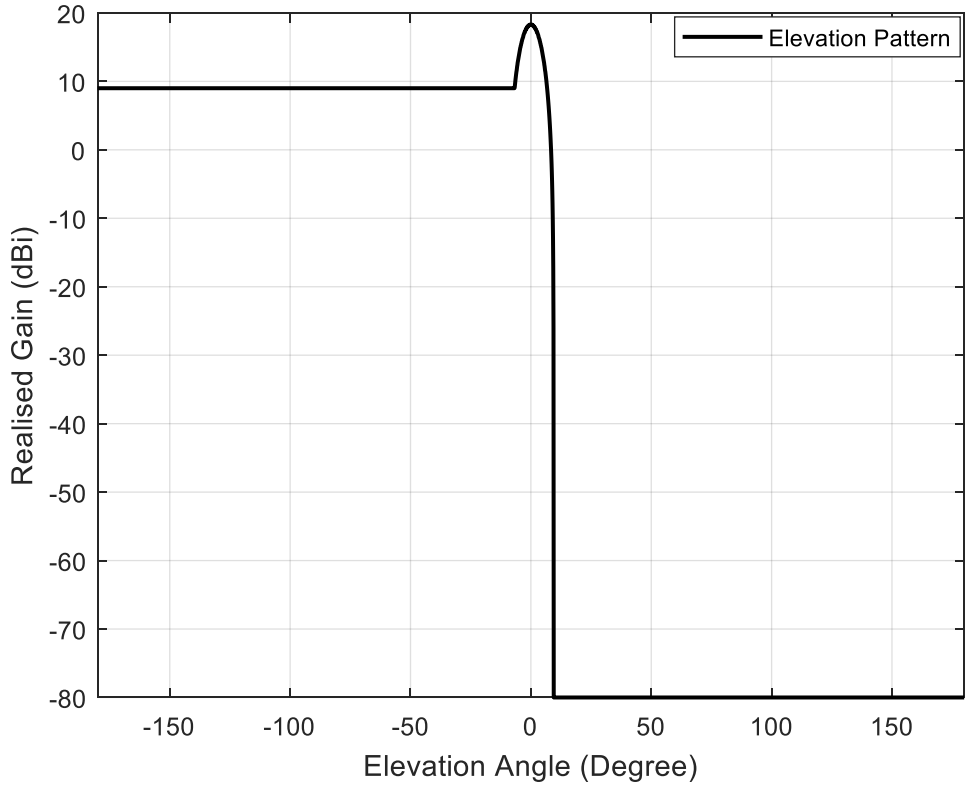

Figure 97: Testing Elevation pattern 1

It can be seen from Figure 98 that, when tilting the antenna downtilt angle at large angle of 14° and 15°, the network coverage is deteriorated significantly and starts becoming noised limited system.

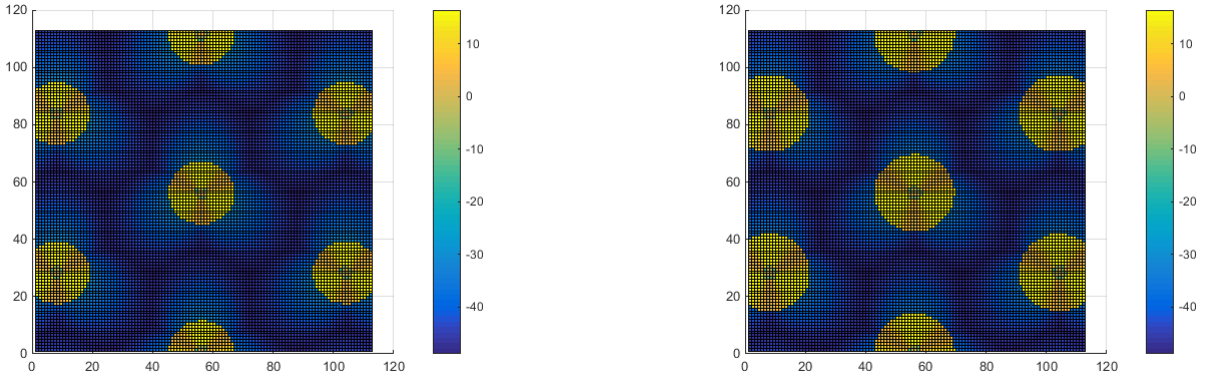

Figure 98: SINR distribution plots at antenna downtilt of a) 14° and b) 15°

6.4.3 Testing Case 2

The testing elevation pattern for the second case based on the original pattern is shown below, in Figure 99. This uses the same pattern structure as testing pattern 1 but has swapped the sidelobe level with constant lower sidelobe level of -80dB and upper sidelobe level of +9dB. The polar plot for this pattern is presented in Figure 96 (upper side right corner) which can be seen is opposite from the testing pattern in case 1.

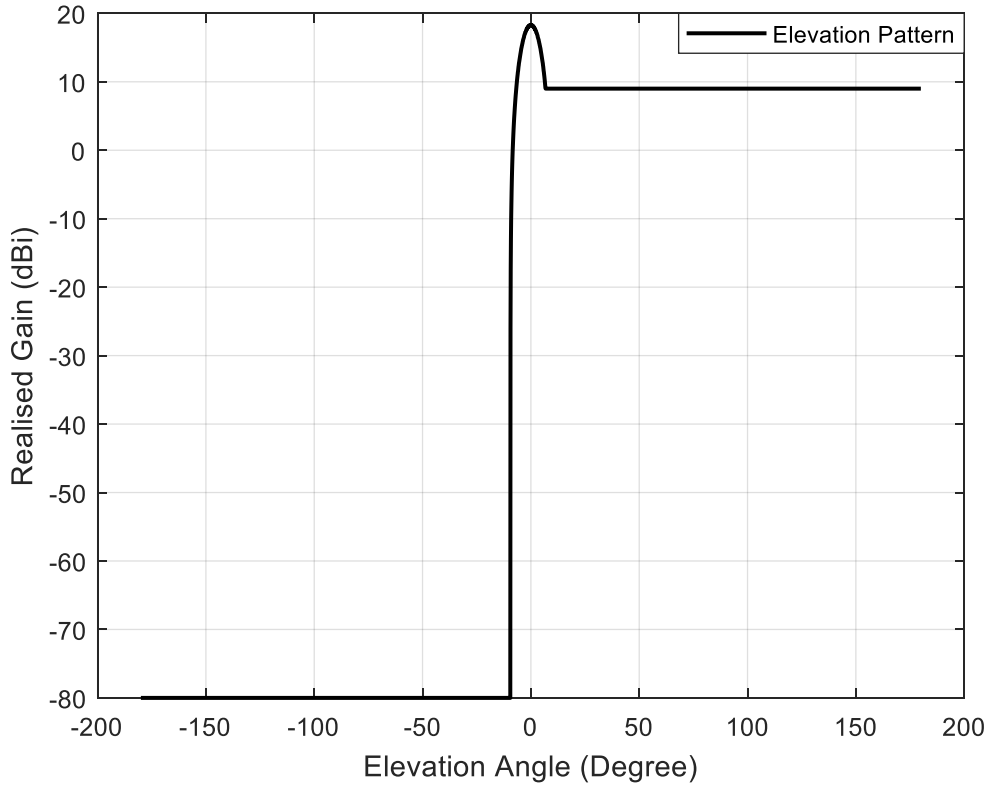

Figure 99: Testing Elevation Pattern 2

The SINR distribution plots for the testing elevation pattern 2 at different antenna downtilt angles are shown in Figure 100: this shows that at large antenna downtilt angle of 15°, the network coverage is almost kept the same as the antenna downtilt angle of 0°. Also, it is worth mentioning that the antenna uptilt effects on coverage is investigated in Figure 100 c) with the uptilt angle of 15°. It shows that with the antenna uptilting of testing pattern 2, the network still keeps good coverage due to the constant upper sidelobe level below the antenna horizontal line which gives back radiation coverage to the mobile network.

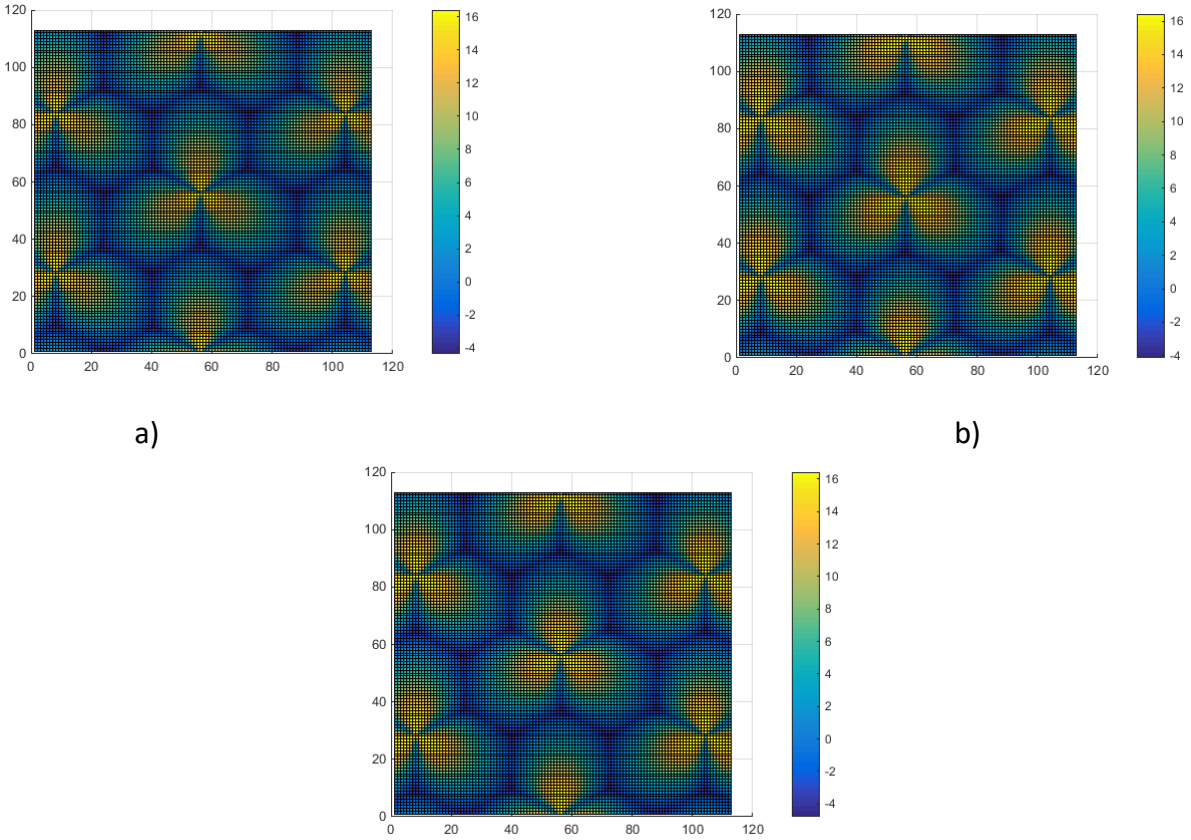

Figure 100: SINR distribution plots at antenna downtilt of a)0°, b)15° and c) -15°

6.4.4 Testing Case 3

Figure 101 shows the testing elevation pattern for the third case based on the original pattern. It can be seen that the testing pattern has the same structure as the case 2 but with the shorter constant upper sidelobe level of +9dB. From the polar plot it can be seen that the testing elevation pattern shown here is almost the half of the pattern in case 2.

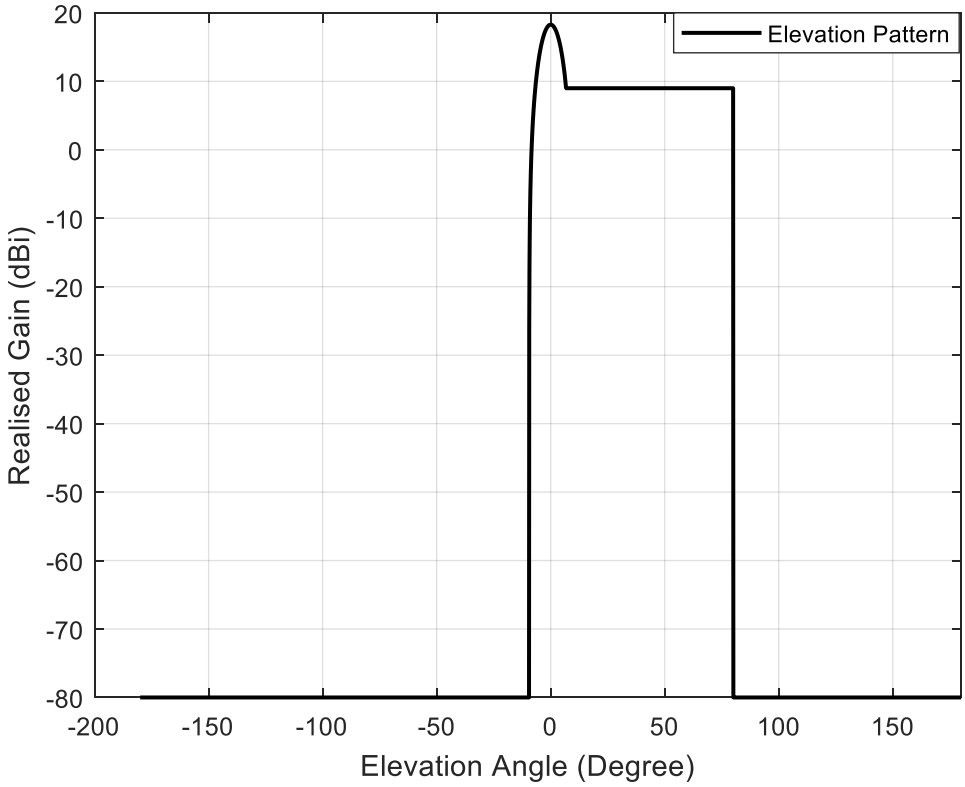

Figure 101: Testing Elevation Pattern 3

The SINR distribution plots for the antenna downtilt and uptilt at different angles are shown in Figure 102. Since this testing elevation pattern has the same structure as the case 2, it shows the similar network coverage map as the case 2 as well with good network coverage at these tilt angles.

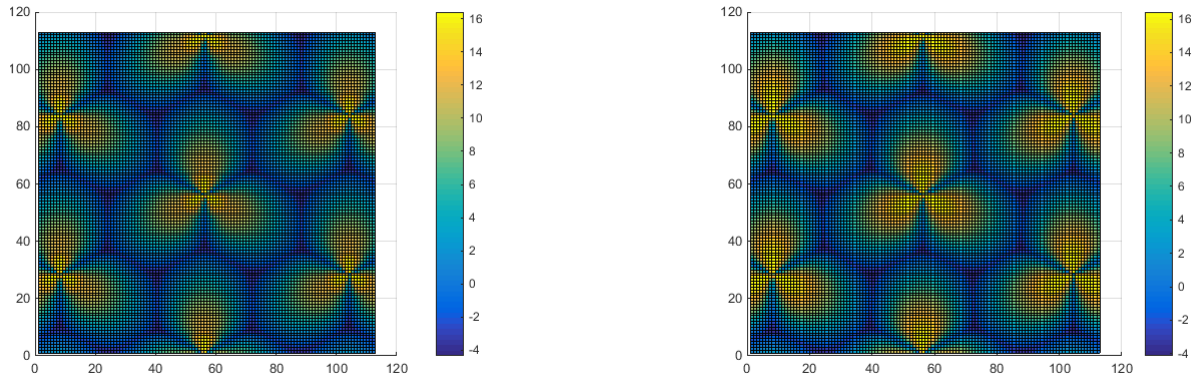

a) b)

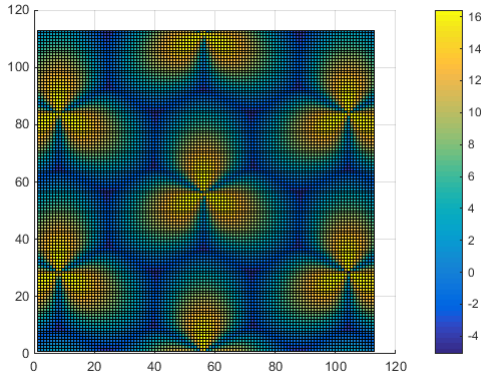

c)

Figure 102: SINR distribution plots at antenna downtilt of a)0°, b)15° and c) -15°

6.4.5 Testing Case 4

The testing elevation pattern 4 is achieved by shifting the testing elevation pattern 3 by 10° on the right side direction as demonstrated in Figure 103

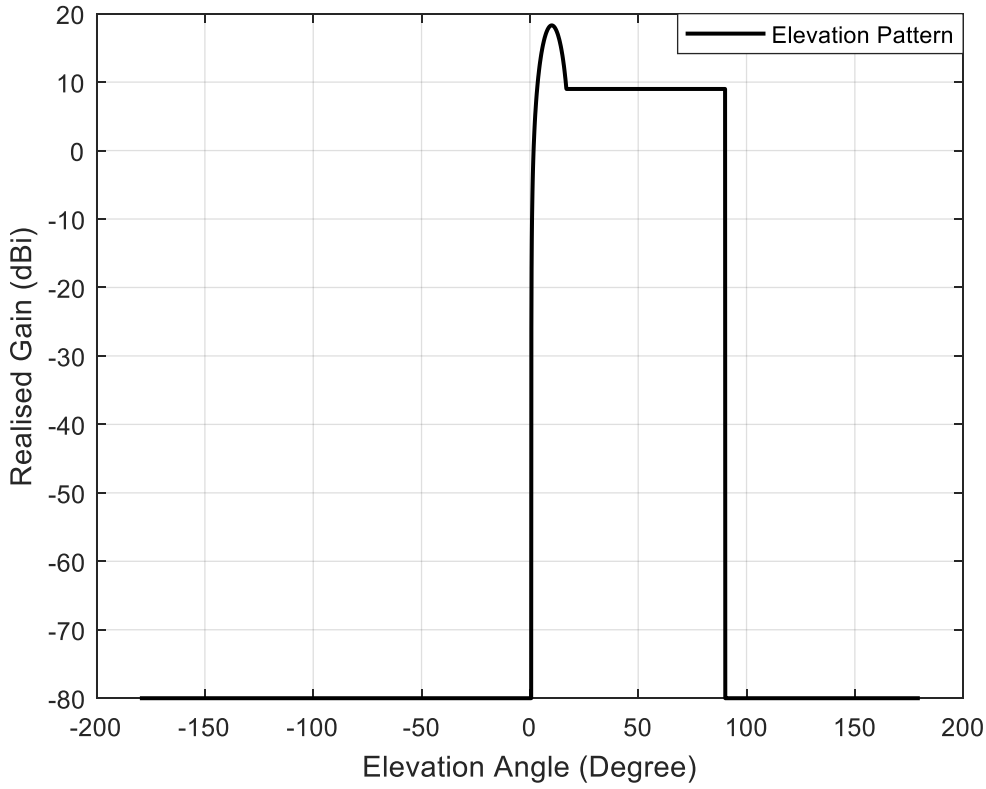

Figure 103: Testing Elevation Pattern 4

As the SINR distribution plots in Figure 104 show, with an antenna downtilt angle of 0° and 10° the network achieves good coverage. However, since the elevation pattern in this case is shifted by 10° of the case 3, the SINR plot at downtilt of 10° is similar as the downtilt of 0° in case 3. Due to the radiation pattern just cutting through the edge of the cell at tilt angle of 0°, the network coverage is kept good in this case.

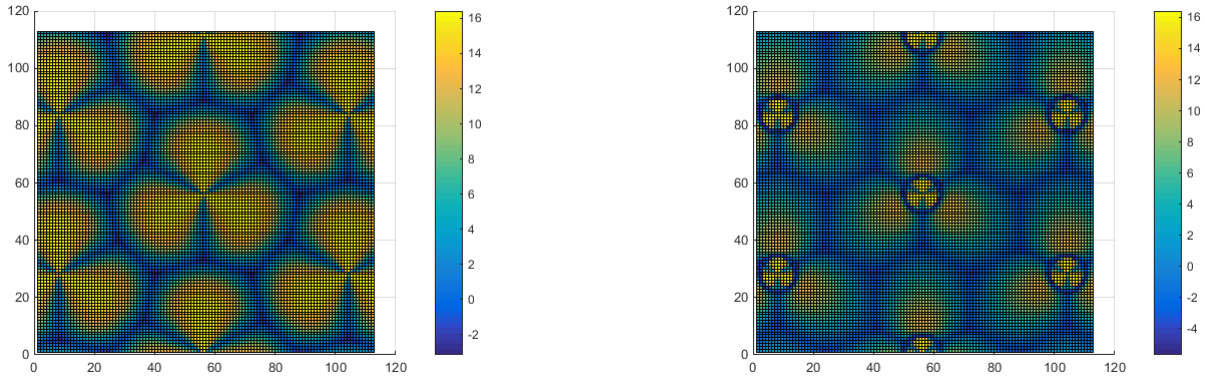

Figure 104: SINR distribution plots at antenna downtilt of a)0° and b)10°

6.4.6 Testing Case 5

The testing elevation pattern 5 is achieved by shifting the testing elevation pattern 4 by 5° on the right side direction as shown in Figure 105. The corresponding polar plot for this pattern is shown in Figure 96 (lower right side).

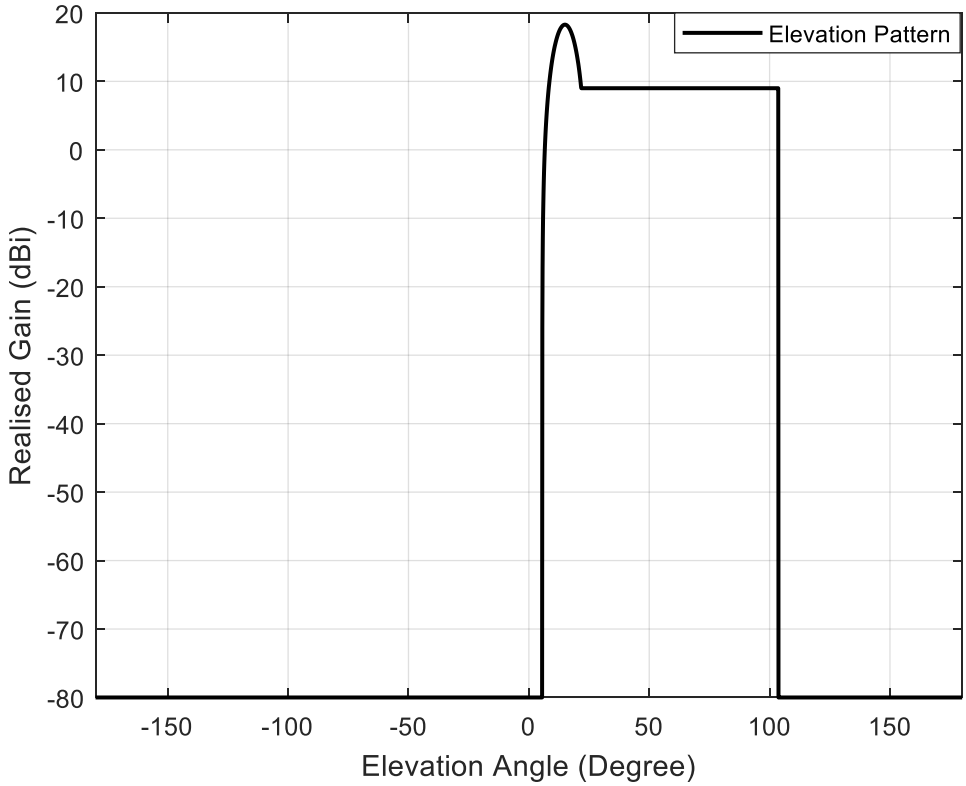

Figure 105: Testing Elevation Pattern 5

The SINR distribution plots in Figure 106 show that for antenna downtilt angels at 0° and 15°, at 0° downtilt case, since there is no power being transmitted in the horizontal direction and the main beam is pointed upwards, the network becomes noise limited rather than interference limited. At downtilt angle of 15° case, the main beam is pointed down towards the horizontal direction, thus the network has good coverage.

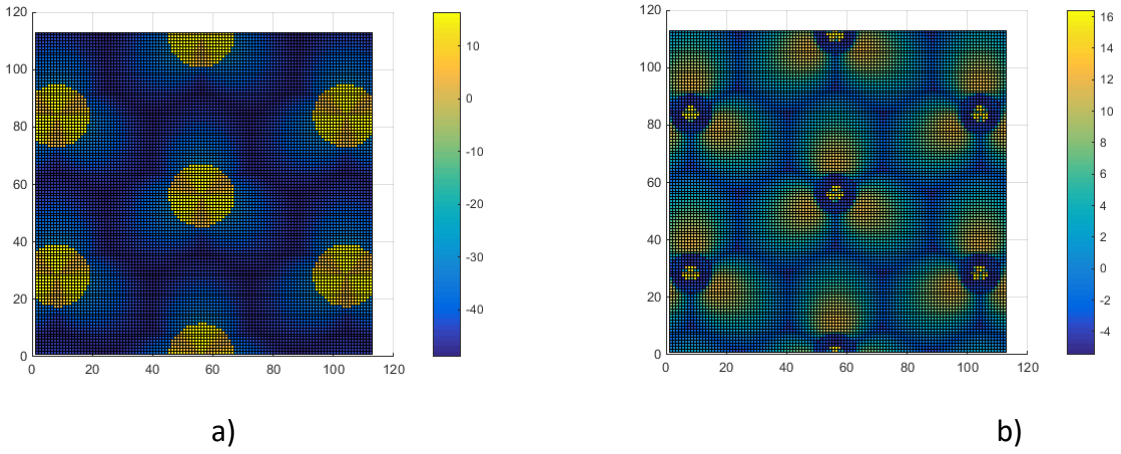

Figure 106: SINR distribution plots at antenna downtilt of a)0° and b)15°

So, from the above five testing elevation patterns, it can be found that the 12-element antenna array used in the mobile network is downtilted towards the lower half-side (the left half –side direction).

6.5 Antenna Elevation Sidelobe Effects On Mobile Network Performances

Here, in this section, the antenna elevation sidelobe effects on mobile network performance in terms of capacity are discussed in order to improve the edge and cell performances at large antenna downtilt angles. With the antenna downtilt direction defined, the sidelobe effects of the original 12-element elevation pattern on network performances (in terms of edge and cell capacity) can also be calculated.

As can be seen from the 5 different testing cases, it indicates that lowering the lower half pattern level and increasing the upper half pattern level can help improve the network coverage at large antenna downtilt cases. So, in order to check the sidelobe effects on mobile network performances and based on the trend from the 5 different testing cases, the first upper sidelobe level is increased to +9dB and the first lower sidelobe level is reduced to -1.5dB. The manipulated sidelobe shaped elevation pattern and the original 12-element antenna array elevation pattern is shown in Figure 107.

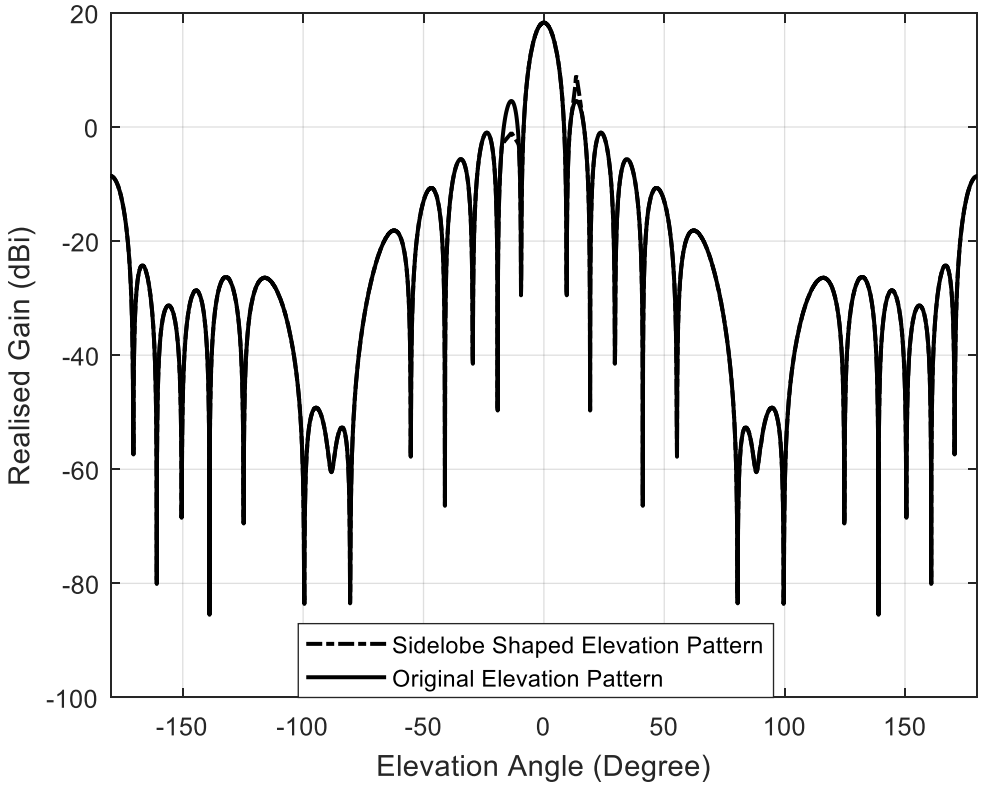

Figure 107: Sidelobe shaped elevation pattern VS Original elevation pattern

To verify the sidelobe effects of the manipulated elevation pattern on edge and cell capacity, the system parameters shown in Chapter 5 Table 24 are applied into an ISD of 500m homogeneous network. The resultant cell edge and cell capacity for the sidelobe shaped elevation pattern and original elevation pattern with antenna downtilt angles from 0° to 15° is shown in Figure 108. As can be seen, by changing the sidelobe level of the original elevation pattern cannot be used to improve the average edge and cell capacity at large antenna downtilt angles and with the sidelobe beam shaping in elevation pattern, the network performances almost keep the same as using the original elevation pattern.

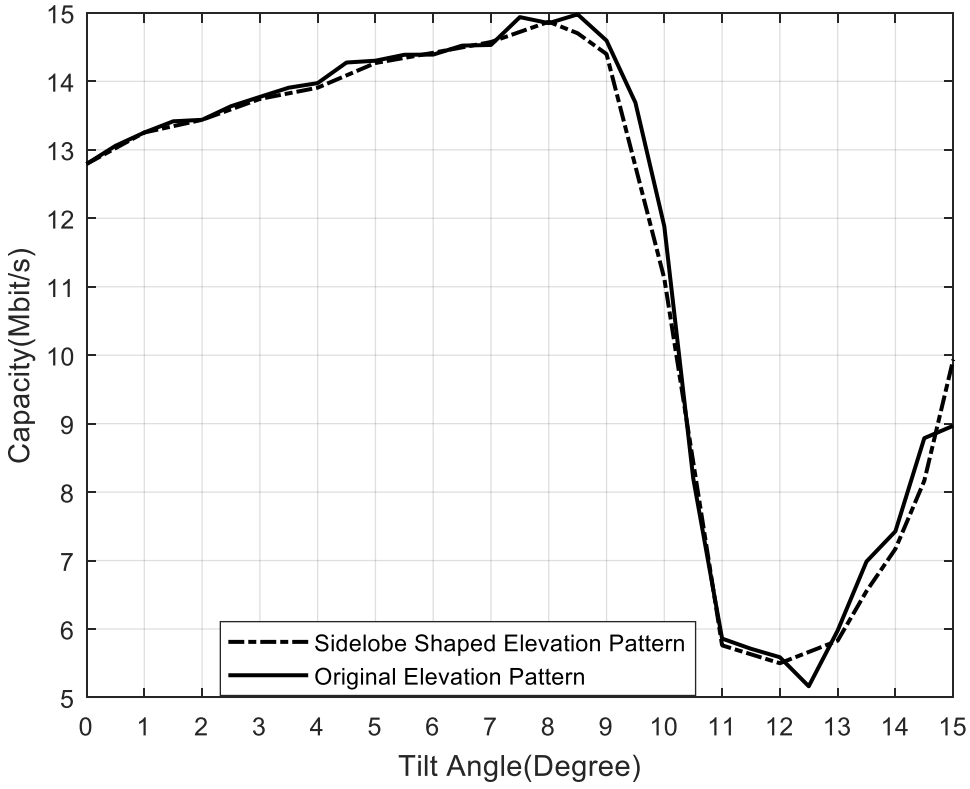
Capacity(Mbit/s)
Tilt Angle(Degree)
Sidelobe Shaped Elevation Pattern
Original Elevation Pattern

a)

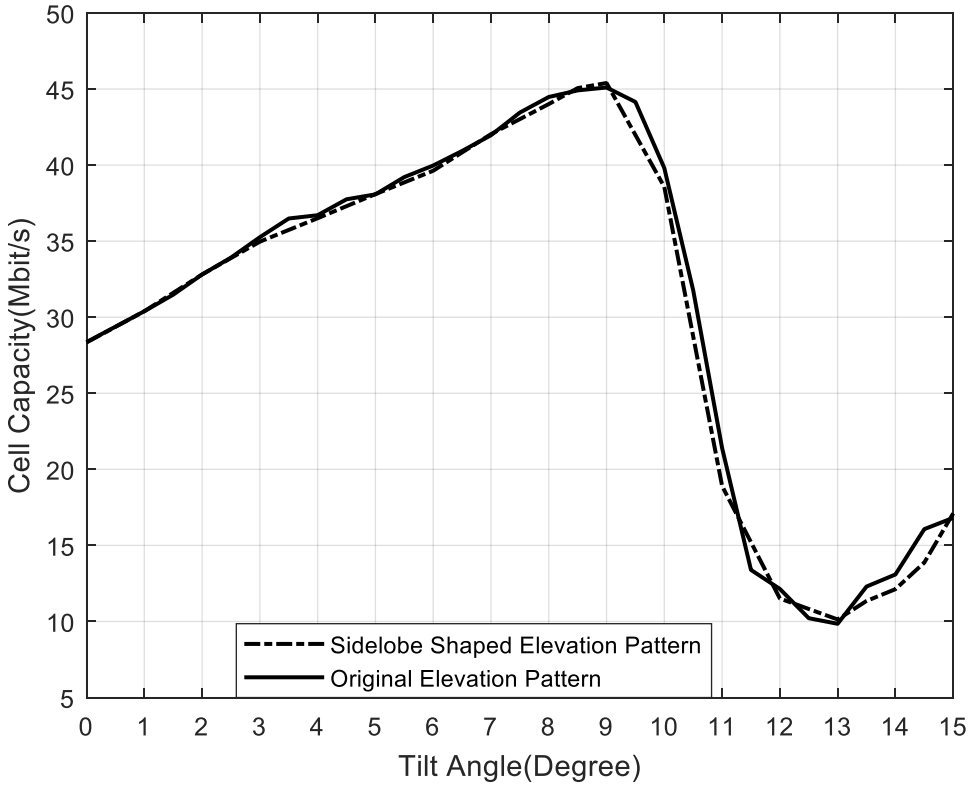
Cell Capacity(Mbit/s)
Tilt Angle(Degree)
Sidelobe Shaped Elevation Pattern
Original Elevation Pattern

b)

Figure 108: a), b) Cell edge and Cell Capacity for Sidelobe shaped pattern VS Original pattern

6.6 Verification of Antenna Elevation Null filling effects on Mobile Network Performances

Since the antenna sidelobe effects of the elevation pattern do not affect the mobile network performances and with the indication from the 5 different testing cases, the other elevation beam shaping technique: antenna null filling is investigated here. As can be seen from the 5 different testing cases, with constant high sidelobe level on the right half-side of the antenna elevation pattern, the network coverage can be improved significantly at high antenna downtilt angles. So, in order to verify this concept with the antenna null filling technique, the simplified elevation shaped beam pattern shown in Figure 94 is used here to obtain the different manipulated null filling patterns. As can be seen from Figure 109, the different manipulated upper side null filling elevation pattern is illustrated with the upper null filling range selected from the first sidelobe position to the second sidelobe position. It is shown from Figure 109 that the first upper nulling pattern is achieved by filling the upper side pattern of the single beam in Figure 94 with constant level of 18.3dB till the first sidelobe position at 7.7°. The other upper null filling patterns are acquired by using the same method through filling the upper side pattern of the elevation beam till different positions of the antenna upper half-side pattern.

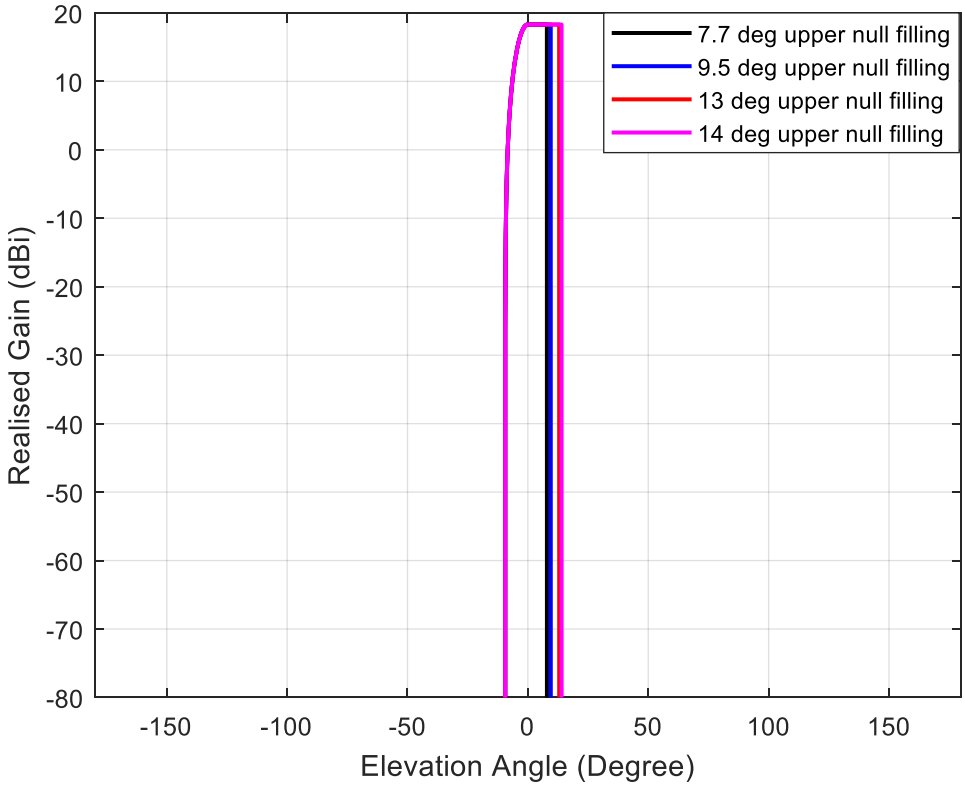

Figure 109: Different upper null filling elevation pattern

Now, to investigate the antenna upper null filling pattern effects on the mobile network performances, the edge and cell capacity with these different elevation patterns at antenna downtilt angles from 0° to 15° is compared here. The same procedure to get the sidelobe effects on network performances is applied here. Figure 110 shows that the average edge and cell capacity has the peak value at different tilt angles for different upper null filling patterns and when the upper-side pattern fills with more constant power level, the peak value can be shifted towards the high tilt angle correspondingly as well. The peak value occurred here is due to the peak antenna gain filled into the upper side elevation pattern. Thus, from the results shown in Figure 110, it can be concluded that with proper upper side null filling in the elevation beam pattern of the original 12-element antenna array, cell performances at high antenna downtilt angles can be improved.

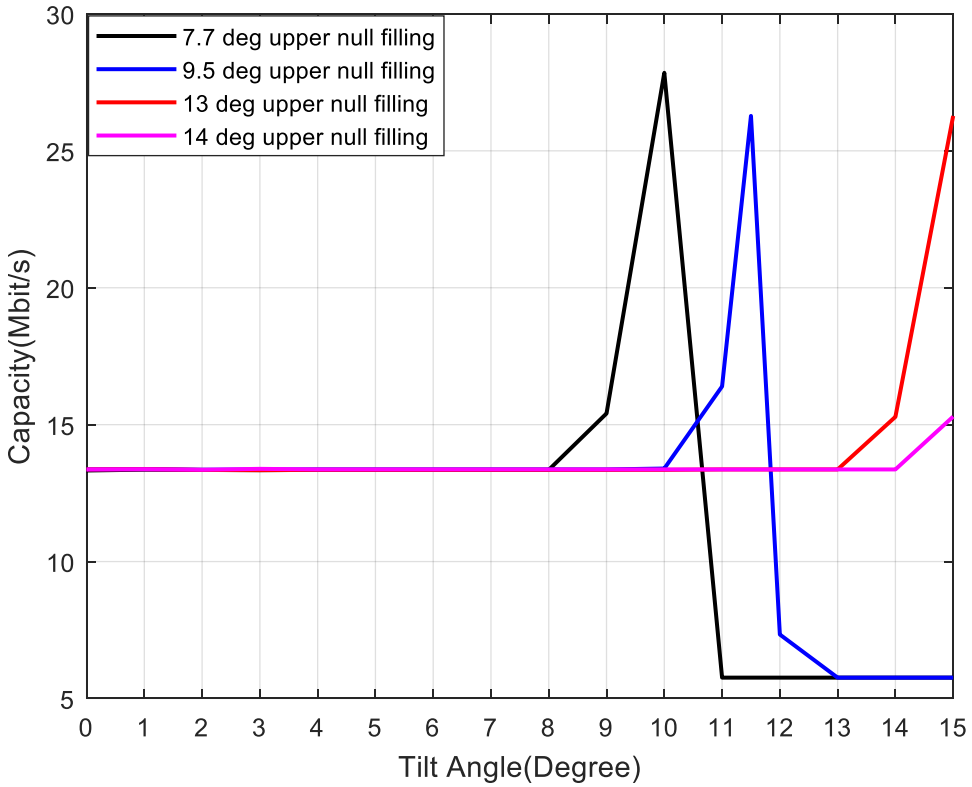

a)

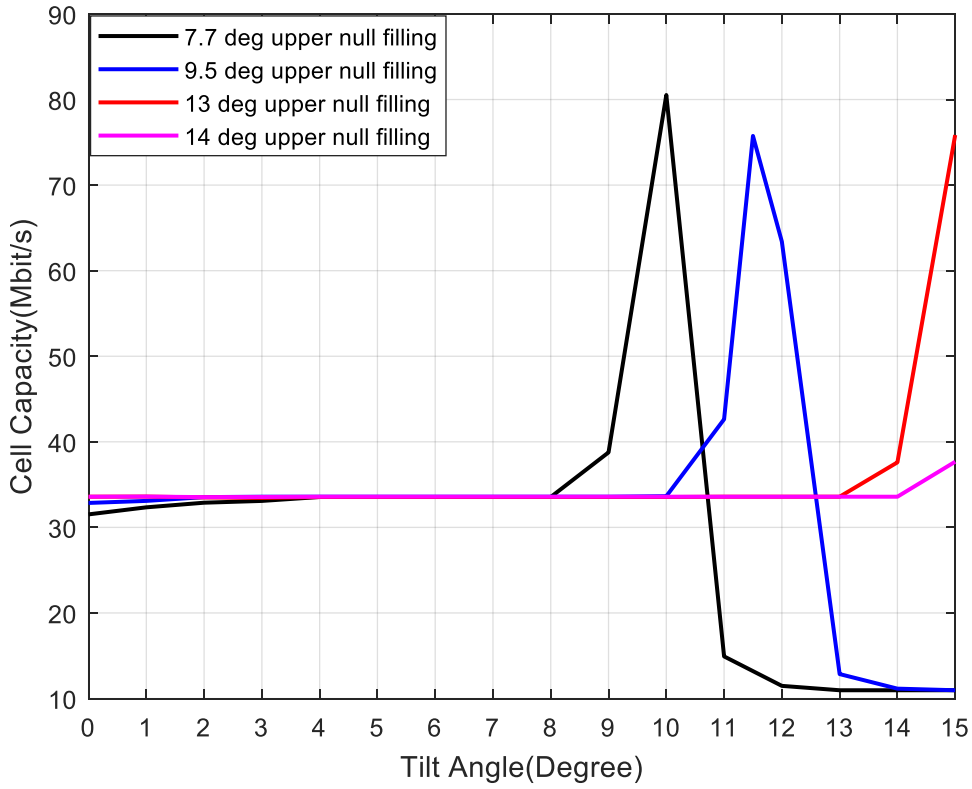

b)

Figure 110: a), b) Cell edge and Cell Capacity for different upper null filling patterns

6.7 Antenna Elevation Beam Shaping Techniques in the original 12-element antenna array pattern

Since the upper side antenna null filling can have impacts on the mobile network performances at high antenna downtilt angles, the proper antenna null filling technique is applied into the original 12-element antenna array elevation pattern. This antenna array shown in Figure 93 is comprised of 12 identical elements with the antenna element spacing of $\lambda/2$ (80mm). By adjusting the power ratios at the outputs along with the length of the cable, the current amplitude and phase of the antenna array is controlled. The original antenna array pattern is achieved by feeding the elements with the currents of equal amplitude and phase. According to the antenna array theory, the nulls occurred at this elevation antenna array pattern can be expressed as follows: [139]

$$\theta = arctan\frac{\pm k}{nd} \tag{6.1}$$

Where k is the number of occurred nulls (1,2…), n is the number of elements and d is the antenna element spacing in wavelength.

The simplest and the most widely-used way to achieve the ideal null-filling elevation shape is by feeding the antenna array elements with unequal amplitude with a suitable power distribution. One of the power distribution methods is called ‘’binominal distribution’’, which is an easy way to feed each antenna element the amplitude proportional to the coefficients of the binominal series.

For an equally spaced antenna array which is symmetrically positioned along the array axis, assuming the array is centred at zero, then the weights applied to the elements at –d and +d are the same. The normalised array factor can be expressed as [141]:

$$(AF)_{2M} = \sum_{n=1}^{M} a_n \cos[(2n-1)u] \;\; for\ even\ number\ elements \tag{6.2}$$

$$(AF)_{2M+1} = \sum_{n=1}^{M+1} a_n \cos[2(n-1)u] \;\; for\ odd\ numer\ elements$$

Here $u = \frac{\pi d}{\lambda} cos\theta$, d is the antenna element spacing and θ is the scanning angle for the array. M represents the antenna elements on one side of the array.

To determine the excitation coefficient of a binomial array, the binomial expansion can be used here as:

$$(1+x)^{n-1} = 1 + (n-1)x + \frac{(n-1)(n-2)}{2!}x^2 + \frac{(n-1)(n-2)(n-3)}{3!}x^3 + \cdots \qquad (6.3)$$

Table 26 shows the current amplitude fed to the antenna array elements by using this method:

Table 26: Comparison between relative amplitude and the number of elements in an array

Number of Elements, N	**Relative Amplitude compared to the Antenna Array**
3	1,2,1
4	1,3,3,1
…	…
12	1,11,55,165,330,462,462,330,165,55,11,1

The shaped elevation beam pattern by using this binominal coefficient fed currents amplitude to the array elements is obtained in Figure 111.

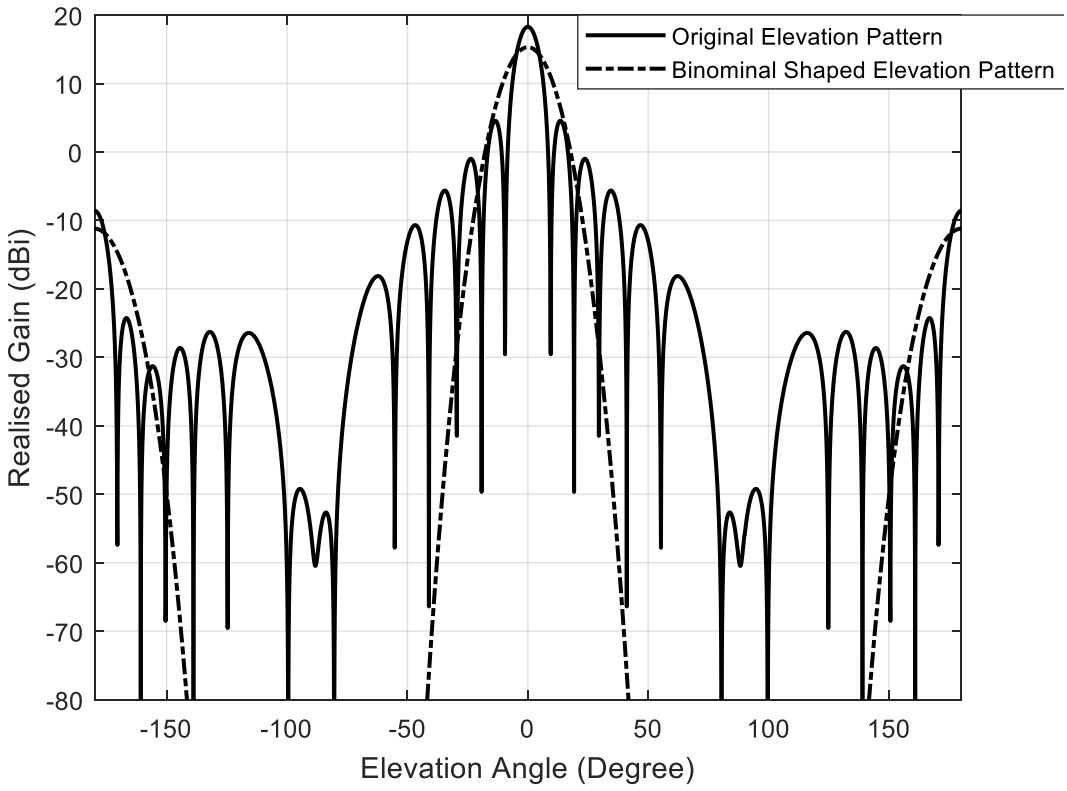

Figure 111: Binominal shaped elevation pattern VS Original elevation pattern

As can be seen from Figure 111, the Binomial amplitude distribution fed array can eliminate the nulls and minor lobes. However, the array beamwidth changes with the compensation of the reduced antenna gain. Also, to feed the large antenna array, it may be difficult to maintain the stability of the different power levels.

The other way to achieve the antenna elevation beam shaping is by using the Dolph-Tschebyscheff distribution. The Dolph-Tschebyscheff excitation coefficients are related to Tschebyscheff polynomials using recursion relation [139] From the normalised array factor shown in equation (6.1), the symmetrical amplitude excitation for the even or odd number array elements should be less than a summation of M or $M+1$ cosine terms. Each term can be written as a series of trigonometric functions, with fundamental frequency as the argument of each one:

$$terms\ of\ m \begin{cases} m = 0,\ \cos(0) = 1 \\ m = 1,\ \cos(u) = \cos(u) \\ m = 2,\ \cos(2u) = 2\cos^2(u) - 1 \\ m = 3, \cos(3u) = 4\cos^3(u) - 3\cos(u) \\ m = 4, \cos(4u) = 8\cos^4(u) - 8\cos^2(u) + 1 \end{cases} \tag{6.4}$$

Based on Euler's formula:

$$[e^{ju}]^m = (cosu + jsinu)^m = \cos(mu) + jsin(mu) \tag{6.5}$$

By equating $cos(u)$ to a new term, z, equation (6.4) can be expressed as Tschebyscheff polynomials ($T_m(z)$). This is outlined in equation (6.6):

$$new\ terms\ of\ m \begin{cases} m = 0, \cos(mu) = 1 = T_o(z) \\ m = 1, \cos(mu) = z = T_1(z) \\ m = 2, \cos(mu) = 2z^2 - 1 = T_2(z) \\ m = 3, \cos(mu) = 4z^3 - 3z = T_3(z) \end{cases} \tag{6.6}$$

The relations between the cosine functions and Tschebyscheff polynomials are valid only in the region $-1 \ll z \ll +1$. Equation (6.7) shows the recursion formula for Tschebyscheff polynomials:

$$T_m(z) = 2zT_{m-1}(z) - T_{m-2}(z) \tag{6.7}$$

An alternative way of expressing the cosine function is:

$$\cos(u) = \frac{z}{z_0} \tag{6.8}$$

Here z_0 is the parameter to control the side lobe levels, as shown in equation (6.9):

$$z_0 = \cosh\left[\frac{cosh^{-1}}{N-1}(R_0)\right] \tag{6.9}$$

Where R_0 is the voltage ratio.

Now, to get the excitation coefficients of the Dolph-Tschebyscheff array of 12 elements with spacing d between the elements and the major to minor lobe ratio is 30 dB. According to the array factor formula shown in equation (6.1), the array factor for the 12 elements antenna array can be expressed as:

$$(AF)_{2M} = \sum_{n=1}^{M=6} a_n \cos\left[(2n-1)u\right] \tag{6.10}$$

Where:

$$u = \frac{\pi d}{\lambda} cos\theta \tag{6.11}$$

Thus, the array factor shown in equation (6.1) can be expanded to form:

$$\begin{aligned}(AF)_{12} = {} & a_1 \cos(u) + a_2 \cos(3u) + a_3 \cos(5u) \\ & + a_4 \cos(7u) + a_5 \cos(9u) + a_6 \cos(11u)\end{aligned} \tag{6.12}$$

From the simulation, it is known that R_0 is equal to 30 dB. The 'true' value of R_0 is therefore equal to $20log_{10}(R_0(dB))$, which is 31.6228. Substituting this into equation (6.9) forms the following expression:

$$z_0 = \cosh\left[\frac{cosh^{-1}}{11}(31.6228)\right] = 1.0719 \tag{6.13}$$

This value for z_0 can itself be put back into equation (6.12), by remembering the expression outlined in equation (6.8). This results in:

$$\begin{aligned}(AF)_{12} = {} & z[(a_1 - 3a_2 + 5a_3 - 7a_4 + 9a_5 - 11a_6)/z_0] \\ & + z^3[(4a_2 - 20a_3 - 56a_4 - 120a_5 + 1124a_6)/{z_0}^3] \\ & + z^5[(16a_3 - 112a_4 + 432a_5 - 1232a_6)/{z_0}^5] \\ & + z^7[(64a_4 - 576a_5 + 2816a_6)/{z_0}^7] \\ & + z^9[(256a_5 - 2816a_6)/{z_0}^9] \\ & + z^{11}[(1024a_6)/{z_0}^{11}]\end{aligned} \tag{6.14}$$

Hence the calculated excitation coefficients are:

$$\begin{cases} a_1 = 8.1641 \\ a_2 = 7.4647 \\ a_3 = 6.2124 \\ a_4 = 4.6528 \\ a_5 = 3.0619 \\ a_6 = 2.1464 \end{cases} \tag{6.15}$$

Since the weights are symmetric, the excitation coefficients for the 12-element antenna array can be summarised as:

$$\begin{cases} a_6 = 2.1464 \\ a_5 = 3.0619 \\ a_4 = 4.6528 \\ a_3 = 6.2124 \\ a_2 = 7.4647 \\ a_1 = 8.1641 \\ a_{-1} = 8.1641 \\ a_{-2} = 7.4647 \\ a_{-3} = 6.2124 \\ a_{-4} = 4.6528 \\ a_{-5} = 3.0619 \\ a_{-6} = 2.1464 \end{cases} \tag{6.16}$$

As can be seen from Figure 112, by using the Chebychev Polynomial weights to feed the 12-element antenna array, the antenna sidelobe level can be controlled with respect to the antenna main lobe level. Dolph-Tschebyscheff designs can be used to achieve the same level of all minor lobes while keeping the antenna element spacing as large as possible.

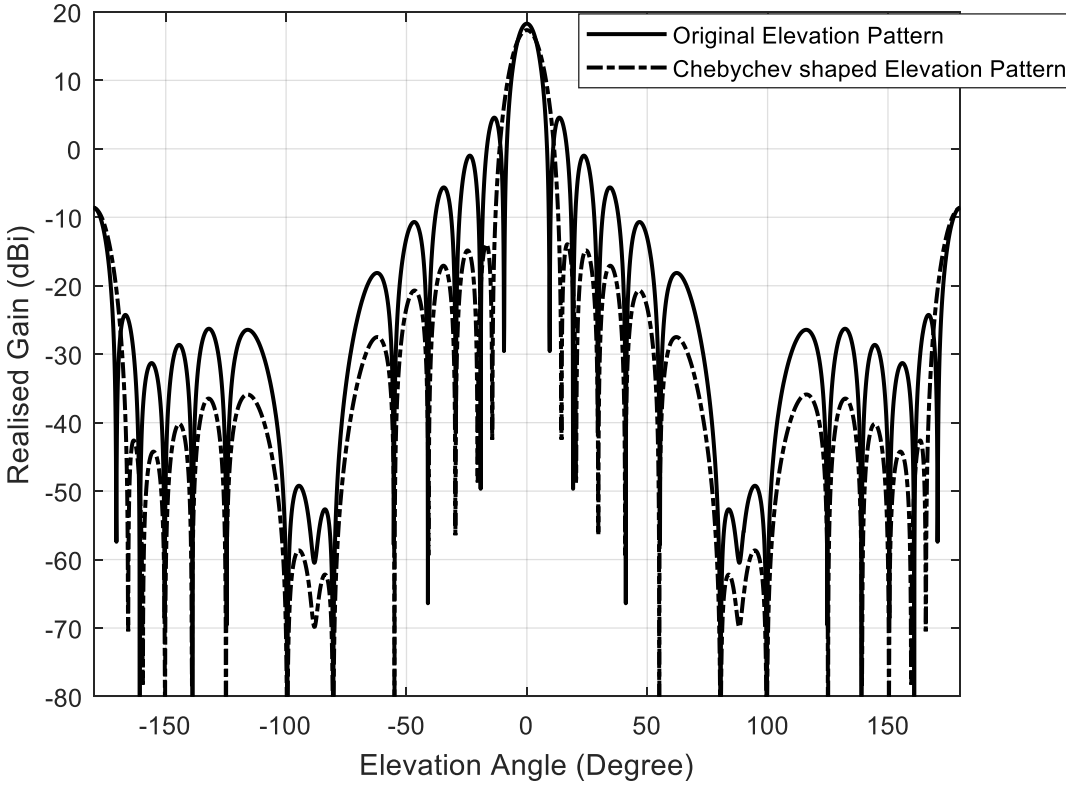

Figure 112: Chebychev shaped elevation pattern VS Original elevation pattern

6.8 Using Taylor Beam Synthesis to achieve the first upper-side null filling without compensating the antenna gain loss.

As demonstrated in Binomial and Chebychev weighting methods, the antenna beam pattern can be shaped either in reducing sidelobe levels or controlling minor lobes. Here, in order to overcome the disadvantages of antenna gain loss by using the other two techniques, Taylor Beam Synthesis is applied here by feeding the antenna elements with a suitable amplitude and phase distribution.

For a line-source distribution of length l, which has been placed symmetrically along the array z-axis, the space factor (SF) can be given by [141]:

$$SF(\theta) = \int_{-l/2}^{l/2} I_n(z') e^{j[kz' cos\theta + \varphi_n(z')]} dz' \tag{6.17}$$

Where $I_n(z')$ and $\varphi_n(z')$ represent amplitude and phase distribution along the source. According to the Taylor space factor function:

$$SF(u, A, \bar{n}) = \left(\frac{\sin(u)}{u}\right)\left(\prod_{n=1}^{\bar{n}-1}\left[1 - \left(\frac{u}{u_n}\right)^2\right] \Big/ \prod_{n=1}^{\bar{n}-1}\left[1 - \left(\frac{u}{n\pi}\right)^2\right] \right) \tag{6.18}$$

Where:

$$u = \pi v = \pi \frac{l}{\lambda} cos\theta \tag{6.19}$$

$$u_n = \pi v_n = \pi \frac{l}{\lambda} cos\theta_n \tag{6.20}$$

Here θ_n represents the locations of the nulls. $\bar{n}$ is a constant to maintain the minor lobes at a constant voltage level of $\left(1/R_0\right)$.

The scaling factor σ is introduced to provide a smooth transition between the inner nulls and outer nulls. It is defined as:

$$\sigma = \frac{\bar{n}}{\sqrt{A^2 + (\bar{n} - \frac{1}{2})^2}} \tag{6.21}$$

The location of the nulls can be identified using equation (6.22):

$$u_n = \pi v_n = \pi \frac{l}{\lambda} cos\theta_n = \begin{Bmatrix} \pm\pi\sigma\sqrt{A^2 + (n - \frac{1}{2})^2} & (1 \le n < \bar{n}) \\ \pm n\pi & (\bar{n} \le n \le \infty) \end{Bmatrix} \tag{6.22}$$

The normalised line-source distribution can be expressed in Fourier series as:

$$I(z') = \frac{\lambda}{l}\left[1 + 2\sum_{p=1}^{\bar{n}-1} SF(p, A, \bar{n}) \cos\left(2\pi p \frac{z'}{l}\right)\right] \tag{6.23}$$

The coefficients $SF(p, A, \bar{n})$ are the samples of the Taylor pattern. By substituting $u = \pi p$, they can be expressed as:

$$SF(p, A. \bar{n}) = \begin{Bmatrix} \frac{[(\bar{n}-1)!]^2}{(\bar{n}-1+p)!(\bar{n}-1-p)!} \prod_{m=1}^{\bar{n}-1}\left[1 - \left(\frac{\pi p}{u_m}\right)^2\right] & (|p| < \bar{n}) \\ 0 & (|p| \ge \bar{n}) \end{Bmatrix} \tag{6.24}$$

Where $SF(-p, A, \bar{n}) = SF(p, A, \bar{n})$.

Since the constant A is related to the maximum sidelobe level, the voltage ratio R_0 can be set as:

$$\cosh(\pi A) = R_0 \tag{6.25}$$

Here, the sidelobe level to main lobe is chosen as 9dB. In order to fill the first upper-side null to 0dB, a sine distribution form of the phase is applied for the elements in the array. By calculating the amplitude weights, the distribution of amplitude for the antenna elements in the array is given by:

$$I(n) = 1.251 + 0.2446\cos(0.4813n) - 0.157\sin(0.4813n \tag{6.26}$$

The sine distribution of the phase for the elements in the array to fill up the first upper-side null is given by:

$$\varphi_n = 7.897\sin(0.4308n - 1.571) \tag{6.27}$$

Figure 113 shows the final resulted excitation amplitude coefficients and phase coefficients for the 12-element antenna array by using the introduced Taylor Beam Synthesis to fill the first upper-side null up to 0dB.

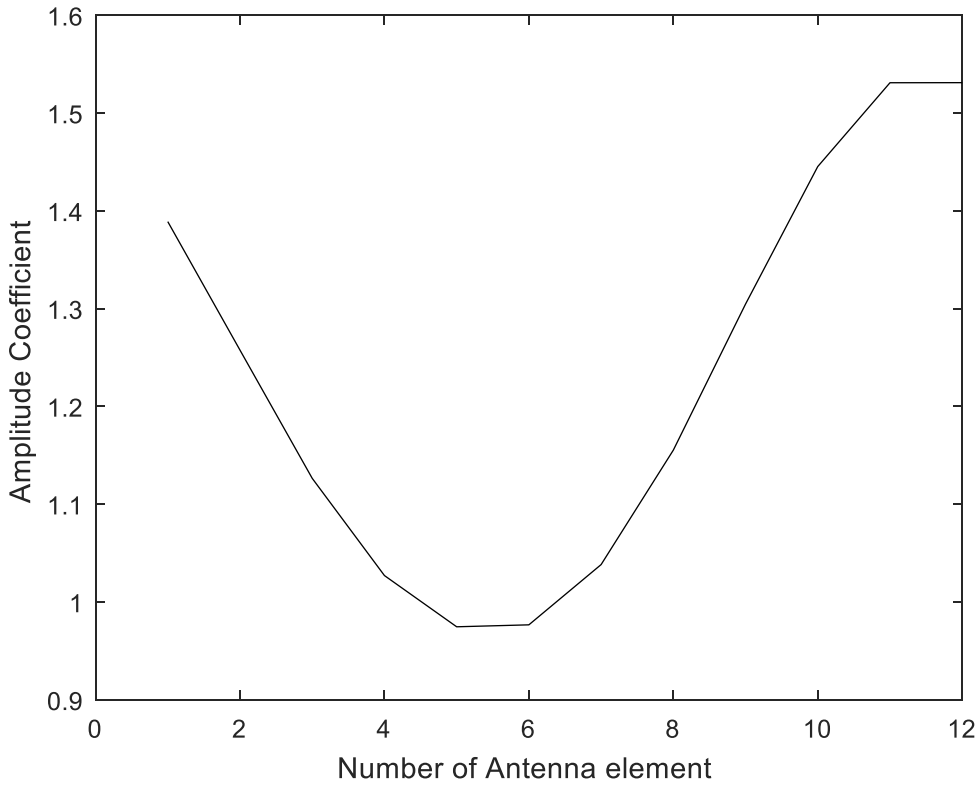

a)

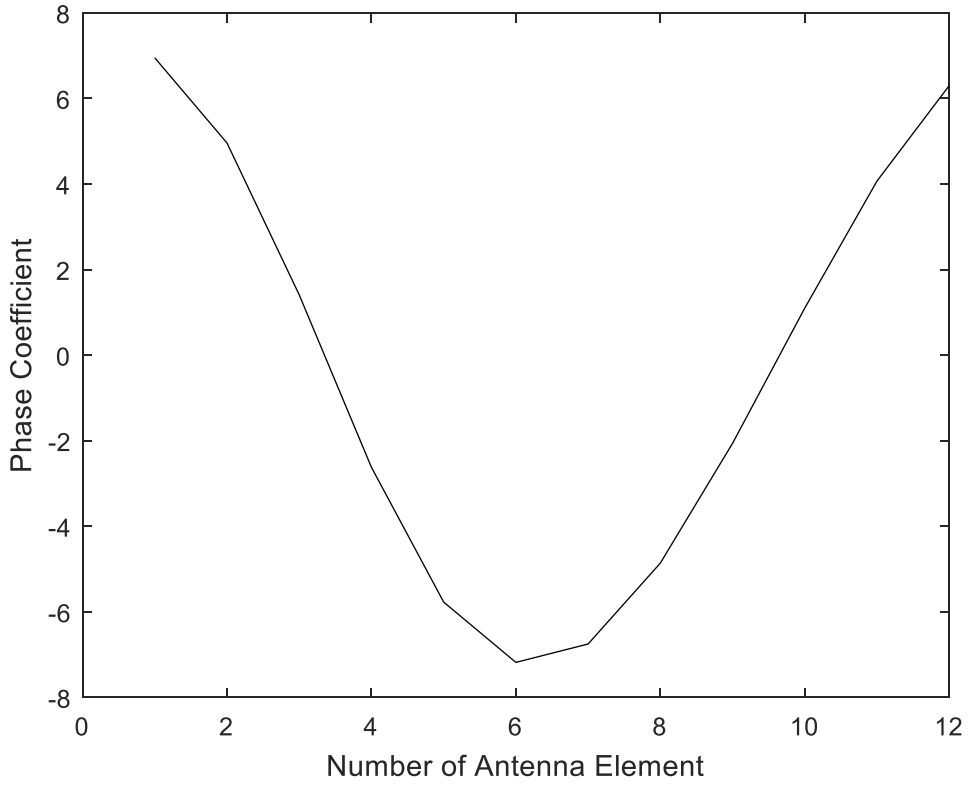

b)

Figure 113: a) Amplitude distribution b) Phase distribution VS Antenna Elements

Now, by specifying the relative sidelobe level to main lobe to 9dB, the first upper-side null can be filled up to 0dB, 3dB, 6dB and 9dB respectively. The antenna element spacing is half-wavelength 80mm. Through using the Taylor beam synthesis for feeding the corresponding amplitude and phase coefficients to the antenna elements in the array, the first upper-side null filling pattern can be obtained as shown in Figure 114.

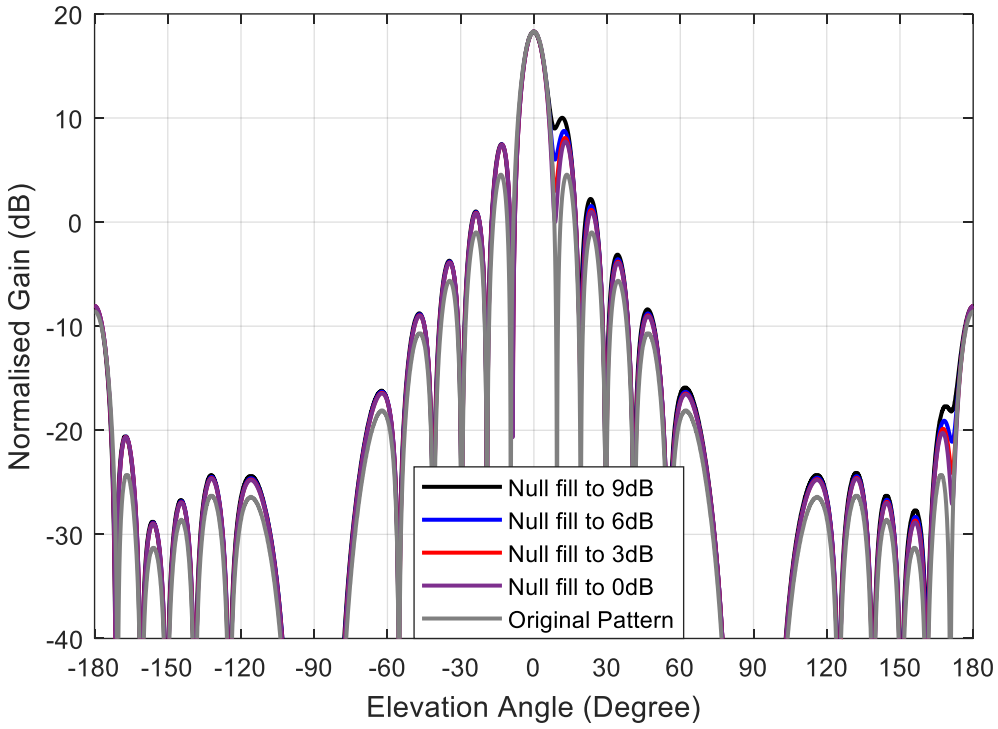

Figure 114: Upper-side null filling patterns VS original elevation pattern

As can be seen from Figure 114 that, through using the Taylor Beam Synthesis, the upper-side first null is filled to 0dB, 3dB, 6dB and 9dB respectively without compensating the antenna gain.

Now, in order to verify the first upper-side null effects on the mobile network performances at high antenna downtilt angles, the resultant elevation pattern is applied into an ISD of 500m homogenous network. The edge and cell capacity for the 12-element antenna array with different upper-side null filling elevation patterns on the 60° azimuth cellular network is shown in Figure 115.

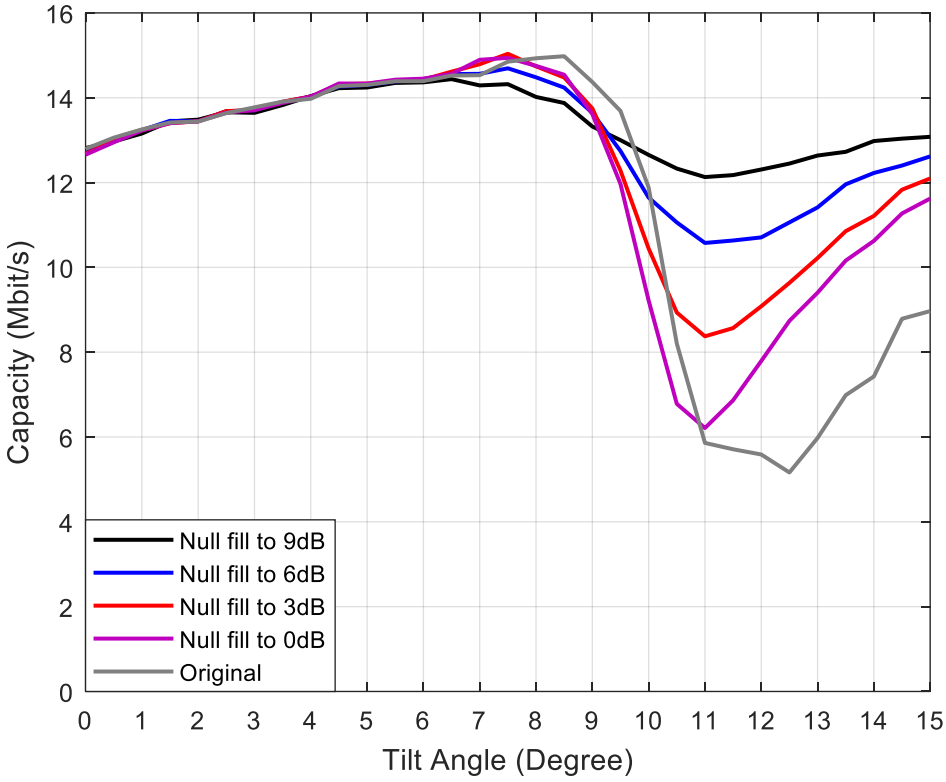

a)

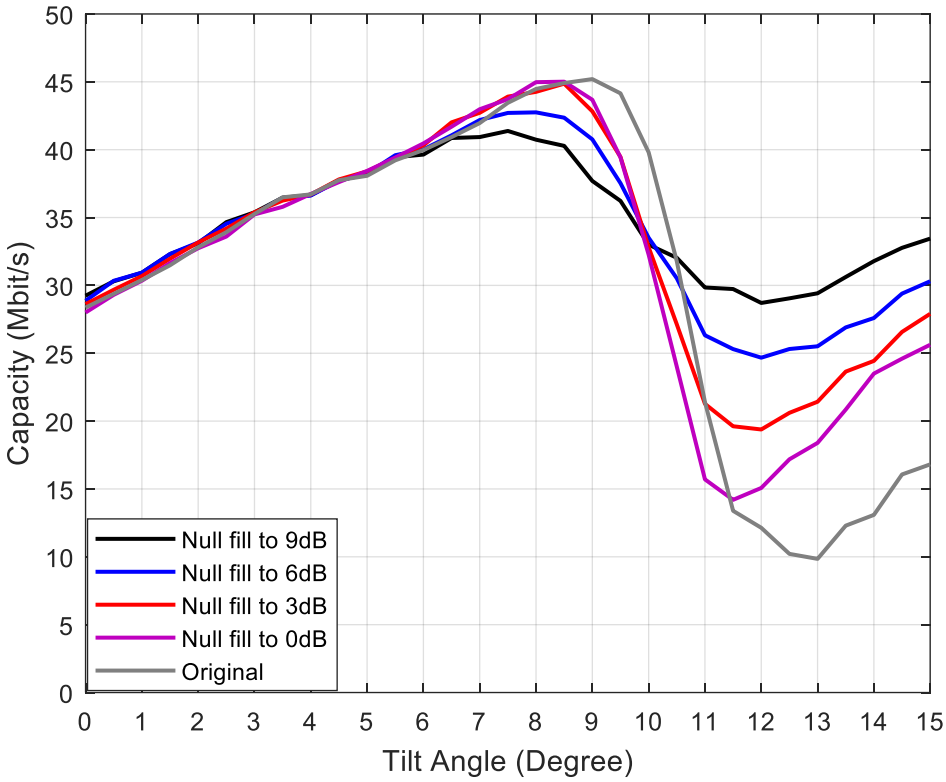

b)

Figure 115: a), b) Edge and cell capacity for different upper-side null filling patterns

It can be seen from Figure 115 that, with the increasing first upper-side null filling levels from 0dB to 9dB, the edge and cell capacity for the 60° azimuth cellular network is improved at high antenna downtilt angles as well. Also when the first upper-side null filling level is increased to 9dB, the edge and cell capacity can be improved by 7Mbit/s and 20Mbit/s respectively at antenna downtilt angle of 13° compared with the original elevation beam pattern. However, there is a trade-off between the network performance improvement at high antenna downtilt angles and the peak network performance at antenna optimum downtilt angle. With the first upper-side null filling level increasing, the network performances at high antenna downtilt angles increase too, while the peak network performances at optimum antenna downtilt angle decreases.

So, by choosing the proper first upper-side null filling levels, the cellular network performances in terms of edge and cell capacity at high antenna downtilt angles can be improved without sacrificing too much peak capacity at optimum antenna downtilt angle.

6.9 Application of Antenna first upper-side null filling pattern in the mobile cellular network

Since antenna beamtilt is an efficient way to tackle the interference at the cell edge and boost the radio links near the basestation, the setting of the beamtilt angle with the first upper-side null filling pattern has been evaluated in a 3-sector for ISD of 500m homogeneous cellular network. As it is discovered that there is a trade-off between the network performances improvement at high tilt angle and the reduction at the optimum tilt angle with the different first upper-side null filling levels. In order to evaluate the system performances in terms of edge and cell capacity in a fair way, the first upper-side null filling level to 6dB pattern is used in this application.

In this case, the 60° azimuth beamwidth and the first upper-side null filling to 6dB elevation pattern is applied into the cellular mobile network. Instead of setting the variable antenna downtilt angles from 0° to 15° for all the cells in the mobile system, here, the variable antenna downtilt angle is only applied into the central cell in the system and keep the other cells in the system the optimum downtilt angle which is 8° by using the first upper-side null filling to 6 dB pattern (shown in Figure 115) in this scenario. The edge and cell capacity for this scenario is then evaluated. This scenario is mainly targeted at optimising the cell/cluster

with the bad network performances which means the quality of service is below network average or the traffic demanding is high in this particular cell/cluster.

In order to achieve the network performances for this scenario, the system parameters shown in Chapter 3 Table 24 is applied into the ISD of 500m homogeneous cellular network simulator. The detailed cell edge detection for the central cell and the surrounding 6 cells at different downtilt angles for the central cell only is shown in Figure 116. The evaluated edge and cell capacity for the first tier cells in this mobile network is shown in Figure 35.

6.9.1 Step 1: Cell edge detection

Comparisons between the edge and cell capacity of the central cell and surrounding 6 cells in the first tier of the mobile network for the varied antenna downtilt angles is possible by using a cell edge detection technique to analyse the cell edge of the central cell and the surrounding 6 cells. As shown in Figure 116, it shows the detected cell edge in the first tier of the network for the antenna downtilt angle of 0°, 6° and 12° on the central cell only and other cells keep the optimum downtilt angle of 8° here.

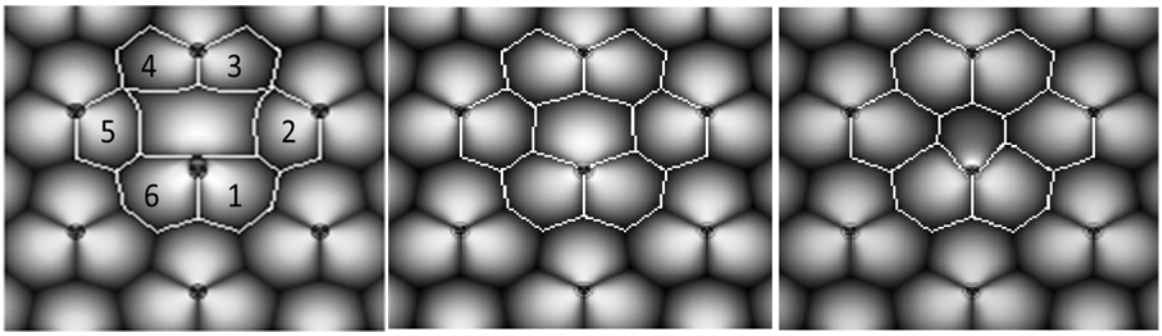

Figure 116: Cell edge detection for tilt angle of 0°, 6°, and 12° of 60° azimuth beamwidth case for ISD of 500m network

6.9.2 Step 2: Cell edge and cell capacity for central cell and surrounding 6 cells

After detecting the edge of the cells in the first network tier (as per Step 1), the cell edge and cell capacity for the downtilt angles of the central cell from 0° to 15° are calculated while the remaining cells are kept at the optimum tilt angle of 8° in the whole process. To evaluate the effect of different elevation beam pattern of the 60° azimuth antenna array on edge and cell

capacity for an ISD of 500m homogeneous mobile network, the parameters used to analysis the system performances are shown in Table 24.

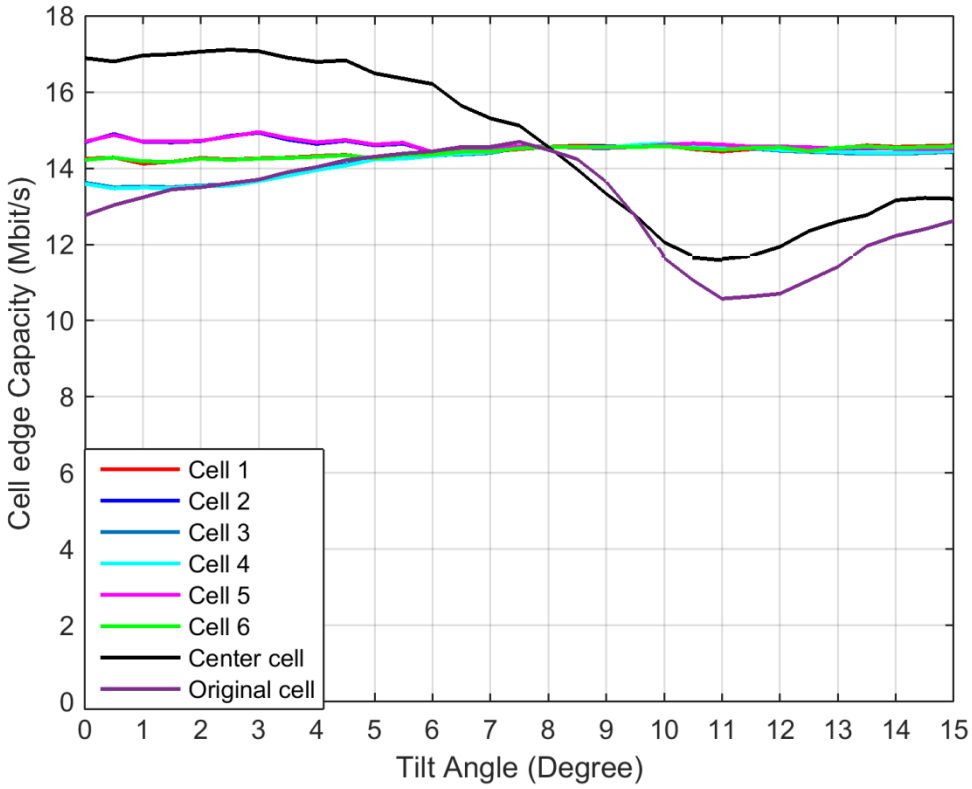

a)

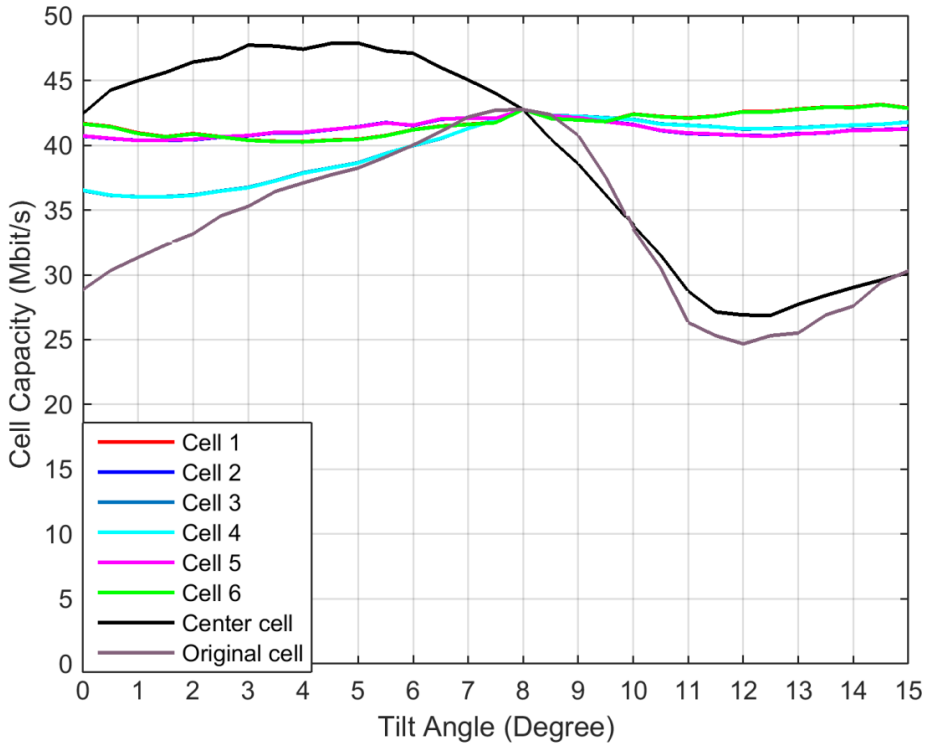

b)

Figure 117: a), b) Cell edge and Cell capacity VS Tilt angle for first upper-side null filling to 6dB pattern

Figure 117shows the comparison of cell edge and cell capacity of central cell and surrounding 6 cells for antenna downtilt angle from 0° to 15° on the all cells and central cell only by applying the first upper-side null filling up to 6dB elevation pattern. It shows that keeping the surrounding 6 cells at optimum downtilt angle of 8° while changing the downtilt angle of central cell from 0° to 15°, the edge and cell capacity of the central cell can be improved up to 12% compared with the antenna downtilt angle variation applied to all cells in the network. Since the symmetrical properties of the surrounding 6 cells, cell 1 and cell 6, cell 2 and cell5, cell 3 and cell 4 have the similar performances.

With antenna tilt angle changes on the central cell only, the surrounding 6 cells' capacity shows the trend of slightly decreasing compared with optimum performance at downtilt angle of 8°. Thus, there is a trade-off between gained cell capacity in central cell and slightly dropped cell capacity in the remaining 6 cells when we change the downtilt angle of central cell only and keep downtilt angle of the remaining cells fixed in the network. However, it is worth mentioning that with the beamtilt setting applied for the specific cell only rather than the whole cells in the system is good for optimising the single cell performance with bad

network quality while without sacrificing too much service quality in the other cells if the optimum tilt angle setting is used for the other cells in the network.

6.9.3 Step 3: Statistical Results for cell edge and cell capacity for the cells in the first tier

In this part, the statistical results show the edge and cell capacity of central cell and surrounding 6 cells in the mobile network compared to the optimum capacity with the antenna downtilt angle of 8° applied to all cells in the mobile network.

Figure 118 to Figure 128 below summarise the edge and cell capacity difference between scenario of applying beamtilt setting for central cell only while keeping the remaining 6 cells the fixed optimum tilt angle of 8° and scenario of beamtilt setting applied to all cells in the mobile network. It is useful information for the operators to adjust the antenna beamtilt properly for the specific cell in order to optimise its performances while without jeopardising the performances of others cells close to it. Table 27 compares the results between two scenarios, to show the effect of the antenna beamtilt on the system performance:

- Scenario 1: Beamtilt setting applied only for the central cell (other cells kept at optimum tilt angle of 8°).
- Scenario 2: Beamtilt setting applied for all cells

Table 27: Statistical results for Edge and cell capacity difference between the two different scenarios for tilt of 7.5° applied to centre cell in Scenario 1.

Tilt angle: 8°	**Cell Edge Capacity (Mbit/s)**	**Cell Capacity (Mbit/s)**	**Cell edge Difference compared with Scenario 2 (%)**	**Cell Difference compared with Scenario 2 (%)**
All cells for Scenario 2	14.56	42.75	n/a	n/a
Tilt angle: 7.5° Centre Cell only for Scenario 1	**Cell Edge Capacity (Mbit/s)**	**Cell Capacity (Mbit/s)**	**Cell edge Difference compared with Scenario 2 (%)**	**Cell Difference compared with Scenario 2 (%)**
Cell 1:	14.50	41.76	-0.41	-2.32
Cell 2:	14.55	42.06	-0.07	-1.61
Cell 3:	14.54	42	-0.14	-1.75
Cell 4:	14.55	41.96	-0.07	-1.85
Cell 5:	14.58	42.08	0.14	-1.57
Cell 6:	14.52	41.74	-0.27	-2.36
Average of 6 cells:	14.54	41.93	-0.14	-1.91
Centre Cell:	15.12	44	3.85	2.92

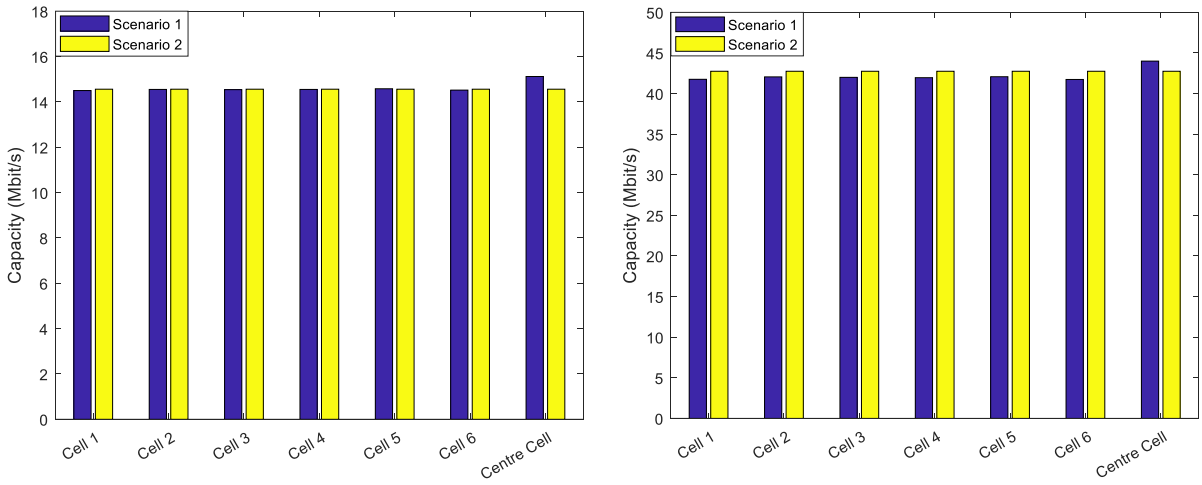

b)

Figure 118: a) cell edge and b) cell capacity for tilt angle of 7.5° at the centre cell only

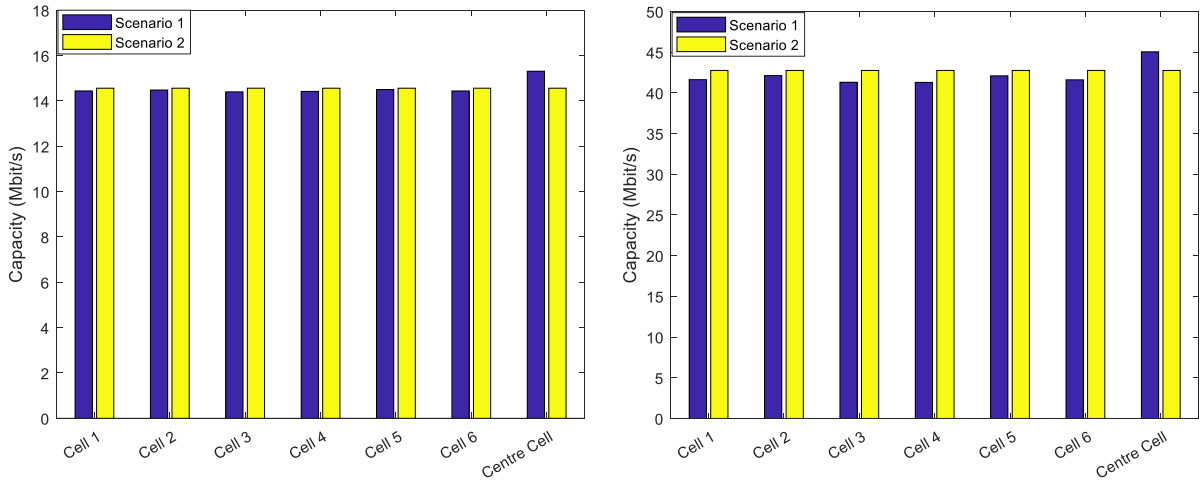

a) b)

Figure 119: a) cell edge and b) cell capacity for tilt angle of 7° at the centre cell only

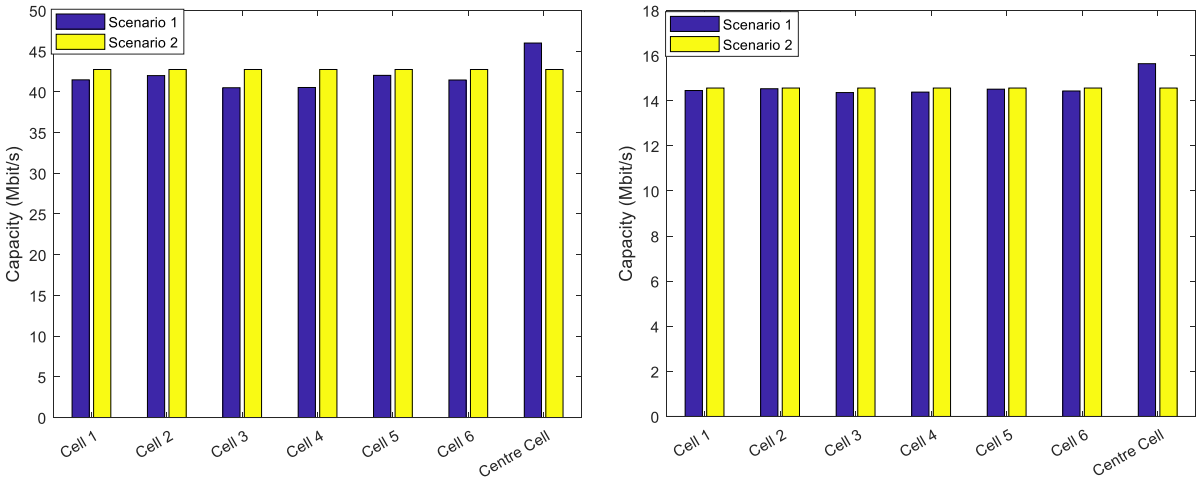

a) b)

Figure 120: a) cell edge and b) cell capacity for tilt angle of 6.5° at the centre cell only

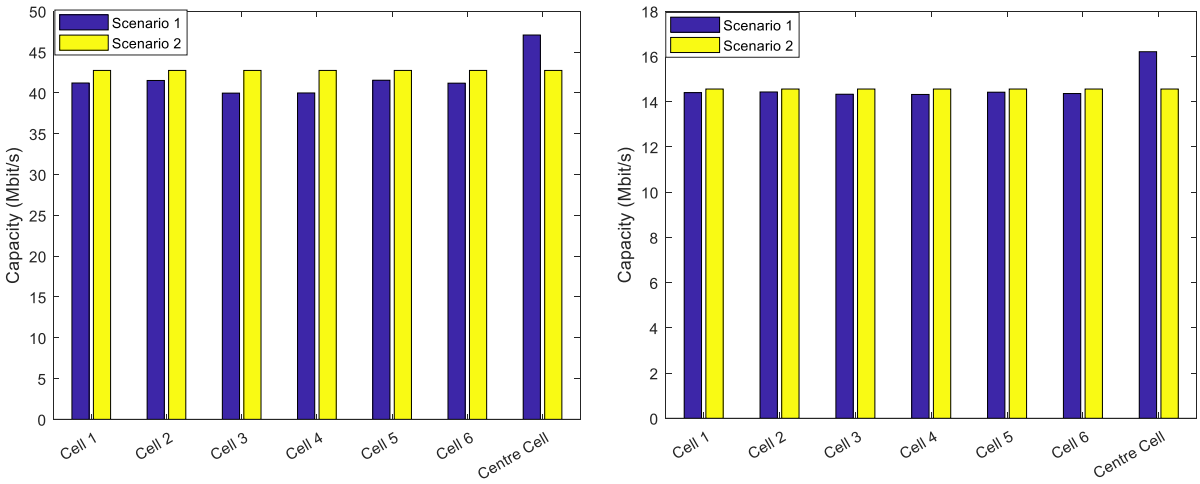

a) b)

Figure 121: a) cell edge and b) cell capacity for tilt angle of 6° at the centre cell only

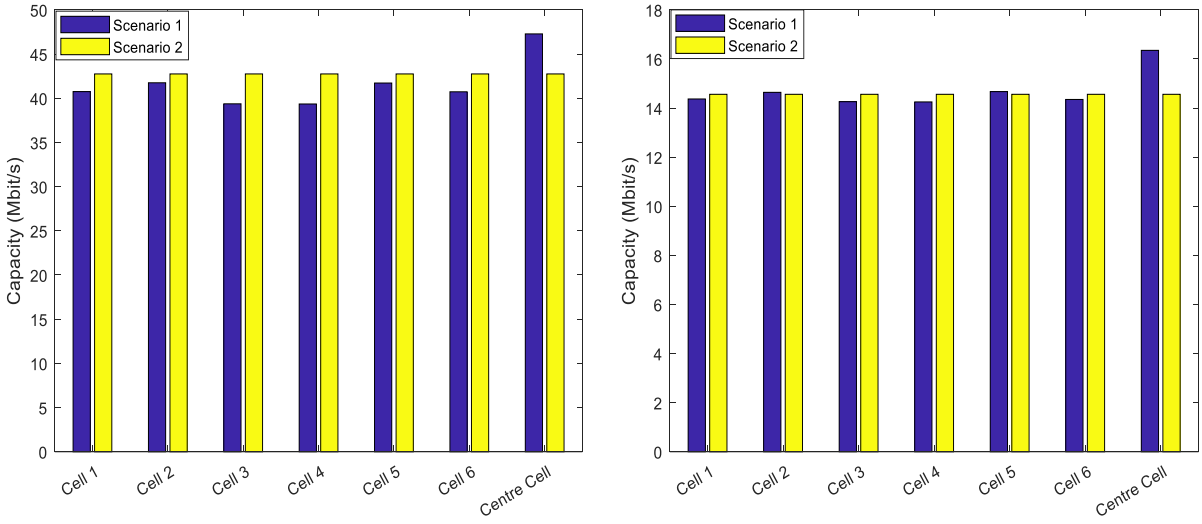

a) b)

Figure 122: a) cell edge and b) cell capacity for tilt angle of 5.5° at the centre cell only

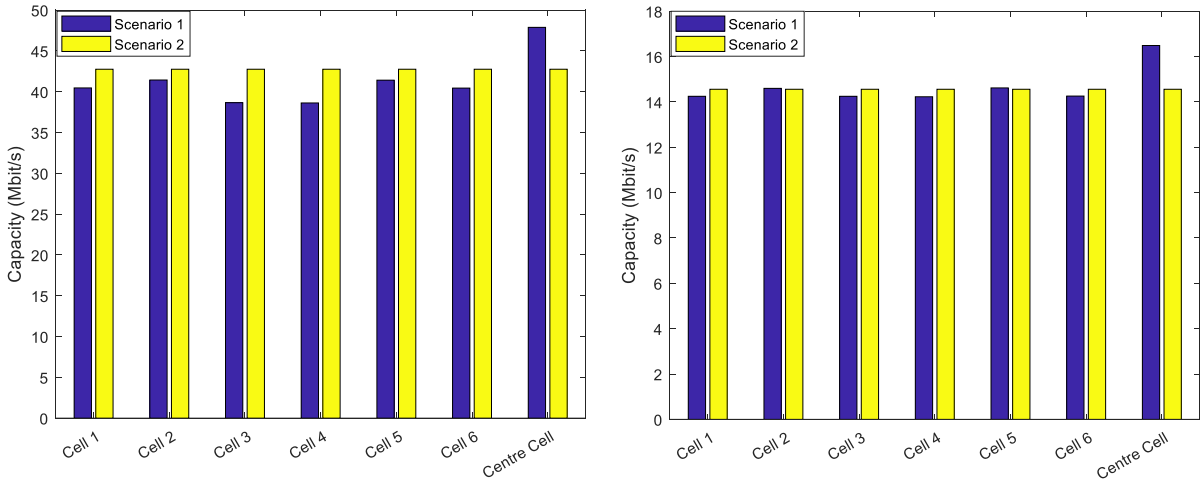

a) b)

Figure 123: a) cell edge and b) cell capacity for tilt angle of 5° at the centre cell only

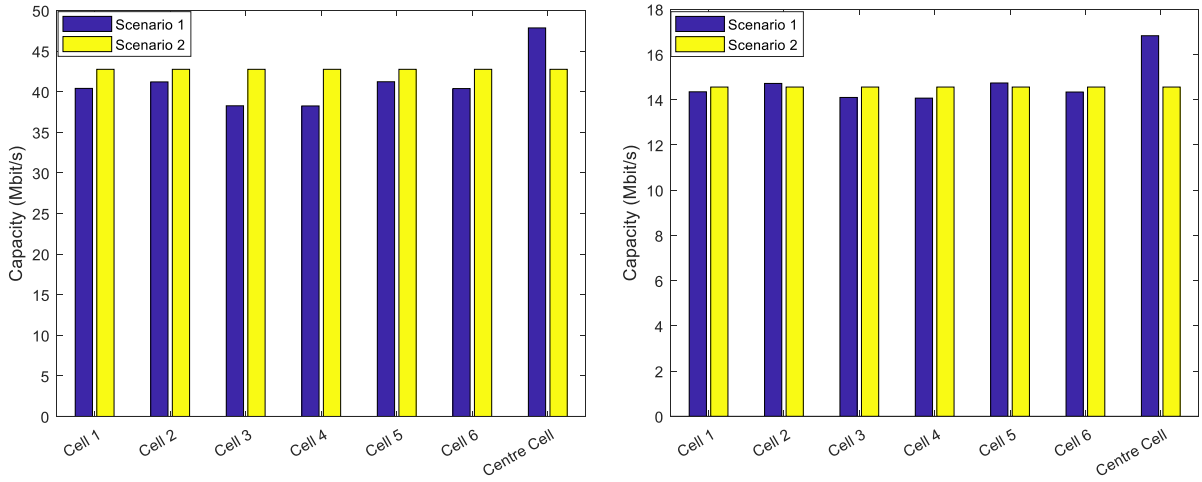

a) b)

Figure 124: a) cell edge and b) cell capacity for tilt angle of 4.5° at the centre cell only

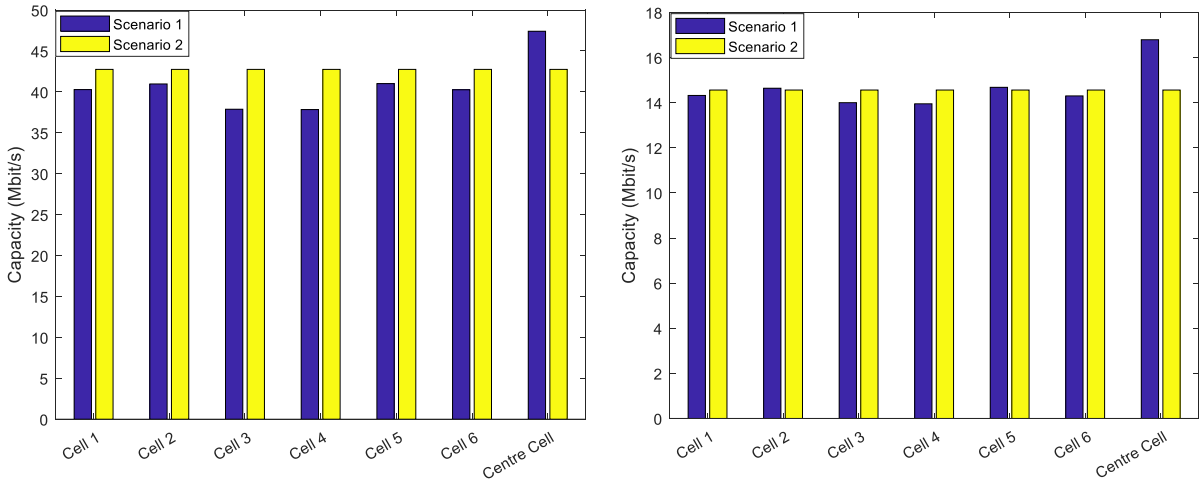

a) b)

Figure 125: a) cell edge and b) cell capacity for tilt angle of 4° at the centre cell only

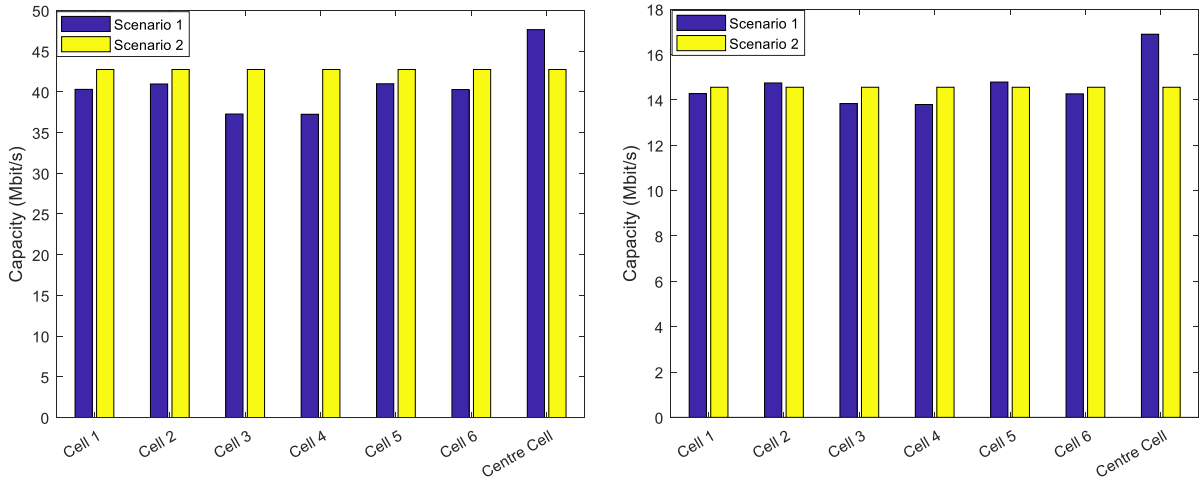

a) b)

Figure 126: a) cell edge and b) cell capacity for tilt angle of 3.5° at the centre cell only

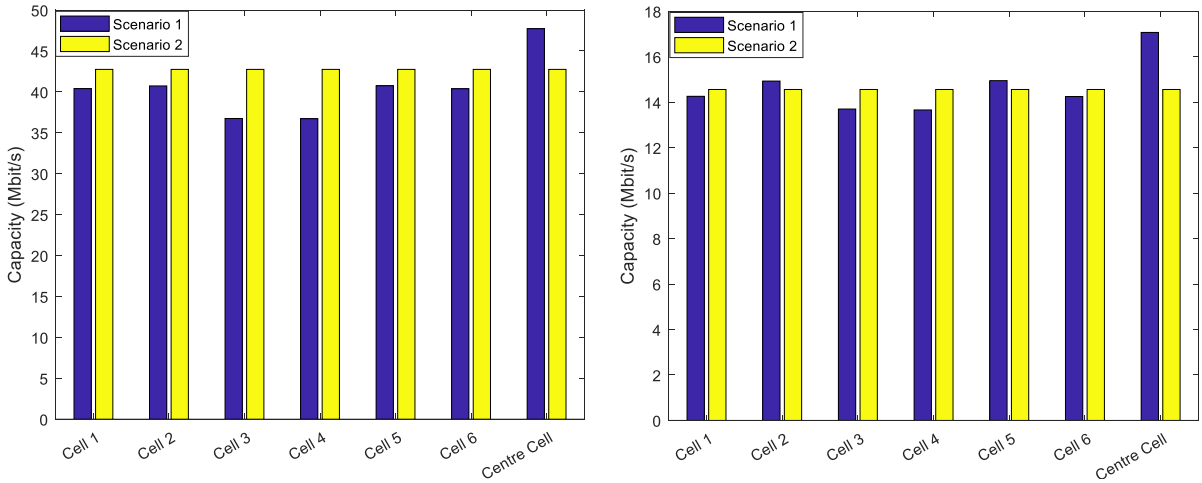

a) b)

Figure 127: a) cell edge and b) cell capacity for tilt angle of 3° at the centre cell only

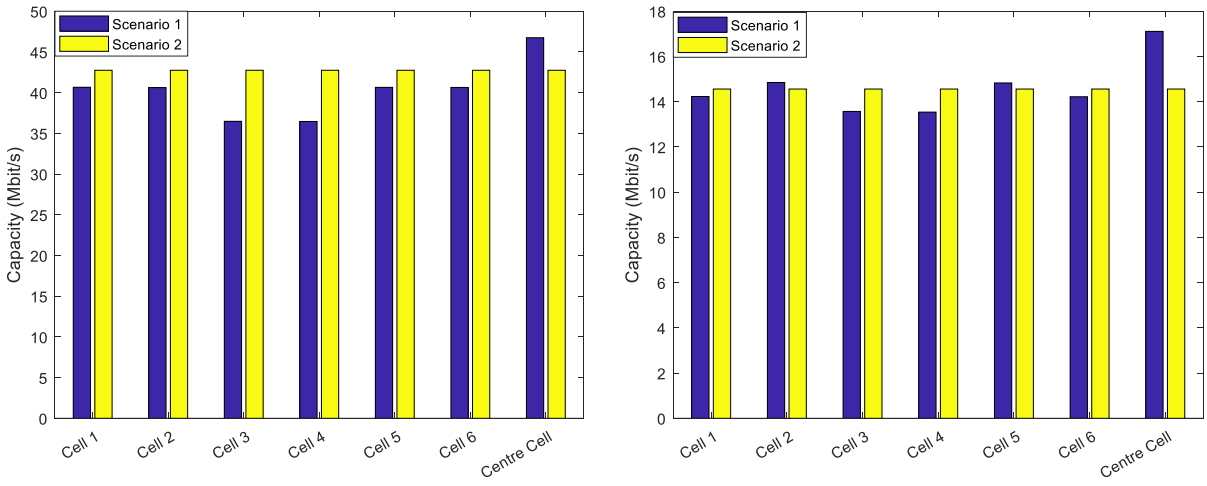

a) b)

Figure 128: a) cell edge and b) cell capacity for tilt angle of 2.5° at the centre cell only

As can be seen from the above statistical results, with the beamtilt setting applied onto the specific cell, the edge and cell capacity for this cell can be improved by around 3% to over 17%, while the other cells nearby can have a capacity drop from around 0.15% to 8%. The other detailed statistical results for the different antenna downtilt angle applied to the centre cell in Scenario 2 can be found in Appendix. So, for optimising the one chosen cell, the beamtilt adjusting can be used here based on the above summarised capacity for the cells in the mobile network.

6.9.4 Discussion

As described in the previous session, by tilting the antenna beam in the elevation plane for the one specific cell/cluster while keeping the other surrounding cells' beamtilt unchanged can help improve the selected cell's network capacity and without sacrificing other cells' performances too much.

One possible scenario in urban region is when one of the cells is detected to have low capacity value which is below network average and the other cells have a reasonable QoS for mobile users in it. It is useful to only vary the problematic cell's beam and maintain the other cells' beam tilt angle at their optimum. In this way, the chosen cell's performance can be improved depending on the selected downtilt angle and other cells' performance can be maintained as well.

The other scenario which can be useful for using the antenna beam tilt technique to optimise the network performance is for rural region. When one cell is detected to be an overshooting cell (usually located at the top of the mountain, line of sight propagation) for the other cells and causes sever interference to other cells, by tilting down this cell's antenna beam at a proper angle, it can improve the other cells' performances and as a result enhance the overall network performances.

6.10 Summary

In this chapter, we investigate the different elevation beam shaping techniques for improving the edge and cell capacity at high antenna downtilt angles. It is found that the nulls at the antenna elevation beam pattern cause the network performance deterioration. Thus, the antenna null filling technique is used here to solve this problem and the technique is based on the Taylor Beam Synthesis. After applying the first upper-side null filling pattern into the mobile network, the edge and cell capacity at high antenna downtilt angles can be improved. In order to apply this null filled elevation beam pattern into the mobile network, a new scenario with applying beamtilt setting for the particular cell only while keeping the other cell' tilt fixed is considered here. As for this scenario, it is good at optimising the particular cell which has bad network service quality by using the beamtilt. And by comparing the edge and cell capacity performance with the scenario which applying the beamtilt for all cells in the mobile network, the operators can now adjust its beamtilt setting based on the information summarised in the statistical results.

This page is intentionally blank.

Chapter 7. Conclusion and Future Work

7.1 Summary

This research has set out a concept for employing a novel pattern-reconfigurable antenna at the basestation for current and future mobile network to provide improved QoS and increased performance at the cell edge when switching the antenna azimuth from narrow one to wider one. Reconfigurable antennas have been widely proposed by both academia and industry and applied for wireless mobile communication in terms of its flexibility and configurability in changing the antenna characteristics such as frequency, radiation pattern and polarisation. Due to these advantages, it has been widely used in Cognitive Radio System, Multiple Input Multiple Output (MIMO) Communication System, Cellular and Personal Communication Systems, Interference Rejection and Wireless Network Security. In today's and future mobile network, due to the highly inhomogeneous distribution of mobile traffic in the geographical coverage of the cell, users can be served at different service level, some users can have good network experience, while others can have bad network service. So, here a novel pattern-reconfigurable antenna has been proposed, designed and tested which can switch its azimuth beamwidth from narrow one to wider one for dynamic azimuth planning. Turing into the basestation antenna, antenna downtilt is the possible way to help mobile network planning needs as well. With the help of a sophisticated self-organising network platform, antenna downtilt can be used to tackle the interference at the cell edge and boost the radio links near the basestation. Thus, combined with the antenna azimuth, antenna downtilt is chosen as the other parameter to help improve the network performances.

As shown in Chapter 3, one application for this pattern-reconfigurable antenna is where users may be distributed towards the edges of the cell. In this situation, the users can suffer lower capacity than the average which may lead to call access failures, drop calls or low throughput. Now, the principle behind the antenna concept in this situation is to instantaneously switch the beamwidth of the basestation to a wider beamwidth. Then these parts of users who located in the same physical location can have higher capacity. Using this concept, the network providers could then choose whether to offer maximum average capacity or improved edge capacity. Since, the pattern-reconfigurable antenna can switch its azimuth from narrow one to wide one, the optimum azimuth to achieve the best network performance regarding to coverage is discussed in Chapter 3 which shows that the 60° azimuth beamwidth can have the best coverage compared to the azimuth of 75°, 90° and 110° in an interference

limited homogeneous network. Also, it has been discovered that when switching the antenna azimuth from 60° to wide 110°, the cell edge performance of 60° azimuth cell can be enhanced most. Based on this result, the pattern-reconfigurable antenna is designed to switch from narrow 60° to wide 110°.

In Chapter 3, in order to test the edge performance by switching the antenna azimuth beamwidth instantaneously, the effects of antenna downtilt (from 0° to 15°) on cell coverage and capacity are also investigated with different ISDs (from 500m to 1500m). It shows that for different cell sizes and different ISDs, the instantaneous cell edge and cell capacity have a similar trend in that switching the beamwidth in this way increases the cell edge capacity but decreases the average cell capacity. It also shows that with the tilt angle of antenna increases, the cell performances of the mobile network can be improved up to an optimum tilt angle of 9°, at which point the cell performances quickly worsen. The design details for this pattern-reconfigurable antenna is shown in Chapter 4. Based on the reflector antenna concept, the radiation pattern reconfigurability of this antenna can be achieved by altering the PIN diodes states. Through changing the current distribution on the antenna surface, the radiation pattern in the azimuth plane can be changed as well. In order to match the antenna gain of industrial standard, a 12-element antenna array is used here to examine the scenario mentioned in Chapter 3. Also, to verify the performance of this pattern-reconfigurable antenna in terms of return loss and radiation pattern, two prototypes of single pattern-reconfigurable antenna which can switch its azimuth from 60° to 110° or 90º are manufactured and tested in an anechoic chamber. It shows that the measured results of this single pattern-reconfigurable antenna is matched well with the simulated ones.

From Chapter 3, it is not difficult to find that at large antenna downtilt angles beyond 10° tilt, the overall network coverage performance can be deteriorated significantly. So, with the expense of cell radius, additional basestation investments maybe needed in this service area. To address this issue, the antenna elevation beam shaping is used here in Chapter 6. By applying the first upper side null filling technique for the pattern-reconfigurable antenna array, it is found that the overall network coverage can be improved for the large antenna downtilt. Also, the application of the first null filling combined with the antenna downtilt is investigated in a scenario where the cell/cluster has the performance below network average. In this case, the antenna downtilt is only applied to the chosen cell only, while the other surrounding cells keep the optimum antenna downtilt angle. The summarised results show

that there is a trade-off between chosen cell capacity and other surrounding cells' ones by varying the chosen cell antenna downtilt angle only. However, it may be useful for mobile operators to choose a proper antenna downtilt angle for this cell to improve its performance while without deteriorating too much network coverage/capacity of other cells. In addition, the effects of number of antenna elements for the antenna array on both the edge and overall network coverage and capacity are investigated. It is found that by increasing the number of antenna elements for the antenna array, the network coverage/capacity can be enhanced as well at its optimum tilt angle due to its high antenna gain. Also, since the users who located outside the antenna's -3dB beamwidth can suffer from 50% up to 90% less signal strength than the mobile users who are located inside the antenna's -3dB beamwidth, it is found that when the number of antenna elements is increased to 40 in our simulation, the network capacity can achieve the maximum at its optimum tilt angle with very narrow elevation beamwidth of around 2.4°. This finding suggests that the high-gain antenna array concept for providing link budget improvement over a homogeneous mobile cellular network can be used for large site separations and fewer installations.

7.2 Work Impact

The contributions of the work to the research of Pattern-reconfigurable antenna for current and future wireless communication system are listed below:

- A novel pattern-reconfigurable antenna is proposed, designed and tested for the mobile communication which can alter its azimuth beamwidth from 60° to 110° by using the electrical switches of PIN diodes. The application of this pattern-reconfigurable antenna array in a homogeneous cellular network helps the dynamic azimuth planning for the inhomogeneous user traffic distribution. By varying the antenna azimuth beamwidth, trade-offs can be made between 1) increasing the available capacity for cell edge users and 2) maximizing the average user capacity.
- The elevation beam shaping technique for the antenna array by filling the first upper side nulls is used for improving the network coverage performance at large antenna downtilt beyond 10° tilt in a homogeneous cellular system.
- The effects of the number of antenna elements in the antenna array on the network coverage and capacity are investigated here. It is found that by increasing the number of antenna elements, the cell coverage and capacity can be increased as well due to the high

antenna gain and when the number of antenna elements reaches 40, the system capacity can reach its maximum at its optimum tilt angle with narrow elevation beamwidth of around 2.4°. The high-gain antenna array concept for providing link budget improvement over a homogeneous mobile cellular network indicates the potential for large site separations and fewer installations.

7.3 Future Work

Future research investigation can be carried in the following areas. First, due to the inhomogeneous distribution of mobile traffic in the current and future mobile network, some users can get good network experience while others can have bad network service level. In order to improve the overall user performances in terms of coverage and capacity by utilising the existing network resources (increasing spectrum efficiency, reducing network interference or boosting radio signal coverage), the antenna azimuth steering can be used in this application. By steering the antenna azimuth to follow the high traffic usage area in time and space in the cell, the overall network coverage and capacity can be improved. Based on the Base station to Mobile station link budget and Shannon capacity law, by exchanging in the link budget the antenna gain with the amplifier RF power resources, the overall network performances in the cell can be enhanced. Since user traffic variation appealing in a day course can be repeatable, to confirm the data traffic distribution in the cell, the trial and error method can be used to collected the traffic samples from the Radio Network Supporting System. After identifying the high usage traffic area in the cell, the antenna azimuth can then be used to head to it. The other application of beam steering antenna can be used in the future 5G mmWave communication system. Since in the mmWave frequency band, the path loss is significantly higher compared with the microwave frequency, it is expected to use a highly directional link between the BS and MS in it. Thus, the antenna beam steering can be used in this situation for overcoming the path loss and providing the high gain in the desired direction and suppressing the signal to the undesired users. Now, antenna azimuth steering capability can be achieved mainly by two methods mechanical and electrical. The mechanical way to achieve the antenna steering can have the advantage of keeping intact the antenna gain while offering the flexibility in the needed steering range. However, it may need to change the structure of the antenna and the switching time for the beam steering is quite long. The electrical beam steering antenna can have the advantage of switching the antenna beam fast. However, it can have problems of non-continuous steering range and high insertion loss and

degraded antenna gain. So, to overcome this issue, the low loss electrical switches can be used to compensate the loss for the electrical beam steering antenna design. Different structure of the reflector surfaces can be explored in the future research to achieve the antenna beam steering including FSS, EBG and other type of metasurfaces. Extend research based on the proposed pattern-reconfigurable antenna can be carried out to fully investigate the reflector surface or by using different reflector structure to achieve the antenna beam steering capability in both the azimuth and elevation plane.

Second, since mobile traffic will be increased by around 1000x in 2020 compared to the current traffic number, how to manage and balance the large number of traffic load is an important issue in the future mobile network system. In any mobile network system, if the traffic load can be equally balanced between each sectors, then the system capacity can reach its maximum. Now, in order to balance the load among the cells which means the overloaded cell can shift its traffic to the underutilised cell, a reconfigurable beam antenna can be proposed for this purpose. This reconfigurable beam antenna can have the capability of altering the azimuth beamwidth as well as steering the beam to different directions. By combining these two functions in this antenna, it can lead to an improved network performance with better capacity utilisation without additional radio resources such as channels, cells or spectrum and it can reduce or delay the CAPEX.

Third, due to the advantages of using beam steering antenna or reconfigurable beam antenna in the current and future mobile network communication system, it is critical to study different beam steering techniques and complement by analytical studies including simulations. Also, to fully understand the expected losses/gains of fixed beam array antenna with mechanical steering vs. electronically steering, intensive simulation and analytical study will be carried on.

This page is intentionally blank.

References

[1] Y. Jay Guo and P. Y. Qin, "Advances in reconfigurable antennas for wireless communications," 2015 9th European Conference on Antennas and Propagation (EuCAP), Lisbon, 2015, pp. 1-4.

[2] Y. Sambo, M. Shakir, K. Qaraqe, E. Serpedin, and M. Imran, “Expanding cellular coverage via cell-edge deployment in heterogeneous networks: Spectral efficiency and backhaul power consumption perspectives,” IEEE Communications Magazine, vol. 52, no. 6, pp. 140–149, 2014.

[3] P. P. Narsinhbhai and M. G. Shajan, “Data rate enhancement for cell edge users in a wireless cellular network.”

[4] B. Yu, L. Yang, H. Ishii, and X. Cheng, “Load balancing with antenna tilt control in enhanced local area architecture,” in Vehicular Technology Conference (VTC Spring), 2014 IEEE 79th. IEEE, 2014, pp. 1–6.

[5] B. Yu, L. Yang, and H. Ishii, “3d beamforming for capacity improvement in macrocell-assisted small cell architecture,” in Global Communications Conference (GLOBECOM), 2014 IEEE. IEEE, 2014, pp. 4833–4838.

[6] C. A. Balanis, Antenna theory: analysis and design: John Wiley & Sons, 2016.

[7] Saunders, S. R. and S. R. Simon (1999). Antennas and Propagation for Wireless Communication Systems, John Wiley \& Sons, Inc.

[8] J. T. Bernhard, Reconfigurable Antennas: Morgan & Claypool, 2007.

[9] C. Zhang, S. Yang, H. K. Pan, A. E. Fathy, S. El-Ghazaly, and V. Nair, "Reconfigurable Antenna for Simultaneous Multi-Service Wireless Applications," in Radio and Wireless Symposium, 2007 IEEE, 2007, pp. 543-546.

[10] C. G. Christodoulou, Y. Tawk, S. A. Lane, and S. R. Erwin, "Reconfigurable Antennas for Wireless and Space Applications," Proceedings of the IEEE, vol. 100, pp. 2250-2261, 2012.

[11] H. F. Abu Tarboush et al., "A Reconfigurable Wideband and Multiband Antenna Using Dual-Patch Elements for Compact Wireless Devices," Antennas and Propagation, IEEE Transactions on, vol. 60, no. 1, pp. 36-43, Jan. 2012.

[12] R. L. Haupt and M. Lanagan, "Reconfigurable Antennas," Antennas and Propagation Magazine, IEEE, vol. 55, no. 1, pp. 49-61, Feb. 2013.

[13] J. K. Smith, "Reconfigurable aperture antenna (RECAP)", DARPA, 1999.

[14] M. R. Hamid, "Wideband reconfigurable antennas," University of Birmingham, 2011.

[15] C. A. Balanis, Modern Antenna Handbook, Hoboken, NJ, USA:Wiley, 2011.

[16] J. Costantine, Y. Tawk, S. E. Barbin and C. G. Christodoulou, "Reconfigurable Antennas: Design and Applications," in Proceedings of the IEEE, vol. 103, no. 3, pp. 424-437, March 2015.

[17] M. J. Slater, H. K. Pan and J. T. Bernhard, "Preliminary results in the development of a compound reconfigurable antenna," 2008 IEEE Antennas and Propagation Society International Symposium, San Diego, CA, 2008, pp. 1-4.

[18] G. H. Huff, J. Feng, S. Zhang, and J. T. Bernhard. "A novel radiation pattern and frequency reconfigurable single turn square spiral microstrip antenna," IEEE Microwave and Wireless Comp. Lettters, vol. 13, no. 2, pp. 57-59, Feb. 2003.

[19] M. K. A. Rahim, M. R. Hamid, N. A. Samsuri, N. A. Murad, M. F. M. Yusoff and H. A. Majid, "Frequency reconfigurable antenna for future wireless communication system," 2016 46th European Microwave Conference (EuMC), London, 2016, pp. 965-970.

[20] E. A. Abbas, A. T. Mobashsher and A. Abbosh, "Polarization reconfigurable antenna for 5G cellular networks operating at millimeter waves," 2017 IEEE Asia Pacific Microwave Conference (APMC), KUALA LUMPUR, Malaysia, 2017, pp. 772-774.

[21] J. Costantine et al., "A radiation pattern reconfigurable antenna for WLAN access," 2016 United States National Committee of URSI National Radio Science Meeting (USNC-URSI NRSM), Boulder, CO, 2016, pp. 1-2.

[22] K. R. Boyle, P. G. Steeneken, Z. Liu, Y. Sun, A. Simin, T. Huang, E. Spits, O. Kuijken, T. Roedle, and F. van Straten, "Reconfigurable Antennas for SDR and Cognitive Radio," in Antennas and Propagation, 2007. EuCAP 2007. The Second European Conference on, 2007, pp. 1-6.

[23] J. Costantine, Y. Tawk, C. G. Christodoulou, Design of Reconfigurable Antennas Using Graph Models, San Rafael, CA, USA:Morgan and Claypool, 2013.

[24] J. T. Aberle, O. Sung-Hoon, D. T. Auckland, and S. D. Rogers, "Reconfigurable antennas for wireless devices," Antennas and Propagation Magazine, IEEE, vol. 45, pp. 148-154, 2003.

[25] D. C. Chang, "Reconfigurable antennas for wireless communication," in Electromagnetics; Applications and Student Innovation (iWEM), 2012 IEEE International Workshop on, 2012, pp. 1-1.

[26] A. R. Weily, T. S. Bird, and Y. J. Guo, "A reconfigurable high-gain partially reflecting surface antenna," IEEE Trans. Antennas Propag., Vol. 56, No. 11, pp. 3382-3390. Nov. 2008.

[27] C. W. Jung, M. Lee, G. P. Li, F. De Flaviis, "Reconfigurable scan-beam single-arm spiral antenna integrated with RF-MEMS switches", IEEE Trans. Antennas Propag., vol. 54, no. 2, pp. 455-463, Feb. 2006.

[28] A. Grau, J. Romeu, M. Lee, S. Blanch, L. Jofre, F. De Flaviis, "A dual linearly polarized MEMS-reconfigurable antenna for narrowband MIMO communication systems", IEEE Trans. Antennas Propag., vol. 58, no. 1, pp. 4-16, Jan. 2010.

[29] T. Tadashi et al., "Deployable antenna with 10-m maximum diameter for space use", IEEE Trans. Antennas Propag., vol. 52, no. 1, pp. 2-11, 2004.

[30] F. Zheng, M. Chen, W. Li, P. Yang, "Conceptual design of a new huge deployable antenna structure for space application", Proc. IEEE Aerospace Conf., pp. 1-7, 2008.

[31] H. King, J. Wong, "Characteristics of 1 to 8 wavelength uniform helical antennas", IEEE Trans. Antennas Propag., vol. 28, pp. 291-296, Mar. 1980.

[32] J. Costantine, Y. Tawk, C. G. Christodoulou, J. Banik, S. Lane, "CubeSat deployable antenna using bistable composite tape-springs", IEEE Antennas Wireless Propag. Lett., vol. 11, pp. 285-288, 2012.

[33] J. Costantine, Y. Tawk, C. G. Christodoulou, "Reconfigurable deployable antennas for space communications", Proc. Int. Workshop Antenna Technol., 2014.

[34] K. L. Ford and J. M. Rigelsford, "Dipole radiation steering using an active artificial magnetic conductor," in Antennas and Propagation Society International Symposium, 2008. AP-S 2008. IEEE, 2008, pp. 1-4.

[35] J. M. Rigelsford, F. Collado, and K. L. Ford, "Radiation steering of a low profile street furniture antenna using an active AMC," in Antennas and Propagation Conference (LAPC), 2010 Loughborough, 2010, pp. 529-53

[36] K. L. Ford and J. M. Rigelsford, "Antenna radiation pattern control using EBG/AMC surfaces for street furniture applications," in Antennas and Propagation Society International Symposium, 2007 IEEE, 2007, pp. 4076-4079.

[37] K. L. Ford and J. M. Rigelsford, "Street Furniture Antenna Radiation Pattern Control Using AMC Surfaces," Antennas and Propagation, IEEE Transactions on, vol. 56, pp. 3049-3052, 2008.

[38] W. Guo, J. M. Rigelsford, L. Ford, and T. O'Farrell, "Dynamic basestation antenna design for low energy networks," Progress In Electromagnetics Research C, Vol. 31, 153-168, 2012.

[39] Y. B. Jung, "Dual-band reconfigurable antenna for base-station applications", Electronics Letters, vol. 46, pp. 195-196, 2010.

[40] S. O. Park, V. A. Nguyen and R. S. Aziz, "Multi-band, dual polarization, dual antennas for beam reconfigurable antenna system for small cell base Station (Invited paper)," 2014 International Workshop on Antenna Technology: Small Antennas, Novel EM Structures and Materials, and Applications (iWAT), Sydney, NSW, 2014, pp. 159-160.

[41] A. Mehta, H. Nakano, D. M. Syahkal, "A switched beam single arm rectangular spiral antenna with hybrid switch network", Proc. IEEE Int. Symp. Antennas Propag., vol. 2B, pp. 589-592, 2005-Jul.

[42] A. Mehta, D. M. Syahkal, "Spiral antenna with adaptive radiation pattern under electronic control", Proc. IEEE Int. Symp. Antennas Propag., vol. 1, pp. 843-846, 2004-Jun.

[43] I. Y. Tarn and S. J. Chung, "A Novel Pattern Diversity Reflector Antenna Using Reconfigurable Frequency Selective Reflectors," in IEEE Transactions on Antennas and Propagation, vol. 57, no. 10, pp. 3035-3042, Oct. 2009.

[44] S. Landström, A. Furuskär, K. Johansson, L. Falconetti, and F. Kronestedt, "Heterogeneous networks–increasing cellular capacity," The data boom: opportunities and challenges, p. 4.

[45] A. Khandekar, N. Bhushan, T. Ji, and V. Vanghi, "LTE Advanced: Heterogeneous networks," in Wireless Conference (EW), 2010 European, 2010, pp. 978-982.

[46] Q. Zhang, W. Wang, W. L. Huang, and J. Zhang, "Cooperative Multi-Antenna Relaying in Heterogeneous Networks," in Vehicular Technology Conference, 2009. VTC Spring 2009. IEEE 69th, 2009, pp. 1-6.

[47] J. Rong-Terng, L. Ding-Bing, and L. Hsin-Piao, "Uplink spectrum sharing for heterogeneous networks based on reconfigurable antenna system," in Antennas and Propagation Society International Symposium (APSURSI), 2012 IEEE, 2012, pp.1-2.

[48] X. Yuan, "Multi-Functional Reconfigurable Antenna Development by Multi- Objective Optimization," UTAH STATE UNIVERSITY, 2012.

[49] A. Bondarik and D. Sjöberg, "Investigation of reconfigurability for a stacked microstrip patch antenna pattern targeting 5G applications," 2015 IEEE-APS Topical Conference on Antennas and Propagation in Wireless Communications (APWC), Turin, 2015, pp. 1202-1205.

[50] J. G. Andrews, S. Buzzi, W. Choi, S.V. Hanly, A. Lozano, A.C.K. Soong, J.C. Zhang, "What will 5G Be?", IEEE Journal on Select. Areas Commun., vol. 32, no. 6, pp. 1065-1082, June 2014.

[51] W. Roh, J.Y. Seol, J. Park, B. Lee, J. Lee, Y. Kim, J. Cho, K. Cheun, F. Aryanfar, "Millimeter-wave beamforming as an enabling technology for 5G cellular communications: Theoretical feasibility and prototype results", IEEE Commun. Mag., vol. 52, no. 2, pp. 106-113, Feb. 2014.

[52] H. Kamoda, T. Iwasaki, J. Tsumochi, T. Kuki, O. Hashimoto, "60-GHz electronically reconfigurable large reflectarray using single-bit phase shifters", IEEE Trans. Antennas Propag., vol. 59, no. 7, pp. 2524-2531, July 2011.

[53] M. Jusoh, T. Aboufoul, T. Sabapathy, A. Alo-mainy, M. Kamarudin, "Pattern-reconfigurable microstrip patch antenna with multidirectional beam for WiMAX application", IEEE Antennas and Wireless Propagation Letters, vol. 13, pp. 860-863, April 2014.

[54] M. A. Hossain, I. Bahceci and B. A. Cetiner, "Parasitic Layer-Based Radiation Pattern Reconfigurable Antenna for 5G Communications," in IEEE Transactions on Antennas and Propagation, vol. 65, no. 12, pp. 6444-6452, Dec. 2017.

[55] A. A. Mojtaba, M. Hani; V. Vakilian, N. Behdad, Nader and H. Jafarkhani, "Reconfigurable Antennas in mmWave MIMO Systems." Cornell University, October 2017.

[56] I. F. Costa, D. H. Spadoti, A. C. Sondre jnr, L. G da Silva, S. Rodriguez, R. Puerta, J. J. V. Olmos and T. Monroy, "Optically controlled reconfigurable antenna for 5G future broadband cellular communication networks." In Journal of Microwaves, Optoelectronics and Electromagnetic Applications, vol 16, no.1, pp. 208-217, March 2017.

[57] S. F. Jilani, S. M. Abbas, K. P. Esselle and A. Alomainy, "Millimeter-wave frequency reconfigurable T-shaped antenna for 5G networks," 2015 IEEE 11th International Conference on Wireless and Mobile Computing, Networking and Communications (WiMob), Abu Dhabi, 2015, pp. 100-102.

[58] K. X. Wang, H. Wong, J. Xiang and Z. Lai, "Polarization reconfigurable millimeter wave antenna with wideband and high gain performance," 2016 IEEE Conference on Antenna Measurements & Applications (CAMA), Syracuse, NY, 2016, pp. 1-3.

[59] C. Xiong, G. Li, S. Zhang, Y. Chen, and S. Xu, "Energy- and spectral-efficiency tradeoff in downlink OFDMA networks," IEEE Transactions on Wireless Communications, Vol. 10, No. 11, 3874-3885, Nov. 2011.

[60] W. Guo, and T. O'Farrell, "Relay deployment in cellular networks: Planning and optimization," IEEE Journal on Selected Areas in Communications (JSAC), Sep. 2012.

[61] A. Alexiou, and M. Haardt, “Smart antenna technologies for future wireless systems: trends and challenges”, IEEE Comm. Mag, Vol. 42, pp 90-97, Sept. 2004.

[62] S. P. Yeh, S. Talwar, G. Wu, N. Himayat and K. Johnsson, "Capacity and coverage enhancement in heterogeneous networks," in IEEE Wireless Communications, vol. 18, no. 3, pp. 32-38, June 2011.

[63] S. Wang, W. Guo, T. O'Farrell, "Optimising Femtocell Placement in an Interference Limited Network: Theory and Simulation," Vehicular Technology Conference (VTC Fall), 2012 IEEE , vol., no., pp.1,6, 3-6 Sept. 2012

[64] C. Chan and G. Wu, “Pivotal Role of heterogeneous networks in 4G deployment”, 2010 [online]. Available: hjttp://wwwen.zte.com.cn/endata/magazine/ztetechnologies/2010/no1/articles/201001/t20100112_179547.html

[65] T. E. Bogale and L. B. Le, "Massive MIMO and mmWave for 5G Wireless HetNet: Potential Benefits and Challenges," in IEEE Vehicular Technology Magazine, vol. 11, no. 1, pp. 64-75, March 2016.

[66] 5G: A Technology Vision, Dec. 2013.

[67] E. Hossain, M. Rasti, H. Tabassum, A. Abdelnasser, "Evolution towards 5G multi-tier cellular wireless networks: An interference management perspective", IEEE Wireless Commun. Mag., vol. 21, no. 3, pp. 118-127, June 2014.

[68] A. Osseiran, F. Boccardi, V. Braun, K. Kusume, P. Marsch, M. Maternia, O. Queseth, M. Schellmann, H. Schotten, H. Taoka, H. Tullberg, M. A. Uusitalo, B. Timus, M. Fallgren, "Scenarios for 5G mobile and wireless communications: The vision of the METIS project", IEEE Commun. Mag., vol. 52, no. 5, pp. 26-35, May 2014

Chapter 3 references.

[69] S. W. O’Malley and L. L. Peterson, “A dynamic network architecture,” ACM Transactions on Computer Systems (TOCS), vol. 10, no. 2, pp. 110–143, 1992.

[70] D. Niyato and E. Hossain, “Dynamics of network selection in heterogeneous wireless networks: an evolutionary game approach,” Vehicular Technology, IEEE Transactions on, vol. 58, no. 4, pp. 2008–2017, 2009.

[71] D. Jiawei, L. Yongxiang, and Z. Biao, “A survey on radiation pattern reconfigurable antennas,” in Wireless Communications, Networking and Mobile Computing (WiCOM), 7th International Conference on. IEEE, 2011, Conference Proceedings, pp. 1–4.

[72] V. Navda, A. P. Subramanian, K. Dhanasekaran, A. Timm-Giel, and S. Das, “Mobisteer: using steerable beam directional antenna for vehicular network access,” in Proceedings of the 5th international conference on Mobile systems, applications and services. ACM, 2007, Conference Proceedings, pp. 192–205.

[73] W. Guo, J. M. Rigelsford, K. L. Ford, and T. O’Farrell, “Dynamic basestation antenna design for low energy networks,” Progress in Electromagnetics Research C, vol. 31, pp. 153–168, 2012.

[74] R. Jain, S. Katiyar, and N. Agrawal, “Smart Antenna for Cellular Mobile Communication,” VSRD International Journal of Electrical, Electronics & Communication Engineering, vol. 1, no. 9, pp. 530-541, 2011.

[75] Y. Zhou, R. S. Adve, and S. V. Hum, “Design and evaluation of pattern reconfigurable antennas for mimo applications,” Antennas and Propagation, IEEE Transactions on, vol. 62, no. 3, pp. 1084–1092, 2014.

[76] J. T. Bernhard, Reconfigurable Antennas. Morgan and Claypool, 2007.

[77] C. G. Christodoulou, Y. Tawk, S. Lane, and S. R. Erwin, “Reconfigurable antennas for wireless and space applications,” Proceedings of the IEEE, vol. 100, no. 7, pp. 2250–2261, 2012.

[78] W. Kang and K. Kim, “A radiation pattern-reconfigurable antenna for wireless communications,” in Antennas and Propagation (APSURSI), IEEE International Symposium on. IEEE, 2011, Conference Proceedings, pp. 1545–1548.

[79] Z. Jiajie, W. Anguo, and W. Peng, “A survey on reconfigurable antennas,” in Microwave and Millimeter Wave Technology. ICMMT2008. International Conference on, vol. 3. IEEE, 2008, Conference Proceedings, pp. 1156–1159.

[80] W. S. Kang, J. Park, and Y. J. Yoon, “Simple reconfigurable antenna with radiation pattern,” Electronics Letters, vol. 44, no. 3, pp. 182–183, 2008.

[81] I. Ben Trad, J. M. Floc’h, H. Rmili, M. Drissi, and F. Choubani, “A planar reconfigurable radiation pattern dipole antenna with reflectors and directors for wireless communication applications,” International Journal of Antennas and Propagation, vol. 2014, pp. 10, 2014. [Online]. Available: http://dx.doi.org/10.1155/2014/593259

[82] S.-H. Chen, J.-S. Row, and K.-L. Wong, “Reconfigurable square-ring patch antenna with pattern diversity,” Antennas and Propagation, IEEE Transactions on, vol. 55, no. 2, pp. 472–475, 2007.

[83] L. Petit, L. Dussopt, and J.-M. Laheurte, “Mems-switched parasiticantenna array for radiation pattern diversity,” Antennas and Propagation, IEEE Transactions on, vol. 54, no. 9, pp. 2624–2631, 2006.

[84] S. Nikolaou, G. E. Ponchak, J. Papapolymerou, and M. M. Tentzeris, “Design and development of an annular slot antenna (asa) with a reconfigurable radiation pattern,” in Microwave Conference Proceedings. APMC 2005. Asia-Pacific Conference Proceedings, vol. 5, IEEE Conference Proceedings, pp. 3, 2005.

[85] F. Costa, A. Monorchio, S. Talarico, and F. M. Valeri, “An active high-impedance surface for low-profile tunable and steerable antennas,” Antennas and Wireless Propagation Letters vol. 7, pp. 676–680, 2008.

[86] Y. Huang, L.-S. Wu, M. Tang, and J. Mao, “Design of a beam reconfigurable thz antenna with graphene-based switchable high-impedance surface,” Nanotechnology, IEEE Transactions on, vol. 11, no. 4, pp. 836–842, 2012.

[87] A. Edalati and T. Denidni, “High-gain reconfigurable sectoral antenna using an active cylindrical fss structure,” Antennas and Propagation, IEEE Transactions on, vol. 59, no. 7, pp. 2464–2472, 2011.

[88] V. C. Sanchez, W. E. McKinzie III, and R. E. Diaz, “Broadband antennas over electronically reconfigurable artificial magnetic conductor surfaces,” 2005.

[89] Y.-L. Tsai, R.-B. Hwang, and Y.-D. Lin, “A reconfigurable beamswitching antenna base on active fss,” in Antenna Technology and Applied Electromagnetics (ANTEM), 15th International Symposium on. IEEE Conference Proceedings, pp. 1–4, 2012.

[90] K. Ford and J. Rigelsford, “Antenna radiation pattern control using ebg/amc surfaces for street furniture applications,” Antennas and Propagation Society International Symposium, IEEE Conference Proceedings, pp. 4076–4079, 2007.

[91] 3GPP, “3rd Generation Partnership Project; Technical Specification Group Radio Access Network; Evolved Universal Terrestrial Radio Access (E-UTRA); Further advancements for E-UTRA physical layer aspects,” no. 9, 2010 [online]. Available: http://www.qtc.jp/3GPP/Specs/36814-900.pdf

[92] Y. A. Sambo et al, “Expanding cellular coverage via cell-edge deployment in heterogeneous networks: spectral efficiency and backhaul power consumption perspectives,” IEEE Communications Magazine, vol. 52, no. 6, pp. 140-149, 2014.

[93] P. P. Narsinhbhai and M. G. Shajan, “Data Rate Enhancement For Cell Edge Users In A Wireless Cellular Network,” International Journal of Inventive Engineering and Science, vol. 1, no. 7, pp. 32-35, 2013.

[94] S. Boddu, S. S. Das, and R. V. Rajakumar, “Performance analysis of flexible reuse in cellular networks,” IET Communications, vol. 9, no.6, pp. 808-818, 2015.

[95] F. Huang, J. Tomasik and V. Vèque, “Improvement of cell edge performance by coupling rb allocation with beamforming,” IEEE International Conference on Communication Systems, pp. 333-338, 2014.

[96] X. Cheng, H. Ishii, L. Yang and B. Yu, “Load balancing with antenna tilt control in enhanced local area architecture,” IEEE 79th Vehicular Technology Conference, vol. 79, pp. 1-6, 2014.

[97] H. Ishii, L. Yang and B. Yu, “3d beamforming for capacity improvement in macrocell-assisted small cell architecture,” IEEE Global Communications Conference, pp. 4833-4838, 2014.

[98] J. Niemelä, Y. S. Fahad and M. Valkama, “Cell planning for outdoor distributed antenna systems in dense urban areas,” Telecommunications Network Strategy and Planning Symposium, vol. 16, pp. 1-7, 2014.

[99] S. M. Kate and M. C. Patil, “Throughput Improvement for Cell-Edge Users Using Selective Cooperation”, International Journal of Science and Research, vol. 4, no. 4, pp. 530-533, 2015.

[100] L. Cuthbert, A. Ma, Y. Wang and X. Yang, “Intelligent resource optimisation using semi-smart antennas in LTE OFDMA systems,” Communications Technology and Applications, IEEE International Conference on, pp. 173-179. 2009.

[101] P. Ren and H. Xu, “Joint user scheduling and power control for cell-edge performance improvement in backhaul-constrained network MIMO,” IEEE 24th Annual International Symposium on Personal, Indoor, and Mobile Radio Communications (PIMRC), pp. 1342-1346. 2013.

[102] S. Badessi, G. A. E. Crone and A. G. Roederer, “Recent activities in beamformers for space applications,” Novel Techniques for Antenna Beam Control, IEE Colloquium on, pp. 8/1-8/8, 1995.

[103] N. Clow et al. “Planar pattern reconfigurable antenna integrated with a WiFi system for multipath mitigation and sustained high definition video networking in a complex EM environment,” Antennas and Propagation & USNC/URSI National Radio Science Meeting, IEEE International Symposium on, pp. 2229-2230, 2015.

[104] J. D. Boerman and J. T. Bernhard, “Performance study of pattern reconfigurable antennas in MIMO communication systems ”IEEE Transactions on Antennas and Propagation, vol. 56, no. 1, pp. 231-236, 2008.

[105] Y. Kim et al. “Pattern-reconfigurable MIMO antenna for high isolation and low correlation,” IEEE Antennas and Wireless Propagation Letters, vo. 13, pp.1373-1376, 2014.

[106] X. Li et al. “Mobile Relay Station with Radiation Pattern Reconfigurable Antenna,” IEEE 79th Vehicular Technology Conference (VTC Spring), pp. 1-5, 2014.

[107] F. Bobor-Oyibo et al. “Modelling and analysis of a smart antenna system with sub-sector dynamic capacity enhancement for mobile telecommunication networks,” Communication Systems, Networks & Digital Signal Processing (CSNDSP), 8th International Symposium on, pp. 1-4, 2012.

[108] J. Hun et al. “Design of a novel graphene terahertz antenna at 500GHz with reconfigurable radiation pattern,” 2015 IEEE International Symposium on Antennas and Propagation & USNC/URSI National Radio Science Meeting, pp. 1462-1463, 2015.

[109] 3GPP, “LTE; Evolved Universal Terrestrial Radio Access (E-ULTRA); Radio Frequency (RF) system scenarios”, version 13, 2016 [online]. Available: http://www.etsi.org/deliver/etsi_tr/136900_136999/136942/13.00.00_60/tr_136942v130000p.pdf

[110] P. Kyosti, J. Meinila, L. Hentila, and X. Zhao, “WINNER II Channel Models: Part I Channel Models version 1.2,” WINNER and Information Society Technologies,” Technical Report, 2007

[111] Y. Okumura, E. Ohmori, T. Kawano, K. Fukuda, “Field strength and its variability in VHF and UHF Land-Mobile radio service”, in Review of the Electrical Communication Laboratory, Volume 16, No. 9-10, pp. 825–873, September-October 1968.

[112] F. Ikegami, S. Yoshida, T. Takeuchi, M. Umehira, “Propagation Factors Controlling Mean Field Strength on Urban Streets”, in IEEE Transactions on Antennas & Propagation, Volume AP-32, pp. 822–829, 1984.

[113] J. Walfish, H.L. Bertoni, “A theoretical model of UHF propagation in urban environment”, in IEEE Transactions on Antennas & Propagation, Volume AP- 36, pp. 1788–1796, December 1988.

[114] CST STUDIO SUITE®, CST AG, Germany, www.cst.com

[115] W. Kang and K. Kim, "A radiation pattern-reconfigurable antenna for wireless communications," 2011 IEEE International Symposium on Antennas and Propagation (APSURSI), Spokane, WA, 2011, pp. 1545-1548.

[116] J. Costantine, Y. Tawk, S. E. Barbin and C. G. Christodoulou, "Reconfigurable Antennas: Design and Applications," in Proceedings of the IEEE, vol. 103, no. 3, pp. 424-437, March 2015.

[117] S. Loredo, M. R. Pino, F. Las-Heras and T. K. Sarkar, "Echo identification and cancellation techniques for antenna measurement in non-anechoic test sites," in IEEE Antennas and Propagation Magazine, vol. 46, no. 1, pp. 100-107, Feb. 2004.

[118] R. Bulter, R. W. Heath Jnr, K. Linehan and X. Li, "Impact of Metro Cell Antenna Pattern and Downtilt in Heterogeneous Networks", 2015 [online]. Available : https://arxiv.org/ftp/arxiv/papers/1502/1502.05782.pdf.

[119] A. Ghosh et al., "Heterogeneous cellular networks: From theory to practice," in IEEE Communications Magazine, vol. 50, no. 6, pp. 54-64, June 2012.

[120] J. G. Andrews, "Seven ways that HetNets are a cellular paradigm shift," in IEEE Communications Magazine, vol. 51, no. 3, pp. 136-144, March 2013.

[121] H. S. Dhillon, R. K. Ganti, F. Baccelli and J. G. Andrews, "Modeling and Analysis of K-Tier Downlink Heterogeneous Cellular Networks," in IEEE Journal on Selected Areas in Communications, vol. 30, no. 3, pp. 550-560, April 2012.

[122] N. Seifi, M. Coldrey, M. Matthaiou and M. Viberg, "Impact of Base Station Antenna Tilt on the Performance of Network MIMO Systems," 2012 IEEE 75th Vehicular Technology Conference (VTC Spring), Yokohama, 2012, pp. 1-5.

[123] Lu, Xiaojia & Tölli, Antti & Piirainen, Olli & Juntti, Markku & Li, Wei. (2011). Comparison of Antenna Arrays in a 3-D Multiuser Multicell Network. Proc. IEEE International Conference on Communications. 1-6. 10.1109/icc.2011.5963126.

[124] N. Gresset, H. Halbauer, J. Koppenborg, W. Zirwas and H. Khanfir, "Interference-Avoidance Techniques: Improving Ubiquitous User Experience," in IEEE Vehicular Technology Magazine, vol. 7, no. 4, pp. 37-45, Dec. 2012.

[125] Halbauer, Hardy & Saur, Stephan & Koppenborg, Johannes & Hoek, Cornelis. (2012). Interference avoidance with dynamic vertical beamsteering in real deployments. . 10.1109/WCNCW.2012.6215509.

[126] 3GPP, “TS 36.211, E-UTRA Physical Channels and Modulation (Rel.8)”

[127] Godara, L.C.. (1997). Applications Of Antenna Arrays To Mobile Communications, Part I: Performance Improvement, Feasibility, And System Considerations. Proceedings of the IEEE. 85. 1031 - 1060. 10.1109/5.611108.

[128] J. E. Padgett, C. G. Gunther, and T. Hattori, “Overview of wireless personal communications,” IEEE Commun. Mag., vol. 33, pp. 28–41, Jan. 1995.

[129] O. N. C. Yilmaz, S. Hamalainen and J. Hamalainen, "Analysis of Antenna Parameter Optimization Space for 3GPP LTE," 2009 IEEE 70th Vehicular Technology Conference Fall, Anchorage, AK, 2009, pp. 1-5.

[130] O. N. C. Yilmaz, S. Hamalainen and J. Hamalainen, "Comparison of Remote Electrical and Mechanical Antenna Downtilt Performance for 3GPP LTE," 2009 IEEE 70th Vehicular Technology Conference Fall, Anchorage, AK, 2009, pp. 1-5.

[131] S. Shahsavari, P. Hassanzadeh, A. Ashikhmin, and E. Erkip, “Sectoring in multi-cell massive MIMO systems,” arXiv preprint arXiv:1707.09070, Jul. 2017.

[132] E. G. Larsson, O. Edfors, F. Tufvesson, and T. L. Marzetta, “Massive MIMO for next generation wireless systems,” IEEE Communications Magazine, vol. 52, no. 2, pp. 186–195, 2014.

[133] J. G. Andrews, W. Choi, and R. W. Heath Jr, “Overcoming interference in spatial multiplexing MIMO cellular networks,” IEEE Wireless Communications, vol. 14, no. 6, pp. 95–104, 2007.

[134] A. D. Gandhi, "Significant gains in coverage and downlink capacity from optimal antenna downtilt for closely-spaced cells in wireless networks," 2014 23rd Wireless and Optical Communication Conference (WOCC), Newark, NJ, 2014, pp. 1-6.

[135] Bieder, S & Häring, Lars & Czylwik, A & Paunov, P & Chalise, Batu. (2007). Realistic Antenna Elements and Different Array Topologies in the Downlink of UMTS-FDD Networks.

[136] J. Pontes, A. Lambrecht, W. Wiesbeck, "Elevation Optimized Antenna Arrays for Future Cellular Systems", CD-ROM International ITG/IEEE Workshop on Smart Antennas, February 2007.

[137] H. J. Orchard, R. S. Elliott and G. J. Stern, "Optimising the synthesis of shaped beam antenna patterns," in IEE Proceedings H - Microwaves, Antennas and Propagation, vol. 132, no. 1, pp. 63-68, February 1985.

[138] T. Binzer and F. M. Landstorfer, "Radio network planning with neural networks," Vehicular Technology Conference Fall 2000. IEEE VTS Fall VTC2000. 52nd Vehicular Technology Conference (Cat. No.00CH37152), Boston, MA, 2000, pp. 811-817 vol.2.

[139] M. Barba, J. E. Page, J. A. Encinar and J. R. Montejo, "Elevation radiation pattern shaping and control in broadband base station antenna arrays," 2005 18th International Conference on Applied Electromagnetics and Communications, Dubrovnik, 2005, pp. 1-3.

[140] V. Kallnichev, "Analysis of beam-steering and directive characteristics of adaptive antenna arrays for mobile communications," in IEEE Antennas and Propagation Magazine, vol. 43, no. 3, pp. 145-152, Jun 2001.

[141] A. Dadgarpour, B. Zarghooni, B. S. Virdee and T. A. Denidni, "Improvement of Gain and Elevation Tilt Angle Using Metamaterial Loading for Millimeter-Wave Applications," in IEEE Antennas and Wireless Propagation Letters, vol. 15, pp. 418-420, 2016.

[142] R. Leberer and W. Menzel, "A dual planar reflectarray with synthesized phase and amplitude distribution," in IEEE Transactions on Antennas and Propagation, vol. 53, no. 11, pp. 3534-3539, Nov. 2005.

[143] J. G. Meana, J. A. Martinez-Lorenzo, M. A. Arias, F. Las-Heras and A. G. Pino, "A Shaped and Reconfigurable Reflector Antenna With Low Sidelobe Level for Cellular Wireless Communications," in IEEE Antennas and Wireless Propagation Letters, vol. 6, pp. 627-630, 2007.

[144] N. Herscovici, M. Champion and A. Borrisenko, "A new omnidirectional shaped beam antenna," 2013 IEEE Antennas and Propagation Society International Symposium (APSURSI), Orlando, FL, 2013, pp. 244-245.

[145] A. Tall, Z. Altman and E. Altman, "Multilevel beamforming for high data rate communication in 5G networks", Cornell University, October 2015 [online]. Available: https://arxiv.org/pdf/1504.00280.pdf.

[146] L. Zhang, J. Liu, K. Liu and Y. Zhou, "On the 3D beamforming and proactive cell shaping with 3GPP 3D channel model," 2014 IEEE Globecom Workshops (GC Wkshps), Austin, TX, 2014, pp. 688-693.

[147] S. N. Shahab, A. R. Zainun, N. H. Noordin, I. I. Mohamed and W. D. Abdullah, "Null steering Optimization based MVDR beamformer using hybrid PSOGSA approach for antenna array system," 2016 IEEE Student Conference on Research and Development (SCOReD), Kuala Lumpur, 2016, pp. 1-6.

[148] H. Kikuchi, E. Yoshikawa, T. Ushio, F. Mizutani and M. Wada, "Application of Adaptive Digital Beamforming to Osaka University Phased Array Weather Radar," in IEEE Transactions on Geoscience and Remote Sensing, vol. 55, no. 7, pp. 3875-3884, July 2017.

[149] A. G. Toshev, "Synthesized shaped beam flat array antenna for digital beam-forming radar applications, utilizing printed technology," 2017 IEEE International Conference on Microwaves, Antennas, Communications and Electronic Systems (COMCAS), Tel-Aviv, 2017, pp. 1-4.

[150] M. Albanil et al., "A 2-D electronic beam steering phased array for point-multipoint communication applications," 2007 European Radar Conference, Munich, 2007, pp. 350-353.

[151] A. K. Singh, S. Elizabeth, P. Srinivasa and P. Dongaonkar, "Ultra Low Side Lobe Electronically Steerable Multi Beam Antenna System for Long Range 3-D Naval Surveillance Radar," 2007 IEEE Radar Conference, Boston, MA, 2007, pp. 457-462.

[152] C. Burns and H. Ecker, "Shaping antenna phase and amplitude distributions for low sidelobes," 1971 Antennas and Propagation Society International Symposium, Los Angeles, CA, USA, 1971, pp. 235-238.

[153] J. Y. Li, Y. X. Qi and S. G. Zhou, "Shaped Beam Synthesis Based on Superposition Principle and Taylor Method," in IEEE Transactions on Antennas and Propagation, vol. 65, no. 11, pp. 6157-6160, Nov. 2017.

[154] H. Wang, Z. Zhang, Y. Li and M. F. Iskander, "A Switched Beam Antenna With Shaped Radiation Pattern and Interleaving Array Architecture," in IEEE Transactions on Antennas and Propagation, vol. 63, no. 7, pp. 2914-2921, July 2015.

[155] J. C. Young, M. Sugano, Y. Shibuya, A. Takahashi and T. Itagaki, "Vertical Beam Shaping with Metal Strips in a Linear Edge Slot Array," The Second European Conference on Antennas and Propagation, EuCAP 2007, Edinburgh, 2007, pp. 1-5.

[156] J. h. Zhao and J. y. Yang, "Double-null pattern synthesis for low-angle tracking," 2007 International Conference on Microwave and Millimeter Wave Technology, Builin, 2007, pp. 1-4.

[157] Y. L. Zhou, J. Gao, Q. Yang and X. Y. Cao, "Design of compact phased array antennas with shaped pattern," Proceedings of 2014 3rd Asia-Pacific Conference on Antennas and Propagation, Harbin, 2014, pp. 499-501.

[158] D. h. Shin, K. b. Kim, J. g. Kim and S. o. Park, "Design of low side lobe level milimeter-wave microstrip array antenna for automotive radar," 2013 Proceedings of the International Symposium on Antennas & Propagation, Nanjing, 2013, pp. 677-680.

[159] Y. B. Jung, A. V. Shishlov and S. O. Park, "Cassegrain Antenna With Hybrid Beam Steering Scheme for Mobile Satellite Communications," in IEEE Transactions on Antennas and Propagation, vol. 57, no. 5, pp. 1367-1372, May 2009.

[160] H. Q. Ngo, E. G. Larsson, and T. L. Marzetta, “Aspects of favourable propagation in massive MIMO,” in *Proc. 22nd EUSIPCO*, Sep. 2014, pp. 76–80.

[161] X. Gao, O. Edfors, F. Tufvesson, and E. G. Larsson, “Massive MIMO in real propagation environments: Do all antennas contribute equally?” *IEEE Trans. Commun.*, vol. 63, no. 11, pp. 3917–3928, Nov. 2015.

[162] J. Hoydis, C. Hoek, T. Wild, and S. ten Brink, “Channel measurements for large antenna arrays,” in *Proc. IEEE Int Symp. Wireless Commun. Syst.*, Paris, France, Aug. 2012, pp. 811–815.

[163] C. Chen, V. Volski, L. Van der Perre, G. A. E. Vandenbosch and S. Pollin, "Finite Large Antenna Arrays for Massive MIMO: Characterization and System Impact," in IEEE Transactions on Antennas and Propagation, vol. 65, no. 12, pp. 6712-6720, Dec. 2017.

[164] 3GPP, “Tr36.814 v9.2.0: Lte; evolved universal terrestrial radio access (e-utra); radio frequency (rf) system scenarios (release 9),” 3GPP, Technical Report, Report, 2017.

I. Appendix: Edge and cell capacity difference between two different scenarios

Optimum Tilt angle: 8°	Cell edge capacity: (Mbit/s)	Cell capacity: (Mbit/s)
All cells for Scenario 2	14.56	42.75

Tilt angle: 7.5° Centre Cell only for Scenario 1	Cell edge capacity: (Mbit/s)	Cell capacity: (Mbit/s)	Cell edge Difference compared with Scenario 2 (%)	Cell Difference compared with Scenario 2 (%)
Cell 1:	14.50	41.76	-0.41	-2.32
Cell 2:	14.55	42.06	-0.07	-1.61
Cell 3:	14.54	42	-0.14	-1.75
Cell 4:	14.55	41.96	-0.07	-1.85
Cell 5:	14.58	42.08	0.14	-1.57
Cell 6:	14.52	41.74	-0.27	-2.36
Average of 6 cells:	14.54	41.93	-0.14	-1.91
Centre Cell:	15.12	44	3.85	2.92

Tilt angle: 7° Centre Cell only for Scenario 1	Cell edge capacity: (Mbit/s)	Cell capacity: (Mbit/s)	Cell edge Difference compared with Scenario 2 (%)	Cell Difference compared with Scenario 2 (%)
Cell 1:	14.44	41.62	-0.82	-2.64
Cell 2:	14.48	42.12	-0.55	-1.47
Cell 3:	14.40	41.30	-1.10	-3.39
Cell 4:	14.42	41.28	-0.96	-3.44
Cell 5:	14.50	42.09	-0.41	-1.54
Cell 6:	14.44	41.60	-0.82	-2.69
Average of 6 cells:	14.45	41.67	-0.78	-2.53
Centre Cell:	15.31	45.04	5.15	5.36

Tilt angle: 6.5° Centre Cell only for Scenario 1	Cell edge capacity: (Mbit/s)	Cell capacity: (Mbit/s)	Cell edge Difference compared with Scenario 2 (%)	Cell Difference compared with Scenario 2 (%)
Cell 1:	14.45	41.48	-0.76	-2.97
Cell 2:	14.53	42	-0.21	-1.75
Cell 3:	14.36	40.51	-1.37	-5.24
Cell 4:	14.38	40.54	-1.24	-5.17
Cell 5:	14.51	42.03	-0.34	-1.68
Cell 6:	14.43	41.46	-0.89	-3.02
Average of 6 cells:	14.44	41.34	-0.80	-3.31

Centre Cell:	15.64	46	7.42	7.60

Tilt angle: 6° Centre Cell only for Scenario 1	Cell edge capacity: (Mbit/s)	Cell capacity: (Mbit/s)	Cell edge Difference compared with Scenario 2 (%)	Cell Difference compared with Scenario 2 (%)
Cell 1:	14.40	41.21	-1.10	-3.60
Cell 2:	14.43	41.52	-0.89	-2.88
Cell 3:	14.33	39.97	-1.58	-6.50
Cell 4:	14.32	39.99	-1.65	-6.46
Cell 5:	14.42	41.55	-0.96	-2.81
Cell 6:	14.36	41.19	-1.37	-3.65
Average of 6 cells:	14.38	40.91	-1.26	-4.32
Centre Cell:	16.21	47.09	11.33	10.15

Tilt angle: 5.5° Centre Cell only for Scenario 1	Cell edge capacity: (Mbit/s)	Cell capacity: (Mbit/s)	Cell edge Difference compared with Scenario 2 (%)	Cell Difference compared with Scenario 2 (%)
Cell 1:	14.37	40.75	-1.30	-4.68
Cell 2:	14.64	41.75	0.55	-2.34
Cell 3:	14.26	39.37	-2.06	-7.91
Cell 4:	14.25	39.35	-2.13	-7.95
Cell 5:	14.67	41.72	0.76	-2.41
Cell 6:	14.35	40.73	-1.44	-4.73
Average of 6 cells:	14.42	40.61	-0.94	-5.00
Centre Cell:	16.35	47.28	12.29	10.59

Tilt angle: 5° Centre Cell only for Scenario 1	Cell edge capacity: (Mbit/s)	Cell capacity: (Mbit/s)	Cell edge Difference compared with Scenario 2 (%)	Cell Difference compared with Scenario 2 (%)
Cell 1:	14.25	40.46	-2.13	-5.36
Cell 2:	14.60	41.43	0.27	-3.09
Cell 3:	14.25	38.65	-2.13	-9.59
Cell 4:	14.23	38.62	-2.27	-9.66
Cell 5:	14.62	41.41	0.41	-3.13
Cell 6:	14.26	40.44	-2.06	-5.40
Average of 6 cells:	14.37	40.17	-1.32	-6.04
Centre Cell:	16.49	47.88	13.26	12

Tilt angle: 4.5° Centre Cell only for Scenario 1	Cell edge capacity: (Mbit/s)	Cell capacity: (Mbit/s)	Cell edge Difference compared with Scenario 2 (%)	Cell Difference compared with Scenario 2 (%)
Cell 1:	14.35	40.4	-1.44	-5.50
Cell 2:	14.72	41.2	1.10	-3.63
Cell 3:	14.10	38.26	-3.16	-10.50
Cell 4:	14.07	38.24	-3.37	-10.55
Cell 5:	14.74	41.22	1.24	-3.58
Cell 6:	14.34	40.38	-1.51	-5.54
Average of 6cells:	14.39	39.95	-1.19	-6.55
Centre Cell:	16.83	47.85	15.59	11.93

Tilt angle: 4° Centre Cell only for Scenario 1	Cell edge capacity: (Mbit/s)	Cell capacity: (Mbit/s)	Cell edge Difference compared with Scenario 2 (%)	Cell Difference compared with Scenario 2 (%)
Cell 1:	14.32	40.28	-1.65	-5.78
Cell 2:	14.64	40.97	0.55	-4.16
Cell 3:	14	37.88	-3.85	-11.39
Cell 4:	13.95	37.84	-4.19	-11.49
Cell 5:	14.68	41.01	0.82	-4.07
Cell 6:	14.3	40.26	-1.79	-5.82
Average of 6 cells:	14.32	39.71	-1.69	-7.12
Centre Cell:	16.79	47.41	15.32	10.90

Tilt angle: 3.5° Centre Cell only for Scenario 1	Cell edge capacity: (Mbit/s)	Cell capacity: (Mbit/s)	Cell edge Difference compared with Scenario 2 (%)	Cell Difference compared with Scenario 2 (%)
Cell 1:	14.28	40.31	-1.92	-5.71
Cell 2:	14.75	40.97	1.30	-4.16
Cell 3:	13.84	37.28	-4.95	-12.80
Cell 4:	13.80	37.25	-5.22	-12.87
Cell 5:	14.79	41	1.58	-4.09
Cell 6:	14.27	40.29	-1.99	-5.75
Average of 6 cells:	14.29	39.52	-1.87	-7.56
Centre Cell:	16.90	47.65	16.07	11.46

Tilt angle: 3° Centre Cell only	Cell edge capacity: (Mbit/s)	Cell capacity: (Mbit/s)	Cell edge Difference	Cell Difference compared with

for Scenario 1			compared with Scenario 2 (%)	Scenario 2 (%)
Cell 1:	14.26	40.40	-2.06	-5.50
Cell 2:	14.93	40.73	2.54	-4.73
Cell 3:	13.70	36.75	-5.91	-14.04
Cell 4:	13.66	36.72	-6.18	-14.11
Cell 5:	14.95	40.75	2.68	-4.68
Cell 6:	14.25	40.38	-2.13	-5.54
Average of 6 cells:	14.29	39.29	-1.84	-8.1
Centre Cell:	17.07	47.72	17.24	11.63

Tilt angle: 2.5° Centre Cell only for Scenario 1	Cell edge capacity: (Mbit/s)	Cell capacity: (Mbit/s)	Cell edge Difference compared with Scenario 2 (%)	Cell Difference compared with Scenario 2 (%)
Cell 1:	14.23	40.66	-2.27	-4.89
Cell 2:	14.85	40.62	1.99	-4.98
Cell 3:	13.57	36.48	-6.80	-14.67
Cell 4:	13.54	36.46	-7.01	-14.71
Cell 5:	14.83	40.65	1.85	-4.91
Cell 6:	14.22	40.64	-2.34	-4.94
Average of 6 cells:	14.21	39.25	-2.43	-8.18
Centre Cell:	17.11	46.75	17.51	9.36

II. Appendix: LTE network system Simulator

In this part, an overall demonstration of the LTE system level simulator used for the system performance analysis will be described here.

A. Functionality

The simulator utilised here involving the following features:

- Homogeneous Cell Deployment of varying inter-site distances
- Heterogeneous Cell Deployment
- Different RATs: LTE, HSPA, Wi-Fi
- Flexible sectorization and frequency reuse patterns
- Antenna height and tilt optimization
- Various propagation models

- Multiple antenna transmission
- User Mobility, Distribution Patterns, Density and Traffic Load
- Uplink and Downlink throughput
- Cooperative Multi-Point (CoMP)
- Sleep Mode
- Relays
- Mobility Model (No Soft-Handover Functionality)

B. Structure

The main code can be divided into the following sections, which will be described in the following part:

1) Input Parameters
2) UE Distribution and Mobility
3) Cell Distribution
4) UE Select Serving Cell
5) Scheduler
6) Downlink and Uplink Throughput
7) Graphical and Numerical Output of Results

Each section of the code is comprised of a series of Key and Sub Functions, that call upon and yield a series Input and Derived parameters

The code in Matlab can be categorised into the following types:

- Input Parameter: A flexible numerical or logical parameter that can be changed
- Derived Parameter: A parameter that is a function of the input parameters. This usually can not be changed.
- Key Function: A global function that is integral to the simulation
- Sub Function: A local function that forms part of the key function that needs to be modified or replaced in order to change the key function.

Operational parameters outline the customizable physical parameters which affect all simulation results and cell deployment. Each one of these parameters is independent and a degree of freedom in the network. Additional parameters in network operation can be added.

C. Simulation Area

Simulation area is currently defined as a circle of a certain radius, depending on the inter-BS distance, so that each simulation area captures 19 BSs for interference purposes. The coordinate system is primarily a Cartesian Coordinate system with the centre (0,0) point at the centre of the simulation area. This coincides with the location of the first and central cell-site.

D. Bandwidth and Frequency Reuse Pattern

Bandwidth is defined as the maximum potential available bandwidth to each cell-sector. The effective bandwidth is affected by the frequency re-use pattern and other parameters. Frequency Re-use pattern is defined as the standard pattern used to mitigate interference between cell-sectors. The accepted values are 1 and 3, and in the case of advanced deployment, 2 and 6 are also accepted. Two operating frequency ranges are defined, that for the normal cell deployment or inner cell sectors and that for outer cell sectors if applicable. The values taken are in MHz and any value is accepted.

Deployment Parameters outline the customizable physical parameters which affect cell deployment. Each one of these parameters is independent and a degree of freedom in the network. Additional parameters in deployment can be added.

E. Cell Radius and Inter-site Distance

The effective cell radius is defined by the physical inter-cell-site distance and the resulting interference pattern. The traditional homogenous cell structure is the hexagonal grid and the specific parameters are:

- Homogeneous Inter-cell-site Distance=1.5 cell radius
- Number of cell-site tiers (t) required to cover the simulation area fully.
- Number of cell-sites for t tiers=$1+6t$ cell-sites

F. Sectorization: Horizontal

The number of horizontal cell-sectors per cell-site is currently limited to:

- 1 Omni-directional Sector

- 3 Directional Sectors
- 6 Directional Sectors

However, this can be expanded to any number of sectors

G. Sectorization: Vertical

The number of vertical cell-sectors per cell-site is currently limited to:

- 1 One set of horizontal sectors
- 2 Two sets of horizontal sectors

Each set of horizontal sectors can be any number. Each vertical sector can off-set its sector direction from other vertical sectors.

H. Overlapping Heterogeneous Cells

Optionally, overlapping heterogeneous cells can be added to the existing homogenous cells. The logical values accepted are 0 for no het-cells and 1 for a pre-defined set of het-cells.

I. Multiple Antennas

Multiple antenna technologies (MIMO) can be added with the logical parameter, which takes the following inputs:

- 11 SISO
- 12 SIMO 1X2 Maximum Radio Combining (MRC) at the UE
- 21 MISO 2X1 Alamouti
- 22 SIMO 2X2 Alamouti

J. Antenna Pattern and parameters

Antenna patterns are defined in the function, which contains data on several antenna patterns appropriate for different situations. The input parameters required for this function are: angle from bore-sight, desired pattern and desired plane. The output parameter is the antenna gain in dB. Furthermore, antenna placement parameters can be changed in terms of its height and down-tilt angle.

K. Offered load and User density

User density is defined as the number of active users demanding a certain minimum QoS. The minimum QoS demanded is given by the parameter, in bit/s. The offered load per unit area can be any numerical value and common values.

L. User Distribution

The users can be distributed either randomly or in a fixed manner. The function responsible for it takes in the parameters: total number of users, simulation radius, and distribution type. In random distribution, the total number of users are generated so that their cartesian position does not exceed the previously defined simulation area. If it is exceeded, a new user is created. In fixed distribution, the users are distributed in a Manhattan grid system. The output of the function is the x and y co-ordinates of the user positions with respect to the centre of the simulation area.

M. Mobility

Mobility is controlled by the key function: Mobility, which has the following customizable features:

- UE speed: The speed of the user in m/s
- Movement Model: 0 for static, 1 for random browning motion, and 2 for manhattan grid movement, which is restricted to be in orthogonal directions only.
- Restriction: 0-1, where 0 means no correlation with previous movement and 1 means full correlation (same as static)

The result is shown in Figure 1 for 2 models: Browning Motion (restriction 0.1) and Manhattan Motion (restriction 0.5).

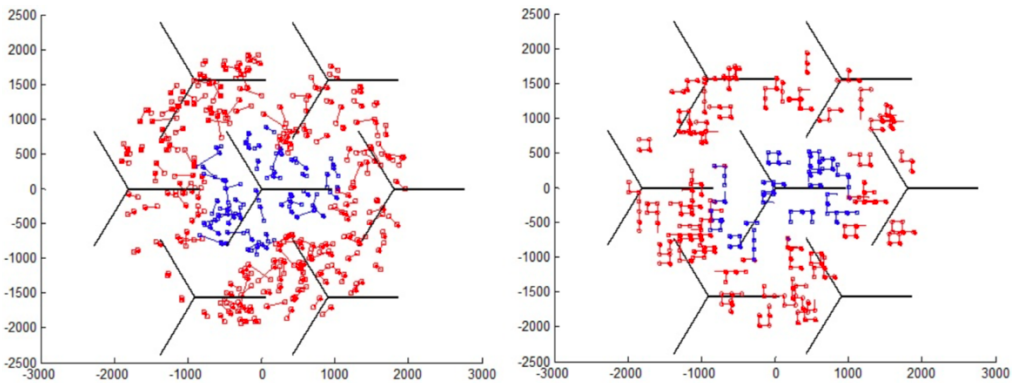

Figure 1: Simulation plot of Users under mobility model for 2 models: Browning Motion and Manhattan Motion.

N. Sleep Mode Management

The sleep mode input is a logical and numerical input which currently takes the following:

- Sleep mode=-1: No sleep mode implemented
- Sleep mode=0: Passive Sleep Mode, whereby cell-sites sleep when no users are inside the cell-site's sectors.
- Sleep mode>0: Aggressive Sleep Mode, whereby cell-sites sleep when there are a number of users in the cell-site's sectors, and this number can be freely defined.

O. Propagation Model: Pathloss

The propagation model is defined in Key Function: Pathloss. The function takes the following derived inputs: Distance between transmitter and receiver (m), central frequency (MHz), height of antenna (m), and the pathloss model required. The following pathloss models have been used:

- Model=1: WINNER II Dense Urban Marco
- Model=2: WINNER II Dense Urban Micro
- Model=3: COST 231 HATA
- Model=4: COST 231 Walfish-Ikegami
- Model=5: Free-space

The output parameter is the pathloss in dB.

Figure 2 presents the different pathloss models over the distances and It can be seen that the difference between the Winner II Urban and Cost Hata path loss model is small (1 to 3dB) for an ISD above 200m, and that the difference between Cost 231 NLOS and the other two path loss models is between 3 to 9dB. Both the Winner II Urban and Cost Hata Path loss models are empirical ones and the Cost 231 NLOS is a semi-empirical model based on the real city structures.

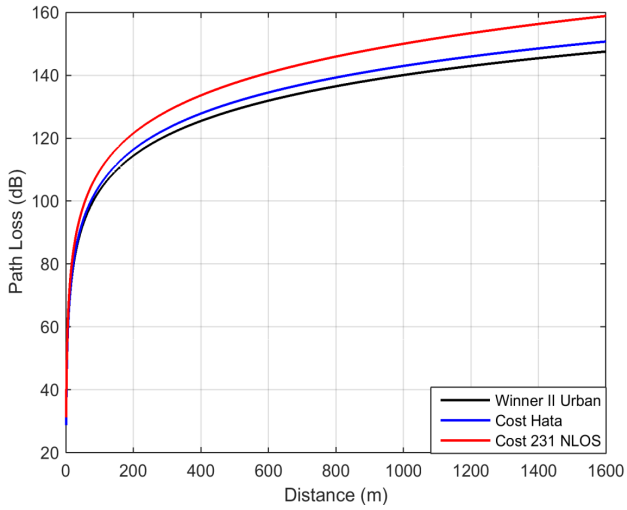

Figure 2: Pathloss Models for: Winner II Urban, COST Hata and COST 231 NLOS

P. Propagation Model: Fading

The multipath fading model is derived from a number of models, from which only one can be employed at a time.

- Independent Rayleigh, whereby each sub-carrier is faded by an independently generated zero mean unit variance circular symmetric gaussian variable
- WINNER II, whereby a number of sub-carriers have a 90% correlation with a common Rayleigh complex fading gain. The number of sub-carriers is determined by the delay spread of the WINNER model considered

The following derived inputs are taken when calling the function:

- MIMO technology
- Channel concerned: 1 for signal channel, 2 for interference channel
- Propagation fading model: 1 for Rayleigh, 2 for WINNER
- Sub-carrier size
- Sequence number, which is the s^{th} sub-carrier for that particular user at that particular position
- Correlated fading value, which is a vector with the complex fading gains of the correlated value, used in WINNER II models

Q. AWGN

The AWGN is defined as the thermal noise at 290 Kelvins with an additional UE noise figure of 8dB. The input parameters are as follows:

- UE Noise Figure: given as 8dB usually
- Thermal Noise per Hz, given as 290Kelvin multiplied by Plank's constant

The derived noise is given by Derived Parameter: Noise, given as the subcarrier size multiplied by the thermal noise, then multiplied by the UE Noise figure.

Having defined all the necessary input parameters, populated the simulation space with users, the simulator now deploys the cell-sites and their associated cell-sectors. The input parameters are as follows: cell radius (m), number of horizontal sectors, number of vertical sectors, heterogeneous cells, frequency re-use pattern, and antenna tilts parameters.

The cell-site tiers are distributed so that they cover the simulation area. This is accomplished with the following algorithm:

- Calculate the minimum number of Tiers of Cell-sites required to at least cover the simulation area. A tier is given the variable *K*. Do this by considering from 1 to an unrealistic large number of tiers and remembering the lowest number that serves the purpose. Each tier of cells has 6(*k*-1) cell-sites, and this is derived from the fact that each tier has at least 6 cell-sites at the hexagonal edges and 6(*k*-2) cell-sites at the tier edges.
- Distribute the cell-sites per tier and remember their x and y co-ordinates. This is done by using the formula that there are always 6 cell-sites in the corners of a tier and 6(*k*-2) cell-sites on the edges.
- Distribute the homogeneous cell-sectors per cell-site and remember their x and y co-ordinates. The co-ordinate of each sector is also the co-ordinate of their parent cell-site. This is done by considering if the cell-site implements vertical sectorization. If not, the section of the code generates the cell-sectors for that configuration.
- Each sector is assigned a frequency pattern number based on the re-use parameter. Antenna tilt for each cell-sector is also remembered here, depending on what type of cell sector it is. For example, a single cell-sector omni-directional antenna is different to a 6-sector directional antenna. The type of cell-sector is defined by Sector-type.

- Distribute the heterogeneous cells and remember their x and y co-ordinates. If the requirement for het-cells is activated, the overlap of het-cells is defined at the cell-site edges.

The output parameters are as follows: the total number of cell-sites and their x and y coordinates from the centre of the simulation area, total number of sectors and their x and y coordinates, the type, angle, antenna pattern and frequency pattern of each cell sector.

After the cells are distributed by the Cell Distribution key function, the UEs select their cells based on a certain criterion. For each UE, the distance, antenna gain, pathloss and hence SNR to each cell's antenna is calculated. From which, the best SNR is selected and the cell sector's identity (*o*) is coupled with the UE's identity (*i*). Furthermore, the cell-site (*n*) associated with each UE is also stored. The horizontal angle of each UE to their serving antenna is stored as well as the target throughput which can optionally depend on the UE's location in the cell. The number of UEs per cell-sector is also computed and stored. Only the central cell-site and its sectors are used to extract performance.

R. Scheduler

- Round Robin: In the round robin scheduler the sub-carriers are evenly partitioned between the UEs. Whether the UE uses all of its resource blocks or just the ones that are enough to satisfy its QoS target depends on the scheduler type, whereby 0 means all the RBs and 1 means QoS dependent
- Proportional fair throughput: Each user generates a matrix with the expected SINR of each sub-carrier potentially available. This is fed into a time-domain scheduler and the throughput is calculated accordingly.
- Proportional fair ECR: Each user generates a matrix with the expected SINR of each sub-carrier potentially available. This is fed into a time domain scheduler and the throughput is calculated accordingly.

S. Throughput

Only the central cell-site and its sectors are used to extract performance. If the central cell-site is in sleep mode, its users are camped onto the neighbouring cells.

- Received SINR

For LTE, the received SINR ($r_{s,k}$) in a sub-carrier (s) for cell k is calculated as a function of the transmit power, antenna gain, interference, noise, shadow fading, multipath fading effects:

$$r_{s,k} = \frac{|h_k|^2 10^{(\lambda_k + s_i + A_{bs,k} + A_{cell}(\theta))/10} P_{s,k}^{DSCH}}{n_o n_{UE} + \sum_{j=1, j\neq k}^{N_{cell}} |h_k| \, |h_j| 10^{(\lambda_j + S_j + A_{bs,j} + A_{cell}(\theta))/10} P_{s,j}}$$

Where $P_{s,j}$ is the transmit power per sub-carrier and j indicates the interfering cells' sub-carriers. Interfering sub-carriers only exist if another user is utilizing that interfering sub-carrier. Log-normal shadow fading is defined as $S = N(0, {\sigma_{shadow}}^2)$. The multi-path fading for each sub-carrier depends on the delay spread.

- Downlink Throughput and Outage Performance

The downlink throughput of each user is given by either the Shannon expression with a back-off or the Modulation and coding system (MSC) Lookup Table. The Downlink throughput takes the following input parameters: received SINR, bandwidth, MIMO antenna configuration and the cell radius, which affects the propagation model and is required to determine the MCS lookup table. In return the function returns the rate for a single sub-carrier for that user.

The commonly used Shannon capacity expression for ideal Gaussian inputs gives an upper throughput performance bound. However, it has been shown that due to mutual information saturation, the bound is particularly inaccurate at a medium-high signal-to-interference-noise-ratio (SINR), where realistic modulation schemes' mutual information is likely to saturate. For this reason, the backed-off Gaussian input expression, which limits the maximum mutual information that can be achieved in the following way:

$$R_{Gaussian,Adjusted,s,k} = \log_2(1 + \frac{r_{s,k}}{F})$$

Where F=1.5 is the adjustment factor.

T. Graphical Output

This is a customizable plot showing the average received SINR as a mesh. The size and resolution of the grid is customized by the following parameters: size and bin. This can be customized to plot SINR distribution and any other already utilized parameter.

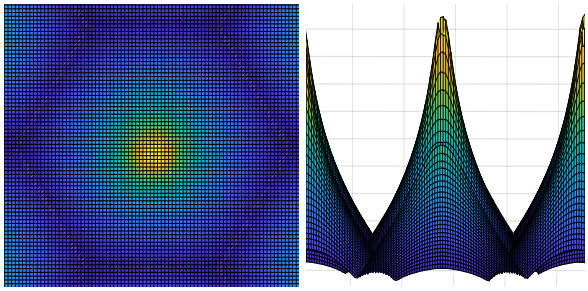

1 Sector with Frequency Re-use Pattern 1 at 1.9GHz for ISD of 500m.

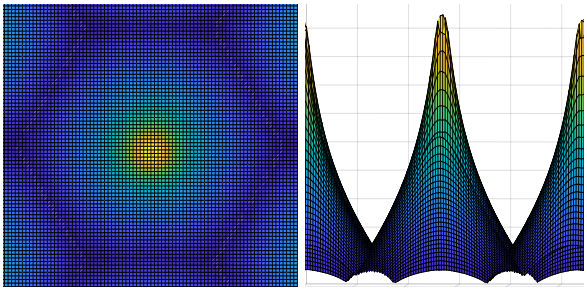

1 Sector with Frequency Re-use Pattern 3 at 1.9GHz for ISD of 500m.

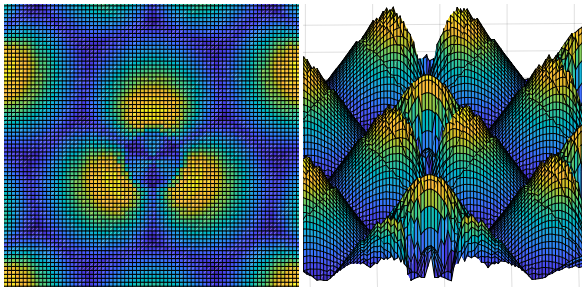

3 Sectors with Frequency Re-use Pattern 1 at 1.9GHz for ISD of 500m.

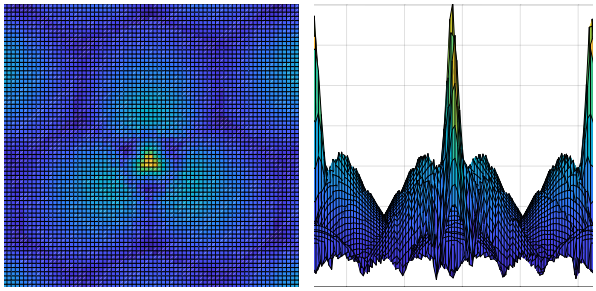

3 Sectors with Frequency Re-use Pattern 3 at 1.9GHz for ISD of 500m.

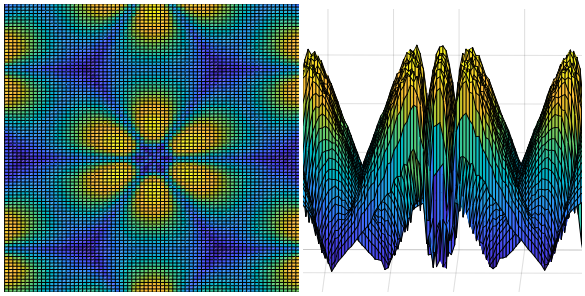

6 Sectors with Frequency Re-use Pattern 1 at 1.9GHz for ISD of 500m.

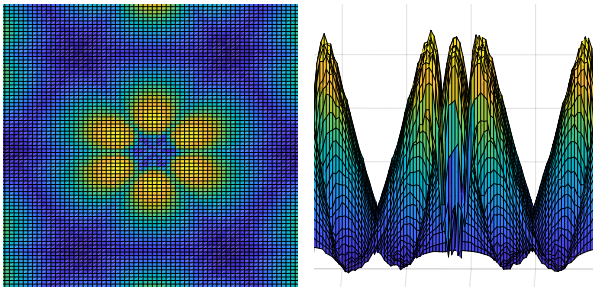

6 Sectors with Frequency Re-use Pattern 3 at 1.9GHz for ISD of 500m.

Figure 3: Averaged Received SINR plot for a variety of deployment scenarios with different number of sectors and frequency re-use patterns.